On Aerothermal Effects of Film Cooling on Turbine Blades with Flow Separation

von der
Fakultät für Luft- und Raumfahrttechnik
der Universität der Bundeswehr München

zur Erlangung des Grades eines
Doktors der Ingenieurwissenschaften
genehmigte Dissertation

vorgelegt von

Dipl.-Ing. Reinaldo Araújo Gomes

Preface

This thesis is an outcome of experimental and numerical work carried out at the Institute of Jet Propulsion of the Universität der Bundeswehr München from 2005 to 2009.

In these years I had the pleasure to (not only) work with many people and it is my wish to thank them for all their support and the good time I spent at the institute. First of all I want to express my gratefulness to Prof. Niehuis, the head of the institute. His dedication to the institute and its staff, his contribution in form of expertise and his encouragements for further researches helped to improve this work greatly. I thank Prof. Hennecke for taking part in the board of examiners and for his precious input to this thesis. Prof. Pfitzner is acknowledged for being the chairman of the board of examiners. After a previous experience with him as my supervisor it was a great pleasure to know he would take this duty. I thank Prof. Staudacher for the confidence he put on me, when I first started at the institute.

Most of the experiments presented here were carried out within the AITEB-2 project and I thank all the partners for the great collaboration. In especially I want to point out Dr. Lutum from MTU Aero Engines for being a wise work package leader — albeit he is still young — and his professional competence. The aid given by the University of Florence and the Turbomachinery and Propulsion Department from the Von Karman Institute in the implementation of the measurement technique with thermochromic liquid crystals is acknowledged. Also the contribution of Prof. Doerffer and his staff from the Polish Academy of Sciences with the development of the air jet vortex generators is acknowledged.

I thank all my colleagues from the past and the present, without any exception, for the good and harmonious atmosphere making the work much more pleasant. Though it is hard to point out single persons I want to highlight some with whom I spent most of these years: I thank my office-mate Marco Montis for being a good friend, his vast knowledge on turbomachinery and beyond and for his ever readiness to help. I thank Dr. Markus Martinstetter, Marco Schwarze, Jens Iseler and Tom Ludewig for the good friendship and the time spent together at the institute. I thank Dr. Christian Wakelam for proofreading parts of the thesis and Martin Breuer for the thorough measurements carried out on the liquid crystals.

Last but not least I thank all the persons close to me which helped and encouraged me through these years: relatives and friends. In especially I thank my parents, for their persistence and devotion shown through all these years what makes them real examples to follow.

Munich, August 2010

Summary

The high pressure turbine of jet engines or stationary gas turbines is set under high thermal stress and efficient cooling techniques have to be used in order to prevent the metallic parts from serious damage. Modern turbine design tries to increase the aerodynamic blade loading in order to reduce the number of blades per stage. This can reduce the needed coolant mass flow and the engine weight increasing the efficiency of the turbomachine, but strong flow separation may counterbalance the positive effects and this limits the achievable aerodynamic load.

In this thesis experimental and numerical analysis with two linear high pressure turbine blade cascades are presented. The blades are film cooled and were designed in order to exhibit massive flow separation on the pressure and, for the second blade, on the suction side. The blade for the suction side studies is equipped with vortex generating jets for control of flow separation. The experiments comprise the measurement of the blade load and of the total pressure losses, near wall flow visualizations and Schlieren pictures at engine relevant Mach and Reynolds numbers. Furthermore the heat transfer and adiabatic film cooling effectiveness was extensively measured on both cascades. Numerical analysis with standard RANS methods and more advanced models, Detached Eddy Simulation (DES) and Large Eddy Simulation (LES), show the applicability of the simulation tools on such flows.

Thermochromic liquid crystals are used for measurements of the surface temperature. Extensive studies on the viewing an illumination angle sensitiveness are carried out and a method is presented which is able to correct the perceived colour for oblique incidences of the camera and the illumination on the surface. A post processing method is also presented which uses FEM to calculate the adiabatic wall temperature on a plexiglas blade. Though plexiglas has a low heat conductivity, heat conduction is still present and the FE-analysis increases significantly the accuracy of the measurements. Furthermore a new formulation is proposed for the evaluation of the overall film cooling effectiveness. While in the measurements the heat transfer and the adiabatic film cooling effectiveness are measured separately, both effects are present simultaneously in the machine. The proposed parameter estimates the film cooling effectiveness in presence of heat transfer into the blade and allows to better evaluate the film cooling effect on the local surface temperature.

The results on the pressure side show that it turns out to be difficult to obtain efficient film cooling when the change on the local heat transfer is taken into account. The numerical tools show some deficits in predicting accurately all the flow phenomena present in the separated flow region. On the suction side, the flow separation can be effectively suppressed and good film cooling effectiveness can be obtained.

Zusammenfassung

Die Hochdruckturbine eines Triebwerks oder einer stationären Gasturbine ist hohen thermischen Belastungen ausgesetzt und effiziente Kühltechniken müssen angewendet werden, um die Metalkomponenten vor Schaden zu bewahren. Bei einer fortschrittlichen Turbinenauslegung wird versucht, die aerodynamische Belastung der Schaufel zu erhöhen, um die Anzahl der Schaufeln pro Stufe zu verringern. Dies kann die benötigte Kühlluftmenge und das Gewicht des Triebwerks verringern, was den Wirkungsgrad der Turbomaschine erhöht, aber starke Strömungsablösung kann die positiven Effekte aufwiegen, was die erreichbare aerodynamische Schaufelbelastung limitiert.

In dieser Arbeit werden experimentelle und numerische Analysen mit zwei linearen Hochdruckturbinen-Gittern vorgestellt. Die Schaufeln sind filmgekühlt und wurden mit der Absicht ausgelegt, eine massive Ablösung an der Druckseite und für die zweite Schaufel an der Saugseite zu erzielen. Die Schaufel für die saugseitigen Studien ist mit wirbelerzeugenden Luftstrahlen ausgelegt, um der Strömungsablösung entgegenzuwirken. Die Experimente umfassen die Messung der Schaufelbelastung und der Totaldruckverluste, Visualisierung der wandnahen Strömung und Schlierenaufnahmen bei maschinenähnlichen Mach- und Reynolds-Zahlen. Des Weiteren wurden der Wärmeübergang und die adiabate Filmkühleffektivität an beiden Kaskaden ausführlich gemessen. Numerische Analysen mit Standard-RANS-Verfahren und aufwendigeren Modellen, Detached Eddy Simulation (DES) und Large Eddy Simulation (LES), veranschaulichen die Anwendbarkeit der Simulationswerkzeuge für solche Strömungen.

Die Oberflächentemperatur wird mit thermochromatischen Flüssigkristallen gemessen. Es werden ausführliche Untersuchungen zur Sensitivität der Kristalle auf die Variation des Beobachtungs- und Beleuchtungswinkels durchgeführt und es wird eine Methode gezeigt, die es erlaubt die aufgenommene Farbe für schräge Inzidenz der Kamera- oder Beleuchtungsachse zu korrigieren. Ein Verfahren zur Nachbearbeitung der Messergebnisse wird vorgestellt das FE-Methoden nutzt, um die adiabate Wandtemperatur auf einer Plexiglasschaufel zu berechnen. Obwohl Plexiglas eine geringe Wärmeleitfähigkeit besitzt, ist dennoch ein Wärmestrom vorhanden und die FE-Analyse erhöht die Genauigkeit der Messungen beträchtlich. Darüber hinaus wird eine neue Formulierung vorgeschlagen, um die gesamte Filmkühleffektivität zu bestimmen. Während in den Experimenten der Wärmeübergang und die adiabate Filmkühleffektivität getrennt gemessen werden, treten beide Effekte in der Maschine gleichzeitig auf. Der vorgeschlagene Parameter bewertet die Filmkühleffektivität bei vorhandenem Wärmestrom in die Schaufel und erlaubt es, den Filmkühleffekt auf die lokale Wandtemperatur besser zu bestimmen.

Die Ergebnisse für die Druckseite zeigen, dass es sich als schwierig erweist eine effiziente Filmkühlwirkung zu erzielen, wenn die Veränderung des lokalen Wärmeübergangs in betracht gezogen wird. Die numerischen Modelle zeigen Defizite bei der Voraussage aller Strömungsphänomene in der Ablösezone. Auf der Saugseite kann die Strömungsablösung effektiv unterdrückt und eine gute Filmkühleffektivität kann erzielt werden.

Contents

List of Figures

List of Tables

Nomenclature

A	$[\text{m}^2]$	area
B	$[\text{-}]$	blue
c	$[\text{m}]$	chord
	$[\text{m/s}]$	velocity of light
c_f	$[\text{-}]$	shear stress coefficient
C_s	$[\frac{\text{kg}}{\text{ms}\sqrt{\text{K}}}]$	Sutherland constant $= 1.458 \cdot 10^{-6}$
c_p	$[\frac{\text{J}}{\text{kg}\cdot\text{K}}]$	specific heat at constant pressure
D	$[\text{m}]$	diameter
E	$[\text{m}^2/\text{s}]$	energy spectrum
	$[\text{V}]$	voltage
f	$[\frac{1}{\text{s}}]$	frequency
G	$[\text{-}]$	green
H	$[\text{-}]$	hue
H_{12}	$[\text{-}]$	shape factor
h	$[\text{m}]$	blade span
	$[\frac{\text{W}}{\text{K}\cdot\text{m}^2}]$	heat transfer coefficient
I	$[\text{-}]$	intensity
	$[\text{A}]$	electric current
K	$[\text{-}]$	acceleration parameter
K_α, K_β, K_M	$[\text{-}]$	coefficients for evaluation with the five-hole probe
k	$[\frac{\text{W}}{\text{K}\cdot\text{m}}]$	heat conductivity
	$[\text{m}^2/\text{s}^2]$	turbulence kinetic energy
l	$[\text{m}]$	length
Ma	$[\text{-}]$	Mach number
Nu	$[\text{-}]$	Nusselt number
n	$[\text{-}]$	refraction index
Pr	$[\text{-}]$	Prandtl number
p	$[\text{m}]$	crystal twist pitch
	$[\text{Pa}]$	pressure
q	$[\text{Pa}]$	dynamic pressure
$\dot{q}$	$[\frac{\text{W}}{\text{m}^2}]$	specific heat flux
R	$[\frac{\text{J}}{\text{kg}\cdot\text{K}}]$	ideal gas constant for air $= 287$
	$[\text{-}]$	red
Ra	$[\text{-}]$	Rayleigh number
Re	$[\text{-}]$	Reynolds number
r	$[\text{-}]$	recovery factor
S	$[\text{-}]$	saturation
	$[\text{K}]$	Sutherland constant $= 110.4$
Sr	$[\text{-}]$	Strouhal number

St	[-]	Stanton number
T	[K]	temperature
Tu	[%]	turbulence intensity
t	[m]	pitch
	[s]	time
U	[$\frac{m}{s}$]	velocity
u	[m]	coordinate in circumferential direction
x,y,z	[m]	cartesian coordinate
Zw	[-]	Zweifel number

Greek

α	[°]	local angle to surface
	[°]	spanwise flow angle
β	[°]	circumferential flow angle
β_s	[°]	stagger angle
γ	[-]	isentropic coefficient
γ_{fs}	[°]	fan-shape angle
γ_r	[°]	compound angle
ζ	[-]	Reynolds number based factor
η	[-]	adiabatic film cooling effectiveness
	[m]	wall distance
Θ	[-]	dimensionless temperature parameter
Λ_x	[m]	integral turbulence length scale
λ	[m]	wave length
μ	[$\frac{kg}{m \cdot s}$]	dynamic viscosity
ν	[$\frac{m^2}{s}$]	kinematic viscosity
ξ	[-]	Reynolds number based factor
ρ	[$\frac{kg}{m^3}$]	density
τ	[s]	time increment
ω	[-]	total pressure loss coefficient

Subscripts

∞	free stream (outside the boundary layer)
0	without film cooling
1	inlet plane
2	outlet plane
amb	ambient
aw	adiabatic wall
ax	axial
bar	bars of wake generator
bck	background image
c	coolant
$cond$	conduction
$conv$	convective

cyl	cylindrical
$eval$	evaluated
FHP	five-hole probe
fs	fan-shape
hf	heating foil
k	chamber (pressure tank)
l	laminar
r	recovery
ref	reference
s	isentropic
t	total, turbulent
th	thermodynamic
VK	settling chamber
w	wall
wg	wake generator
$'$	time dependent variation
$*$	critical value (for Ma=1)

Abbreviations

ACARE	*A*dvisoury *C*ouncil for *A*eronautics *R*esearch in *E*urope
AITEB	*A*erothermnal *I*nvestigations on *T*urbine *E*ndwalls and *B*lades
AJVG	*a*ir *j*et *v*ortex *g*enerators
CCD	*c*harge *c*oupled *d*evice
CFD	*c*omputational *f*luid *d*ynamics
CTA	*c*onstant *t*emperature *a*nemometry
DES	*d*etached *e*ddy *s*imulation
FC	*f*ilm *c*ooling
FCE	*f*ilm *c*ooling *e*ffectiveness
HPT	*h*igh *p*ressure *t*urbine
HT	*h*eat *t*ransfer
HTC	*h*eat *t*ransfer *co*efficient
LED	*l*ight *e*mitting *d*iode
LES	*l*arge *e*ddy *s*imulation
PPD	*p*rofile *p*ressure *d*istribution
RMS	*r*oot *m*ean *s*quare
RTD	*r*esistance *t*emperature *d*evice
TLC	*t*hermochromic *l*iquid *c*rystals
WG	*w*ake *g*enerator

1 Introduction

Since the beginning of industrialization, and especially in the western world, the lifestyle has been marked by an increase in energy consumption without parallel in man's history. This energy consumption has mostly been "fuelled" in the true sense of the word with fossil fuels such as coal, oil, natural gas and in minor scale wood. The energy is mainly used for heating, electricity generation and transport allowing a very comfortable or even luxurious life and today's world is almost unthinkable without such high energy consumption.

The continuously higher energy consumption is leading to a rapid diminishing of the available resources and to an increase of the carbon-dioxide emissions. The latter has gained a lot of interest in the past decades since it is taken to be the major cause for the increase of the world average temperature observed in the last 150 years and what is known as greenhouse effect. The fourth assessment report of the Intergovernmental Panel on Climate Change [132] has stated quite clear that the human fingerprint on this temperature rise is indubitable. The aviation contributes with 2% to the total emissions of CO_2 [62] and predictions for the air traffic is to increase continuously. The urge to invert the trend of increasing emission of green house gases for jet engines can be illustrated in the so called ACARE goals [61]. In 2001 a 50% reduction in carbon-dioxide emissions were fixed as objective for 2020 whereas the engine should contribute with 15 to 20% to this reduction.

Nevertheless, due to cost considerations the efficiency of the jet engines has been improved continuously since the first applications of gas turbines on aircrafts in the 1940's. One method to reduce the specific fuel consumption is by increasing the thermodynamic cycle efficiency of the gas turbine. The cycle efficiency gives the ratio of the power output by the heat introduced with the fuel burning process and, as shown in fig. 1.1, it is dependent on the turbine inlet temperature.

Given this effect of the increased turbine inlet temperature, the allowable temperatures have been rising and are now in a range well beyond the metal melting temperature. This has only been possible by use of efficient cooling techniques. The first technique implemented was the convective cooling where the metal parts are cooled from the inside by circulation of cooler air taken out from the compressor. But the largest step was gained with film cooling as can be seen in Bunker [23]. With the film cooling technique, cooling air is ejected from small holes bored into the airfoil or endwall of the turbine and a thin layer covers the metal, protecting it from the hot environment. In fig. 1.2 one can see a nozzle guide vane with film cooling on the platform and on the vane. The vane is also internally cooled and turbulators enhance the convective heat transfer inside the blade.

Since with the film cooling technique the coolant air is directly injected into the main flow path, a large interference is introduced into the flow and several considerations have to be taken into account in order to evaluate the whole effect of the film cooling technique. Firstly, the thermodynamic process is changed with the injection of cooler air into the main flow. In that manner the average total temperature is lowered reducing the possible enthalpy change in the turbine. Also, a part of the compressor work is used for generating cooling air which does not enter into the heat increasing process in the burning chamber. This means that the work output of the turbine has to be higher than in an uncooled case. Finally, the coolant injected
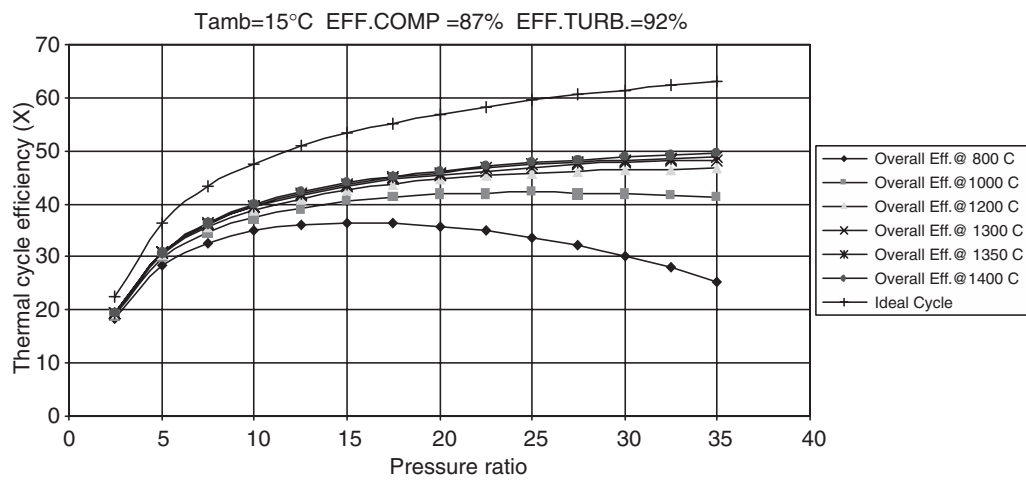
Figure 1.1: Thermodynamic cycle efficiency as function of the pressure ratio and turbine inlet temperature, from Boyce [18]
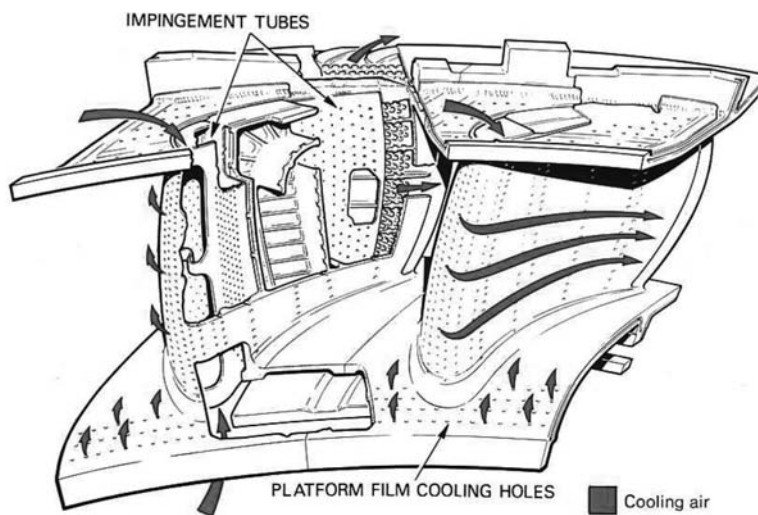
Figure 1.2: View of nozzle guide vane cooling, from [117]

into the main path also significantly disturbs the flow, often increasing the total pressure losses due to turbulent dissipation. Despite all these problems the film cooling technique has allowed an increase in thermal efficiency of the gas turbines in large scale. Today film cooling is a well established technique and the theoretically possible efficiency maximum is almost reached as is shown in cycle efficiency analysis by Wilcock et al. [156] and defended by Cumpsty [32].

Since improved thermodynamic cycle efficiency is becoming difficult to achieve, turbine design has been focusing on other aspects such as to achieving lighter machines with less parts and less maintenance costs. For a jet engine a reduction in turbine parts and hence in machine weight has the additional positive effect of lowering the specific fuel consumption since less mass has to be carried with the aeroplane. One way to achieve this goal is to increase the blade loading by increasing the distance between the blades which results in less blades along the circumference of the blade ring, see Haselbach and Schiffer [77]. Conventional high pressure turbine blade designs already operate with relatively high loading at transonic conditions. Increasing the blade pitch will massively increase the problems arising from strong positive pressure gradients, especially at shock locations at high supersonic velocities. The adverse pressure gradient can result in flow separation which is undesired due to the enthalpy losses it causes. A design for higher aerodynamic loading has therefore to use flow control mechanisms in order to reduce the flow separation. Otherwise the increase in aerodynamic losses would be incompatible with the goals to reduce the specific fuel consumption and the operating costs. Some techniques were successfully used in the past for controlling flow separation, such as on aeroplane wings or low pressure turbine blades, and a survey of the practicable techniques will be given in the following chapter. Some of these techniques could be used in modern high pressure turbine design in order to increase the blade loading and to control the undesired flow separation, so that no additional losses are seen at higher blade pitch.

The AITEB-2 project was launched in 2005 in order to face new challenges in modern turbine design for obtaining lighter and more efficient machines. Some of the topics of this project are high-lift technology, advanced trailing edge cooling for supersonic outlet flow, turbine endwall cooling including effusion cooling, rotor tip cooling and aggressive turbine interducts. The development of all these technologies is accompanied by techniques to enhance the CFD process by accelerating the CFD interaction with the design process and increasing the confidence on the numerical simulations by verification and validation of the simulation tools. As contribution to the development of the high-lift technology, experiments on linear cascades were run at the unique test facility of the University of the German Federal Armed Forces *UniBw*: the High-Speed Cascade Wind Tunnel. This thesis provides a detailed account of measurements and simulations on linear highly loaded turbine blade cascades and is a contribution to increase the knowledge on the aerothermal effects of film cooling in flows with large flow separation.

Objectives of the Current Work   In the here presented work, flow analysis is carried out on linear cascades with high pressure turbine blade design. The goals are to obtain efficient flow control mechanisms which account for a variety of issues on turbine blades: One is the aerodynamic aspect, where total pressure losses can be reduced by suppressing the flow separation. The second one is the thermal aspect. Since high pressure turbine blades face severe heat loads the film cooling has to guarantee an efficient cooling of the blade and the heat transfer has to be predicted correctly. This is challenging for modern numerical tools as will be shown.

Two techniques for flow separation control are analysed in this work. One uses film cooling and the second one employs streamwise vortices generated by fine air jets. The first part of

the work concentrates on pressure side flow separation. Analysis of the heat transfer and the adiabatic film cooling effectiveness with emphasis on the flow separation zone are presented. The discussion of the pressure side studies starts with general aspects of the pressure side flow and a detailed view on the complex phenomena present at the flow separation with its repercussion on the heat transfer and film cooling effectiveness. Then the effect of film cooling on the flow separation, film cooling effectiveness and heat transfer is analysed. For turbine design three main objectives of the studies on the pressure side can be set:

- Is the extension of the flow separation reduced by film cooling?

- Is the separation zone effectively cooled since the heat transfer is expected to increase at smaller separation bubble?

- Is numerical flow simulation capable of reproducing the heat load on the blade in such complex flow?

The second part of the thesis analyses suction side flow separation at a largely increased blade pitch in order to achieve a lower number of blades on the machine. At this higher blade pitch the aerodynamic loading is strongly increased and relatively high Mach numbers are obtained on the suction side of the blade. Strong shocks are present at such high velocities when the flow decelerates towards the outlet velocity. The high pressure gradients at the shock location and its interaction with the boundary layer can cause strong flow separation which has a detrimental effect on the aerodynamic performance of the blade. The flow separation and its control have also an effect on the temperature distribution on the blade. Therefore the studies on the suction side comprise the measurement of total pressure loss as well as of heat transfer and film cooling effectiveness. These results are compared to simulations with modern numerical tools. Guidelines are derived for the control of flow separation taking into account all of the mentioned effects.

For the measurements of the heat transfer and the adiabatic film cooling effectiveness, the wall temperature was measured with thermochromic liquid crystals (TLC). The technique was implemented in the test facility and is explained in detail in this thesis. Guidelines for accurate measurements with TLC are presented as well as a technique for temperature measurements at oblique incidents of the light source and of the image acquisition device. With the method described here, the confidence of the measurements with TLC is highly increased and improved signal quality is achieved by illuminating at oblique angles. Furthermore, a data correction process using finite element analysis was developed in order to increase the accuracy of the measurements.

For the data post-processing a new data reduction process is presented which allows to capture the film cooling effectiveness on a non-adiabatic blade. This is mandatory for a complete analysis of the flow in a real engine. While many publications do not account for the effect of film cooling on a metal blade with interior (convective) cooling, the method described here allows to apply the measurements on a numerical analysis of the full blade with thermal transport into the blade.

2 Flow Separation and Flow Control

The flow in a turbine is subjected to several changes in state which are often complicated and not analytically solvable. As shown in fig. 2.1, the state of the flow also has repercussions on the local heat transfer. At the stagnation point, the heat load is very high, since total conditions of the fluid are present and a new thermal and aerodynamic boundary layer is formed. For the stagnation point heat transfer several correlations are known, mainly for cylinders in cross flow. The correlations from Lowery and Vachon [95] or Mehendale et al. [104] are widely used examples. On the pressure side, the flow might rapidly detach due to positive pressure gradients in flow direction and reattach turbulent. Görtler instabilities are also possible due to the concave curvature. Due to a strong acceleration of the flow towards the trailing edge the flow on the pressure side is likely to relaminarize. On the suction side in general, laminar flow is present from the leading edge on or due to relaminarization at high flow acceleration. Further downstream the flow in general turns into turbulent. For the transition from laminar into turbulent flow three variants are well-known in literature, see Mayle [101]:

Natural transition occurs for cases where the turbulence intensity of the main flow is low when the momentum thickness reaches a critical value. Due to small instabilities two-dimensional waves are formed (Tollmien-Schlichting waves), see Schlichting and Gersten [118]. Further downstream the instabilities form three-dimensional structures which rapidly form turbulent spots. These turbulent spots grow downstream until fully turbulent flow is obtained.

In a by-pass transition, which occurs at higher free stream turbulence levels, the two and three dimensional instabilities do not occur. The turbulent spots are directly formed due to the disturbances in the free stream.

The transition over a separation bubble is commonly seen at positive pressure gradients. When facing higher pressure in streamwise direction, the boundary layer profile changes its shape as shown in fig. 2.2. At the point where $(\partial u/\partial y)_{y=0} = 0$ is reached, the flow separates due to the adverse pressure. A schematic of a transition over a separation bubble is shown in fig. 2.3. After
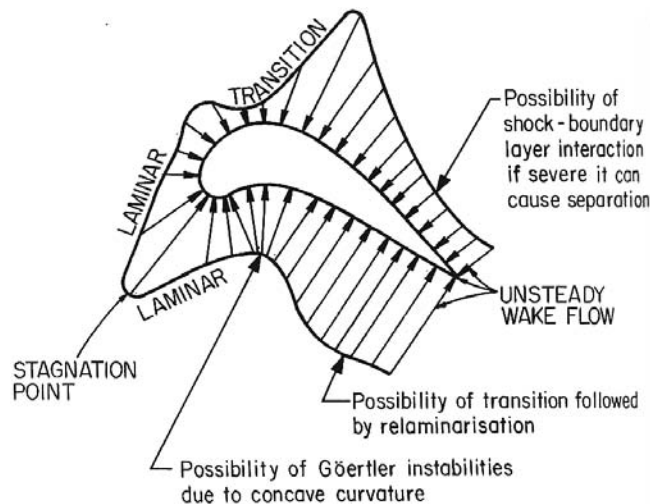
Figure 2.1: Heat load on a turbine blade, from Lakshminarayana [94]
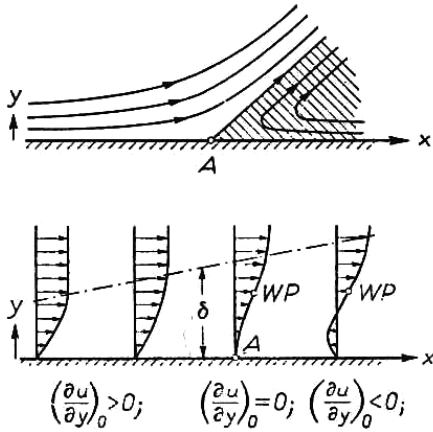
Figure 2.2: Boundary layer profiles at positive pressure gradient, from Schlichting and Gersten [118]
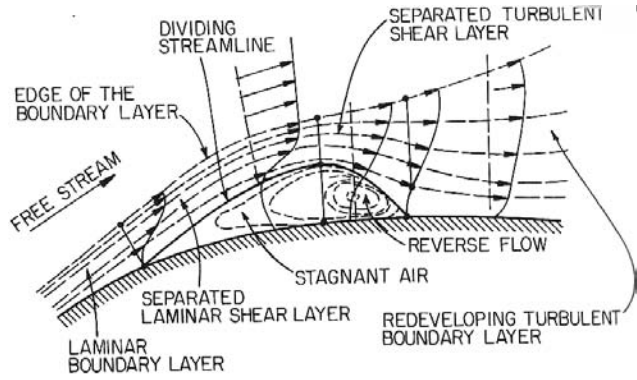
Figure 2.3: Sketch of a transition over a separation bubble, from Lakshminarayana [94]

separation the flow in the shear layer outside the separation bubble is subjected to instabilities. After turning into turbulent the flow in general reattaches. At very high pressure gradients the flow might remain separated up to the trailing edge.

In transonic flow, shock-induced flow transition may occur with or without separation since the flow experiences shock waves in the transition from supersonic to subsonic Mach numbers. In case of a normal shock the transition to subsonic velocity is almost instantaneous and the flow suffers a steep pressure increase. While in the supersonic region, the pressure increase can not be felt upstream, the velocity inside the boundary layer, however, decreases continuously to the wall. Therefore the supersonic region and the shock wave do not reach the wall and inside the boundary layer an elliptic regime is found, where the pressure increase can be experienced upstream. In fig. 2.4 a schematic representation of the flow close to the wall around a shock is drawn. Inside the boundary layer and below the sonic line the flow is subsonic and the pressure increase is therefore experienced upstream of the shock location. This leads to an increase in the boundary layer thickness and hence the non-viscous flow outside of the boundary layer is turned generating several oblique shocks which join to one single line at the triple point. At the triple point of the lambda foot (Ackeret et al. [2]) the oblique shock joins the main shock. Downstream of the oblique shock wave, the flow is compressed to the same pressure as behind the main shock through a second compression wave. Downstream of the second oblique wave, the flow may still be supersonic as is the case e. g. in Schreiber and Starken [124] or in Schreiber [125]. In this case Prandtl-Mayer expansion waves can be seen when the boundary layer thickness decreases again downstream of the interference zone, what is followed by a second shock. If the main shock is strong enough, flow separation is present. While for laminar flow weak shocks can cause flow separation, the Mach number should be of at least 1.3 to cause shock-induced flow separation in a turbulent flow, see Delery [37].

Within the interference length, a region defined by a rapid thickening of the boundary layer, the pressure increase is much more gradual than with the theory for inviscid flow. As explained in Bell [14] for laminar flow, a first pressure rise close to the wall is noticed at the beginning of the compression, see fig. 2.5. The pressure increase for the inviscid solution is p_{th} while p_w is the experienced pressure at the wall. At the first oblique shock, the boundary layer increases and
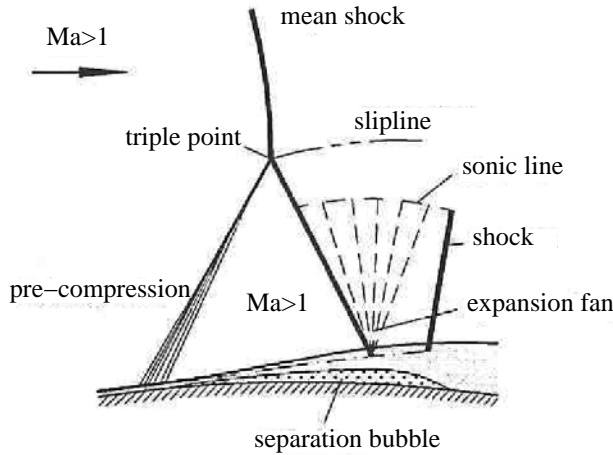
Figure 2.4: Schematic representation of shock-boundary layer interaction with laminar flow and flow separation, from Bell [14]
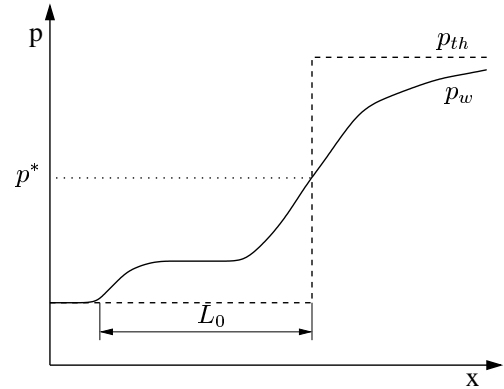
Figure 2.5: Exemplary near wall pressure at the shock location with laminar flow

the pressure rises slightly. Around the shock location, the pressure rise is steeper and further downstream it approximates the curve for the inviscid solution.

The interaction length L_0 as used by Delery [37] starts at the first pressure rise and extends up to the main shock location or Ma = 1 at the wall. This length decreases with increasing Reynolds number and for turbulent flow a rapid pressure rise is perceived near the wall followed by a gentle approximation to the inviscid solution.

2.1 Control of Flow Separation

Separated flow has several undesired aspects. On turbine blades every flow separation is linked with total pressure loss or, in case of large flow separation with possibly no reattachment, to a loss of the airfoil lift. As exemplary extreme case in compressors, the stall phenomena impose serious limitations on the operability of the machine. Large flow separations on turbine airfoils also influence the flow turning and hence the work output. Therefore an efficient blade design tries in general to avoid flow separation. Exceptions to this can be separation bubbles with very limited influence on the flow when the superposition with other aspects, such as a long extension of the laminar boundary layer, result in an overall positive effect.

Another positive aspect of the separation bubbles is that they act as a thermal insulation of the surface against the hot gas and very low heat transfer coefficients are experienced below them. When flow separation is suppressed the increased heat load at this location has to be taken into account.

In order to avoid flow separation, the blade design may try to keep the loading low and at low positive pressure gradients in streamwise direction. One method to achieve this is to keep the blade spacing small, which increases the number of blades per stage. On the other hand by increasing the number of blades more surface is in contact with the flow, increasing the viscous

losses and the amount of needed cooling flow. The increased demand for cooling flow replies directly on the higher output on the shaft needed to drive the compressor. The manufacturing and maintenance costs are also increased due to the higher number of parts. For jet engines, additionally, the higher engine weight plays a role in the overall efficiency of the aircraft.

Consequently advanced designs try to increase the blade loading but also to control the negative effects of flow separation. The known methods from literature according to Gad-el-Hak [56] or Schlichting and Gersten [118] are

1. wall movement,

2. momentum addition to near wall flow,

3. boundary layer suction,

4. blowing of foreign gas,

5. profiling,

6. wall cooling.

Of the identified techniques, the second and fifth technique seem to be the most appropriate for a gas turbine. The profiling technique is very advanced and few improvements are to be expected here. Therefore the second item has been the focus of many studies on separation control. The momentum addition can be provided by passive or active devices. The passive devices either trip the boundary layer into turbulent prior to the separation point or create vortices, which increase the momentum of the flow near the wall. Active devices inject air either to directly increase the momentum of the near wall flow or to create vortices. Tripping of the boundary layer flow into turbulent is evidently only practicable with a laminar boundary layer where a laminar separation bubble has to be suppressed. A turbulent boundary layer is less likely to separate, but at strong shocks at Mach numbers above 1.3 a turbulent boundary layer is also likely to separate. These Mach numbers are reached in transonic turbine flow with high aerodynamic blade loading, as it is of interest in these investigations. Therefore the momentum addition close to the wall by blowing off or by creation of streamwise vortices seem to be the most viable techniques to be implemented in such cases. Since the creation of streamwise vortices requires less additional flow to be blown off from the holes, this approach is followed in this work for the suppression of suction side flow separation at strong shocks.

Passive vortex generating devices are shown in literature to suppress shock induced separation by creation of streamwise vortices. A recent publication by Zare Shahneh and Motallebi [130] compares various configurations of sub-boundary layer vortex generators with tetrahedron geometry and it is shown how flow separation at Ma=1.4 is efficiently suppressed. A drawback of this passive devices is their constant influence on the flow, even at flow conditions where no flow separation occurs. Therefore the aerodynamic efficiency of these devices is strongly Mach and Reynolds number dependent.

A way of improving the flow control is the generation of vortices by fine air jets at shallow tangent and high compound angle. Downstream of the air jets, vortex pairs are formed which transport high momentum fluid towards the surface, reducing the tendency of the flow to separate, even in presence of strong shocks. Some of the first promising results using air jets

are reported in Wallis [154]. In this study, different configurations of air jets are compared to metal vanes and it is found that inclined jets lead to an effective modification of the boundary layer increasing the momentum close to the surface.

Johnston and Nishi [87] confirm the creation of streamwise vortices by inclined air jets. Like in Wallis, jets with a compound angle are by far more effective in creating vortices and reducing the flow separation than streamwise aligned jets. It is found that a velocity ratio between jets and main flow of at least 0.8 is needed to reduce flow separation effectively. Rixon and Johari [116] measured the flow field downstream of an air jet with laser doppler velocimetry and show the development of the vortices in streamwise direction at different velocity ratios. First a pair of vortices is formed. Farther downstream one of the pairs weakens more rapidly leading to one single vortex.

Applications of air jet vortex generators for control of shock induced boundary layer separation are shown in Szwaba et al. [142, 143]. By using air jet generated vortices, the large flow separation zone vanishes almost completely and the shock unsteadiness is strongly reduced. Similar air jets are used in the present thesis for control of boundary layer separation on a turbine blade. The air jets were optimised numerically and validated in a test section presented in Doerffer et al. [45].

2.2   The Influence of the Flow State on Heat Transfer

The flow state has a huge impact on local convective heat transfer due to energy transport within the boundary layer. While in laminar flow the heat transfer coefficient decays rapidly with growing thermal and aerodynamic boundary layers, in turbulent flow the cross stream fluctuations and the high shear stress increase the thermal transport significantly within the boundary layer and therefore the heat exchange between surface and fluid. A correct prediction of the state of the flow is therefore essential for heat flux computations. If, for example, the transition from laminar to turbulent flow on the suction side is not matched, errors of 100% or more can be obtained for the heat transfer predictions, see Dunn [51].

Some similarity parameters are commonly used to describe heat transfer. For heat transfer in a flow field large enough to have a zone without influence of the boundary layer, the Nusselt number Nu is commonly used, where the heat transfer h is scaled by the conductivity k of the fluid and a length scale l:

$$\mathrm{Nu} = \frac{h \cdot l}{k}. \tag{2.1}$$

For flows where the fluid is heated or cooled during its travel along a hotter or cooler surface, such as in a pipe, the Stanton number is often used as dimensionless number. The Stanton number describes the ratio of heat transfer to the thermal capacity of the fluid:

$$\mathrm{St} = \frac{h}{c_p \cdot \rho \cdot u}. \tag{2.2}$$

Both numbers are linked together via

$$\mathrm{St} = \frac{\mathrm{Nu}}{\mathrm{Re} \cdot \mathrm{Pr}}. \tag{2.3}$$

With the aid of these dimensionless numbers some correlations are found in literature for various types of simple flows. For a thermal laminar boundary layer expressed with

$$\Theta = \frac{T_w - T}{T_w - T_\infty} \tag{2.4}$$

on a semi infinite flat plate with constant wall temperature and constant flow velocity U_∞, a similar solution as for the aerodynamic boundary layer is obtained and for $\mathrm{Pr} = 1$ a simple relationship between heat transfer and skin friction coefficient is known: $\mathrm{St} = c_f/2$. Using the Blasius equation [16] and Newton's law of cooling

$$\dot{q} = h \cdot (T_w - T_\infty), \tag{2.5}$$

one can obtain an analytical solution for the local Nusselt number $\mathrm{Nu_x}$ based on Prandtl and local Reynolds number $\mathrm{Re_x}$ which can be integrated numerically or approximated for $0.5 < \mathrm{Pr} < 15$ with

$$\mathrm{Nu}_x = 0.332 \cdot \mathrm{Pr}^{1/3} \cdot \mathrm{Re}_x^{0.5}. \tag{2.6}$$

Solutions and correlations for various types of laminar flow can be found in Kays et al. [90].

In turbulent flow the heat transport outside the viscous sublayer is dominated by the unsteady fluctuations of the velocity and temperature. Similar to a turbulent eddy viscosity μ_t, a turbulent Prandtl number $\mathrm{Pr_t}$ is defined by

$$\mathrm{Pr}_t = \frac{\mu_t \cdot c_p}{k_t}, \tag{2.7}$$

with the eddy conductivity k_t, see Kays et al. [90]. As a very simple approach, one can make use of the Reynolds analogy setting $\mathrm{Pr}_t = 1$ and the same solution as for the laminar boundary layer is obtained

$$\mathrm{St} = \frac{c_f}{2}. \tag{2.8}$$

In reality, outside the viscous sublayer, empirical values of about 0.85 were obtained for the turbulent Prandtl number e. g. by Fulachier et al. [64]. With pressure gradients the complexity increases since the logarithmic law of the wall is valid for the thermal boundary layer only at zero pressure gradient. In Volino and Simon [152] some results are presented showing e. g. the influence of pressure gradient in delaying flow transition in accelerated flows. The same authors present in [153] some improved correlations which agree well with experimental values for the dimensionless Temperature T^+ as function of the normalized wall distance y^+. Daris and Bézard [33] define T^+ as function of $y^+/(1 + p^+ y^+)$ which improves the similarity of the measured curves.

The prediction of heat transfer is very complicated since the correct flow field must be known and additional complexity is added to the differential equations via new variables with more degrees of freedom. This is especially true for non similar aerodynamic and thermal boundary layers. Nevertheless, using the Reynolds analogy of eq. (2.8), one can get an idea of the expected heat transfer when the flowfield is known. In fig. 2.6, the shear stress is qualitatively shown for laminar and turbulent boundary layer on a flat plate with natural transition and over a separation bubble. Due to the increasing boundary layer thickness, the shear stress diminishes downstream. In the transition region the shear stress increases considerably. The heat transfer
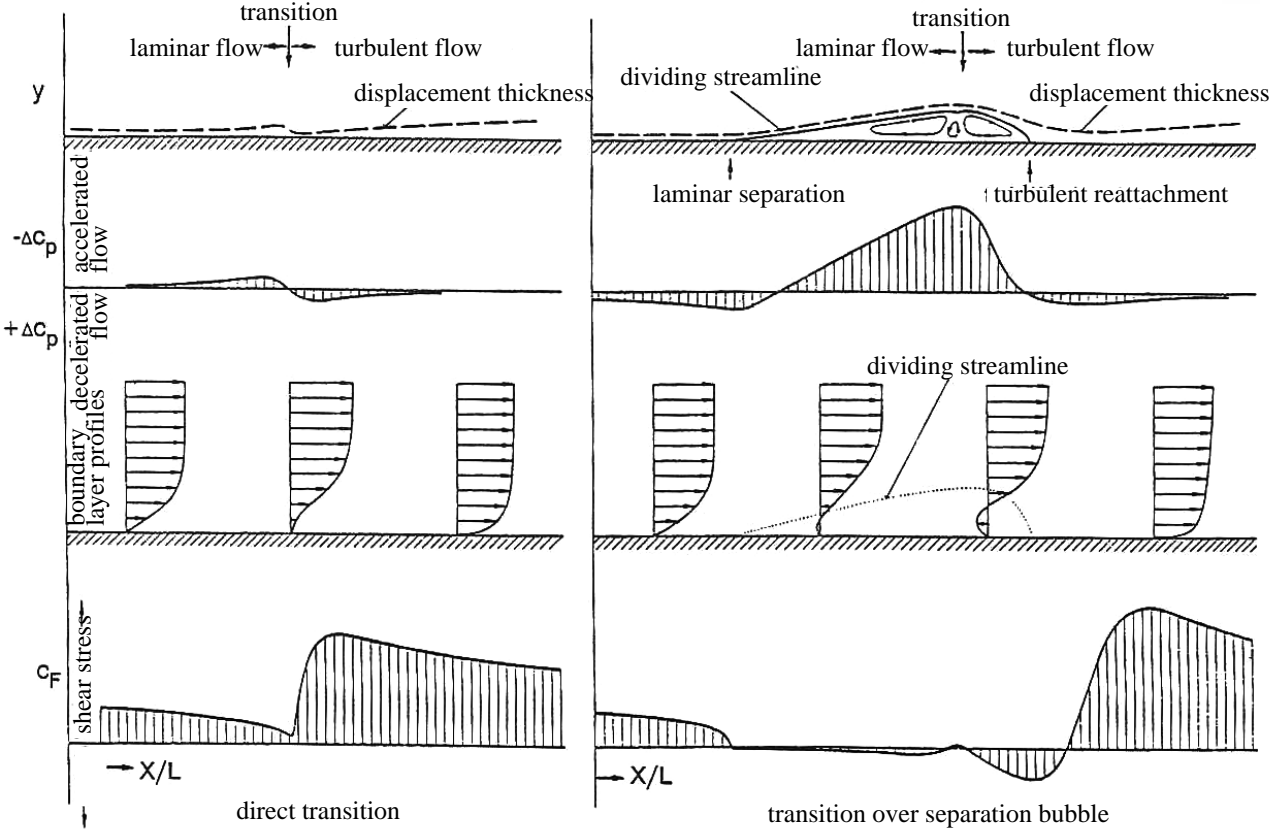
Figure 2.6: Qualitative shear stress distribution along a flat plate, from Wunderwald [161]

coefficient profile is similar with rapidly decreasing heat transfer and a step in the transition to turbulent.

When flow separation is present, the shear stress is zero in the separation and reattachment points since the velocity gradient perpendicular to the wall is also zero. The heat transfer follows quite well the Reynolds analogy for the separation point with very low heat transfer values, but in the reattachment point the heat transfer in general reaches a local maximum since a new thermal boundary layer is formed, followed by a rapid increase in shear stress due to turbulent reattached flow. The heat transfer values are low inside the separation bubble because the shear stress values are also rather low and the boundary layer thickness is large. Bräunling et al. [20] show this fact for a shock induced separation bubble. Experiments by Wolff et al. [159] and simulations from de la Calzada and Alonso [35] compare typical heat transfer profiles for large separation bubbles on the pressure side of a turbine blade under largely decreased angle of attack. Some results are shown in fig. 2.7. In fig. 2.7(a) the shear stress for varying incidence angles is shown, while the local heat transfer under the same conditions is plotted in fig. 2.7(b). At the separation point, the heat transfer decreases instantaneously and the peak heat flux is observed shortly downstream of the reattachment point. The heat flux inside the separation bubble is strongly influenced by the size and number of vortices created and can only be assessed by unsteady computation as stated by Alonso and de la Calzada [5].

Bellows and Mayle [15] studied the flow features of a laminar separation located shortly downstream of the leading edge on a flat plate with large leading edge radius. In their test section, the flow can not follow the curvature change from the semicircle leading edge towards the flat plate and separates followed by a turbulent reattachment. The separation bubble is very short, extending only about 0.25 times the radius of the leading edge. They show that the Stanton number after reattachment agrees very well with slightly modified flat plate correlations for turbulent boundary layer, when the Reynolds number is computed starting at the separation location and not at the leading edge.

Terekhov et al. [147] measured the flow field and the heat transfer downstream of ribs and backward facing steps. With ribs the separation length is much longer and the static pressure distribution gently approaches the values of the free stream. For the step a peak in static pressure is seen shortly downstream of the reattachment line. The same occurs with the heat transfer. Downstream of the step, the heat transfer decreases inside the separation region and a short length farther downstream the heat transfer rate reaches its maximum at the reattachment line. The heat transfer reaches the values of the flat plate without obstacle very quick. Behind the rib, the heat transfer also decreases but especially at longer separation lengths no peak in heat transfer is observed at the reattachment line. Flow field measurements show that the maximum velocity fluctuations are situated close to the wall downstream of the step while, behind the rib, the maximum velocity variation is seen far more distant from the wall. The different structure of the recirculating flow leads to different temperature profiles which affects the local heat transfer coefficient. They conclude, therefore, that the profile of the heat transfer coefficient is strongly dependent on the structure of the vortices inside the separation bubble.

Schobeiri et al. [122] show measurements on a turbine blade with separation bubbles on both pressure and suction side. Typical effects are seen with low heat transfer inside the separation zone and a local peak in the reattachment line. Higher free stream turbulence level or periodic unsteady inflow with high turbulent wakes downstream of moving cylindrical bars reduce or completely suppress the flow separation. In that case, the heat transfer shows no drop at the
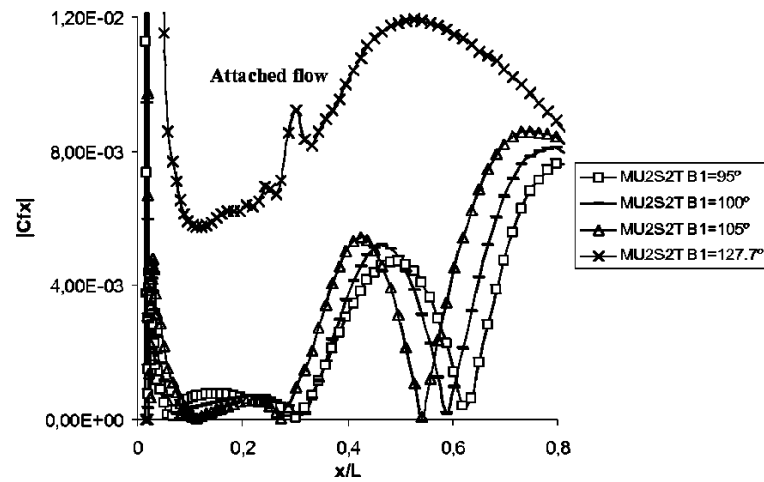
(a) Shear stress
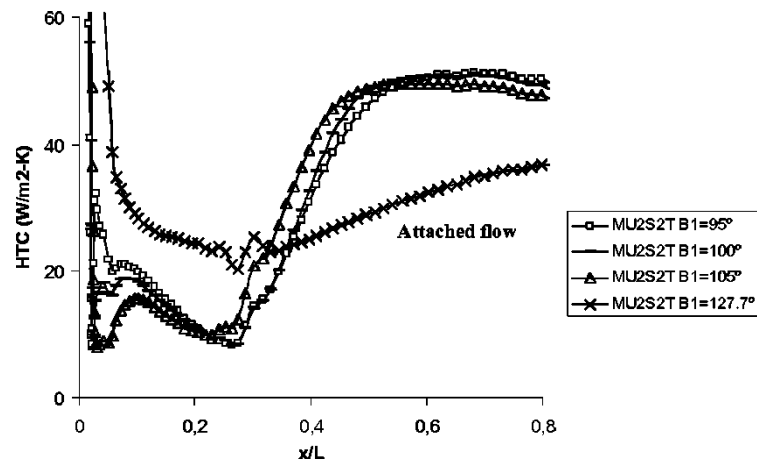
(b) Heat transfer coefficient

Figure 2.7: Shear stress and heat transfer coefficient for simulations of largely separated flow on the pressure side of a turbine blade, from de la Calzada and Alonso [35]

previous location of the bubble and the increase seen with flow separation is not present any more on the pressure side, while on the suction side it is reduced with normal transition to turbulent boundary layer state. Downstream of the separation zone the heat transfer levels are reduced with suppressed flow separation since the velocity fluctuations are also reduced. With flow separation the velocity fluctuations are very high due to the unsteady behaviour of the separation bubble.

2.2.1 Heat Transfer and Film Cooling on Turbine Aerofoils

The heat transfer and film cooling on turbine aerofoils are influenced by many parameters. In Arts and Lambert de Rouvroit [9], the influence of various parameters on heat transfer are analysed at real engine conditions on a linear transonic cascade and the cases were widely used for comparison of numerical codes. The free stream turbulence level is an important parameter, which in general increases heat transfer at higher rates and shifts laminar to turbulent transition upstream. In their case they show how flow transition can also be triggered by a shock. A parameter with strong influence is the free stream Reynolds number, which influences the overall heat transfer as well as the transition of the flow to turbulent. The free stream Mach number, in contrast, has almost no effect on local heat transfer.

Giel et al. [67, 68] published measurements on a linear turbine cascade showing some effects as in Arts and Lambert de Rouvroit [9] and compared their results with numerical simulations. On the pressure side, they show that the flow relaminarizes at lower Reynolds numbers due to the strong acceleration. They compare the heat transfer at different Reynolds numbers and deduce the laminar or turbulent flow state if the change in heat transfer rate is proportional to $Re^{0.5}$ or $Re^{0.8}$ for laminar or turbulent flow respectively. The dependency of the Stanton number on the local Prandtl and Reynolds numbers for flow over a semi-infinite flat plate is well known from literature.

Dullenkopf and Mayle [50] show that not only the turbulence intensity is important for local heat transfer but also the integral length since a laminar boundary layer is sensitive to disturbances within a limited frequency range. This is especially important for stagnation point heat transfer, as they show how various experimental data agree with their new correlation.

Ammari et al. [7] studied the influence of flow acceleration on heat transfer with and without film cooling. They show that, although the flow did not relaminarize, the acceleration was sufficient to reduce the relative velocity fluctuations and consequenty the local heat transfer. Also the increased heat transfer with flow ejection from the cooling holes could be well reduced with accelerating flow.

Increased complexity arises when periodic wakes from upstream airfoils are present. These wakes have a high turbulent core, which enhance the heat transfer and generally shift the transition on the suction side upstream. Also the inlet angle suffers a change due to the velocity deficit in the wake. This changes the location of the stagnation point and, in case of the leading edge film cooling, the distribution of coolant to the pressure or suction side. Studies of the impact of periodic wakes on the heat transfer can be found e. g. in Schobeiri et al.[121], Marziale and Mayle [99] or Dullenkopf and Mayle [49]. Allan et al. [4] compare measurements on a linear cascade with upstream moving cylindrical bars to new experiments on a full turbine stage and show that the agreement between both experiments is very good. In both these

publications and in Dénos et al. [38] important effects of moving shocks on the unsteady heat transfer rate are seen.

Effect of Film Cooling

Film cooling by blowing off coolant from discrete holes bored into the airfoil or into the endwalls has been used for decades and, as referenced in Bunker [23], is responsible for most of the increase of the turbine inlet temperature over this period. The parameters commonly found to characterize the aerodynamics of film cooling are based on the ratio of mass flow or momentum between coolant flow and the main flow at the ejection location. The definition for the blowing ratio is

$$M = \frac{(\rho \cdot u)_c}{(\rho \cdot u)_\infty} \tag{2.9}$$

while the momentum ratio is defined by

$$I = \frac{(\rho \cdot u^2)_c}{(\rho \cdot u^2)_\infty}. \tag{2.10}$$

Furthermore, the ratio of the densities, of the velocities or of the temperatures of coolant and main flow can be used as similarity parameter.

A lot of research on film cooling has studied the influence of various parameters on the cooling effectiveness of this technique. For example, studies on cooling geometry can be found for simple cylindrical holes in Lutum and Johnson [96]. Increasing the cross section area towards the exit (so called fan-shaped holes) can improve film cooling effectiveness as shown in Lutum et al. [97]. Newer geometries using trenches can be found in Waye and Bogard [155].

Most of the studies on film cooling were carried out on flat plates while the turbine airfoils have a more or less pronounced curvature along a long part of the chord. This curvature has strong effects on film cooling not only due to the pressure gradients but also on the aerodynamics of the film cooling jets due to radial momentum at the curvature and direct interaction with the pathlines of the jets. Schwarz and Goldstein [126] present flow visualisations and film cooling effectiveness measurements on a concave surface showing jet detachment close to the ejection location and jet impact on the surface farther downstream, since the surface crosses the original pathline of the jets. Ito et al. [85] deduce from momentum conservation, that on convex surfaces the film cooling effectiveness should be increased with a tangential momentum ratio $I \cdot \cos \alpha < 1$ while on a concave surface the opposite is true, i. e. the tangential momentum ratio should be larger than unity for more effective cooling. They confirm this with experimental results as well as in Schwarz et al. [127] on a concave surface. Goldstein and Stone [72] tried to empirically obtain an optimum injection angle for cylindrical holes on concave surfaces, but found that the optimum angle depends on the blowing ratio. Mayle et al. [100] see higher effectiveness on a convex surface than on a concave surface, while only blowing ratios below unity were used in their studies.

Analysis of film cooling effectiveness on turbine blades by Drost and Bölcs [47] show higher film cooling effectiveness at higher free stream turbulence levels for the pressure side, due to coolant diffusion in the boundary layer. On the suction side the effect of free stream turbulence on the adiabatic film cooling effectiveness is small, while the suction side presents a high sensitivity on variation of local Mach and Reynolds numbers due to different boundary layer thicknesses.

Colban et al. [30] also perceive enhanced cooling on the pressure side due to better coolant diffusion in the boundary layer. Using shower head film cooling at the leading edge, the cooling effect from the downstream lying fan-shaped holes is enhanced close to the holes where normally jet detachment is present. The higher turbulence due to the shower head film cooling enhances the mixing of the coolant in the jet separation zone. At the leading edge, the film cooling effectiveness is reduced with higher free stream turbulence at lower blowing ratios, while at a blowing ratio of 1.2 almost no effect is seen in Ekkad et al. [55]. Turbulence increase also enhances film cooling effectiveness in Schmidt and Bogard [119] at a momentum ratio larger than unity due to the same effect with jet separation.

Arts and Lapidus [10] measure the combined effect of film cooling and heat transfer by means of heat transfer coefficient on a non-adiabatic vane with temperature difference between coolant and main flow. On the suction side of a turbine vane, they measured an overall film cooling effectiveness by measuring the heat transfer with and without film cooling. They show the problem that film cooling on a non-adiabatic blade may have detrimental effect. This is seen close to the ejection location, where the heat transfer increases with film cooling as well as at the transition location, since film cooling shifts the transition location upstream and the heat transfer into the blade is increased due to the enhanced mixing process.

The effects of periodic high turbulent wakes are analysed e. g. in Funazaki et al. [65] and Mehendale et al. [105]. Both show decreased film cooling effectiveness due to the turbulent mixing of the film. Teng et al. [146] report decreased film cooling effectiveness in the line downstream of the holes but almost no effect in the pitchwise averaged results. This means that the incoming wakes enhance the lateral distribution of the coolant. Heidmann et al. [78] show that, due to the different inflow angle downstream of the wake, the coolant from the leading edge is displaced towards the pressure side.

Coulthard et al. [31] show the effect of jet pulsing on film cooling on a flat plate. For high blowing ratios with jet lift off, high-cycle pulsing results in higher effectiveness due to prevention of jet lift off, though less coolant mass flow is used. This effect of prevention of jet lift off can be positive for inflow with periodic wakes, as is reported in Womack et al. [160]. For the same test section but with periodic wakes created by cylindrical bars, film cooling effectiveness is decreased for low blowing ratios but strongly increased at the high blowing ratio with jet lift off.

Ethridge et al. [58] point out again that momentum ratio is the most appropriate correlation parameter for film cooling.

2.2.2   Summary of Effects on Heat Transfer and Film Cooling

A high pressure turbine airfoil is subjugated to a high thermal load and manifold techniques are used to decrease the average as well as local maxima of the temperature in the blade or vane. A low heat transfer coefficient limits the thermal transport from the fluid to the blade, but it is strongly linked to the aerodynamics of the flow. In a laminar boundary layer the heat transfer is rather low, while in turbulent flow the cross flow fluctuations enhance the heat exchange. For a turbine flow several causes have a large, in most cases detrimental, impact on the heat transfer and are seldom evitable. Some of the effects observed in turbines are the turbulence level of the free stream, periodic wakes from upstream lying airfoils, Reynolds and Mach number variations and flow acceleration or deceleration.

A way of decreasing the metal temperature is using film cooling, which itself has a strong impact on the flow field and temperature distribution. Heat transfer is increased especially close to the ejection location due to the interference with the main flow and when the flow transition is shifted upstream. The film cooling itself is also influenced by most of the effects named above and which have a large impact in heat transfer. At high momentum ratios, in general larger than 1, the coolant flow is likely to detach and high free stream turbulence or periodic wakes can enhance film cooling in that case. For an attached coolant film, higher turbulence deteriorates the cooling effect. Velocity variations of the main flow as well as the geometry of the film cooling holes or of the airfoil may also change the film cooling effect.

While some of these aspects are well studied the effect of the combination of various parameters at engine like conditions seems not to be fully understood. In a turbine all of these factors are present altogether in varying magnitude and the interaction between all of them has to be studied. For flows with severe separation, which are not yet typical for turbine airfoils, and applying flow control to reduce the separation the complexity increases.

The scope of this work is to study flows with large separation zones and means of controlling this separation. For advanced turbomachinery design with increased aerodynamic loading, further studies on these types of flows are mandatory in order obtain some knowledge and to increase the predictability in such cases. The search for efficient flow control mechanisms, in order to allow higher blade pitches in the high pressure turbine, can not be done without considering both aerodynamic as well as thermal aspects. The total pressure losses have to remain at an acceptable level and efficient film cooling has to be provided for the blade. The grade of predictability is verified with modern numerical tools and a deeper inside in the flow phenomena is taken in order to capture some hints for future code development and utilisation.

3 Implementation of Thermochromic Liquid Crystals for Temperature Measurements at the High-Speed Cascade Wind Tunnel

The measurements presented in this thesis comprise a variety of measurement techniques which shall be explained in the next chapter. For the measurements of thermal parameters, such as heat transfer coefficient and adiabatic film cooling effectiveness, a new measurement technique was introduced in the test facility. Thermochromic liquid crystals were used to measure surface temperatures on the blade and several tests were conducted in order to validate the technique, see Gomes [73]. The measurement of temperature by means of liquid crystals was already used in the high-speed cascade wind tunnel (HGK) of the Institute of Jet Propulsion by Ganzert [66]. With the method described by Ganzert, wave length filters are used to obtain isothermal lines on the surface of the blade. For the measurements presented here a different technique was used where full colour maps are taken giving detailed surface contours of the heat transfer coefficient and adiabatic film cooling effectiveness. The method and a new correction technique increasing the accuracy of the measurements is described in detail in this chapter.

3.1 The Theory of Liquid Crystals and Their Implementation for Temperature Measurements

Liquid crystals are organic molecules and they are found in numerous variations with distinct properties. All of them have in common, that a fourth phase besides solid, liquid and gaseous state is found. In the so-called mesomorphic phases the liquid crystals show properties typical of liquids and crystals at the same time. They present some degree of freedom in their ordering but present sharp Bragg reflections [128] when exposed to x-rays. During their transition from solid to liquid the liquid crystals show a cascade of transitions before reaching the liquid state, see [34]. The different states can be classified as:

- smectic,

- chiral nematic or cholesteric,

- nematic.

Within these three states, there are numerous sub-divisions and the difference between them all is the number of degrees of freedom and the orientation of the molecules. Thermotropic liquid crystals change between the phases in dependency of the temperature and some of them show fascinating optical properties when they are in the chiral nematic state, which is a special form of the nematic state. The chiral nematic state is often referred to in literature as cholesteric because the first compounds showing such properties were derivatives of cholesterol [76]. In the chiral nematic state, the molecules which have a longitudinal shape are twisted around an axis perpendicular to their main axis and exhibit a helical structure as shown in fig. 3.1. In the optically active state the pitch of a 360° twist is in the range of some 100 nm, i. e. in the range of the wavelength of visible light. In this state, selective reflection of nearly circularly polarized light occurs [91]. Since the pitch of the twist decreases with increasing temperature, the reflected
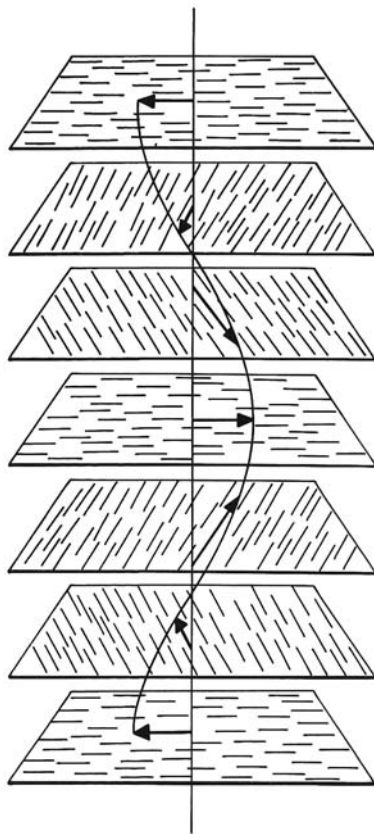
Figure 3.1: Schematic representation of the helical structure of liquid crystals, from Chandrasekhar [27]
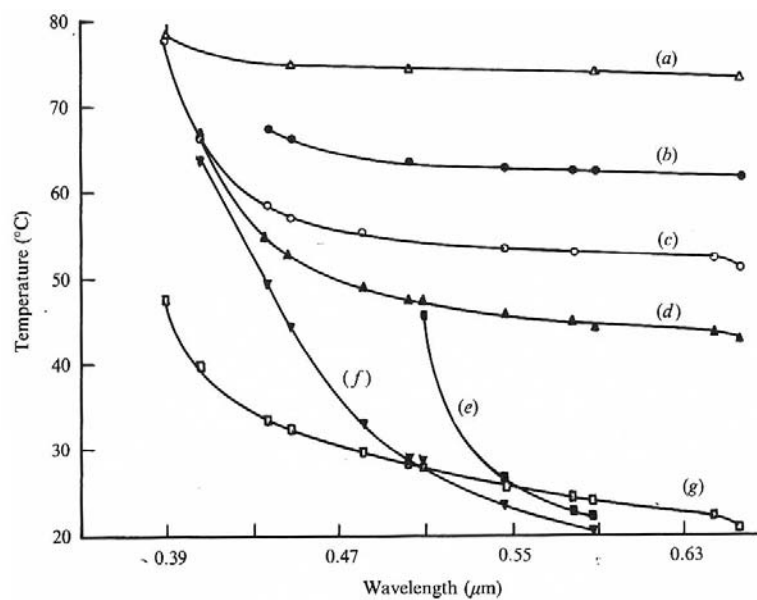
Figure 3.2: Correlation between pitch and temperature for different types of TLC labelled as "a" to "g", from Chandrasekhar [27]

light changes with the temperature as well. In fig. 3.2, taken from Chandrasekhar [27], the pitch of the molecules is plotted as function of the temperature for different liquid crystals.

As pointed out by de Vries [36], due to the turning of the molecules in the chiral nematic state, only a single band of light waves is reflected when the light is parallel to the axis of turn, which lies in the range of a wavelength λ of

$$\lambda = p \cdot n \qquad\qquad (3.1)$$

with the pitch for one revolution p and the main refractive index n. Since the pitch changes with temperature an observer will experience a changing coloration of the liquid crystals as function of the temperature. At starting temperature, the crystals reflect long wave light which is red and with increasing temperature gradually light of higher frequency is reflected up to the so-called clearing point, when the liquid crystals get isotropic. During the temperature increase from starting temperature to the clearing point the reflected light changes from red passes green up to blue. A diagram showing the colour transition with changing temperature is given in fig. A.2. The stable relation between temperature and coloration of the TLC makes them a suitable instrument to measure temperature. By using different types of thermochromic liquid crystals or by mixing of more than one type of TLC the temperature range where they are optically active can be adjusted. Today commercial TLC are available for red starting temperatures between $-30°$ C and $120°$ C and bandwidths from red start to clearing point temperature between $1°$ C and $20°$ C. These properties make them suitable for temperature measurements. As reported in Kasagi et al. [89] they are easy to handle, have small effect on the flow and have a rapid response time, reason why they have some advantages compared to other measurement techniques. Nowadays temperature measurements with TLC are a well established technique and numerous applications are found in the literature for heat transfer measurements. The articles from Ireland and Jones [84] or Stasiek and Kowalewski [138] show well explained examples for the technical use of TLC for determination of the temperature distribution and the identification of details of the near wall flow.

3.1.1   Image Acquisition and Digitisation

The development of image acquisition techniques with charged coupled devices (CCD) has made measurements with TLC much easier since the image processing can be made automatically with a simple desktop computer [137]. Digital cameras have either one or three CCD chips with 768x576 image sensors per chip in the PAL-system. The CCD was developed in the Bell Laboratories [19] and is an efficient way of transportation for electric charges. CCD use positive doped semiconductor (in general silicon) as substrate and electrodes such as metal plates. Both are divided by a dielectric as shown in fig. 3.3. By applying a negative charge on the electrode, the holes of the impure substrate accumulate at the interface to the dielectric. On the other hand, applying a positive charge on the electrode causes a negative charge to accumulate in the substrate close to the interface. By clocking the charge of the electrode, electrons can be transferred from one cell to the next as shown in fig. 3.4. The electrons are shifted from cell 1 to 2 when positive charge is set on the electrode of cell number 2 and the charge on the electrode number 1 is decreased (time step $t = t_3$ to $t = t_5$). Please note that in the example of fig. 3.4 the time steps are not equal. Detailed information on CCD can be found e. g. in Howes and Morgan [83].

For image acquisition the electrons collected in the CCD cells are generated by the photoelectric effect. As referred in Sears [128], electrons are released from the atoms of a material exposed
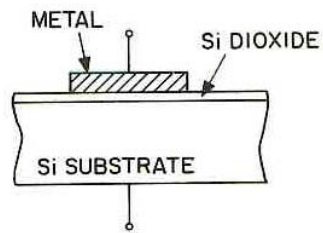
Figure 3.3: Model of a CCD, from Howes and Morgan [83]
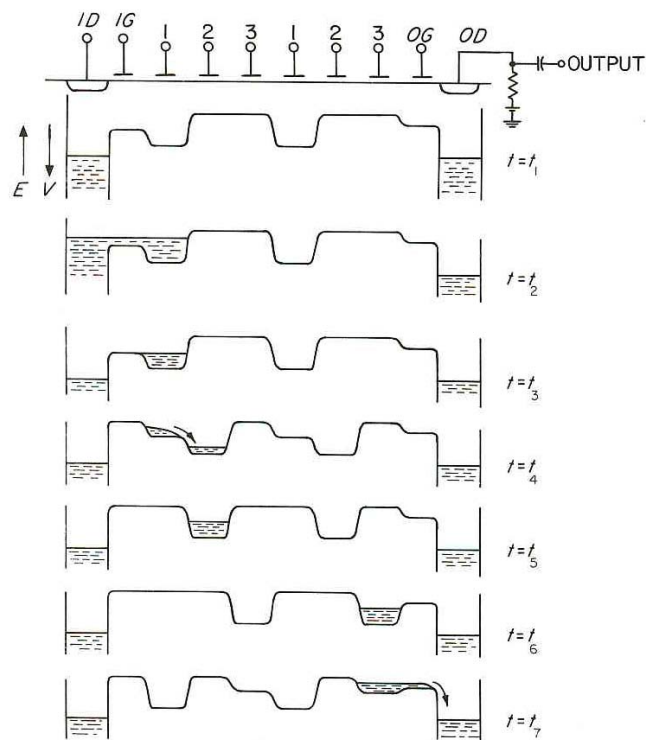
Figure 3.4: Schematic of the charge transfer in a CCD, from Howes and Morgan [83]
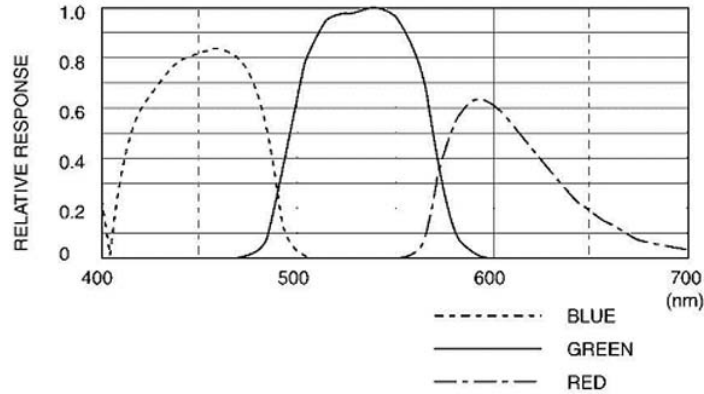
Figure 3.5: Sensitiveness of the three CCD chips, from [133]

to light, which is called the photoelectric effect. Einstein set the relation that the energy E needed for a photon to force an electron to penetrate the potential barrier is proportional to the frequency f of the electromagnetic wave

$$E = h \cdot f, \tag{3.2}$$

with the Planck's constant h, see McGervey [102]. The amount of "liberated" electrons correlates with the amount of incoming photons or the intensity of the light.

For an image acquisition system this means that the accumulated electronic charge per cell and time is a function of the intensity of the incoming light or the amount of photons per time. This charge is transferred to a multiplexer with the method described before and the voltage per cell is amplified and measured.

A simple CCD sensor is not able to distinguish colours. Cameras use optical filters for colour based image acquisition in order to limit the spectral bandwidth of the electromagnetic waves reaching the silicon substrate. In the case of the cameras used at the Institute of Jet Propulsion the incoming light beam is split in a prism into three beams with nearly completely distinct wavelength spectra. Each of the beams is captured by a dedicated CCD chip and for each pixel distinct values for the red, green and blue components of the light are obtained. The sensitiveness of the chips as function of the wavelength is given in fig. 3.5.

The charge per cell or pixel accumulated during one period is amplified and the intensities of the light components red, green and blue are read. The voltage for each pixel and light component are read in a frame grabber (*"Data Translation" DT3154*) and digitised. The frame grabber has a resolution of eight bits per channel and therefore 256^3 combinations of red, green and blue are possible.

Uncertainties With the Image Acquisition

The signals measured at the digital cameras are subjected to a certain noise which can deteriorate the signals and increase the level of uncertainty. Schmidt [120] identifies mainly following sources for noise:

Figure 3.7: 3D view of the RGB system

Figure 3.6: Signal level for the red, green and
blue signals at closed diaphragm

- dark current: are thermally generated carriers,

- shot noise: uncertainty due to Poisson probability distribution,

- photo response nonuniformity: systematic difference between the cells,

- trapping noise: due to ineffective transfer,

- reset or kTC-noise: due to thermal noise through resistors and occurs when a capacitor
  is charged.

Also the data transfer to the frame grabber and the frame grabber card itself contribute to a
certain amount of noise. In order to capture most of this noise, images were taken with the
cameras at closed diaphragm. A sample of the signal captured is given in fig. 3.6. As can be
seen, the signal for the green channel is considerably higher than the ones for the other two
channels. This non-uniformity would lead to a miss-tuned signal as will be shown later. The
variances of the signals seen here are taken into account as uncertainty of the captured signal.

3.1.2   Colour Analysis

The camera gives for each pixel different intensities of the light components red, green and blue.
The colours can be viewed in a Cartesian system as shown in fig. 3.7. The resulting colour $\vec{F}$
is then a composition of these three colours $\vec{R}$, $\vec{G}$ and $\vec{B}$ with

$$\vec{F} = i_r \cdot \vec{r} + i_g \cdot \vec{g} + i_b \cdot \vec{b} = \vec{R} + \vec{G} + \vec{B}, \tag{3.3}$$

(a) Without subtraction of noise   (b) With subtraction of noise
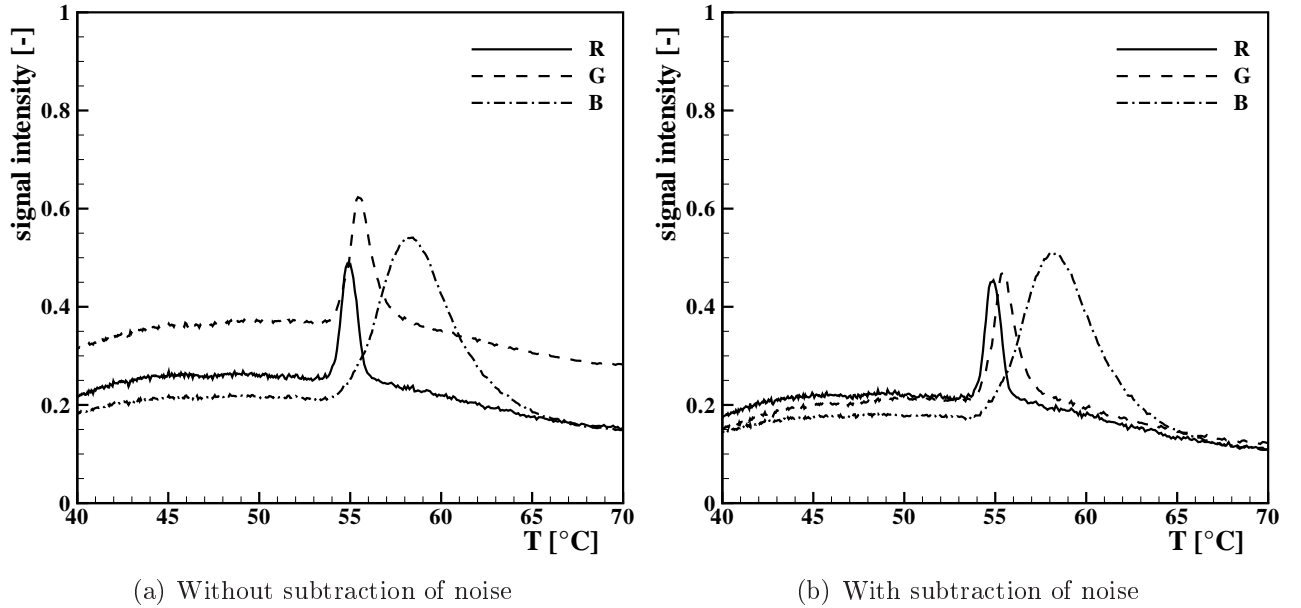
Figure 3.8: R, G and B as function of the temperature for a TLC sample

as explained in Frey [63]. The variables i_r, i_g and i_b are the intensities of every component and $\vec{r}$, $\vec{g}$ and $\vec{b}$ are the three directions of the Cartesian system. The vectors $\vec{R}$, $\vec{G}$ and $\vec{B}$ shall from this point on be referred without vector lines. For each combination of R, G and B the resulting point lies inside the cube displayed by dashed lines and the three colours can adopt any integer value between 0 and 255 in conformity with the resolution of the frame grabber. For the data analysis the values of the colour components R, G and B are normalized from 0 to 1 by dividing them by 255.

Using the colour components alone turns it difficult to make an explicit correlation of the colour to the temperature. As shown in fig. 3.8(b) there exists almost no unique value of R, G or B for a certain temperature. In this figure the signals are displayed as function of the temperature of the crystals. As can be seen, by increasing the temperature the crystals get red, which is visible with the increase of R while the other two signals remain at a rather low level. When passing to yellow and then to green R gets weaker, while G increases. It then continues with the increase of B when passing to blue.

Another point of interest is that the raw image (shown in fig. 3.8(a)) has no equal levels of R, G and B in the regions where the crystals are not active, e. g. for temperatures below 55° C. The reason for this is the offset signal which is seen with closed shutter as shown in fig. 3.6. The plot from fig. 3.8(b) is for the same image as in fig. 3.8(a) but the values R, G, B were subtracted by the offset.

A way of getting a non-ambiguous relationship between colour and temperature is to transform the colours into the HSI-space. In the HSI-space every point inside the cube of fig. 3.7 is defined by its

- hue H,

- saturation S,
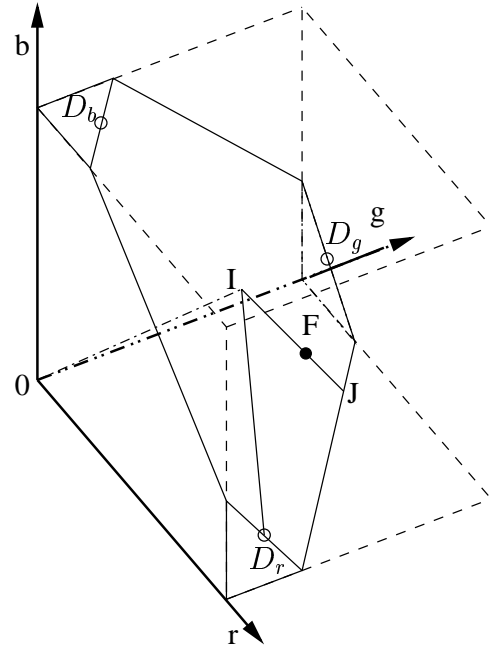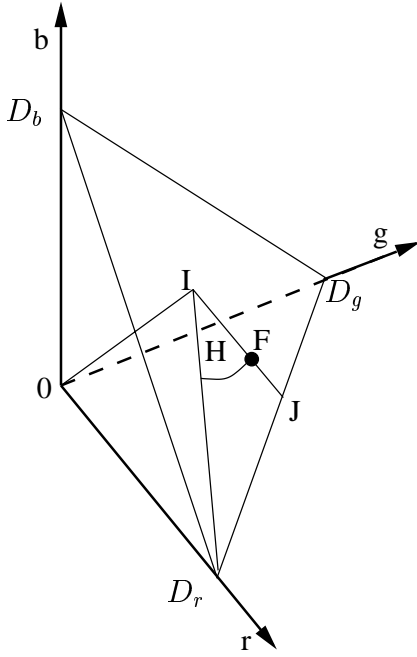
Figure 3.9: Schematic for the definition of H, S and I at $I \leq 0.3$

Figure 3.10: Schematic for the definition of H, S and I at $I > 0.3$

- intensity I.

In fig. 3.9 the definition of the three values H, S and I is shown. The colour F is defined by the angle H comprised by the vectors $\vec{ID_r}$ and $\vec{IJ}$, the intensity I which is the distance $|\vec{0I}|$, and the saturation S which defines how close the point F is to the edges of the triangle $D_r D_g D_b$:

$$S = \frac{|\vec{IF}|}{|\vec{IJ}|}. \tag{3.4}$$

The plane perpendicular to the vector of gray scale $\vec{0I}$ is in the most simple way a triangle as in fig. 3.9. For an intensity higher than 0.3 the shape changes to an octahedron as shown in fig. 3.10. For $I \geq 0.6$ the plane is again a triangle but turned by 60° compared to the one of fig. 3.9. By geometric analysis and norming the values to unity at maximum one obtains following definition for the intensity and saturation:

$$I = \frac{R + G + B}{3}, \tag{3.5}$$

$$S = \max\left[1 - \frac{\min[R, G, B]}{I}, \frac{I - \max[R, G, B]}{I - 1}\right]. \tag{3.6}$$

In Frey [63] only the first part of eq. 3.6 is given. But this is only valid for $I \leq 0.5$. The definition of hue often seen in literature is only valid for angles $\leq 180°$. Here three angles are
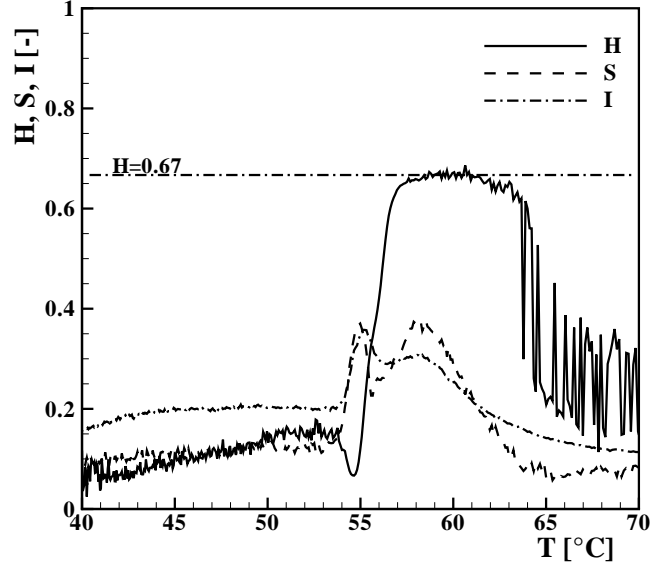
Figure 3.11: H, S and I as function of the temperature for a TLC sample

computed and H is found with:

$$H_r = \arccos \left(\frac{2 \cdot R - G - B}{\sqrt{6 \cdot \left[(R-I)^2 + (G-I)^2 + (B-I)^2 \right]}} \right)$$

$$H_g = \arccos \left(\frac{2 \cdot G - R - B}{\sqrt{6 \cdot \left[(R-I)^2 + (G-I)^2 + (B-I)^2 \right]}} \right)$$

$$H_b = \arccos \left(\frac{2 \cdot B - R - G}{\sqrt{6 \cdot \left[(R-I)^2 + (G-I)^2 + (B-I)^2 \right]}} \right)$$

$$H = \begin{cases} H_r & \text{if } H_r + H_g = 2/3 \cdot \pi \\ H_g + 2/3 \cdot \pi & \text{if } H_g + H_b = 2/3 \cdot \pi \\ H_b + 4/3 \cdot \pi & \text{if } H_b + H_r = 2/3 \cdot \pi \end{cases} \tag{3.7}$$

After transformation into the HSI-system a unique relation between hue and temperature exists within the range of optically active crystals. In the case presented in fig. 3.11 the crystals are active between 55° C and about 58° C. It is also visible in this picture that the hue value does not exceed 2/3 when there are no other interferences. $H = 0.\overline{6}$ represents pure blue which is the end of the visible spectrum at the shorter wave lengths. Higher values of hue are possible by mixing e. g. blue and red but no single electromagnetic wave can give such a colour. As can also be deduced from fig. 3.11, a criterion must be found in order to define whether the crystals are optically active or not. It was found, that a minimum saturation is suitable for determination of their active state.
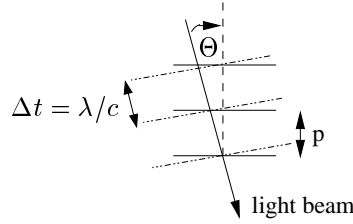
Figure 3.12: Schematic of Bragg reflection with the incident light at an angle θ

3.2 Influence of Illumination and Viewing Angle on TLC

Due to its crystal structure the light is subjected to Bragg reflection when the incident wave is not parallel to the rotation axis. When light is incident at an angle θ on a pure crystal, as in fig. 3.12, light with wavelength λ will be reflected:

$$\lambda = p \cdot n \cdot \sin(\theta). \tag{3.8}$$

As pointed out by Dreher and Meier [46] at oblique light incidence higher-order harmonics of this wavelength can appear. A simple approach by Fergason [60] does not account for these harmonics but is much more easy to handle in the experiments and, as will be shown, gives satisfactory results. Fergason gives the relationship between the wavelength of maximum reflection λ to the wavelength at normal incidence λ_n as

$$\lambda = \lambda_n \cdot \cos\left[\frac{1}{2}\sin^{-1}\left(n^{-1}\sin\phi_i\right) + \frac{1}{2}\sin^{-1}\left(n^{-1}\sin\phi_s\right)\right], \tag{3.9}$$

with ϕ_i and ϕ_s as the incidence and reflective angle respectively towards the perpendicular axes on the surface, see also fig. 3.14. The mean refraction index is usually around 1.5.

Several studies are known from open literature where the influence of viewing and light incidence angle is assessed, but few try to solve the problem. In fact to the author's knowledge Fergason is the only one who gives a relationship between the pitch of the crystals and the illumination and observation angle. Farina et al. [59] measured the calibration curve for sprayable micro-encapsulated TLC from *Hallcrest* with red start temperature at 35° C and a bandwidth of 5° C (R35C5W). They captured the curves with the relation hue to temperature at different lighting and observation angles. Either light source and camera were moved together (called on-axis) or the camera remained mounted perpendicular to the surface and the light source moved. The authors show that in the on-axis case the variation up to angles of 25° is negligible. In the off-axis case, however, when only the light source moves, the hue curve is shifted towards lower temperatures with increasing angle between camera and light. Behle et al. [13] extend the analysis to larger angles and looked also on TLC sheets. They confirm the only small influence of oblique incidence onto the surface, when the camera and the illumination are on the same axis, up to 70°. Large deviations are seen with the camera remaining perpendicular to the surface and the light source moving. They also report a higher sensitivity with the TLC sheet for the on-axis configuration, while the differences are lower with sheet for the off-axis configuration. The reason given by the authors for the sensitivity with the sheet at higher angles and on-axis configuration is the ordered and planar structure of the crystals and the low
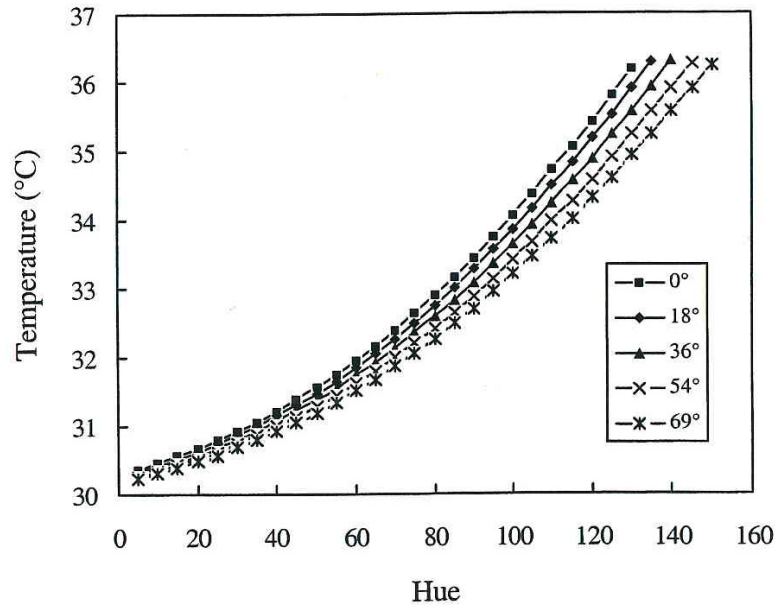
Figure 3.13: Relationship between hue and temperature for varying incidence angle of the on-axis configuration, from [26]

reflectivity at high angle. With sprayable TLC the degree of disorder is much higher and light is reflected in any direction.

Chan et al. [26] calibrated sprayable microencapsulated thermochromic liquid crystals with on-axis configuration with incidences up to 72°. They found slightly higher sensitivity of the hue distribution on the viewing and illumination angles than Farina et al. [59]. As shown in fig. 3.13, in their experiments the relation of temperature with hue gets more linear with increasing incidence angle. Barigozzi and Benzoni [11] conclude in their experiments that with varying angle up to 20° with an on- axis configuration the variances in the hue to temperature correlation are small.

3.3   Calibration of TLC Under Varying Illumination and Observation Angles

Measurements with thermochromic liquid crystals require carefulness in order to make the temperature acquisition insensitive to various influences which are sometimes inevitable. Some can be minimized by using always the same configurations of the illumination and image acquisition devices and by transformation of the RGB-signals into the HSI-system. Others such as the influence of viewing and illumination angle have to be accounted for when measuring on a curved surface such as a turbine blade. Following the results from literature [13, 59] the on-axis configuration was used for the calibration and for the measurements in order to reduce its influence. Nevertheless for high accuracy measurements and difficult illumination access the influence of the incidence angles was investigated and a correction technique following Fergason [60] was implemented.

3.3.1   Hardware Set-up for TLC Calibration

The calibration hardware set-up is shown in fig. 3.14. An aluminum sheet is heated on one
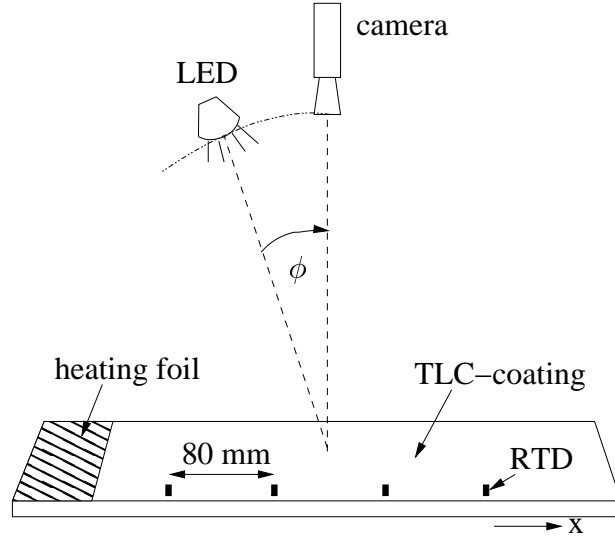
Figure 3.14: Set-up for TLC calibration

extremity with a heating foil creating in such manner a temperature gradient in x-direction. The opposite extremity of the plate could be cooled, as used by many authors, but with the crystals analysed here and with the surface subjected to natural convection this was not needed. The upper surface of the plate is first sprayed with black backing from *Hallcrest* in order to reduce the undesired reflections from the surface. Afterwards several coatings of sprayable microencapsulated TLC are sprayed. The TLC used for the angle sensitivity study have red start temperature of 31° C and a declared bandwidth of 3° C (R31C3W). The plate is thermally insulated towards the sides and the bottom and the upper surface is open. The only light source are white light LED and the image of the surface is captured by a 3CCD camera. Both LED and camera are placed at a distance from the surface of 1.5 m and can be rotated by an angle ϕ towards the perpendicular axes to the surface. This means for the definition of the incidence and outgoing angle according to eq. (3.9) that when the light source is moved $\phi_i = \phi$ and when the camera is moved $\phi_s = \phi$. The surface temperature is monitored with four resistance temperature devices (RTD) at a distance from one RTD to the next of 80 mm yielding in a total calibration length from the first to the last RTD of 320 mm. The height of the plate is $\Delta y = 10$ mm and the width is $\Delta z = 100$ mm. In fig. 3.15 the definition of the coordinate system and a schematic of the calibration apparatus is shown.

Most authors using a temperature gradient for calibration of TLC with a single image use some kind of window on the top of the surface in order to reduce natural convection and to get an almost linear temperature gradient. Some drawbacks can occur with it, such as undesired reflections which must be filtered as far as possible with polarizing filters. Also the light refraction in the window makes the evaluation of the position of each pixel at oblique observation angles and the correction of angle influences more complicated. Therefore, the calibration surface was not covered here and almost the same conditions as later for the measurements are given. Due to natural convection (the surface is hotter than the surrounding air) the temperature distribution along the x-axis is not linear. The temperature distribution along the plate is obtained by solving the differential equation of the temperature as function of the
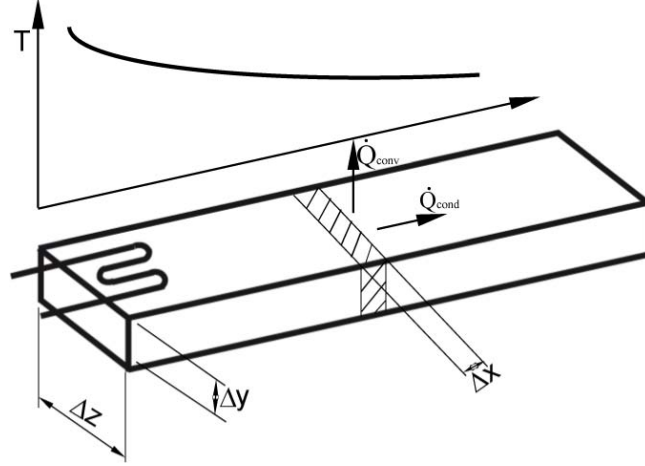
Figure 3.15: Schematic for the calibration of the TLC and exemplary temperature distribution

natural convection heat transfer coefficient h

$$-k\frac{\partial^2 T}{\partial x^2} \cdot \Delta y \cdot \Delta z = \frac{\dot{Q}_{conv}}{\Delta x} = h \cdot \Delta z \cdot (T_w - T_\infty). \tag{3.10}$$

The heat transfer coefficient is calculated from the Nusselt number Nu given by the equation from Churchill [29] as it is referred in [150]

$$\mathrm{Nu} = \begin{cases} 0.766 \left[\mathrm{Ra} \cdot \mathrm{f}\left(\mathrm{Pr}\right)\right]^{1/5} & \text{for } \mathrm{Ra} \cdot \mathrm{f}\left(\mathrm{Pr}\right) < 7 \cdot 10^4 (\text{laminar flow}) \\ 0.15 \left[\mathrm{Ra} \cdot \mathrm{f}\left(\mathrm{Pr}\right)\right]^{1/3} & \text{for } \mathrm{Ra} \cdot \mathrm{f}\left(\mathrm{Pr}\right) > 7 \cdot 10^4 (\text{turbulent flow}) \end{cases},$$

$$\text{with } \mathrm{f}\left(\mathrm{Pr}\right) = \left[1 + \left(\frac{0.322}{\mathrm{Pr}}\right)^{11/20}\right]^{-20/19}. \tag{3.11}$$

From the definition of the Nusselt number

$$\mathrm{Nu} = \frac{h \cdot l}{k}$$

the heat transfer coefficient h is easily obtainable.

Since the Rayleigh number Ra is a function of the Grashof number Gr which itself is a function of the wall temperature, eq. (3.10) can not be solved analytically but must be solved iteratively. For solving this equation the two outer RTD are used for setting the boundary conditions (fixed temperature) and the two inner RTD serve as control of the accuracy of the calibration line. With this technique, an agreement between measured and calculated temperature of better than $0.1°C$ can be achieved. The two inner RTD do not influence the result of the temperature curve, therefore they are a good indicator of the quality of the calibration process.

For the analysis of the angle influence on the reflected light, three configurations were used. In the first configuration the light source and camera move together which gives the on-axis configuration. For the off-axis configuration two cases were analysed. In the first case the camera remains perpendicular to the surface, while the light source moves. In the second of the
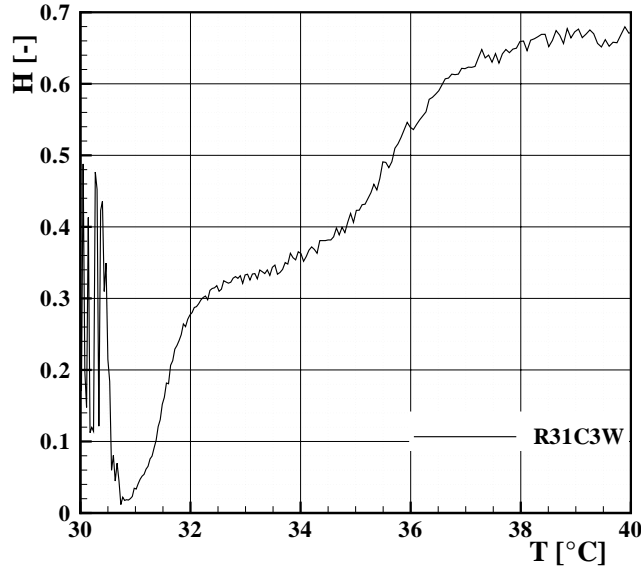
Figure 3.16: TLC calibration curve for TLC R31C3W

off-axis cases the light source remains perpendicular to the surface and the camera moves. The angle variations used for these analyses extend from 0° to 45°, with 0° as the perpendicular view.

3.3.2 Illumination and Observation Angle Influence on Reflected Light

The TLC used for these experiments have a declared bandwidth of 3° C and a red start temperature of 31° C. The calibration curve for the whole spectrum is given in fig. 3.16. This curve was taken on a different plate than the one explained before. This plate has a thickness of 1.5 mm which allows to have larger temperature gradients along the plate and the acquisition of the entire colour spectrum of these crystals. One can see that from the red start point on, the hue increases strongly with increasing temperature until a plateau is reached at green ($H = 0.33$). Afterwards the curve exhibits again a strong increase of hue up to the point where blue colour is reached ($H = 0.67$). This is due to the sensitivity of the CCD chips as shown in fig 3.5. In the wavelength region between 600 and ≈ 560 nm the sensitivity of the chip for red decreases continuously while the one for green increases. At 560 nm $\geq \lambda \geq 500$ nm almost only the chip for green colour gives any response, reason why a plateau is observed for hue. At λ between 500 and 480 nm hue increases again towards blue. This gives usually a double S-shaped curve, which is often seen in open literature. Therefore intermediate colours between red and green as well between green and blue are best suitable for measuring the temperature.

As referenced e. g. in Chandrasekhar [27], the twist of the crystals increases exponentially towards very small wavelengths, but for TLC comprising the whole visible wavelength spectrum the relation is linear over nearly the entire spectrum. Therefore the curve of fig 3.16 is set as function of the wavelength by assuming linearity in the changing twist of the crystals with temperature. A wavelength of 650 nm is set at 30.9° C and 400 nm is set for 38° C. The hue values as function of the wavelength are then approximated by a polynomial and the same is
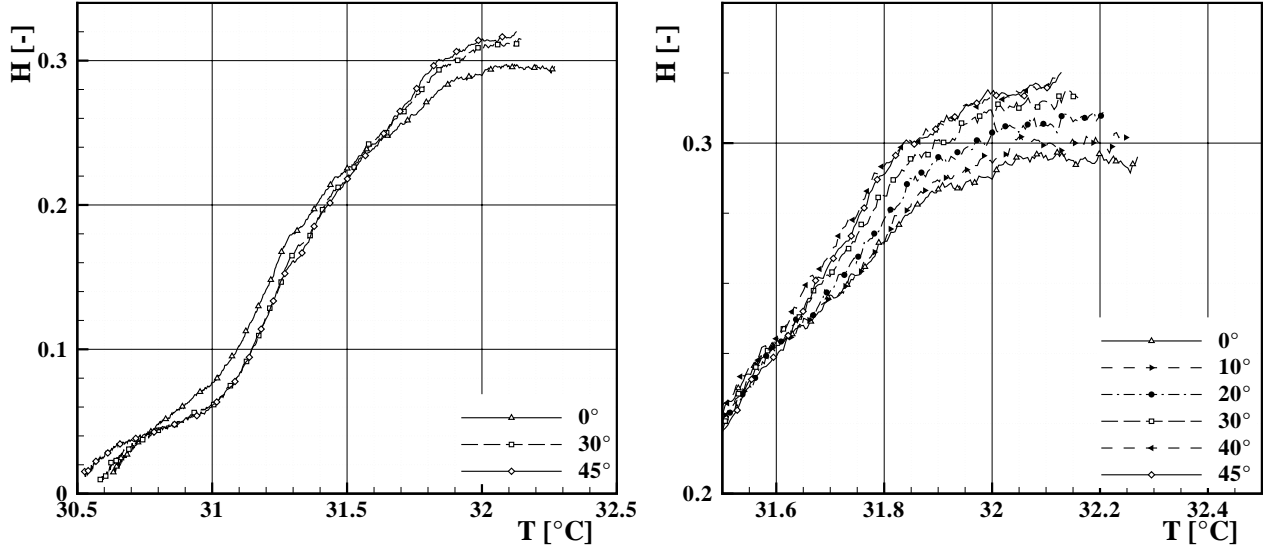
Figure 3.17: TLC calibration curve for on-axis arrangement without background image calibration

done the other way round:

$$H \quad = \quad p_1(\lambda) \tag{3.12}$$
$$\lambda \quad = \quad p_2(H). \tag{3.13}$$

By this approximation the wavelength can be calculated from the measured hue and a correction following Fergason's approach of eq. (3.9) can be used to calculate the correct pitch of the liquid crystals. The hue, which would be obtained with normal incidence, is calculated from the corrected wavelength with the second polynomial.

The thicker aluminium plate was used for the analysis of the angle sensitiveness of the TLC. Very low temperature gradients are present and a high spatial resolution is achieved with this plate. As drawback not the entire spectrum can be acquired at once and the results shown are for a colour range from red to green ($0 \leq H \leq 0.4$).

First the on-axis arrangement is discussed, i. e. according to eq. (3.9) $\phi_i = -\phi_s$. In fig. 3.17 hue is plotted as function of the temperature for illumination and observation angles of 0°, 30° and 45°. On the left the measured spectra is shown while on the right a detailed view of the transition region to green is shown. It is visible that the differences are very small and at same hue the variation in temperature is over most of the range below 0.1° C. Only at temperatures $T \geq 32°$ C the curves deviate stronger. Nevertheless the differences are slightly larger than the uncertainty and there seems to be a constant drift towards stronger slope of the curve as the viewing angle increases. As reported in Breuer [21], this drift is similar to the one of Chan et al. [26].

Possible explanations for this behaviour can be interferences with other wavelengths, either higher harmonics for oblique incidence or other reflections such as the background or the capsules of the TLC. In fact, a defined colour is captured by the camera in an optically non active state of the crystals. In fig. 3.18 the measured hue and intensity is plotted along the length of

33
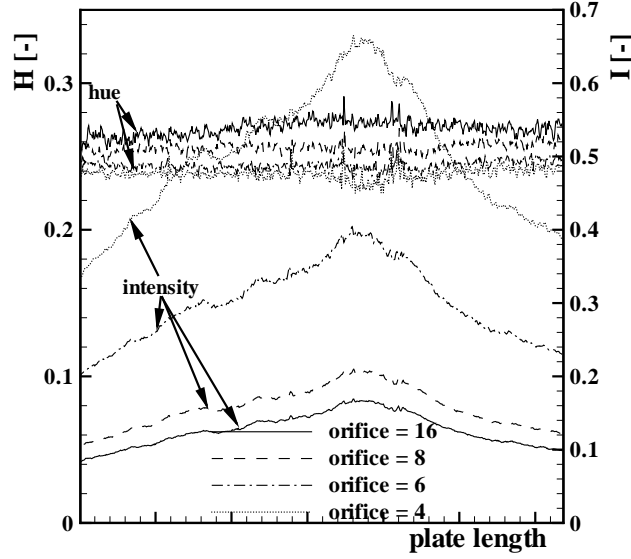
Figure 3.18: H and I for optically inactive TLC

the plate for optically inactive crystals at perpendicular observation and lighting. The curves are taken with changed aperture of the orifice of the camera in order to change the intensity of the reflected light. One can see that, though the intensity varies very strongly from about 0.1 to the septuple of it, the hue remains almost constant at about 0.25 which represents a yellowish colour. This background image is superimposed on the reflection of the TLC changing the whole perceived image. When the lighting and observation angle is changed, the influence of the background image decreases since most of the light rays will reflect into the opposite direction. The reflection and incidence angles are the same according to Huygens' principle.

Background images with inactive TLC where taken for all viewing angles which allows to calibrate the images of the active TLC. Therefore the average hue H_{bck} and saturation S_{bck} of the background image is calculated. The intensity $I_{eval}(x, y)$ for each pixel of the evaluation image scaled by a proportional factor $\xi = I_{ref,bck}/I_{ref,eval}$ is used to transform the background hue and saturation into the RGB-system:

$$(H_{bck}, S_{bck}, I_{eval}(x, y) \cdot \xi) \rightarrow (R_{bck}(x, y), G_{bck}(x, y), B_{bck}(x, y)). \qquad (3.14)$$

The reference intensity for the background image $I_{ref,bck}$ and the intensity for the evaluation image $I_{ref,eval}$ are taken at the same point inside the measured area. The scaling parameter ξ is used in order to account for the fact that, when lighting and data acquisition are kept constant, the intensity of the light with optically active crystals is higher than when they are not active. The evaluation image is then calibrated by subtracting the RGB-values from the background taken from eq. (3.14):

$$R(x, y) = R_{eval}(x, y) - R_{bck}(x, y) \qquad (3.15)$$

$$G(x, y) = G_{eval}(x, y) - G_{bck}(x, y) \qquad (3.16)$$

$$B(x, y) = B_{eval}(x, y) - B_{bck}(x, y). \qquad (3.17)$$

Using the background images to calibrate the evaluation image, the curves of fig. 3.19 are obtained. On the left the curves are displayed for the whole measured spectrum and at the
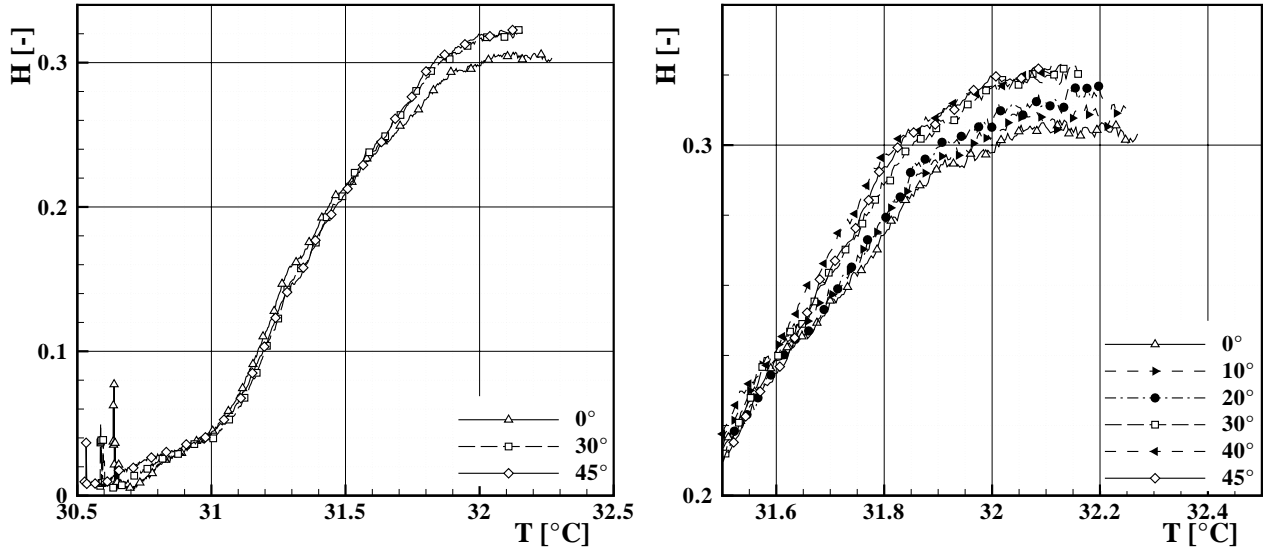
Figure 3.19: TLC calibration curve for on-axis arrangement with background image calibration

(a) Without calibration image

(b) With calibration image
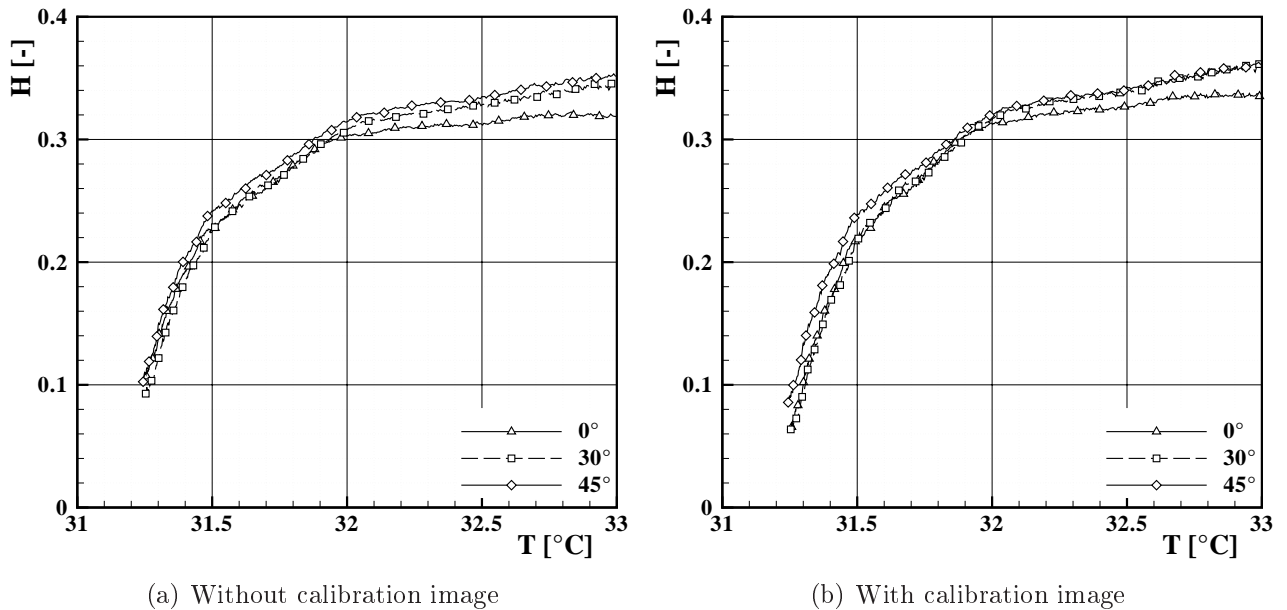
Figure 3.20: TLC calibration curve for on-axis arrangement for $31°$ C $< T <$ $33°$ C

right a close-up view at higher temperatures is given. The temperature differences at same hue values are within $0.02°$ C and therefore well below the measurement uncertainty of the RTD. Only towards green colour the curves for steeper views drift a little bit as can be seen on the right of fig. 3.19. A possible explanation could be a small drift of the hue value of the background at lower intensities towards the end of the measured range, since no completely homogeneous illumination was obtainable for such a large area.

In fig. 3.20(a) the hue distribution for slightly higher temperatures without image calibration

(a) Without angle correction   (b) With angle correction
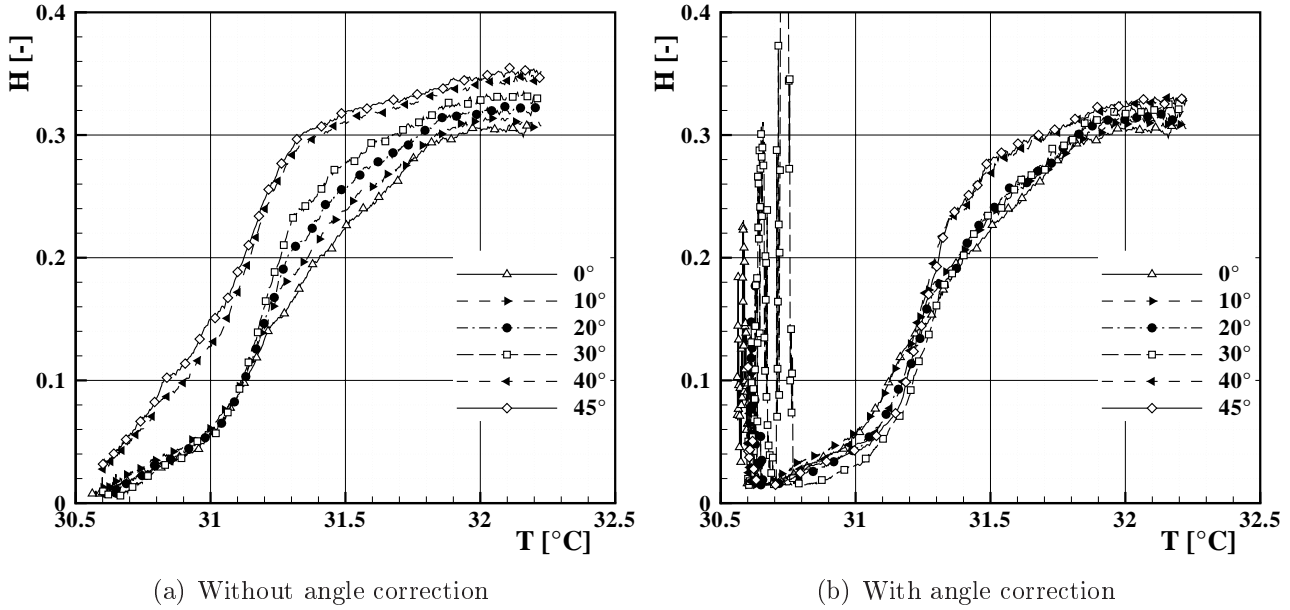
Figure 3.21: TLC calibration curve for off-axis arrangement and perpendicular illumination for $30.5°$ C $< T < 32.5°$ C

is shown while in fig. 3.20(b) the same is given with background correction. Again the use of the background image improves the accuracy of the measured hue to temperature correlation.

While moving light source and camera together the changes in the perceived colours are small, the situation is quite different for the off-axis configurations. Images were taken with either the camera or the light source aligned perpendicular to the surface, while the other component (light source or camera respectively) where turned stepwise up to an incidence angle of $45°$. For the case with moving camera and perpendicular illumination ($\phi_s = \phi$ and $\phi_i = 0$) the calibration lines up to $31.5°$ C are plotted in fig. 3.21(a). It is well visible that with increasing viewing angle the curves are shifted towards higher hue values which is equivalent to shorter wave length. This is explainable by Bragg reflection. In fig. 3.21(b) the calibration lines with corrected wavelength are shown. Applying the correction method using eq. (3.9) with a main refraction index of $n = 1.5$ and the polynomials from eq. (3.12) the curves almost collapse together and the variance in temperature is below $0.2°$ C in the region between red and green. As said before, this is one of the two most indicated regions for measurements, where a lower uncertainty in the determination of the temperature from hue is obtainable.

The same occurs when the camera is kept perpendicular to the surface and the illumination is turned, i. e. $\phi_s = 0$ and $\phi_i = \phi$. In fig. 3.22(a) the hue is plotted as function of the temperature without angle correction. The deviation of the lines towards higher hue values with increasing illumination angle is similar to the case when the camera is moving and the light is placed perpendicular to the surface. By applying the correction method the variances get considerably smaller as shown in fig. 3.22(b).

For slightly higher temperatures the calibration curves are given in fig. 3.23 and 3.24. Also here the application of this correction method increases by far the accuracy of the measurements, when illumination and viewing angle angle are different.

36
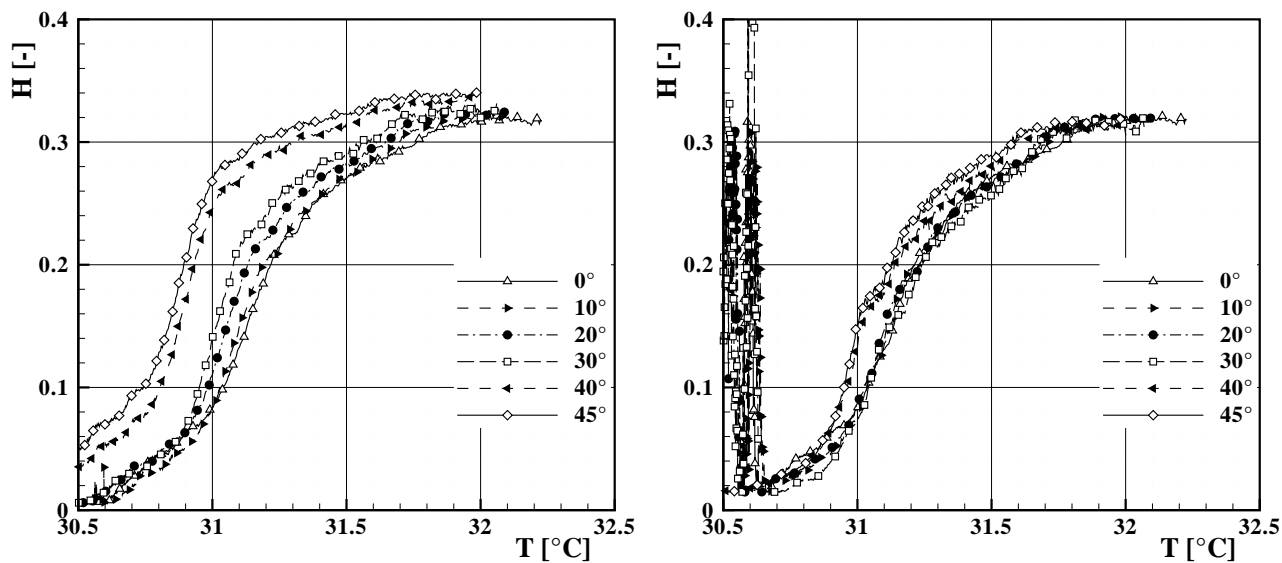
(a) Without angle correction

(b) With angle correction

Figure 3.22: TLC calibration curve for off-axis arrangement and perpendicular camera view for $30.5°\,C < T < 32.5°\,C$
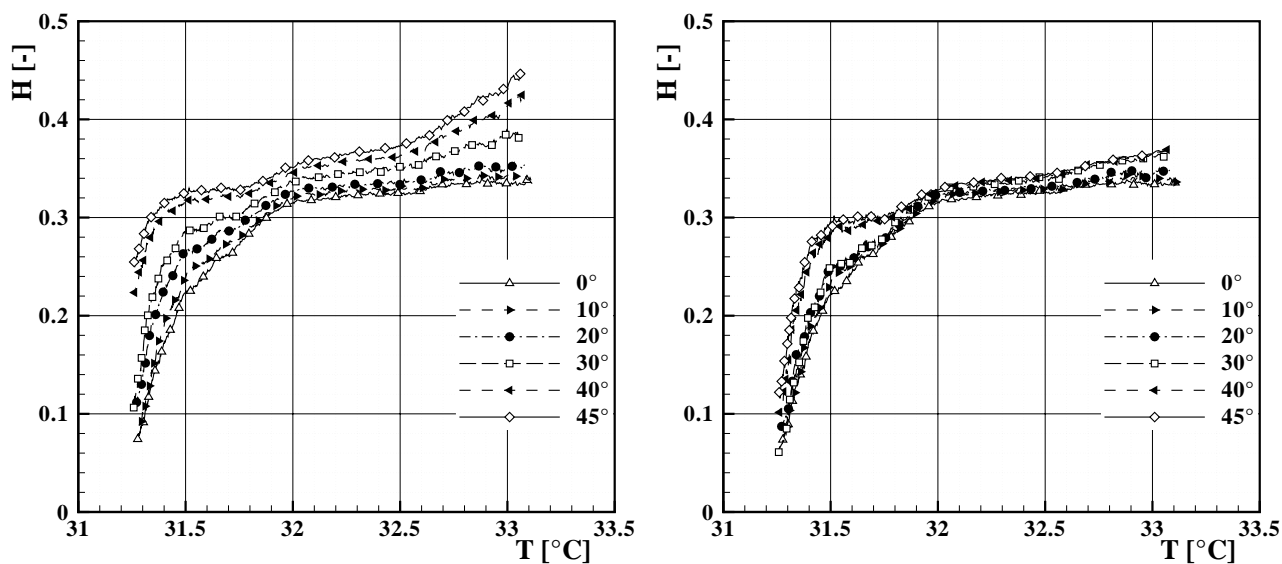
(a) Without angle correction

(b) With angle correction

Figure 3.23: TLC calibration curve for off-axis arrangement and perpendicular illumination for $31°\,C < T < 33.5°\,C$

(a) Without angle correction

(b) With angle correction
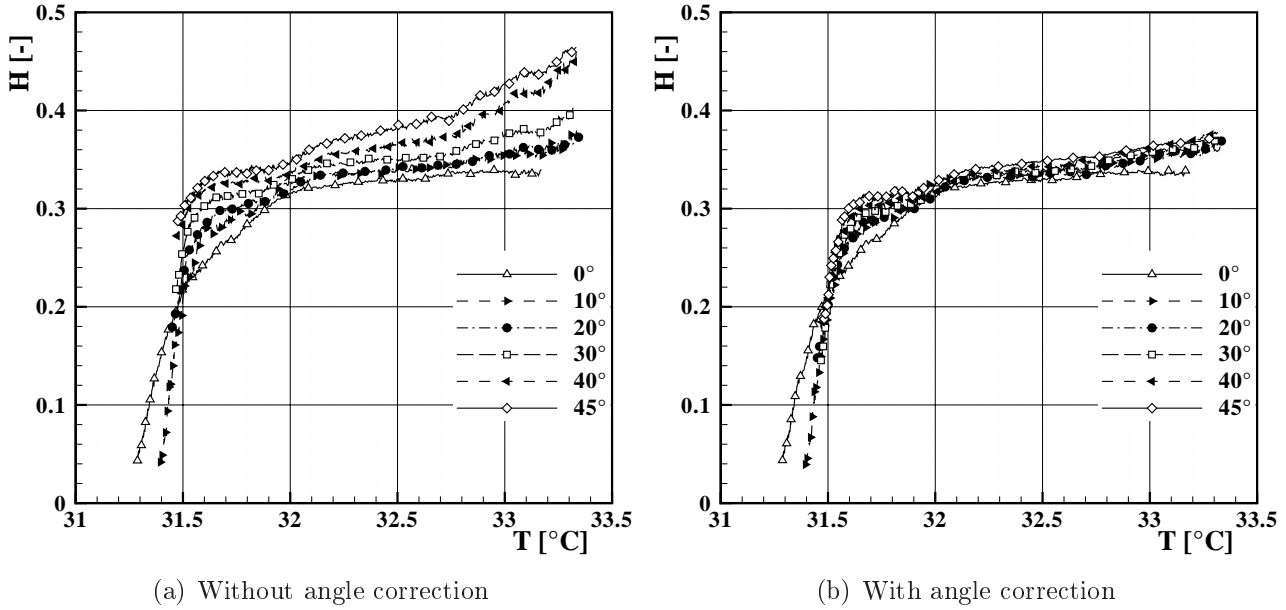
Figure 3.24: TLC calibration curve for off-axis arrangement and perpendicular camera view for $31°\,C < T < 33.5°\,C$

Summary of the Correction Method for TLC Measurements

In this chapter, a technique using thermochromic liquid crystals for temperature measurements was explained. A digital camera is used for capturing images of a surface with sprayable liquid crystals. The TLC change their colour in dependency of their temperature and are suitable for temperature measurements on surfaces. It was shown that the perceived colour depends on various factors, such as light source, background reflections, image acquisition device and orientation of the camera and light source relative to the surface with TLC.

The calibration method presented here uses a differential equation for determination of the relation between temperature and colour of the crystals. This allows to obtain an uncertainty below $0.1°\,C$ for this determination.

For oblique observation and illumination of the surface, it was shown that an on-axis configuration with the light source in line with the camera is the most appropriate way to measure the temperature with TLC. The increase in uncertainty due to turning of the camera and light source was of $0.02°\,C$ for angles up to $45°$. In cases where camera and light source can not be in the same axis, the curves of hue as function of temperature are shifted due to Bragg reflection. A correction method allows to account for this change in perceived frequency of the light and reduces the uncertainty in the off-axis configuration to $0.2°\,C$. This method is indicated to be applied for cases with difficult illumination. Different observation angles are inevitable on curved surfaces and the intensity of the reflections decreases with increased deviation from the perpendicular direction. An image taken with an illumination from a different angle than the observation angle can enhance the quality of the signal due to the increased intensity in regions with very shallow observation angle. In that case the correction method is mandatory to obtain the correct temperature.

4 Test Set-up

The investigations on film cooling in regions with main flow separation were experimentally conducted on two cascades. The cascade *T120C* has a rather conventional blade loading with pressure side film cooling while the cascade *T120S* is based on the same blade geometry but featuring an increased loading and suction side film cooling.

4.1 Cascade and Film Cooling Geometry

The *T120C* cascade was designed by *Rolls-Royce Deutschland* for the purposes of the AITEB project, see Janke [86]. The airfoil of the *T120* cascades has a quasi typical high-pressure turbine (HPT) blade design but with the intention to force a large main flow separation on the pressure side (PS). Therefore the profile presents a strong concave curvature on the PS starting shortly after the leading edge, as can be seen in fig. 4.1. Together with the high pitch to chord ratio, relatively strong positive pressure gradients are present on the pressure side resulting in flow separation. Typically for HPT blades, a high turning is imposed on the flow and it is designed for high exit Mach numbers — close to sonic — at the exit. The aerodynamic and geometric data for the *T120C* cascade at design conditions are listed in tab. 4.1. For the definition of the geometric data please refer to the sketch next to the table.

In fig. A.1 — taken from Homeier [80] — the isentropic Mach number along the blade surface is plotted as function of the normalized axial position for the design inflow angle and various operation points. One can see that the flow undergoes a strong acceleration on the suction side and can reach values well beyond Ma=1. It then decelerates, in general via shock waves, very quickly at a relative axial position between 0.7 and 0.9 depending on the exit Mach number. On the pressure side a strong separation is visible in the measurements. The flow separates shortly after the stagnation point and reattaches at about half of the axial chord length. The separation and reattachment points on the PS are confirmed by hot film measurements and near wall flow visualizations in Homeier [80].

The *T120C* blade has two film cooling rows located on the pressure side of the blade. The first row is placed shortly after the stagnation point and has cylindrical holes with compound angle against the main stream direction. The second row presents fan-shaped, laid-back holes with zero compound angle and is located at approximately 20% of the axial chord length. The
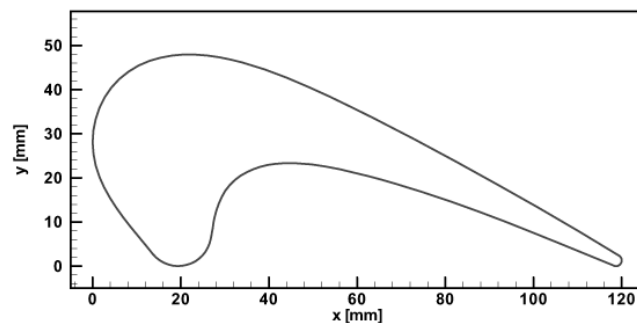
Figure 4.1: Contour of the *T120* blade, from [80]

Inlet Mach Number	Ma_1	0.295
Inlet Reynolds Number	Re_1	175,000
Exit Mach Number	$Ma_{2,s}$	0.87
Exit Reynolds Number	$Re_{2,s}$	390,000
Inlet Flow Angle	β_1	138.6°
Exit Flow Angle	β_2	19.2°
Blade Span	h	176 mm
Pitch to Chord Ratio	t/c	1.007
Stagger Angle	β_s	46.25°
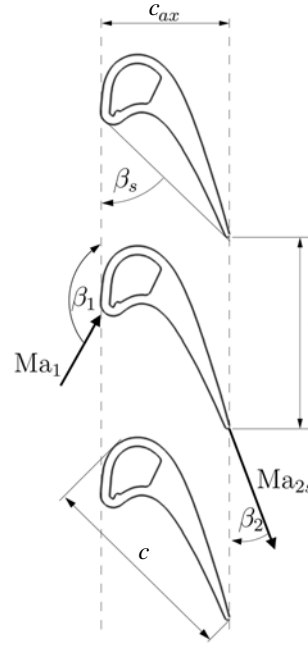
Table 4.1: Aerodynamic and geometric data of the *T120C* cascade at design point
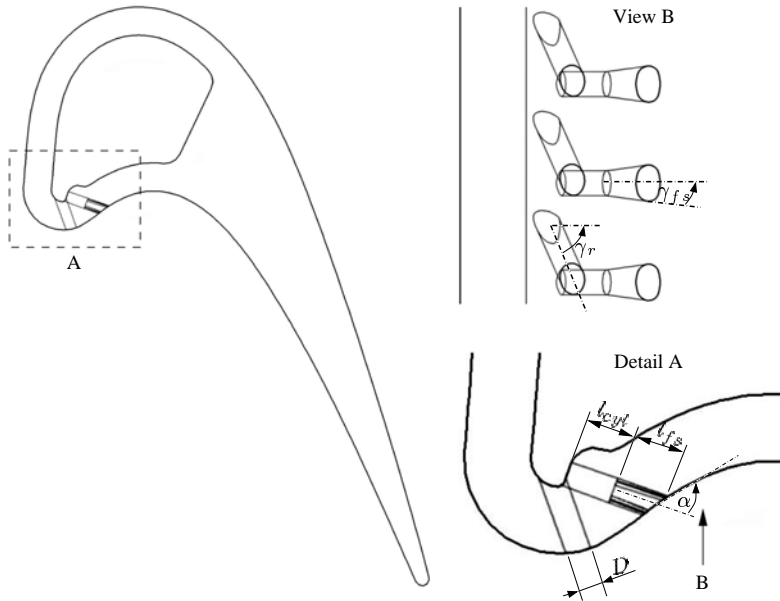
Figure 4.2: *T120C* blade with film cooling rows displayed

intention of the second row is, among others, to re-energize the boundary layer of the main stream and hence reduce the flow separation. A plot with the film cooling configuration and the definition of the geometry is shown in fig. 4.2 and an overview on the data is given in tab. 4.2.

The cooling air is supplied from one single plenum to all film cooling holes. Therefore the blowing and momentum ratios can not be set independently for each film cooling row. The

		1st row	2nd row
Number of Holes	n	21	21
Relative Axial Location	x_{ax}/c_{ax}	0.118	0.198
Diameter of Holes to Chord Ratio	D/c	0.0167	0.0167
Hole Pitch to Diameter Ratio	t/D	4	4
Cylindrical Hole Length to Diameter	l_{cyl}/D	3.4	1.9
Fan-shaped Hole Length to Diameter	l_{fs}/D	0	1.8
Local Angle to Surface	α	82.7°	56.2°
Compound Angle	γ_r	37.1°	0°
Fan-shape Angle	γ_{fs}	0°	7.5°

Table 4.2: Geometric data of the Film Cooling Configuration for the *T120C* blade

Inlet Mach Number	Ma_1	0.33
Inlet Reynolds Number	Re_1	195,000
Exit Mach Number	$Ma_{2,s}$	0.87
Exit Reynolds Number	$Re_{2,s}$	390,000
Inlet Flow Angle	β_1	138.6°
Exit Flow Angle	β_2	20°
Blade Span	h	176 mm
Pitch to Chord Ratio	t/c	1.13
Stagger Angle	β_s	46.25°

Table 4.3: Aerodynamic and geometric data of the *T120S* cascade at design point

rows of film cooling holes extend throughout the whole span of the blade of $h = 176$ mm and the plenum is large enough to have nearly identical mass flow per hole in spanwise direction, as is confirmed in numerical simulations in Pons and Gomes [114] for a similar blade called *T120D*.

The *T120S* cascade is an evolution of the *T120C* cascade. In order to increase blade loading obtaining in such a manner high Mach numbers on the suction surface leading to a shock induced separation, the blade pitch was increased from $t/c = 1.0$ in the original cascade to a ratio of $t/c = 1.13$. The design of the new cascade is presented in Starke and Janke [136] and Doerffer and Flaszynski [39]. The geometric data of the cascade and the aerodynamic design conditions are given in tab. 4.3.

Air jet vortex generators (AJVG) were introduced on the suction side in order to reduce the size of the separation bubble. The holes with small diameter are used to blow off air and generate streamwise vortices upstream of the shock induced separation. The design of the AJVG is presented in Doerffer and Flaszynski [40] and results from tests on a reference case are shown in Doerffer et al. [41, 42, 43]. The *T120S* cascade is equipped with two rows of film cooling holes on the suction side, one close to the leading edge and a second one in the acceleration region before the AJVG. The design of the film cooling holes is reported in Täge [144]. The geometric data of the film cooling holes and of the AJVG are given in tab. 4.4 and tab. 4.5 respectively.

		1st row	2nd row
Number of Holes	n	27	27
Relative Axial Location	x_{ax}/c_{ax}	0.0169	0.0329
Diameter of Holes to Chord Ratio	D/c	0.0021	0.0021
Hole Pitch to Diameter Ratio	t/D	3	3
Hole Length to Diameter	l/D	3.4	4–5.4
Local Angle to Surface	α	45°	35°
Compound Angle	γ_r	90°	0°

Table 4.4: Geometric data of the film cooling configuration of the *T120S* cascade

Number of Holes	n	41,20,13
Relative Axial Location	x_{ax}/c_{ax}	0.373
Diameter of Holes to Chord Ratio	D/c	0.0008
Hole Pitch to Diameter Ratio	t/D	5,10,15
Hole Length to Diameter	l/D	6.9–7.9
Local Angle to Surface	α	30°
Compound Angle	γ_r	65°
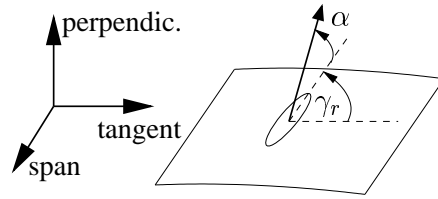
Table 4.5: Geometry definition of the AJVG

The distance between the AJVG holes can be changed in order to validate experimentally the optimum pitch, resulting in different number of holes per blade. At the right of tab. 4.5 a sketch shows the definition of the compound angle and the local angle to the surface. Looking in streamwise direction, the hole axis is first turned around an axis perpendicular to the surface by the compound angle γ_r followed by a second turn by α towards the upright direction.

A cross section view of the *T120S* blade used in the film cooling experiments is shown in fig. 4.3(a). One can see two plenum chambers allowing different pressures for film cooling and AJVG. For measurements of the blade loading and aerodynamic losses in cases without film cooling, a blade with only one plenum chamber and AJVG holes as shown in fig. 4.3(b) was used. The film cooling and AJVG holes are marked with dashed lines. For heat transfer measurements on the pressure and suction side without film cooling a massive solid blade was used which has no plenum chambers nor holes.

4.2   The High-Speed Cascade Wind Tunnel

The High-Speed Cascade Wind Tunnel in which the experiments were carried out is a open-loop test facility with open test section. The wind tunnel is enclosed inside a pressure tank. Since the static pressure inside the tank can be lowered down to 30 hPa and the total temperature of the inlet flow in the test section is controlled, the Reynolds number can be changed within certain limits independently from the Mach number. This allows the conduction of experiments on turbo-components at realistic flow conditions with an improved spatial resolution. Details on the facility are explained in Sturm and Fottner [141].

(a) With FC   (b) Without FC
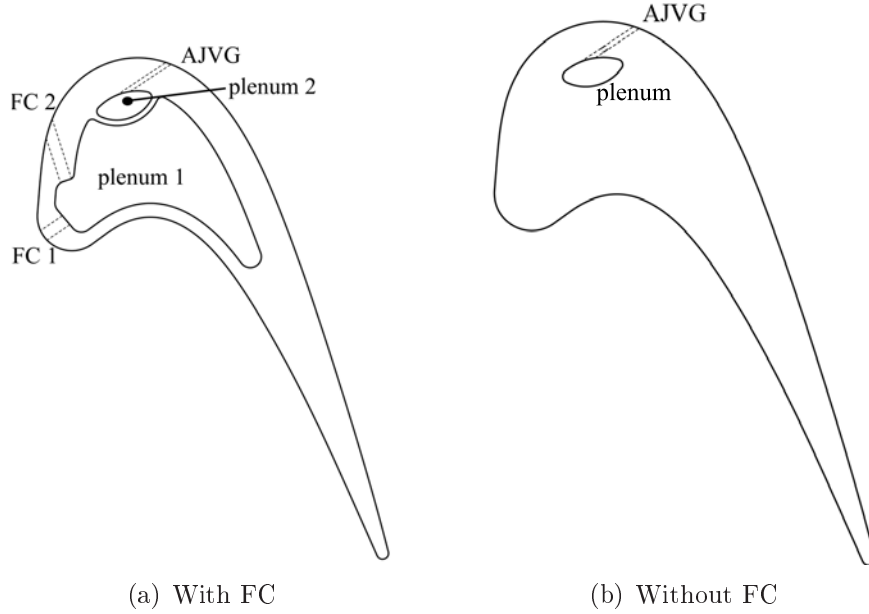
Figure 4.3: *T120S* blades with plenum chambers and FC/AJVG-holes for experiments with and without film cooling

The facility and its main characteristic data is displayed in fig. A.5. It is composed of following main components:

- air supply (axial compressor with variable rotational speed),

- settling chamber,

- nozzle with rectangular cross section and test section,

which are completely insulated from the ambient pressure conditions by the pressure tank. The 1.3 MW electric motor, the hydraulic coupling and the gear box are placed outside the pressure tank. The static pressure inside the tank is controlled with a vacuum pump with 75 kW and a second one with 20 kW.

The operation point is controlled assuming isentropic-adiabatic flow from the inlet to the outlet of the cascade. Mach and Reynolds numbers are calculated for the outlet conditions in case of turbine cascades. Sutherland's law for calculation of the kinematic viscosity is used therefore as well as the measured quantities: total inlet pressure, static outlet pressure, total inlet temperature and blade chord. The isentropic Mach number is given by

$$\mathrm{Ma}_{2,s} = \sqrt{\frac{2}{\gamma - 1} \cdot \left[\left(1 + \frac{q_{2,s}}{p_k} \right)^{\frac{\gamma - 1}{\gamma}} - 1 \right]}, \tag{4.1}$$

with $q_{2,s} = p_{t1} - p_k$. The Reynolds number is calculated for the chord length c using the

constants $S = 110.4\,\mathrm{K}$ and $C_s = 1.458 \cdot 10^{-6}\,\mathrm{kg/(m\,s\,\sqrt{K})}$ with

$$\mathrm{Re}_{2,s} = \sqrt{\frac{\gamma}{R}}\frac{l}{C_s}\frac{\mathrm{Ma}_{2,s} \cdot p_k \cdot \left(\frac{T_{t1}}{1 + \left(\frac{\gamma-1}{2}\right)\cdot\mathrm{Ma}_{2,s}^2} + S\right)}{\left(\frac{T_{t1}}{1 + \left(\frac{\gamma-1}{2}\right)\cdot\mathrm{Ma}_{2,s}^2}\right)^2}. \tag{4.2}$$

For measurements with film cooling the secondary flow circuit can be set in two ways:

- A 1 MW screw compressor is used to suck air from the chamber and after cooling the air is reintroduced into the chamber feeding the blades with cooling air for ejection from the film cooling holes or from the AJVG.

- A 130 kW compressor controls the pressure in a vessel between 6200 and 7000 hPa. The air from the vessel is dried, cooled and passes a valve before feeding the plenum chambers with coolant. In order to maintain the static pressure at the outlet of the cascade constant, the vacuum pumps of the wind-tunnel are kept running in order to extract the added mass.

The first set-up has the advantage, that the static pressure inside the tank is kept constant by definition of the flow circuit. On the other hand, when very low temperatures of the coolant are needed, the second set-up is mandatory in order to dry the air to a dew-point of $-70\,^{\circ}\mathrm{C}$. Otherwise the dryer is not capable of drying the whole mass flow at such low pressures as the static pressure at the cascade outlet.

Creation of Periodic Unsteady Wakes

The blades in turbomachines are exposed to a periodic unsteady flow due to the relative movement between rotor and stator. In order to simulate the unsteadiness of an upstream lying row of vanes, a wake generator (called EIZ) is used in the wind-tunnel. It has cylindrical bars moving upstream of the cascade parallel to it, see fig. 4.4 and refer to Acton and Fottner [3]. The bars can be moved with a velocity of up to 40 m/s and, according to Pfeil and Eifler [111], produce a similar wake as a blade. Measurements and simulations by Pluim et al. [112] confirm the quality of the cylindric bars in producing wakes similar to the ones by airfoils over a wide range of flow conditions. The bars are moved in fig. 4.4 from the bottom to the top upstream of the cascade inlet, are turned after passing in front of the whole cascade, move then downwards downstream of the cascade at sufficient distance not to interact with the cascade flow and make a second turning reinitializing the cycle. In that manner continuous periodic wakes are achieved.

In previous measurements with unsteady inflow the geometric angle between the cascade and the symmetry axis of the wind tunnel was not equal to the flow angle because of the flow deviation. This was due to the leakage at the bar passage between nozzle exit and cascade inlet. For the thermal measurements on the $T120C$ cascade this approach was followed in conformity with the previous aerodynamic measurements. For the measurements on the $T120S$ cascade a blockage system using sealing air was designed, which reduces the leakage to a minimum and allows to have the same geometric angle and inlet flow angle with the wake generator installed.
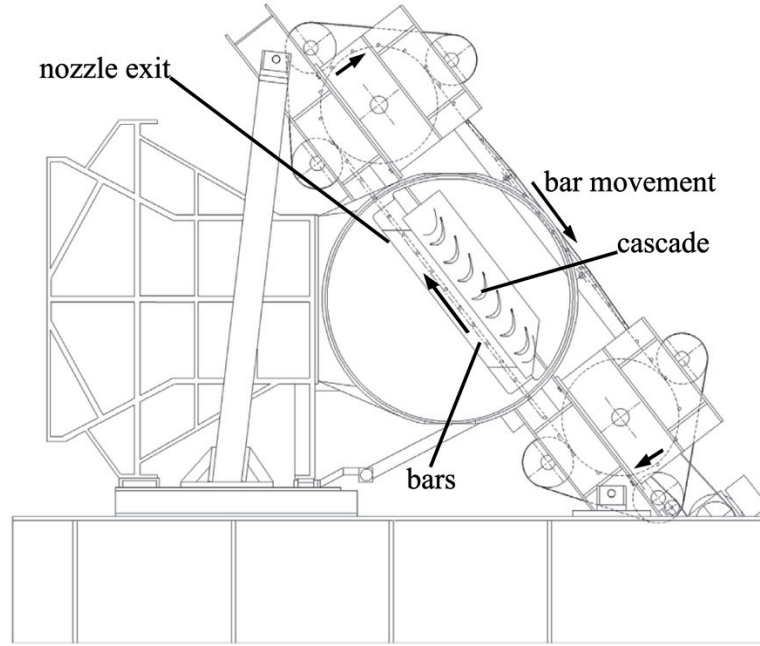
Figure 4.4: Installed wake generator and nozzle

For a periodic excitation in a flow the Strouhal number Sr can be used as similarity parameter. In this report the Strouhal number is defined with the bar frequency f_{wg} by

$$\text{Sr} = f_{wg} \cdot \frac{c_{ax}}{u_{ax}} = \frac{u_{bar} \cdot c_{ax}}{t_{bar} \cdot u_{ax}}. \tag{4.3}$$

4.3   Cascade Instrumentation and Measurement Techniques

The cascades are composed of five blades in total whereas film cooling and AJVG are only provided to the three inner blades. A drawing of the *T120S* cascade mounted in the wind tunnel for steady inflow is shown in fig. 4.5. Both cascades consist of five blades in total and two adjustable tailboards at the circumferential extremities of the cascade.

The total pressure is measured with a pitot tube at about mid-height of the nozzle and the static pressure at the nozzle exit p_1 is measured with nine pressure taps equidistantly distributed along the nozzle height. The tailboards at the top and bottom of the cascade are adjusted in order to have a homogeneous distribution of the static pressure along the nozzle height. The total inlet temperature T_{t1} is measured in the settling chamber with four class A platinum RTD. Assuming adiabatic flow, this temperature can be set equal to the total inlet temperature at the cascade inlet. This assumption is valid considering that the air in the pressure chamber is almost heated up to the flow temperature and therefore, due to the small temperature gradient inside the walls of the nozzle, they can be considered as adiabatic. The outlet or chamber pressure p_k for setting the operation point with eq. (4.1) and (4.2) is measured inside the pressure chamber in a calmed zone.

All pressures are measured as differential pressures with "98RK" pressure scanners from *Esterline* with an uncertainty less than 0.05% of the full scale range. For obtaining an absolute
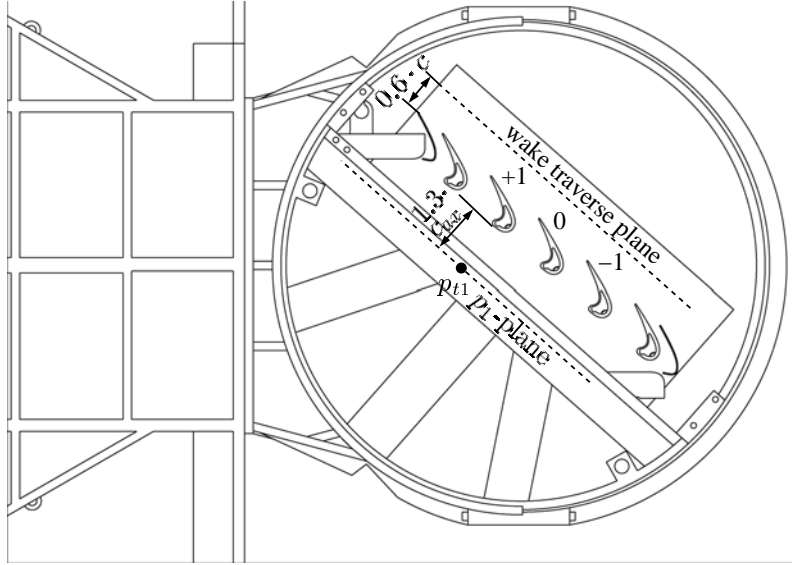
Figure 4.5: Test section of the *T120S* cascade for steady inflow

cascade	*T120C*	*T120S*
d_1	$0.95 \cdot c_{ax}$	$1.23 \cdot c_{ax}$
d_2	$1.58 \cdot c_{ax}$	$1.81 \cdot c_{ax}$
d_3	$0.6 \cdot c_{ax}$	$1.02 \cdot c_{ax}$

Table 4.6: Distances between the measurement planes and the cascade with installed wake generator

pressure it must be measured as differential to the ambient pressure, either directly or through a chain of successive measured pressures obtaining the difference to the ambient pressure. The ambient pressure is obtained with a precise barometer with an uncertainty < 0.1 hPa.

For the tests with periodic unsteady inflow the measurement set-up suffers some minor changes in order to fit the wake generator between nozzle and cascade. In fig. 4.6 a sketch of this measurement set-up is given. The distances between the planes of fig. 4.6 are listed in tab. 4.6. The distance between the plane where the bars are moved along and the cascade leading edge in axial direction is d_1 and the plane where the total inlet pressure and inlet static pressure are measured lies at a distance d_2 upstream of the leading edge. The plane were the inlet conditions with periodic wakes are measured (labeled as "HWA meas. point" in fig. 4.6) lies d_3 upstream of the leading edge in axial direction. The location of the "HWA meas. point" in blade pitch direction is at half pitch between the leading edge of the central blade and the one below for the *T120C* cascade and in the flow direction directly upstream of the leading edge of the central blade for the *T120S* cascade. The experiments with the *T120C* cascade were always conducted with installed wake generator. In case of steady inflow the bars were removed from the wake generator in order not to disturb the inflow.
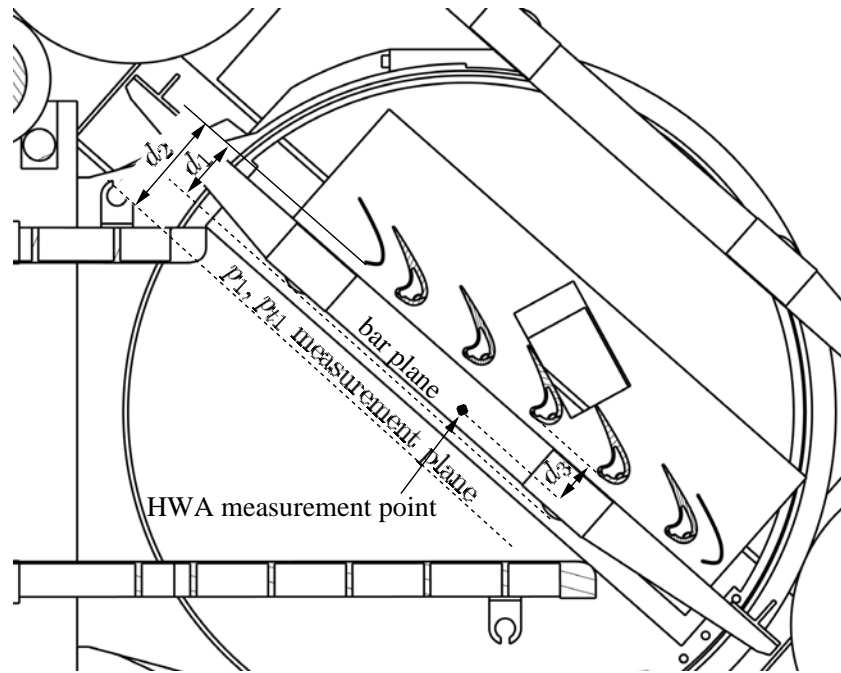
Figure 4.6: Test section of the *T120S* cascade with inserted wake generator

(a) *T120C*   (b) *T120S*
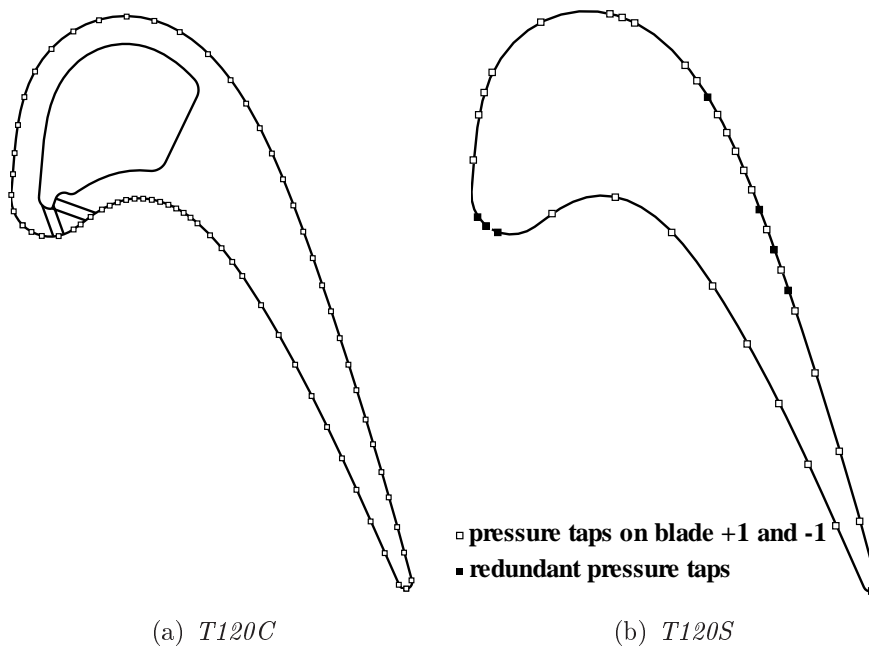
Figure 4.7: Static pressure taps location on the *T120* blades

4.3.1   Profile Pressure Measurements

The profile pressure distribution is measured at the three inner blades. The suction side profile pressure is measured at the blade over the centre blade, in fig. 4.5 named as "+1". The *T120C* blade is instrumented with 35 pressure taps on the suction side and the *T120S* blade with 29. The static pressure at the pressure side is captured at the blade below the centre blade and is named as "-1". The number of pressure taps on the pressure side is 36 and 11 for the *T120C* and *T120S* blade respectively. In the *T120S* cascade additionally the centre blade (called "0") is instrumented with seven pressure taps. Those taps are a repetition of positions measured also at the blades "+1" and "-1" and serve to control the periodicity of the flow. The redundant pressure taps at the centre blade are positioned in order to capture the stagnation line at the leading edge and the shock location at the suction side and for all measurements a very good agreement was found between the three blades. Plots of the blades with the position of the pressure taps are given in fig. 4.7. The doubled instrumented pressure taps in the *T120S* blade are marked with filled symbols. The measured static pressure at each position x is plotted here as isentropic Mach number assuming constant total pressure:

$$\text{Ma}_x = \sqrt{\frac{2}{\gamma - 1} \cdot \left[\left(\frac{p_{t1}}{p_x} \right)^{\frac{\gamma - 1}{\gamma}} - 1 \right]}. \tag{4.4}$$

The measured quantities for the profile pressure measurements are:

$p_x - p_k$	difference of local static to chamber pressure
$p_{t1} - p_k$	difference of total inlet to chamber pressure
$p_k - p_{amb}$	difference of chamber to ambient pressure
p_{amb}	ambient pressure
T_{t1}	total inlet temperature

4.3.2   Wake Traverses

For the *T120S* cascade the aerodynamic losses and outlet conditions for the centre blade passage were obtained by traversing with a five-hole probe with a spheric head parallel to the cascade at half blade span and along one blade pitch. The head of the probe is shwon as cross-section view in fig. 4.8. The traversing plane is located at $0.6 \cdot c$ downstream of the cascade exit in axial direction, see fig. 4.5. The coordinate system is set according to fig. 4.9. The connecting line between trailing edge and the origin of the coordinate system and the circumferential direction of the cascade enclose an angle of 20°. Positive u-values are on the pressure, while negative values for the coordinate u lie on the suction side. For each measurement point following quantities are taken:
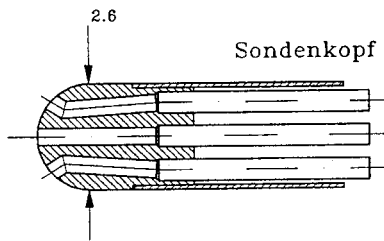
Figure 4.8: Geometry of the five-hole probe head
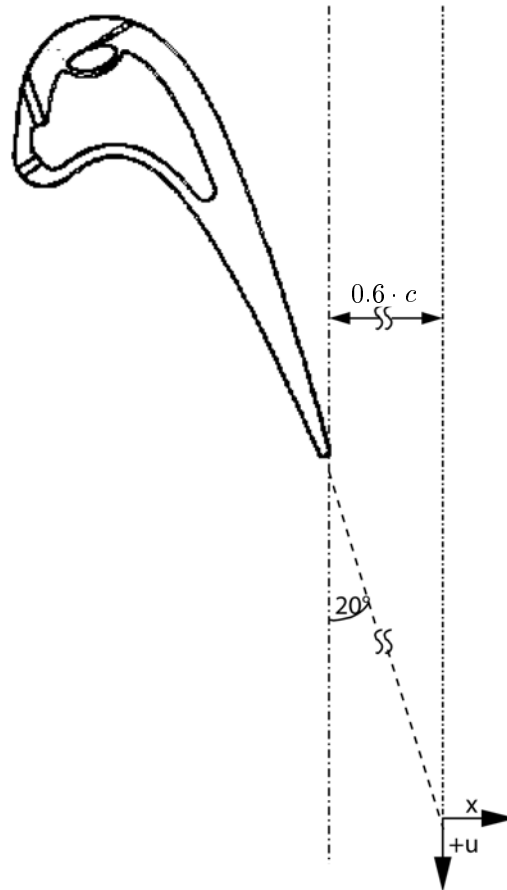
Figure 4.9: Coordinate system for the wake traverse

$p_{t1} - p_k$	difference between total inlet and chamber pressure
$p_k - p_{amb}$	difference chamber to ambient pressure
$(p_0 - p_1)_{FHP}$	differential pressure between holes 0 and 1 on five-hole probe
$(p_0 - p_3)_{FHP}$	differential pressure between holes 0 and 3 on five-hole probe
$(p_3 - p_1)_{FHP}$	differential pressure between holes 3 and 1 on five-hole probe
$(p_4 - p_2)_{FHP}$	differential pressure between holes 4 and 2 on five-hole probe
$p_{t1} - p_{0,FHP}$	difference between total inlet pressure and pressure at hole 0 of five-hole probe
$p_{0,FHP} - p_{amb}$	difference between pressure at hole 0 of five-hole probe and ambient pressure
$p_1 - p_k$	difference between static inlet and chamber pressure
p_{amb}	ambient pressure
T_{t1}	total inlet temperature

With the measured differential pressures on the five-hole probe the values

$$
\begin{aligned}
K_\alpha &= \left(\frac{p_3 - p_1}{\Delta p} \right)_{FHP}, \\
K_\beta &= \left(\frac{p_4 - p_2}{\Delta p} \right)_{FHP}, \\
K_M &= \left(\frac{\Delta p}{p_0} \right)_{FHP}, \\
\text{with} \quad \Delta p &= \left(p_0 - \frac{p_1 + p_3}{2} \right)_{FHP}
\end{aligned}
\tag{4.5}
$$

are computed. The flow angles α and β, the Mach number and the coefficient for calculation of the total pressure are then computed with a triple sum of polynomials up to fifth order using the values from eq. (4.5) and coefficients from a prior calibration. Details concerning the evaluation of measurements with the five-hole probe can be found in Bohn and Simon [17] or Brückner [22]. Due to the high exit Mach numbers present at the outlet of the *T120S* cascade the coefficients for the polynomial are optimized for Mach numbers between 0.68 and 0.98. With these values the following quantities are obtained for every position u:

- circumferential outlet angle $\beta_2(u)$

- spanwise outlet angle $\alpha_2(u)$

- outlet Mach number $Ma_2(u)$

- total pressure loss coefficient $\omega(u) = \left(\frac{p_{t1} - p_{t2}}{p_{t1} - p_k} \right)_u$

The average value for any outflow dimension $\overline{\xi}$ is obtained by area averaging:

$$
\overline{\xi} = \frac{1}{t} \int_{u=0}^{t} \xi(u) \, du.
\tag{4.6}
$$

The integral values obtained are the turning $\overline{\beta_1 - \beta_2}$, the total pressure loss coefficient $\overline{\omega} = \frac{p_{t1} - p_{t2}}{p_{t1} - p_k}$ and the axial velocity ratio $\overline{(\rho_2 \cdot c_2 \cdot \beta_2) / (\rho_1 \cdot c_1 \cdot \beta_1)}$.

Another way of obtaining average cascade outlet values is the method described in Amecke [6]. This averaging process suffices the conservation of mass, momentum and energy. The assumptions made are that the normal and tangential stresses are small compared to the impulse and pressure forces. The flow homogenization is taken to be adiabatic and two-dimensional. As drawback the uncertainties are unreasonably high for small flow exit angles. Following the calculation proposed by Amecke one obtains the average outflow angle with

$$\overline{\beta_2} = \arccos\left(\frac{I_3}{I_1}\frac{\Theta_2}{2 \cdot \psi}\right) = \arccos\left(\Omega\right) \tag{4.7}$$

with the variables I_3, I_1, Θ_2 and ψ obtained after extensive calculations and not explained in detail here. The uncertainty of the outflow angle is then calculated by differentiation of eq. (4.7):

$$\Delta\overline{\beta_2} = \left|\frac{-1}{\sqrt{1-\Omega^2}}\right| \cdot \Delta\Omega. \tag{4.8}$$

As the outlet angle is approximately 20° (or 0.35 in radians) Ω must be nearly 1 (0.99998 for $\overline{\beta_2} = 20°$). Inserting this Ω-value in eq. (4.8) one obtains $\Delta\overline{\beta_2} = 158 \cdot \Delta\Omega$ which in general will be not practicable. For smaller outflow angles the uncertainty will tend towards infinity. The average total outlet pressure is then computed from $\overline{\beta_2}$ and the uncertainty is for such small outflow angles larger than 100%. Therefore the area averaging process was used for the experiments with the *T120S* cascade.

4.3.3 Measurements with Film Cooling

Using secondary air for film cooling or AJVG, the total secondary mass flow is measured with an orifice according to DIN EN ISO 5167-2. If both film cooling and AJVG are being used, the flow is split after the orifice and the AJVG mass flow is measured with a flow meter "FC01-CA" from *ETA*. The flow meter is based on a calorimetric principle where a heated probe is cooled as function of the flow velocity. The output signal of the flow meter is a current from 0–20 mA proportional to the specified range for the velocity and for the temperature sensor.

Measurements with film cooling or AJVG require the additional measurement of following quantities for mass flow measurements with an orifice and for monitoring the coolant total conditions inside the plenum:

$p_v - p_n$	static pressure difference between the planes upstream and downstream of the orifice
p_{Bl}	static pressure upstream of the orifice
p_{tc}	total pressure inside the plenum (for coolant or AJVG)
T_{Bl}	total temperature at the orifice
T_c	total temperature inside the plenum

In order to account for the additional mass flow for film cooling and AJVG for estimation of the profile losses, a correction of the parameters has to be done. According to Ardey [8] with a corrected total inlet pressure of

$$p_{t1}^{**} = \left(\frac{\dot{m}_1 c_{p1} T_{t1} \left(p_{t1}\right)^{\frac{1-\gamma}{\gamma}} + \sum\left(\dot{m}_c c_{p,c} T_{tc} \left(p_{tc}\right)^{\frac{1-\gamma}{\gamma}}\right)}{\dot{m}_1 c_{p1} T_{t1} + \sum\left(\dot{m}_c c_{pc} T_{tc}\right)}\right)^{\frac{\gamma}{1-\gamma}} \tag{4.9}$$

the thermodynamic total pressure loss parameter can be obtained:

$$\omega_{th} = \frac{p_{t1}^{**} - \overline{p_{t2}}}{p_{t1}^{**} - p_k}. \tag{4.10}$$

With eq.(4.10) also the losses inside the film cooling holes are taken into account. If one wants to discriminate the losses in the external flow field the parameter ω_{ex} is calculated by replacing p^{**} with p^*. p^* is obtained from eq. (4.9) by replacing p_{tc} with the coolant pressure at the outlet of the hole p_{ex}.

Because of non-disclosure agreements within the AITEB-project all the losses are normalized by the average total pressure losses at design conditions without film cooling and without AJVG.

4.3.4 Constant Temperature Anemometry

The inlet conditions for steady inflow are measured with a 3D-hot wire probe in order to obtain the turbulence level of the free stream and the integral turbulence length scale. The principal of measurement is based on the convective heat transfer of an infinite cylinder. The probe is calibrated in a free stream nozzle at the same static pressure and total temperature as foreseen for the measurements. Voltage is applied on the wires in order to keep the temperature sensitive resistance constant, leading to a constant temperature in the wire. The relation between applied voltage E and the velocity of the flow U is given by the equation of King [92]

$$E_i^2 = A_i + B_i \cdot U_i^{n_i} \quad \forall \quad i = 1 \ldots 3. \tag{4.11}$$

The coefficients A_i and B_i and the exponent n_i are obtained for each wire i with a velocity calibration using a least square fit approximation. The velocity components U_x, U_y and U_z are set into relation to the measured wire cooling velocity U_i with the set of equations

$$\begin{bmatrix} U_x^2 & 2U_xU_y & 2U_xU_z & U_y^2 & 2U_yU_z & U_z^2 \\ U_x^2 & 2U_xU_y & 2U_xU_z & U_y^2 & 2U_yU_z & U_z^2 \\ U_x^2 & 2U_xU_y & 2U_xU_z & U_y^2 & 2U_yU_z & U_z^2 \end{bmatrix} \cdot \begin{bmatrix} a_0 \\ a_1 \\ a_2 \\ a_3 \\ a_4 \\ a_5 \end{bmatrix} = \begin{bmatrix} U_1^2 \\ U_2^2 \\ U_3^2 \end{bmatrix}. \tag{4.12}$$

The coefficients $a_0 \ldots a_5$ are found with a prior directional calibration. The three velocity components lead then to the velocity magnitude U with $U = \sqrt{U_x^2 + U_y^2 + U_z^2}$. The coordinate system of the probe and the definition of the angles α and β for the angles comprised by the velocity components $(\sqrt{U_x^2 + U_y^2}; U_z)$ and $(U_y; U_x)$ respectively is shown in fig. 4.10. The x-axis is aligned to the probe stem.

The average velocity is computed for N samples with

$$\overline{U} = \frac{\sum_{n=1}^{N} U_n}{N}, \tag{4.13}$$

where U_n is the measured velocity or velocity component for each sample n. The root mean
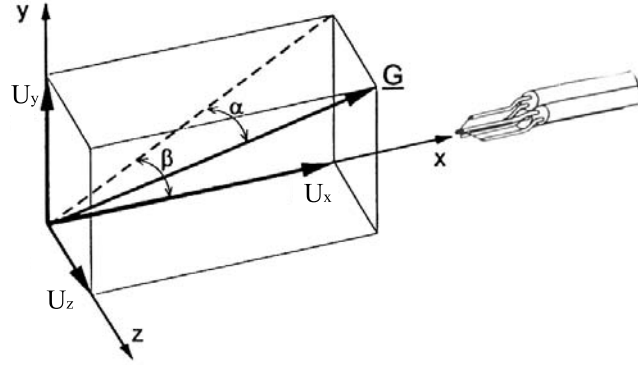
Figure 4.10: Coordinate system of the hot wire probe

square RMS and the turbulence intensity Tu are then found with

$$RMS_x = \sqrt{\frac{\sum_{n=1}^{N}(U_{n,x} - \overline{U}_x)^2}{N}}, \tag{4.14}$$

$$RMS_y = \sqrt{\frac{\sum_{n=1}^{N}(U_{n,y} - \overline{U}_y)^2}{N}}, \tag{4.15}$$

$$RMS_z = \sqrt{\frac{\sum_{n=1}^{N}(U_{n,z} - \overline{U}_z)^2}{N}} \tag{4.16}$$

and

$$Tu = \frac{RMS_x + RMS_y + RMS_z}{\sqrt{3} \cdot \overline{U}} \cdot 100\%. \tag{4.17}$$

In order to obtain a turbulence length scale the method described e. g. in Hilgenfeld [79] or Wunderwald [161] is applied using the Taylor hypothesis [145] that the turbulent structures are stable and are convected with a constant velocity in streamwise direction. Following this approach, the time dependency is used for the normalized autocorrelation function $R_x(\tau)$ defined by

$$R_x(\tau) = \frac{\overline{u'_x(t) \cdot u'_x(t + \tau)}}{\overline{u'_x(t)^2}}, \tag{4.18}$$

with the instantaneous velocity variation $u'_x(t) = U_x(t) - \overline{U_x}$. Only the time correlation in x-direction is computed, since it is the streamwise direction and therefore the only axis where a correlation between time and dimension of the eddies exists. The length scale Λ_x also known as macro-length scale is then obtained by integration of eq. (4.18) up to the first zero passing of the autocorrelation function:

$$\Lambda_x = \overline{U} \cdot \int_0^{R_x(\tau)=0} R_x(\tau) \, d\tau, \tag{4.19}$$

with the average velocity $\overline{U}$.

The turbulence energy spectrum is based on the autocorrelation function

$$Q_i(\tau) = \overline{u'_i(t) \cdot u'_i(t + \tau)}, \tag{4.20}$$

for the velocity components i and a fast Fourier transformation is done on $Q_i(\tau)$ in order to obtain the energy spectrum $E(f)$. The integral of the turbulence energy spectrum is consistent with the energy contribution of the fluctuations of one velocity component:

$$\int_0^\infty E(f)\,df = u_i'^2. \tag{4.21}$$

Boundary Layer Measurements

Traverses were run on the pressure side of the *T120C* cascade with a single-wire CTA probe in the region inside and around the separation bubble. For the traverses, several calibrations would be necessary in order to account for different static pressure around the profile. As referred e. g. in Stainback and Nagabushana [135] the applied voltage is not only a function of the velocity but rather of the Mach and Reynolds numbers or for low Reynolds numbers of the Mach and Knudsen numbers. Moving towards low static pressures the relation $\mathrm{Nu} \cdot \mathrm{Re}^{0.5}$ changes to a linear relation between Nusselt and Reynolds number. As shown in Johnston and Fleeter [88] for density variations up to 6%, also at ambient conditions the voltage changes almost linearly to the density of the fluid. During the measurements at the high-speed cascade wind tunnel it was found, that up to a variation of at least 10% in fluid density the applied voltage follows fairly good the relationship

$$E^2 = A + B \cdot \left(U \cdot \rho^2 \right)^n. \tag{4.22}$$

As example in fig. 4.11 two lines computed with calibrations at static pressures of 344 and 317 hPa are compared together with the actual values for $p = 344$ hPa. The calibration was run on a nozzle designed for calibration purposes at a constant static pressure of either 317 or 344 hPa and adapted total pressure for different velocities. The coefficients A, B and n obtained from these calibrations are then used to compute the velocity for the calibration points at $p = 344$ hPa and are plotted in fig. 4.11 as lines. The standard deviation between measurement and approximated curves is below 7% for both cases and, except for very low velocities, no advantage is seen for one curve or the other.

The density used in eq. (4.22) for the measurements inside the boundary layer is obtained from the isentropic Mach number on the blade and the total density of the fluid for adiabatic-isentropic expansion and with Prandtl's hypothesis of constant static pressure across the boundary layer.

4.3.5   Schlieren Pictures

The velocity of light changes with the density of the propagation medium. This is used in the Schlieren technique, first developed by Toepler [148], e. g. for determination of large density gradients at shock waves. A strong light source sends parallel rays through the medium and a knife is placed at the focus of the opposite lens. In case of density gradient the ray is deflected and cut by the knife. These zones can then be seen as dark regions on the reception image.

The measurement principle of Schlieren pictures at the wind tunnel is shown in fig. A.6. The light path follows a z-profile and two parabolic mirrors send the light beam of parallel rays through the test section. Windows are placed at the sidewalls allowing the passage of the light
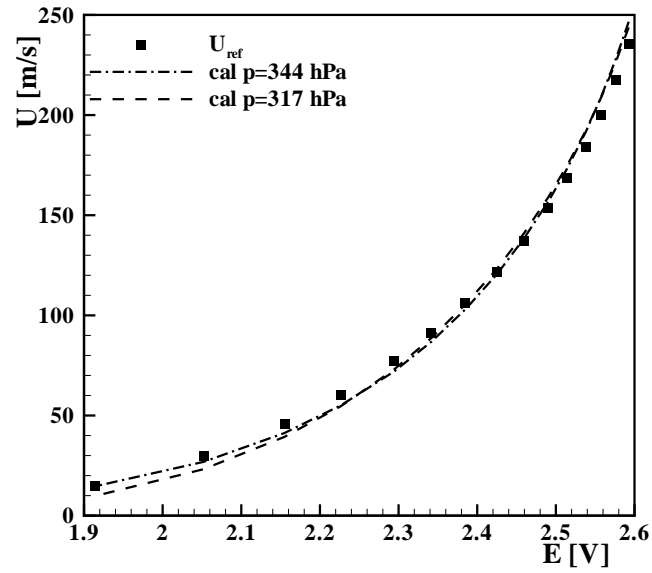
Figure 4.11: Evaluation of the calibration line with the coefficients (A, B, n) obtained with calibrations at different static pressures

material	BK7
planarity	$\lambda/4$
parallelism	$< 1\,\mathrm{armin}$

Table 4.7: Properties of the windows for Schlieren pictures

through the monitoring area. Details of the measurement principle and test set-up can be found in Bell [14]. The properties of the windows is specified in tab. 4.7.

The design of the cascade does not allow to visualize the flow close to the blade profile at a blade span of 176 mm. This is the reason why the Schlieren pictures do not capture the flow up to a distance of at least 2 mm from the blade surface.

4.3.6 Heat Transfer Measurement Set-up

The heat transfer coefficient h is measured on a non-adiabatic surface by heating the surface with a heating foil and by applying Newton's law of cooling:

$$h(x,y) = \frac{\dot{q}}{T_w(x,y) - T_r(x)}, \tag{4.23}$$

where T_w is the measured wall temperature and T_r the recovery temperature of the flow. The heating power $\dot{q}$ is derived from the applied voltage E and electric current I on the heating foil and its surface area A_{hf}:

$$\dot{q} = \frac{E \cdot I}{A_{hf}}. \tag{4.24}$$

The recovery temperature T_r is defined as

$$T_r = T + r\frac{u^2}{2c_p}. \tag{4.25}$$

The recovery factor is calculated for turbulent flow as being $r = \mathrm{Pr}^{1/3}$ and for laminar flow with $r = \mathrm{Pr}^{1/2}$ or it is measured, as it is the case for the suction side of the *T120S* blade.

Two ways of heating the surface were used for these investigations:

1. For the pressure side investigations with the *T120C* cascade a heating foil with a copper wire aligned as meander with small spacing of the wire along the surface was used. A photo of the front side of the heating foil is shown in fig. 4.12. Holes are cut at the position of the film cooling holes on the blade surface and the wire is placed surrounding the holes. Two kapton sheets insulate the electric conductor. On the other side of the surface — the one in contact with the flow — a thin aluminium layer with a thickness of 0.1 mm is glued on the foil in order to reduce heating inhomogeneity due to the spacing between the wire. The heating foil has an overall thickness of 0.33 mm and is glued on the blade. The blade was previously milled in order to create the space so that the foil fits in and the surface stays smooth along the change from the heated to the non-heated part of the blade.

2. For the investigations on the *T120S* cascade a foil of inconell with a thickness of 0.025 mm is glued on the surface and both extremities are connected to an electric circuit. A schematic of the sheets on the plexiglas blade is given in fig. 4.13. The black backing and the crystals are sprayed over the inconell foil. The foil together with the adhesive has an overall thickness of 0.075 mm. This allows to have larger temperature gradients along the surface than in the first case. It allows also to reuse the blade, since the foil is removable. But for this technique the whole cascade had to be designed taking care to allow for a homogeneous electric current along the surface.
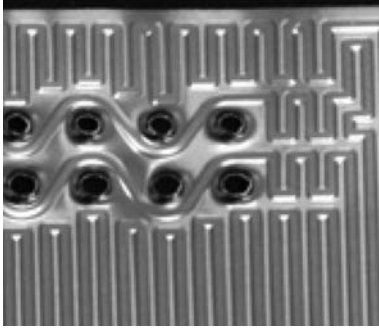
Figure 4.12: Extract of the heating foil for the *T120C* blade with holes — Aluminium sheet on the back
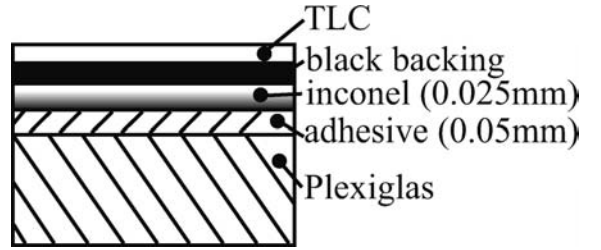
Figure 4.13: Schematic of the applied sheets for heat transfer measurements on the *T120S* blade

The state of the boundary layer on the pressure side is taken to be turbulent during a significant part of the surface, especially in the main flow separation zone. Further downstream with the strong acceleration of the flow a relaminarisation of the boundary layer is likely to occur. Therefore the acceleration parameter

$$K = \frac{\nu}{u^2}\frac{du}{dx} \tag{4.26}$$

is build. According to Mayle [101] the flow is regarded as being laminar for $K > 3 \cdot 10^{-6}$ and turbulent for lower values of K. On the suction side of the *T120S* blade the recovery factor was measured. Therefore the surface temperature was acquired at different main flow temperatures adjusting the pressures in order to keep the outlet Mach and Reynolds numbers constant. The flow velocity is calculated from the isentropic Mach number on the blade and the recovery factor is then obtained from eq. (4.25). The measured recovery factor on the suction side without film cooling for the three operating points is given in fig. 4.14. The recovery factor from correlations as function of the Prandtl number are drawn with solid lines. For all three operating points the measured recovery factor rapidly reaches the values for turbulent boundary layer and drops then to values meeting well with the correlation for laminar boundary layer. At the shock location the recovery factor drops rapidly to values of about 0.75 which is below the expected recovery factor for a turbulent boundary layer. This temperature drop is believed to be related to the phenomenon called in literature as energy separation and reported extensively for cylinders in cross flows with vortex shedding, e. g. in Eckert and Weise [54] or Goldstein and Kulkarni [71]. Further explanations are given in the appendices B.

The reference temperature T_{ref} for determination of the temperature dependent physical properties of the gas is given in Kays et al. [90] as

$$T_{ref} = T + 0.5 \cdot (T_w - T) + 0.22 \cdot (T_r - T), \tag{4.27}$$

with T_w as the actual wall temperature.

The flow temperatures are measured with resistance temperature devices and the surface temperature is measured with liquid crystals. Since the TLC used have smaller bandwidths of 1°C or 3°C, in general it is not possible to obtain the values for the whole surface with one single measurement. The inlet temperature is kept constant for not changing the flow parameters.
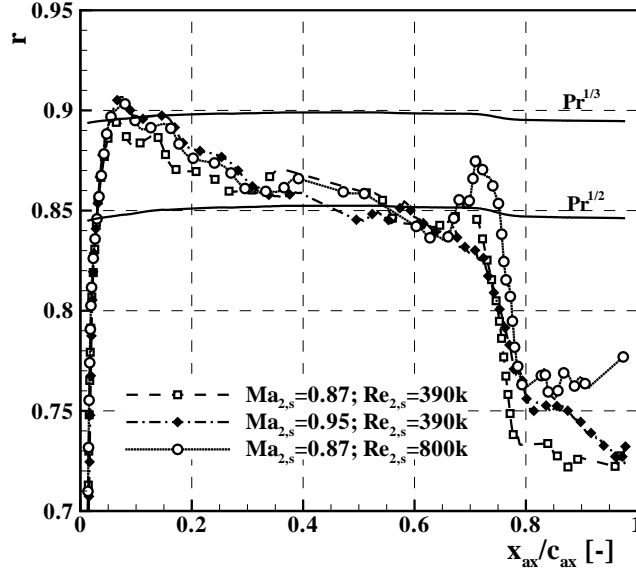
Figure 4.14: Distribution of the measured recovery factor on the suction side of the *T120S* blade as function of the axial chord and calculated recovery factor from correlations for laminar and turbulent boundary layer

Hence the heating power of the foil is changed in order to fetch the heat transfer coefficient over the whole surface. A schematic of the technique is presented in fig. A.3. The heating power is increased successively in order to have another zone on the plate with active crystals which can be evaluated. For each heating power a new picture is taken and the flow condition is monitored. The final evaluation of the HTC over the surface is done combining the evaluation of all pictures to one single field. As rule of thump one can expect to need 10 to 20 images in order to capture the heat transfer coefficient along the whole surface. A validation was done applying this technique on a flat plate and the results are presented in Gomes [73].

The heat transfer coefficient is presented here with the dimensionless parameter called Nusselt number, built with the true blade chord as length scale and the heat conductivity for air k_{air} at T_{ref}:

$$\mathrm{Nu} = \frac{h \cdot c}{k_{air}}. \tag{4.28}$$

4.3.7   Film Cooling Effectiveness Measurement Set-up

Measuring the wall temperature with the TLCs and the coolant total temperature with a RTD, the film cooling effectiveness η is calculated with

$$\eta = \frac{T_r - T_{aw}}{T_{t1} - T_{t,c}} \tag{4.29}$$

with T_{aw} as the adiabatic wall temperature, T_{t1} the free stream total and T_r the recovery temperature and $T_{t,c}$ being the total coolant temperature inside the plenum, which in these experiments was up to 70° C below T_{t1}.

For varying η over the surface one of the three parameters T_{t1}, T_w or $T_{t,c}$ has to be changed in order to measure an extensive range of FCE. The interval of measurable wall temperature is fixed by the crystals. The total inlet temperature is kept constant for not changing the operation point. Hence the coolant temperature $T_{t,c}$ is changed for numerous measurements in order to get various values of FCE. The scheme of the technique is analogous to the one for the measurement of the heat transfer coefficient in fig. A.3 but instead of increasing the heating power the coolant temperature is increased stepwise in order to have another part of the blade with active crystals. The final distribution over the surface is then again the combination of the evaluation of the numerous pictures and about 20 pictures might be needed to obtain a complete map of film cooling effectiveness with the crystals used here.

Data Post Processing

The blades for thermal measurements are made of plexiglass in order to reduce the heat conductivity. Nevertheless a perfectly adiabatic wall can not be achieved. In order to account for this problem a post processing technique was developed which allows to obtain the adiabatic wall temperature. This technique is here described using the example of the *T120C* blade.

The *T120* blades are aerodynamically highly loaded as is shown in fig. A.1 and hence have also a considerable temperature difference between suction and pressure side. In fig. 4.15 an exemplary result of the recovery temperature is plotted as function of the axial position for the suction and pressure side of the *T120C* blade. The isentropic Mach number — computed from the measured profile pressure distribution — was used for the calculation of the recovery temperature with eq. (4.25). The static temperature is calculated for isentropic expansion to the profile Mach number and the recovery factor r is defined with

$$r = \begin{cases} r_l = \mathrm{Pr}^{1/2}, & \text{for laminar flow} \\ r_t = \mathrm{Pr}^{1/3}, & \text{for turbulent flow} \\ r(x_{ax}) = r_l + (r_t - r_l) \cdot \frac{x_{ax}/l_{ax} - x_a}{x_b - x_a}, & \text{for SS at transition from } x_a \ldots x_b \end{cases} \qquad (4.30)$$

like referenced in Lakshminarayana [94] from Eckert and Drake [53]. For the transition zone (between 0.75 and 0.82 for design case) a linear approximation between the recovery factors for turbulent and laminar flow is set. In fact, as shown in Burmeister [24] for supersonic flow, the recovery factor can reach a peak value in the transition zone. But the slope of the curve of the recovery factor as function of the coordinate is almost constant along most part of the covered distance. As was shown previously, for the *T120S* blade the recovery factor differs from the correlations downstream of the shock, but in the case of the *T120C* case the shock is too weak and the boundary layer increase too small in order to create vortex separation.

This temperature difference between pressure and suction side surface and plenum leads to a constant heat flux throughout the blade and hence in general to an error in the measured FCE. Due to the geometry of the blade and the unknown heat flux on the suction side of the *T120C* blade, a combination of a finite element model and known correlations for the Nusselt number on simplified geometries are used in order to estimate the heat flux. For the finite element analysis the commercial program ANSYS 11.0 is used on a model of the blade. The applied boundary conditions on the non measured surfaces are the reference flow temperature and heat transfer coefficient. Symmetry condition is applied on the sidewalls and constant temperature is applied on the analysed surface for heat transfer or film cooling effectiveness, since this is
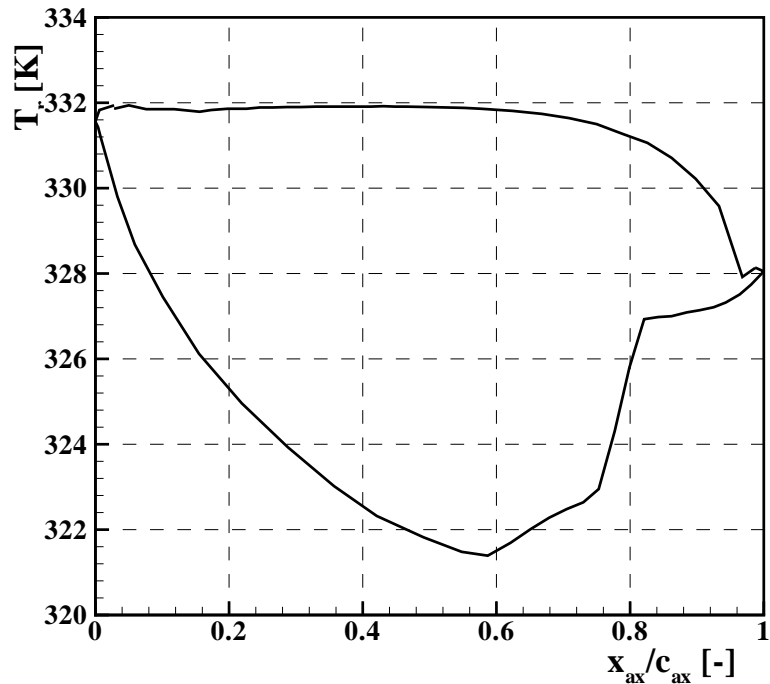
Figure 4.15: Recovery temperature over axial coordinate on the *T120C* blade
for $\text{Ma}_{2s} = 0.87$, $\text{Re}_{2s} = 390,000$ and $T_{t1} = 59°\text{C}$
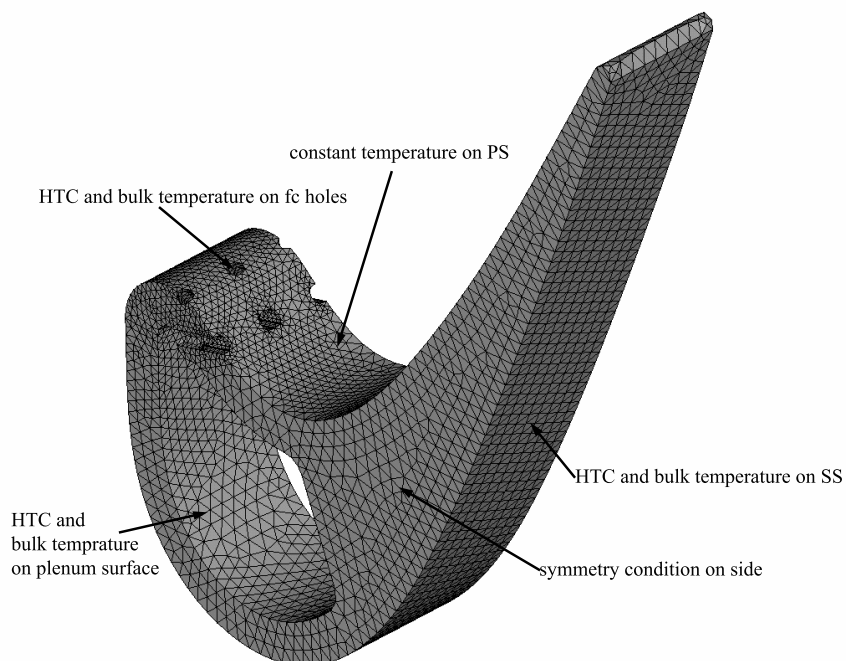
Figure 4.16: Finite element model of the *T120C* blade and applied boundary
conditions

measured in the experiments. A picture of the *T120C* model with indication of the applied
boundary conditions is given in fig. 4.16.

For the estimation of the Nusselt number on the suction side of the *T120C* blade the correlations for flat plate convection with constant wall temperature are used. According to Pohlhausen [113] and Merker [109] the Nusselt number can be estimated with

$$
\text{Nu}_x = \begin{cases}
\text{Nu}_{x,l} = 0.332 \cdot \sqrt{\text{Re}_x} \cdot \text{Pr}_x^{1/3}, & \text{for } \frac{x_{ax}}{l_{ax}} = 0 \dots x_a \text{ laminar} \\
\text{Nu}_{x,t} = 0.0287 \cdot \text{Re}_x^{0.8} \cdot \text{Pr}_x^{0.6}, & \text{for } \frac{x_{ax}}{l_{ax}} = x_b \dots 1 \text{ turbulent} . \\
\text{Nu}_{x,l} + (\text{Nu}_{x,t} - \text{Nu}_{x,l}) \cdot \frac{x_{ax}/l_{ax} - x_a}{x_b - x_a}, & \text{for } \frac{x_{ax}}{l_{ax}} = x_a \dots x_b
\end{cases} \tag{4.31}
$$

Again a linear approximation is set for the transition zone between laminar and turbulent boundary layer.

For the plenum and the film cooling holes an average Nusselt number is set based on the guidelines from [150]. These guidelines use for laminar flow the correlations of Martin [98], partially based on the results of Shah[129], Stephan [139] and Gnielinski [69]. The Nusselt number for laminar flow and constant wall temperature is then defined as

$$
\text{Nu}_{m,l} = \left[\text{Nu}_{m,1}^3 + 0.7^3 + (\text{Nu}_{m,2} - 0.7)^3 + \text{Nu}_{m,3}^3 \right]^{1/3}, \tag{4.32}
$$

with

$$
\text{Nu}_{m,1} = 3.66, \tag{4.33}
$$

$$
\text{Nu}_{m,2} = 1.615 \left(\text{Re} \cdot \text{Pr} \cdot \frac{D}{l} \right)^{1/3}, \tag{4.34}
$$

$$
\text{Nu}_{m,3} = \left(\frac{2}{1 + 22 \cdot \text{Pr}} \right)^{1/6} \cdot \left(\text{Re} \cdot \text{Pr} \frac{D}{l} \right)^{1/2} . \tag{4.35}
$$

If the Reynolds number is higher than 2300, the Nusselt number for turbulent flow is calculated with the equation from Gnielinski [70]

$$
\text{Nu}_{m,t} = \frac{(\xi/8)\,\text{Re} \cdot \text{Pr}}{1 + 12.7\sqrt{\xi/8}\left(\text{Pr}^{2/3} - 1 \right)} \left[1 + \left(\frac{D}{l} \right)^{2/3} \right], \tag{4.36}
$$

$$
\xi = (1.8 \cdot \log(\text{Re}) - 1.5)^{-2} .
$$

For cases $2300 < \text{Re} < 10^4$ the average Nusselt number ist defined using eq. (4.32)– (4.36) to

$$
\text{Nu}_m = (1 - \zeta) \cdot \text{Nu}_{m,l}(\text{Re} = 2300) + \zeta \cdot \text{Nu}_{m,t}(\text{Re} = 10^4), \tag{4.37}
$$

$$
\zeta = \frac{\text{Re} - 2300}{10^4 - 2300}. \tag{4.38}
$$

Since the velocity inside the plenum is low the convective heat transfer is also small. The natural convection is therefore taken into account for the plenum with the correlation from Küblbeck [93] for a closed recipient with square cross section which is referenced in Merker [109]:

$$
\text{Nu}_{pl,free} = 0.138 \cdot \text{Ra}^{0.31}. \tag{4.39}
$$

The total Nusselt number for the plenum is then according to Churchill [28] and using eq. (4.32) and (4.39) for $\text{Nu}_{pl,conv} = \text{Nu}_{m,l}$ and $\text{Nu}_{pl,free}$ respectively:

$$
\text{Nu}_{pl,t} = \left(\text{Nu}_{pl,conv}^3 + \text{Nu}_{pl,free}^3 \right)^{1/3} . \tag{4.40}
$$
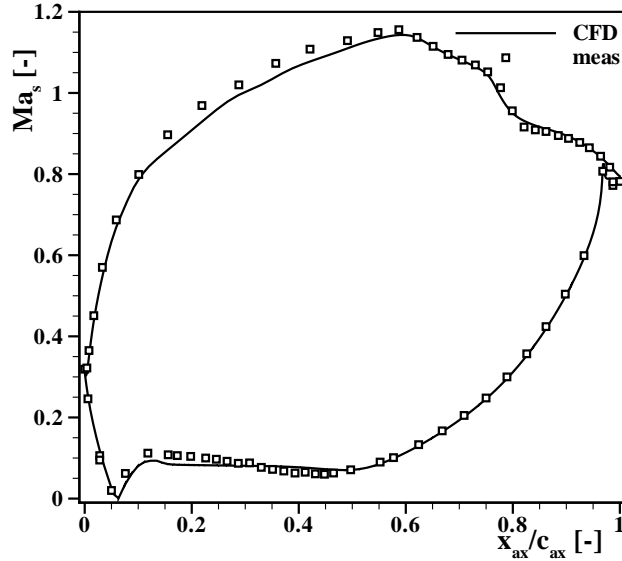
Figure 4.17: Isentropic Mach number distribution along the surface of the *T120C* blade: CFD and measurement

The reference flow temperature is the total cooling temperature $T_{t,c}$ for the plenum, the recovery temperature of the coolant flow $T_{r,c}$, based on the measured total temperature and the mass flow, for the film cooling holes and the recovery temperature of the main flow for the outer surfaces.

For determining the FCE the measured wall temperature T_w is then corrected with the calculated heat flux inside the blade $\dot{q}_{cond}$

$$T_{w,corr} = T_w - \frac{\dot{q}_{cond}}{h_{PS}(x)} \qquad (4.41)$$

which would be the measured wall temperature T_{aw} if an adiabatic wall would be present. The heat transfer coefficient on the pressure side $h_{PS}(x)$ is gained from the heat transfer experiments.

Several correlations for determination of heat transfer coefficient on the boundaries of the blade are used in this approach. These correlations are derived for idealistic geometries and flows which do not exactly match with the ones around the blade. Therefore the actual heat transfer on the real blade should be different than the applied, but the overall effect is reduced compared to the other uncertainties in the measurement. For a quantification of the differences, a CFD analysis for the reference point was done with the commercial solver CFX 11.0. The isentropic profile Mach numbers for the CFD simulation and the measurement at reference operation point without film cooling are presented in fig. 4.17. The results from the simulation (represented by the curve) agree very well with the measurements (symbols).

The calculated heat transfer coefficient on the suction side and the estimated HTC with flat plate correlations are plotted in fig. 4.18(a). The correlations for flat plate underestimate the results from the simulation, especially at presence of laminar boundary layer. On the blade suction side, an accelerating flow is present during the first half of axial chord resulting in thinner boundary layer compared to the flat plate case. This increases the heat transfer compared to the flat plate case with constant main flow velocity.

(a) HTC on suction side

(b) evaluated FCE
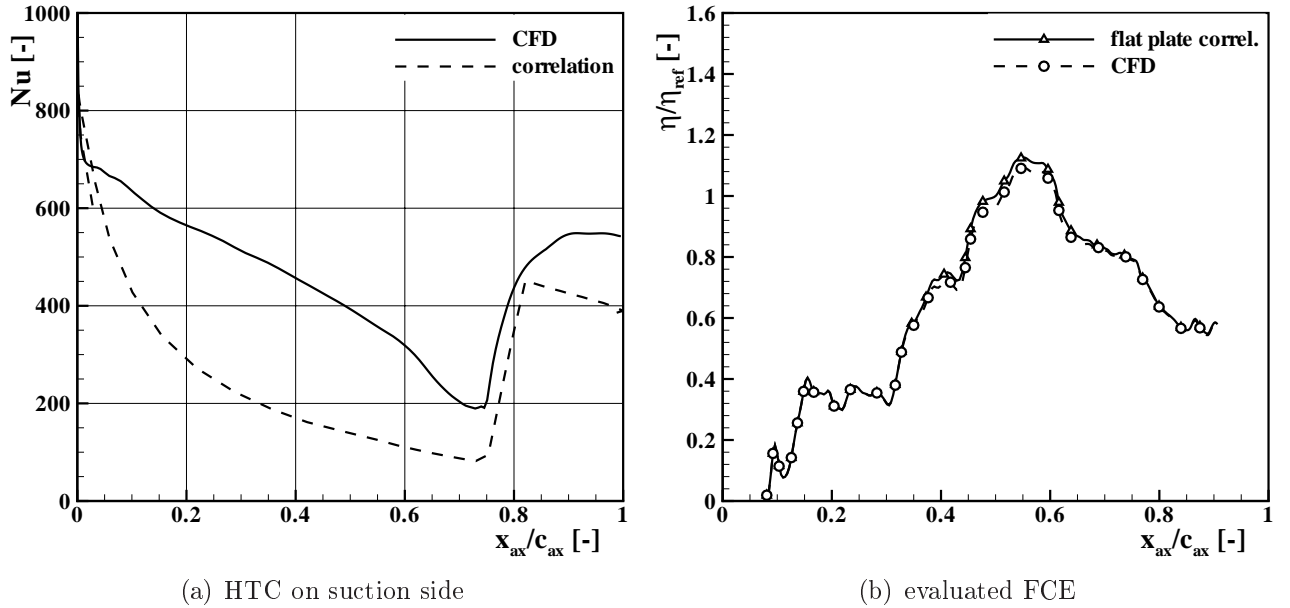
Figure 4.18: Heat transfer coefficient on the suction side and resulting adiabatic film cooling effectiveness at design conditions: CFD-simulation and flat plate correlations

Nevertheless, the impact on predicted film cooling effectiveness on the pressure side is very low as can be seen in fig. 4.18(b). There the corrected FCE η for two different HTC distributions on the suction side are plotted as function of the axial chord length. One using the CFD prediction the other one using flat plate correlations for the heat transfer on the suction side. It is clearly visible, that the differences between both curves are small and limited to the region $0.4 \leq x_{ax}/l_{ax} \leq 0.6$. The front part is essentially influenced by the heat transfer into the plenum and the film cooling holes. The influence of the different heat transfer coefficients on the suction side are less than 4% and limited to a region extending over 20% of the axial chord.

For the measurement of the heat transfer coefficient the conducted heat is calculated in a similar way and the convective heat q_{conv} is obtained with

$$q_{conv} = E \cdot I - q_{cond}, \tag{4.42}$$

obtaining the true heat transfer coefficient $h = q_{conv}/(T_w - T_r)$.

Using this data correction method, the accuracy of the measurements can be increased largely even using geometries with small wall thickness. While in some test facilities a large wall thickness reduces the heat conduction inside the plexiglass in a cascade the geometry can only be changed within certain limits by increasing the size of the blades. This makes it necessary to capture the heat conduction inside the blade. In fig. 4.19 the influence of the correction method is visualized. Especially close to the film cooling holes the film cooling effectiveness would be largely overestimated since convective cooling reduces the wall temperature in the regions close to the ejection location. Also close to the velocity peak on the suction side the influence of the heat conduction is well noticeable. An appropriate data post processing method seems therefore to be necessary in order to accurately measure the adiabatic film cooling effectiveness or the heat transfer coefficient when the wall thickness is limited.
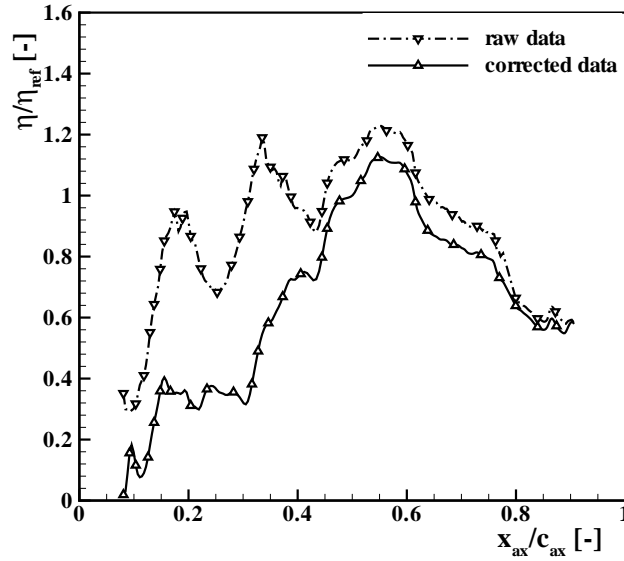
Figure 4.19: Film cooling effectiveness on the pressure side of the *T120C* blade with and without correction of the measured wall temperature
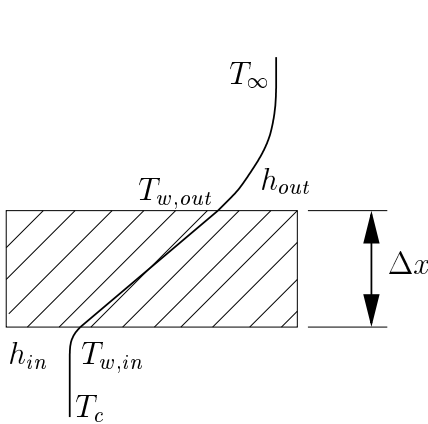
Figure 4.20: Schematic of steady state convective cooling
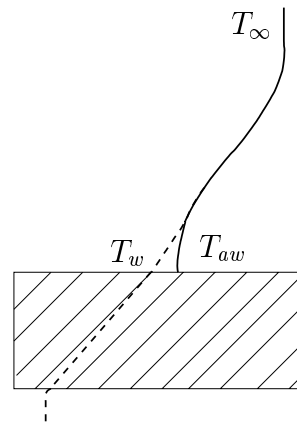
Figure 4.21: Schematic of the temperature along the boundary layer with film cooling

4.3.8   Evaluation of Film Cooling on a Non-Adiabatic Wall

An adiabatic wall, as used for the definition of the adiabatic film cooling effectiveness, is not present in a real engine. Convective cooling is used in general parallel to the film cooling. When convective cooling is used, the inner part of the blade is cooled keeping a constant heat flux from the outer surface of the blade to the inside. As shown in fig. 4.20, the maximum metal temperature is lowered by having low temperatures in the inside of the blade. This effect is enhanced by having a large heat transfer coefficient at the inside of the blade h_{in}, a high heat conduction parameter for the blade k and low heat transfer coefficient at the outside h_{out}[1]. For

---

[1]For simplicity reasons the use of a thermal barrier coating is not regarded in this approach.

steady state incompressible flow, the heat flux from the hot gas to the blade and successively to the coolant inside the blade is

$$\dot{q} = h_{out} \cdot (T_{\infty} - T_{w,out}) = \frac{k}{\Delta x} \cdot (T_{w,out} - T_{w,in}) = h_{in} \cdot (T_{w,in} - T_c) . \qquad (4.43)$$

When applying film cooling, the adiabatic wall temperature is reduced which leads to the differences in wall temperature as shown in fig. 4.21 for an incompressible flow.

While both techniques (convective and film cooling) separately decrease the wall temperature, the addition of film cooling may decrease the cooling effect compared to convective cooling alone. Due to the turbulent mixing of the film cooling jets with the main flow, the heat transfer coefficient h_{out} is increased with film cooling compared to the blade without film cooling. But when h_{out} increases in eq. (4.43), $T_{w,out}$ and $T_{w,in}$ have also to increase, with the increase of $T_{w,out}$ being higher than the one of $T_{w,in}$. Hence, for the film cooling to have an overall positive cooling effect on an non-adiabatic blade, the adiabatic wall temperature has to be lowered so that the heat flux

$$\dot{q}_c = h_c \cdot (T_{aw} - T_{w,out}) \qquad (4.44)$$

is not higher than the heat flux for the non film cooled case in eq. (4.43).

Mick and Mayle [110] use an approach for incompressible fluid using the definitions of heat flux for the film cooled and the uncooled surface[2]

$$q_c \quad = h_c \cdot (T_{aw} - T_{w,c}) \qquad \text{film cooled,} \qquad (4.45)$$
$$q_0 \quad = h_0 \cdot (T_{\infty,0} - T_{w,0}) \qquad \text{uncooled.} \qquad (4.46)$$

Using the definition of the adiabatic film cooling effectiveness for incompressible flow

$$\eta = \frac{T_{aw} - T_{\infty,c}}{T_c - T_{\infty,c}}, \qquad (4.47)$$

the heat flux ratio is set to

$$\frac{q_c}{q_0} = \frac{h_c}{h_0} \cdot \frac{\eta \cdot (T_c - T_{\infty,c}) + T_{\infty,c} - T_{w,c}}{T_{\infty,0} - T_{w,0}} . \qquad (4.48)$$

The authors then implicitly assume that the main stream and wall temperatures are equal in both cases obtaining in that manner for the heat flux ratio

$$\frac{q_c}{q_0} = \frac{h_c}{h_0} \cdot \left[\frac{\eta \cdot (T_c - T_{\infty})}{T_{\infty} - T_w} + 1 \right]$$
$$= \frac{h_c}{h_0} \cdot \left(1 - \frac{\eta}{\varphi} \right), \qquad (4.49)$$

with the overall effectiveness $\varphi = (T_{\infty} - T_w) / (T_{\infty} - T_c)$. In lack of further details they set φ to a constant value of 0.6, which is a typical value for modern gas turbine components, and use an average heat transfer coefficient for the uncooled case h_0. This method is widely used in literature but has some deficits as the unknown value of φ, which will not be constant along the blade, and the assumption of equal main stream and wall temperatures in the film cooled as in the uncooled case which will be seldom realistic.

The approach followed in this thesis is based on following assumptions:

---

[2]subscripts c and 0 for the temperatures T_{∞} and T_w not used by the authors in their publication

1. The wall temperature is equal in the film cooled as in the uncooled case. The fixed wall temperature might be the maximum allowable metal temperature.

2. The main flow temperature is variable. The goal of the film cooling would then be to increase the main flow temperature in order to increase thermodynamic efficiency of the machine by keeping the same wall temperature as in the uncooled case. The maximum wall temperature can be adjusted to the requested design criteria, such as efficiency or longevity and maintenance costs.

3. The heat flux into the blade's interior is equal in both cases since the outer wall temperature is equal and the properties of the material and the convective cooling inside the blade is not changed.

For incompressible flow eq. (4.45)–(4.47) can be combined by setting $q_c = q_0$ to

$$h_0 \cdot (T_{\infty,0} - T_{w,0}) = h_c \cdot [\eta (T_c - T_{\infty,c}) + T_{\infty,c} - T_{w,c}] . \tag{4.50}$$

Following eq.(4.43), the same heat transfer can be described with the temperature difference between the outer and the inner wall of the blade multiplied by a constant factor $K_1 = k/\Delta x$. The inner wall temperature is also dependent on the coolant temperature inside the blade, which will usually be different than the film cooling temperature, and on the heat transfer coefficient inside the cavity. The wall temperature will be $T_{w,in} = \xi \cdot T_c$ with the a priori unknown factor ξ. For simplicity reasons a fourth assumption is added to the other three:

4. The inner wall temperature is set equal to the film cooling temperature: $T_{w,in} = T_c$.

This assumption can be taken not to be too far from reality since the heat transfer coefficient in the interior of the airfoil is relatively high decreasing the temperature differences between wall and fluid temperature and the coolant temperature of the film cooling jets will be higher than inside the cavity due to the convective heat transfer from the metal to the fluid. With this fourth assumption one gets for the conductive heat transfer:

$$\dot{q}_c = \dot{q}_0 = K_1 \cdot (T_w - T_c) \tag{4.51}$$

$$\Leftrightarrow T_c = T_w - \frac{h_0}{K_1} (T_{\infty,0} - T_w) . \tag{4.52}$$

Combining eq.(4.52) with (4.50) one obtains

$$h_0 \cdot (T_{\infty,0} - T_{w,0}) = h_c \cdot \left\{ T_{\infty,c} (1 - \eta) + \eta \left[T_w - \frac{h_0}{K_1} (T_{\infty,0} - T_w) \right] - T_w \right\}$$

$$\Leftrightarrow (T_{\infty,0} - T_w) \left(h_0 + h_c \cdot \eta \frac{h_0}{K_1} \right) = (T_{\infty,c} - T_w) \cdot h_c (1 - \eta)$$

$$\Leftrightarrow \frac{T_{\infty,0} - T_w}{T_{\infty,c} - T_w} = \frac{h_c}{h_0} \frac{1 - \eta}{1 + \frac{h_c \cdot \eta}{K_1}} . \tag{4.53}$$

For compressible flow, one obtains after some derivation

$$(T_{r,0} - T_w) \cdot h_0 \cdot \left(1 + \frac{h_c}{K_1} \eta \right) = h_c \left[(T_{r,c} - T_w) \cdot (1 - \eta) - \frac{u^2}{2 \cdot c_p} \cdot (1 - r) \cdot \eta \right], \tag{4.54}$$

or as temperature difference ratio

$$\frac{T_{r,0} - T_w}{T_{r,c} - T_w} = \frac{h_c}{h_0} \left[\frac{1 - \eta}{1 + \frac{h_c \cdot \eta}{K_1}} - \frac{\frac{u^2}{2 \cdot c_p} \left(1 - r\right) \cdot \eta}{\left(T_{r,c} - T_w\right) \left(1 + \frac{h_c}{K_1} \eta\right)} \right]. \tag{4.55}$$

For low velocities or for a recovery factor $r = 1$ one obtains for eq. (4.55) the solution for incompressible flow eq. (4.53). The right summand of eq. (4.55) accounts for the temperature reduction of the coolant at high velocities.

For a recovery factor $r < 1$, which holds true for air, one can reduce eq. (4.55) to

$$\frac{T_{r,0} - T_w}{T_{r,c} - T_w} < \frac{h_c}{h_0} \frac{1 - \eta}{1 + \frac{h_c \cdot \eta}{K_1}}. \tag{4.56}$$

Since in the machine the temperature difference $T_{r,c} - T_w$ will be considerably larger than $\frac{u^2}{2 \cdot c_p} \left(1 - r\right) \cdot \eta$, eq. (4.56) can be used as approximation for estimation of the temperature difference ratio

$$\frac{\Delta T_0}{\Delta T_c} = \frac{T_{r,0} - T_w}{T_{r,c} - T_w} \approx \frac{h_c}{h_0} \frac{1 - \eta}{1 + \frac{h_c \cdot \eta}{K_1}}. \tag{4.57}$$

A thermal conductivity k of $25 \, \text{W}/(\text{K} \cdot \text{m})$ is a reasonable value for a nickel based alloy at high temperatures, see [150]. For a jet engine blade a constant wall thickness of 3 mm is used obtaining with these values $K_1 = 8333 \, \text{W/m}^2$ for estimation of the overall effectiveness in this work.

The temperature difference ratio is used in this thesis as parameter to estimate the overall film cooling effectiveness on a real engine blade. This is a more relevant parameter for the application on a real engine and seems to be more appropriate for estimation of the film cooling than the heat flux ratio which is widely used in literature. The accuracy of this parameter can be increased by knowing the heat transfer coefficient inside the plenum h_{in} as well as the geometry of the interior of the blade. Using the measured heat transfer coefficient and the adiabatic film cooling effectiveness on the outer surface of the blade, the heat transfer coefficient at the inner surfaces and the real wall thickness and material properties, the temperature difference parameter can be accurately estimated iteratively and the assumption 4 is not longer needed. This method then allows also to apply the same measurements of the heat transfer coefficient and of the adiabatic film cooling effectiveness on blades with varying geometry of the channels in the interior of the blade. The heat flux inside the blade can then be optimized in order to enhance the overall cooling effectiveness.

4.3.9 Measurement Uncertainties

The measurement uncertainties are all evaluated using error propagation analysis:

$$\Delta y = \sum_{i=1}^{n} \left| \frac{\partial f\left(x_1, \ldots, x_n\right)}{\partial x_i} \right| \cdot \Delta x_i. \tag{4.58}$$

The variation Δx_i of the measured value x_i is based on the guaranteed accuracy of the measurement sensors and on variances from calibration procedures.

The profile pressure measurements are plotted as isentropic Mach number and the maximum possible variation can be of about 0.1 for very low velocities. In general the uncertainty is below 0.5%. The total pressure loss parameter uncertainty is 5%.

The uncertainty for the measurements of the adiabatic film cooling effectiveness depends on the actual value. At high values of FCE or high heat conduction the coolant temperature approaches the one of the main stream, which increases largely the uncertainty. Therefore, especially close to regions of high heat conduction where the FCE decreases after data post processing, the uncertainty can reach values of 30%. But for most of the surface the variation of FCE can be of 5 to 10%.

The uncertainty in measured heat transfer coefficient is more constant along the surface and amounts to in general 5%.

5 Numerical Simulation Set-up

Numerical tools are widely used in turbomachinery design and flow analysis. The application of such tools for flow simulation allows to analyse a high number of parameter variations at relatively low costs when compared to experiments. The simulations allow also to gain a more extensive view into the flow than single point measurements. Big improvements have been made in the past decades in order to improve the accuracy of the models applied, but still experiments are needed to validate the simulations and to reveal deficits of the models.

The emphasis of this thesis is clearly set on the experimental work. Nevertheless, some simulations on heat transfer and film cooling effectiveness were made in order to estimate the accuracy and the applicability of standard and more sophisticated numerical models. The numerical flow simulations were carried out with the commercial solver "ANSYS CFX" in its version 11.0. "ANSYS CFX" is not an open-source program and therefore the details on the solver given here can only be based on the information provided by ANSYS. CFX solves numerically the Navier-Stokes equations and ideal gas properties were set for the equations of state and buoyancy effects were neglected. As spatial discretization it utilizes the finite-volume method. The whole fluid domain is divided into numerous finite volumes and the set of differential equations is integrated over each volume element. For the advection term the high-resolution scheme was used which uses a blend based on the boundedness principles of Barth and Jesperson [12].

Turbulent flow is set to instantaneous fluctuations which in most cases are small compared to the mean flow convection. In a time mean scale the average of these fluctuations is zero whereas the product of two fluctuating quantities is not zero. By accounting for these fluctuations, Reynolds based Navier-Stokes equations are obtained with additional terms for the average of the product of the fluctuations $\overline{\phi_i' \phi_j'}$. In order to account for the Reynolds stresses — based on the velocity fluctuations — various turbulence models are available in order to compute the turbulence viscosity which is added to the molecular viscosity of the mean flow. For the simulations run for these investigations the shear-stress-transport (SST) turbulence model was used. This turbulence model is based on the $k - \omega$ model of Wilcox [157] and the blending developed by Menter [106]. The transition model solves two additional equations for computation of the intermittency and boundary layer Reynolds number as used in Menter et al. [108]. The SST model is currently the most indicated turbulence model for heat transfer predictions with CFX, see Esch et al. [57], Menter et al. [107] and Vieser et al. [151].

A far more complex way of solving the flow structures is based on the large eddy simulation (LES) theory. There the bigger eddies are solved directly while smaller eddies are filtered and taken into account using subgrid-scale models. As subgrid-scale model the algebraic Smagorinsky model [131] was used. A fine grid and very small time steps have to be used in order to compute the large eddy fluctuations. This increases by large the computational resources needed to solve the flow.

In the detached eddy simulation (DES) the features of RANS and LES are combined. In CFX the Strelets model [140] is used. Whenever the computed turbulent length is larger than the grid spacing the LES model is used, while the shear stress transport model is used in the other case.
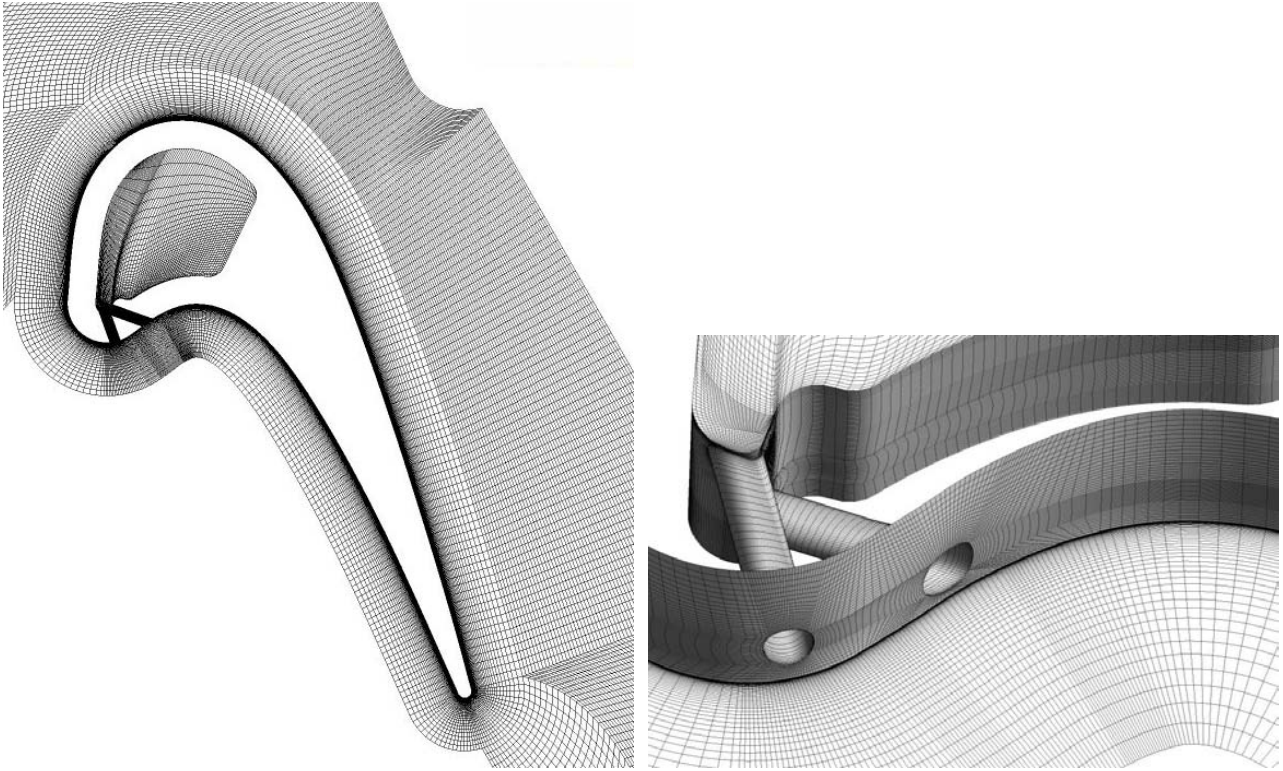
Figure 5.1: Views of the structured 3D mesh used for DE simulation on the
$T120C$ blade

Different grids were used for the simulations. For the RANS simulations of the heat transfer and the film cooling effectiveness on the $T120C$ blade a 2D grid with 14,000 hexahedra and a 3D grid with $1.8 \cdot 10^6$ hexahedra was used. For the DES simulations a structured grid with $2.8 \cdot 10^6$ hexahedra was applied. Snapshots of the DES mesh are shown in fig. 5.1. In the viscous layer the grid spacing is finer perpendicular to the wall, because the gradients are larger. Outside the boundary layer, the grid has almost same grid spacing in the three directions of space since the eddies filtered in the LES are statistically isotropic, see Spalart [134]. Due to this reason and in order to have an isotropic mesh with small increase of cell size in any direction far away from the wall, a complete unstructured mesh with $8.5 \cdot 10^6$ tetrahedra came to use for the LES run. Some plots showing the unstructured mesh are given in fig. 5.2. The time step chosen for the DES run was of $1 \cdot 10^{-5}$ and a periodic solution was obtained after about 700 time steps. The large eddy simulation was run with adaptive time step which was of about $2 \cdot 10^{-6}$. For the achievement of a periodic solution about 8,000 time steps were needed.

The heat transfer on the $T120S$ blade was simulated for a solid blade without film cooling with a 2D structured mesh with 23,000 hexahedra. The mesh is displayed in fig. 5.3. For these analyses the SST model was used.

The values for the boundary conditions applied for the simulations varied with the operation points and were set in conformity with the measurements. The types of boundary conditions are listed in table. 5.1 and a plot with the name of the zones is given in fig. 5.4.
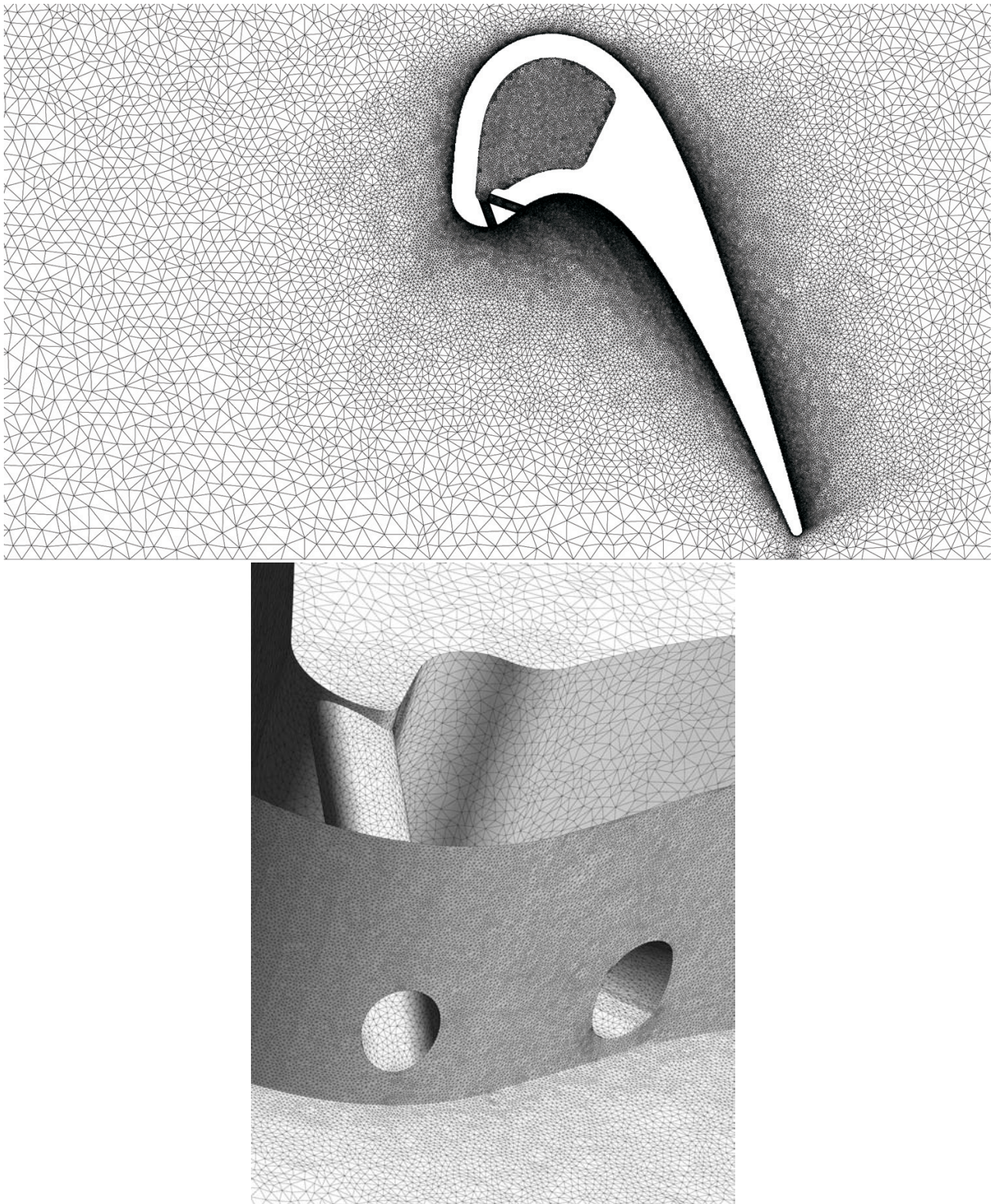
Figure 5.2: Views of the unstructured 3D mesh used for LE simulation on the *T120C* blade
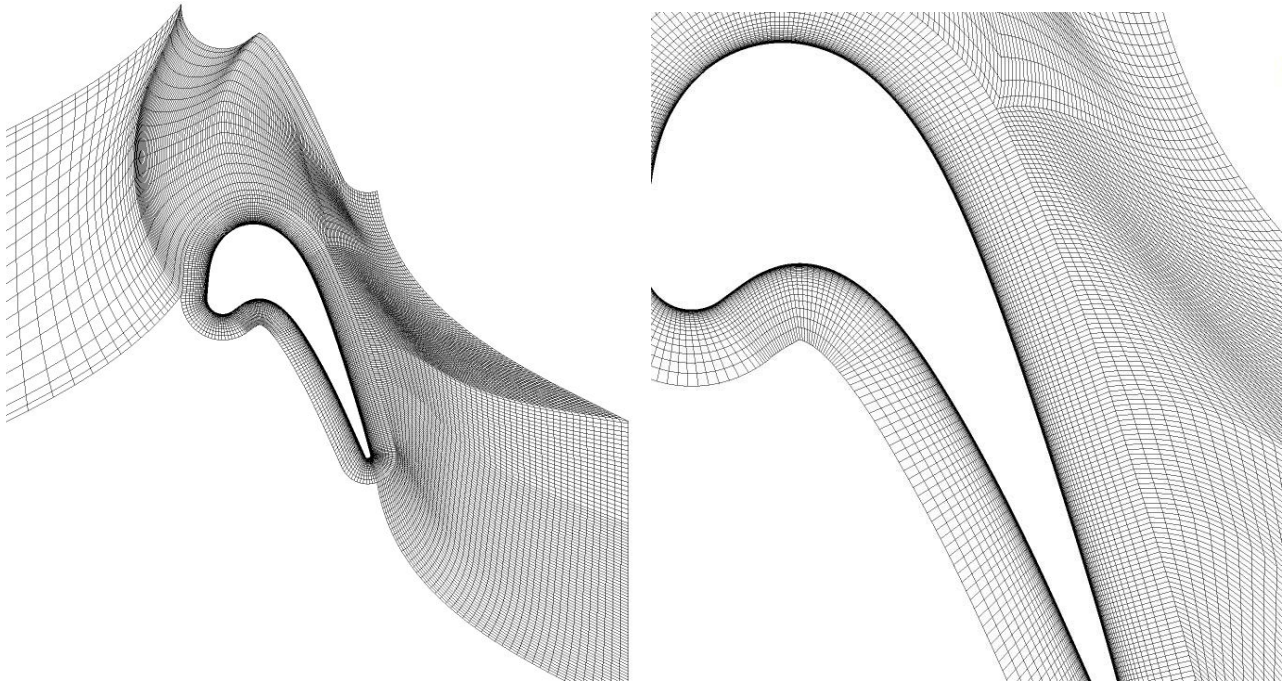
Figure 5.3: Views of the 2D mesh used for RANS simulation on the *T120S* blade

boundary	type
inlet	total pressure
	total temperature
	flow direction
	turbulence level and length scale
outlet	average static pressure
blade	non-slip adiabatic wall
	constant heat flux (for HTC simulation)
plenum	non-slip adiabatic wall
plenum side	non-slip adiabatic wall (no FC)
	mass flow (FC)
hub / tip	periodic

Table 5.1: Boundary conditions applied for the simulations
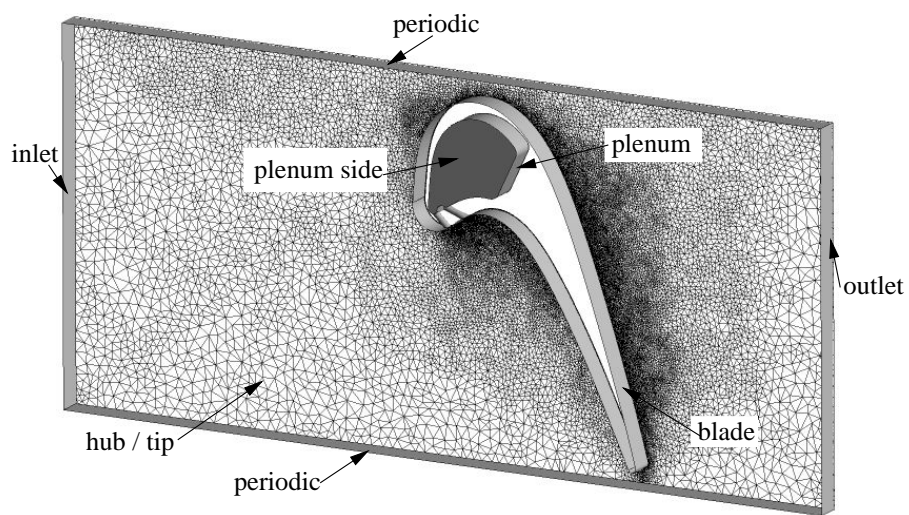
Figure 5.4: Boundary condition zones for CFD simulation

6 Heat Transfer and Film Cooling Effectiveness in Separated Flow on the Pressure Side

Measurements of the heat transfer coefficient and of the adiabatic film cooling effectiveness were carried out on the pressure side of the *T120C* blade. Some of these results are compared to numerical simulations showing the feasibility of the use of simulations for flow prediction in such complicated flow. Measurements with single hot wire anemometry inside the separation bubble give a better insight into the flow phenomena and increase the data base for comparison with the simulations. The inlet conditions were measured with a 3D hot-wire probe and free stream turbulence levels for the three operation points between 5 and 6% were obtained.

For the measurements on the pressure side, the correction method for oblique light incidence as proposed in chapter 3.3.2 is used for determination of the surface temperature in specific zones on the blade. As seen in fig. 6.1, the light from both cameras cross in the marked concave zone. Hence, both cameras see reflected light from on-axis and off-axis illumination when the light source from the other camera is on. This is in principle undesired since, as seen before, the temperature-hue curve drifts towards lower temperatures with off-axis illumination. On the other hand e. g. for camera 1, the viewing angle on the surface increases towards $x_{ax}/c_{ax} = 0.5$ which leads to low reflectivity and hence a bad signal to noise ratio. The intensity of the incoming light can be increased by lighting the second light from camera 2. In that way a correction of the perceived hue-value turns necessary. The correction method is validated on the *T120C* airfoil for measurements of the heat transfer coefficient. In fig. 6.2 the measured heat transfer coefficient for design flow conditions without film cooling is plotted for three different illumination configurations. The solid curve displays the measured heat transfer with normal configuration, i. e. with light source and camera on-axis. The dashed curve with triangles
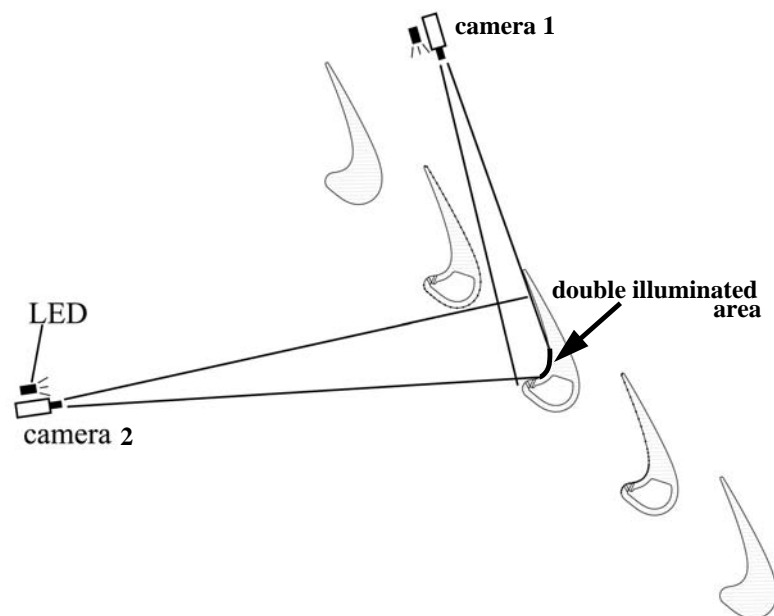
Figure 6.1: Schematic of the image acquisition on the *T120C* blade and region with illumination from both sides
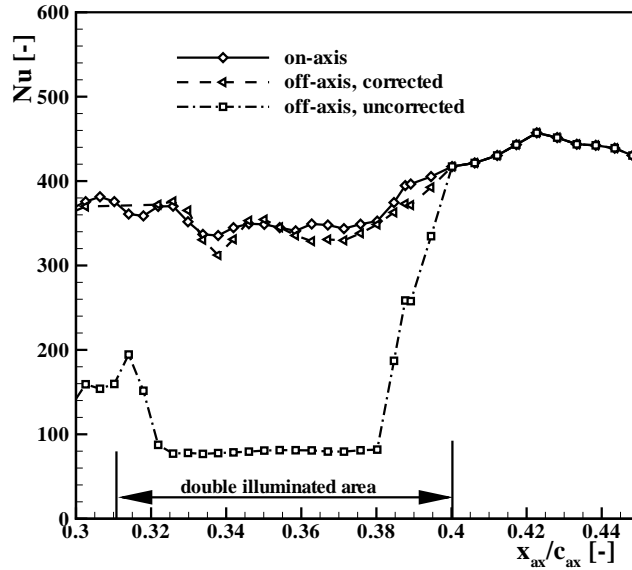
Figure 6.2: Nusselt number on the blade for on- and off-axis configuration

	RANS	DES
$\omega_{sim}/\omega_{meas}$	1,2	1,25
$\beta_{2,sim} - \beta_{2,meas}$	$-1,6°$	$-1,5°$

Table 6.1: Aerodynamic parameters from simulation

represents the same values for illumination from the second camera and the applied correction method. The dashed-dotted curve with square symbols is the measured HTC for the same configuration, but without the correction due to off-axis arrangement. The area with oblique incident light is marked in the plot. It is visible, that the applied method does very well in correcting the measured hue values for the off-axis illumination configuration and the method can be used for evaluation of the measurements.

6.1 Datum Heat Transfer Without Film Cooling

The *T120C* blade is a transonic highly loaded blade. In fig. 6.3(a) the isentropic Mach number on the blade is plotted as function of the axial chord for the three flow conditions without film cooling. While on the suction side the flow rapidly accelerates to supersonic velocities, it suffers a strong deceleration on the pressure side shortly after the stagnation point leading to flow separation at about $x_{ax}/c_{ax} = 0.15$. The reattachment occurs only at about mid-chord and the flow then accelerates very quickly towards the outlet Mach number. A near wall flow visualization from Homeier [80], shown in fig. 6.4, illustrates the flow separation and reattachment line. The axial coordinates are marked on the left of the figure. The flow acceleration after reattachment is quite strong as is shown in fig. 6.3(b). The values of the acceleration parameter K are well beyond $3 \cdot 10^{-6}$ where relaminarization of the flow is expected, see Mayle [101].

A 2D steady RANS simulation with SST turbulence model and γ-θ transition model reproduces
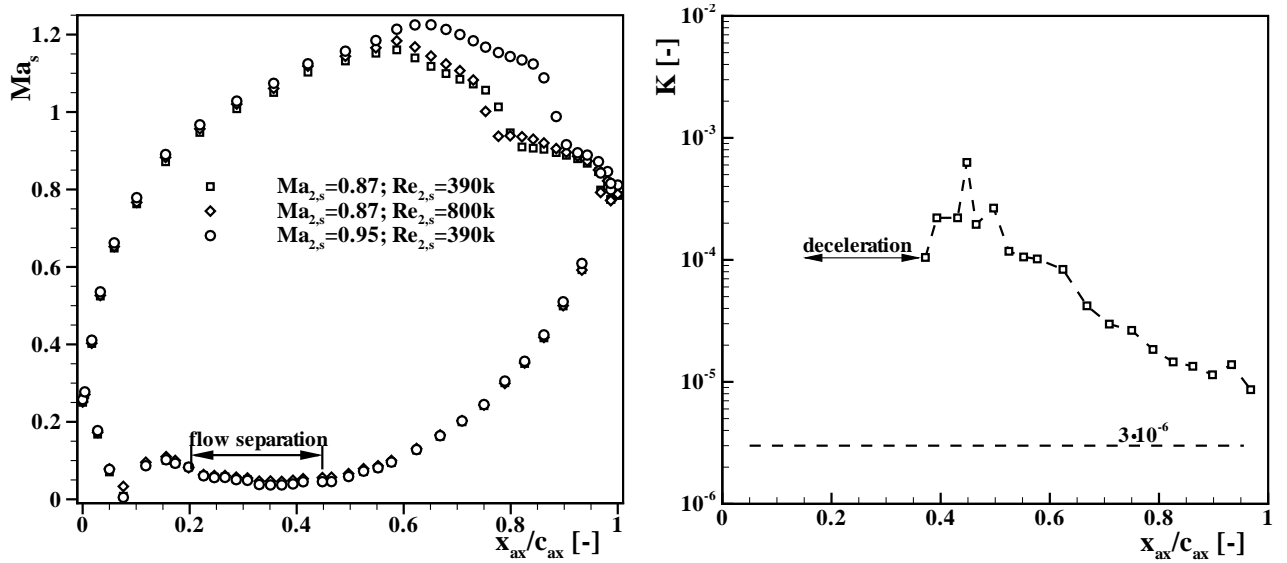
(a) Isentropic Mach number on *T120C* blade at various main flow conditions

(b) Acceleration parameter on the PS of the *T120C* blade at $Ma_{2,s} = 0.87$; $Re_{2,s} = 390,000$ (390 k)

Figure 6.3: Flow properties on the *T120C* blade without film cooling
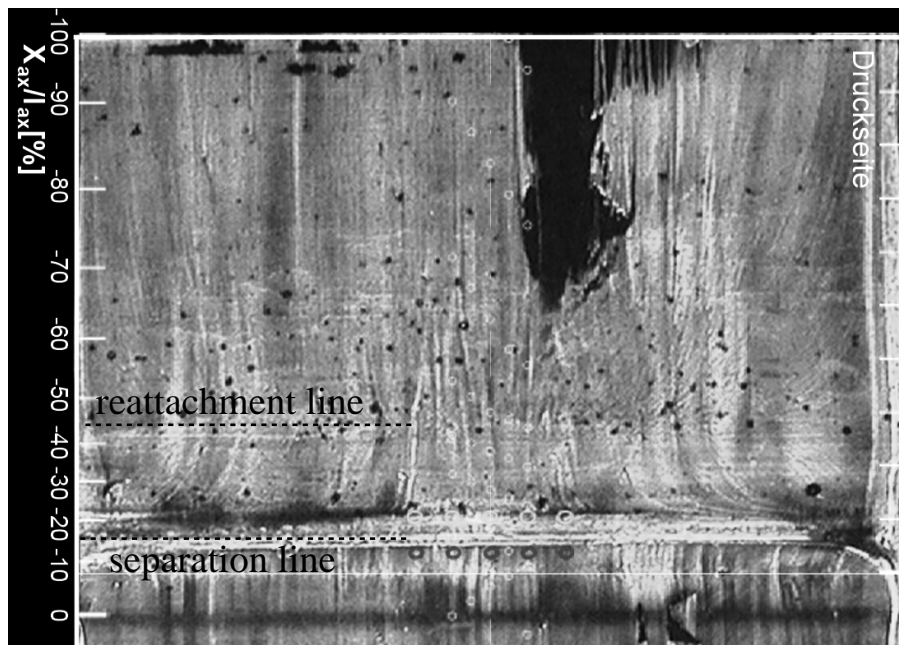
Figure 6.4: Oil flow visualization of the pressure side of the *T120C* blade at design flow conditions, from Homeier [80]

(a) Nu at various main flow conditions

(b) Sketch of the flow separation process
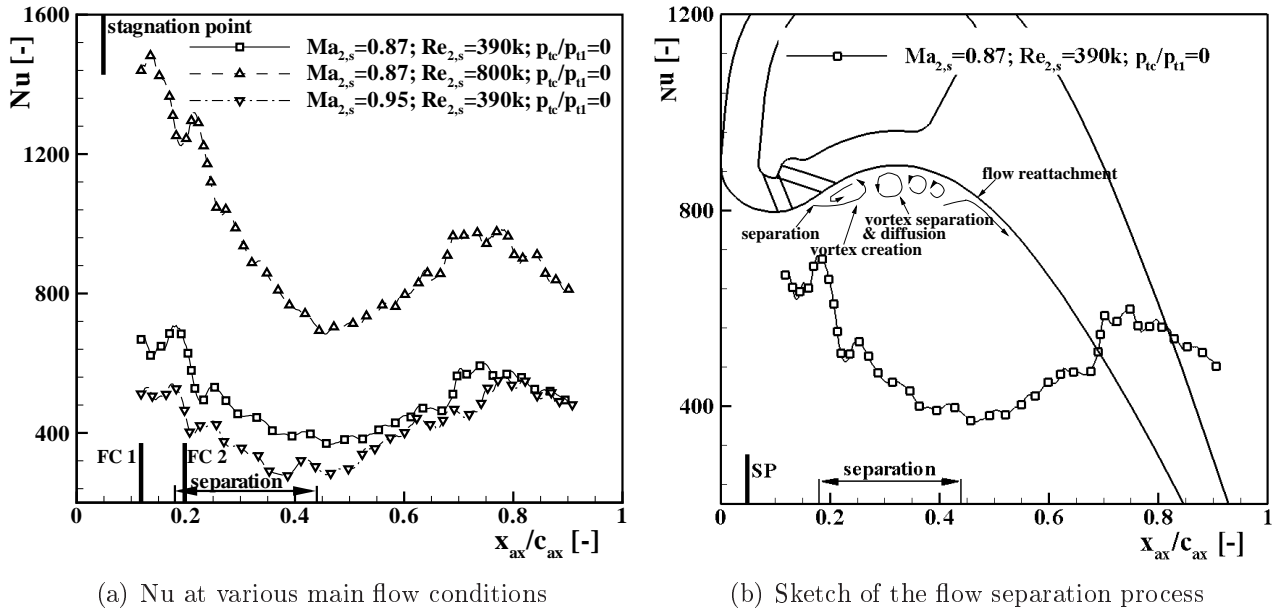
Figure 6.5: Heat transfer on the T120C blade without film cooling

(a) Nu at design main flow and flat plate correlations

(b) Nu at design main flow and flat plate correlation for Re starting at $x_{ax}/c_{ax} = 0.5$
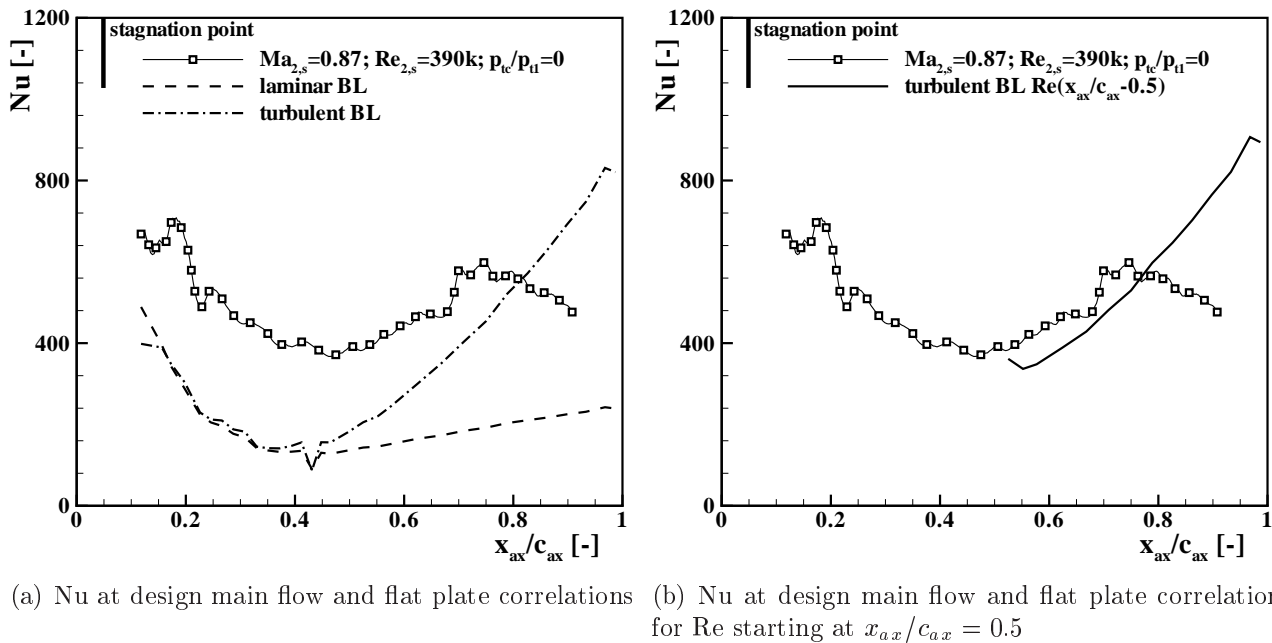
Figure 6.6: Nu at design flow conditions without film cooling and for correlations

quite well the aerodynamic features. The pressure distribution for the design case is already given in fig. 4.17. The average values over one blade pitch in the outlet plane are given in tab. 6.1 in forms of ratio of computed and measured total pressure loss $\omega_{sim}/\omega_{meas}$ and difference of the outlet angle $\beta_{2,sim} - \beta_{2,meas}$. The simulation predicts too high total pressure losses because the computed flow separation on the pressure side is estimated too long and also a small separation on the suction side is predicted which is not seen in the experiments.

The Nusselt number distribution on the pressure side of the *T120C* blade without film cooling is plotted in fig. 6.5(a). At $\mathrm{Re}_{2,\mathrm{s}} = 800$ k the heat transfer is increased due to the higher Reynolds number, but the shape of the curve is similar to the one at the same Mach but lower Reynolds number. All three distributions have in common that a peak is seen close to the first film cooling row. At the separation point, the heat transfer coefficient decreases which is typical for a flow detachment line. A local peak in heat transfer is observed for the three operation points downstream of the second film cooling row. Since the holes were not sealed, an effect similar to the one reported in Camci and Arts [25] could at first glance be present. The authors observed a local peak downstream of a film cooling row when the holes are not closed, though air could not penetrate through one hole and evade from another because the plenum was closed. Since they have comparative measurements on a solid blade without film cooling holes where this effect does not take place, they can conclude that the presence of the holes is sufficient to disturb the boundary layer forcing the flow to separate and to reattach farther downstream. While this is true for attached flow, as it is the case in Camci and Arts, the flow separates before the second film cooling hole of the *T120C* blade and another phenomenon must be the cause for this peak.

The flow separation process is quite complex and in fig. 6.5(b) a sketch of a possible solution of the separation process on the pressure side is drawn. At the detachment line vortex shedding is very likely to occur which is highly unsteady. Eddies are formed which enlarge and separate from the source point moving then downstream. The local peak, seen downstream of the second film cooling hole, is a small vortex which is formed close to the separation line which reattaches closely downstream of the film cooling hole leading to locally enhanced heat transfer. This vortex detaches, moves downstream with the main flow and a new vortex is formed.

Looking back to fig. 6.5(a), further downstream of the local peak at $x_{ax}/c_{ax} \approx 0.25$ the heat transfer decreases up to the reattachment line. It shows then a continuous increase further downstream up to 70% of the axial chord where the curves flatten. The increase of the heat transfer downstream of the reattachment line correlates well with correlations for turbulent boundary layer on a flat plate when the local velocity is applied for determination of Re_{x}, as can be seen on fig. 6.6(a). The match of the curves improves even more by changing the correlation, similar to the method used by Bellows and Mayle [15]. In fig. 6.6(b) the correlation is computed for a turbulent boundary layer with unchanged coefficients, but with the Reynolds number starting at the reattachment point. This indicates a turbulent reattached flow. No peak is seen in the reattachment zone, probably due to an unsteady movement of the reattachment line and the periodic striking of the eddies. From $x_{ax}/c_{ax} = 0.7$ up to almost the trailing edge the curves flatten and do not follow the trend of the curve for turbulent boundary layer what might be due to a certain calmation or relaminarization of the flow caused by the high flow acceleration.

In fig. 6.7(a) the parameter $\mathrm{Nu}/\mathrm{Re}^{0.5}$ is plotted for the same flow conditions. For a laminar boundary layer and constant Prandtl number, the correlation $\mathrm{Nu} \propto \mathrm{Re}^{0.5}$ is well known. The curves for different Reynolds numbers do not collapse which indicates a non laminar state of the boundary layer. Especially close to the separation point the heat transfer seems to be strongly enhanced at the higher Reynolds number. Downstream of the reattachment point at $x_{ax}/c_{ax} = 0.55$, all three curves collapse together when the Nusselt number is scaled by $\mathrm{Re}^{0.8}$, as can be seen in fig. 6.7(b). For a turbulent boundary layer $\mathrm{Re}^{0.8}$ is proportional to the Nusselt number if the Prandtl number is unchanged. With this fact and the above mentioned match with flat plate correlations one may assume that a turbulent boundary layer is present

(a) $Nu/Re^{0.5}$

(b) $Nu/Re^{0.8}$
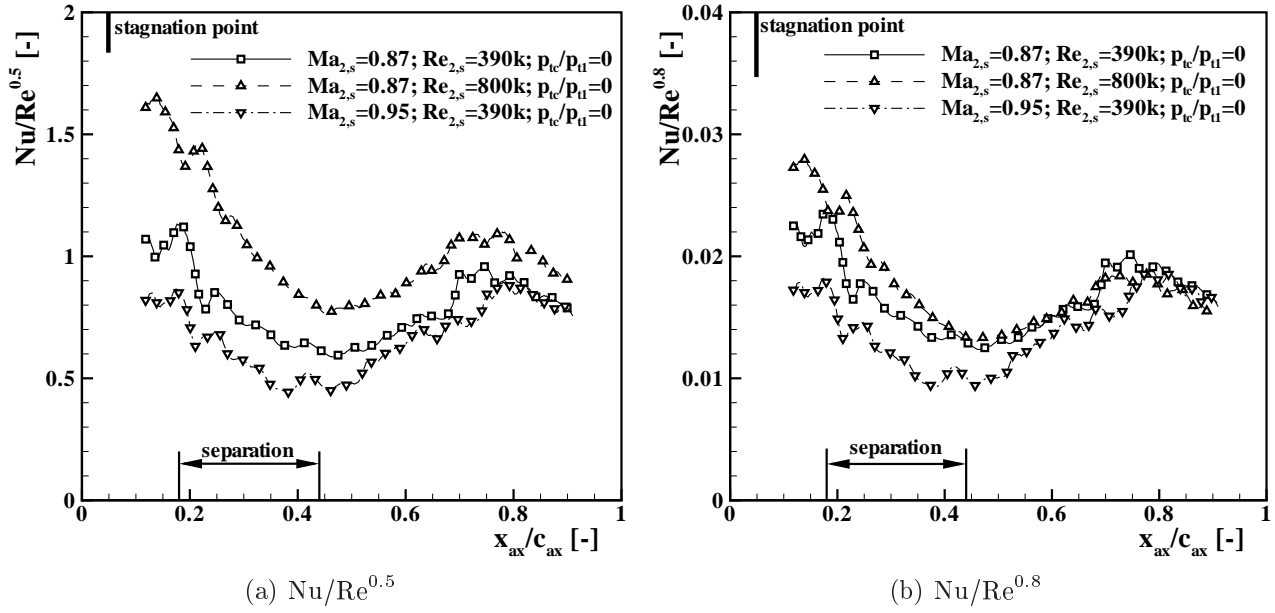
Figure 6.7: Nusselt number scaled by Reynolds number on the T120C blade without film cooling

downstream of the reattachment point. In that case the thermal and aerodynamic boundary layers at different operation points are similar. Latter assumption seems not to be true for the separation zone since on this picture one can also see that the heat transfer close to the separation line is increased at the higher exit Reynolds number and the separation start seems to be shifted slightly downstream to $x_{ax}/c_{ax} \approx 0.2$.

Focusing the attention on the area with flow separation, the measured heat transfer is very different than the one expected from steady RANS simulations with SST turbulence model and $\gamma - \theta$ transition model. The computed and measured Nusselt number distributions for the design flow without film cooling are presented in fig. 6.8. The predicted heat transfer is typical for the flow pattern given by the steady simulation in fig. 6.9, where the velocity vectors with normalized length are plotted for the region on the pressure side with flow separation. CFD predicts a large recirculation bubble with defined separation and reattachment points. The flow shows relaminarization behaviour shortly downstream of the reattachment point, when looking to the recovery temperature on an adiabatic wall or on the boundary layer shape factor H_{12} in fig. 6.10(a) and fig. 6.10(b) respectively. Though the flow experiences very favourable pressure gradients, the shape factor is above the values for a turbulent boundary layer and increases towards the trailing edge. Due to the calming of the boundary layer, the heat transfer in the simulation then does not augment, even with increasing velocity, and significant discrepancies to the measured values are found. Unsteady RANS shows no significant difference and the separation bubble does not vary with time. The changes in computed HTC between steady and unsteady RANS simulation are very small, reason why the comparison is not presented here. The unsteady and steady simulations predict a very stable flow with relatively low turbulence levels inside the separation bubble, whereas in reality the flow inside the separation bubble is highly unsteady and turbulent.

This unsteady and highly turbulent process can be deduced from boundary layer velocity profiles

Figure 6.8: Nusselt number on the *T120C* blade at design flow conditions without film cooling, simulation and measurement

Figure 6.9: Vector plot of the separation zone on the PS for RANS simulation of the *T120C* blade
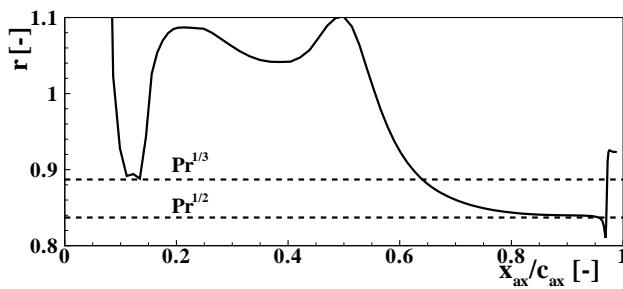
(a) Recovery temperature on the pressure side
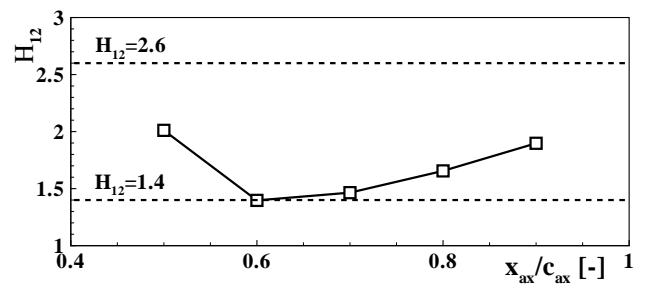
(b) Shape factor after flow reattachment

Figure 6.10: Recovery temperature and boundary layer profiles from 2D simulation

(a) $x_{ax}/c_{ax} = 0.1$ (b) $x_{ax}/c_{ax} = 0.15$ (c) $x_{ax}/c_{ax} = 0.18$ (d) $x_{ax}/c_{ax} = 0.3$ (e) $x_{ax}/c_{ax} = 0.5$
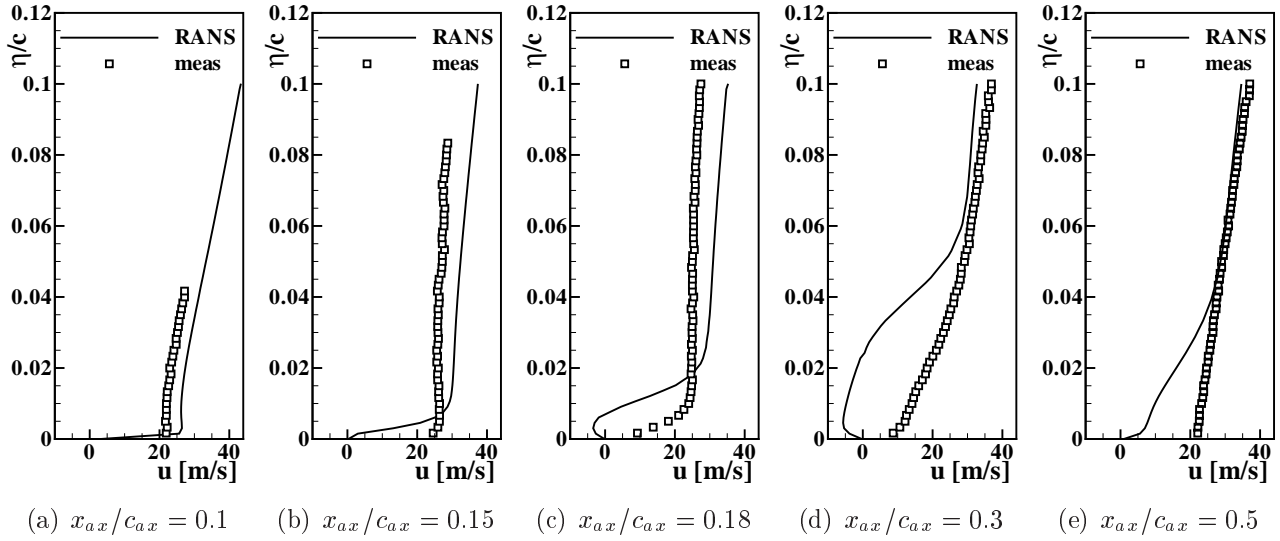
Figure 6.11: Boundary layer velocity profiles on the *T120C* blade at $\mathrm{Ma}_{2,s} = 0.87$, $\mathrm{Re}_{2,s} = 390\,\mathrm{k}$

in fig. 6.11. The first of the chosen traverses of the measurement lies at $x_{ax}/c_{ax} = 0.1$, shortly upstream of the separation line. The second one is at $x_{ax}/c_{ax} = 0.15$ which is about the separation line location. The traverse at $x_{ax}/c_{ax} = 0.18$ is already inside the separated flow region as well as the traverse at $x_{ax}/c_{ax} = 0.3$. At the last traverse position at $x_{ax}/c_{ax} = 0.5$ the flow is expected to be already reattached. The measured and the calculated velocities outside the boundary layer agree fairly well and the profile shapes are for most of the points comparable. Considerable differences are seen inside the separation bubble at $x_{ax}/c_{ax} = 0.18$ and $x_{ax}/c_{ax} = 0.3$. The simulation shows clearly backward moving flow with the dividing streamline of the forward and backward moving flow being at the zero velocity passage at $\eta/c = 0.08$ and $\eta/c = 0.22$ respectively. The measurements, however, do not show any local minimum along the surface distance η/c. This is explainable by unsteady flow resulting in the time average in a similar velocity along the surface distance. The high unsteadiness of the flow in the separation bubble is visible in fig. 6.12 where the measured and simulated turbulence kinetic energy is plotted for the five boundary layer traverses. Shortly upstream and inside the separation bubble the measured flow shows much higher turbulence due to the vortex shedding and downstream moving bulks. After flow reattachment, the predicted turbulence kinetic energy inside the boundary layer is then higher than the measured.

When looking into the energy spectrum of the flow in the boundary layer one can depict two characteristic frequencies as shown for $x_{ax}/c_{ax} = 0.1$ in fig. 6.13. The peak at a frequency of approximately 260 Hz could be related to the Karman street from the turbulence grid in the nozzle. Using continuity condition for determination of the velocity at the turbulence grid and a Strouhal number of 0.21 one would expect a frequency of about 190 Hz. The pronounced peak at $f \approx 2700\,\mathrm{Hz}$ is only visible at the locations close to the separation line and may give the oscillations of the separating swirl. For $x_{ax}/c_{ax} = 0.1...0.18$ peaks at frequencies close to 30 kHz are visible. It is not yet clear whether these frequencies are characteristic for the flow or a problem of the measurement technique since they lie close to the low-pass filter cut-off frequency of 30 kHz.

(a) $x_{ax}/c_{ax} = 0.1$ (b) $x_{ax}/c_{ax} = 0.15$ (c) $x_{ax}/c_{ax} = 0.18$ (d) $x_{ax}/c_{ax} = 0.3$ (e) $x_{ax}/c_{ax} = 0.5$
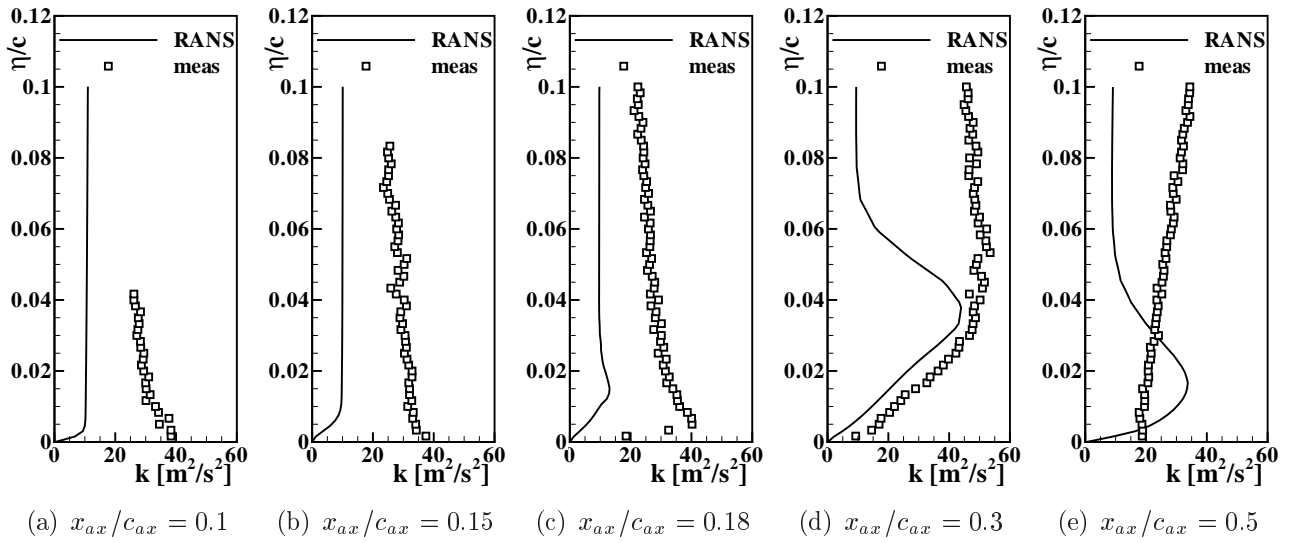
Figure 6.12: Boundary layer turbulent kinetic energy profiles on the *T120C* blade at $Ma_{2,s} = 0.87$, $Re_{2,s} = 390\,k$

(a) $x_{ax}/c_{ax} = 0.1$ (b) $x_{ax}/c_{ax} = 0.15$ (c) $x_{ax}/c_{ax} = 0.18$

(d) $x_{ax}/c_{ax} = 0.3$ (e) $x_{ax}/c_{ax} = 0.5$
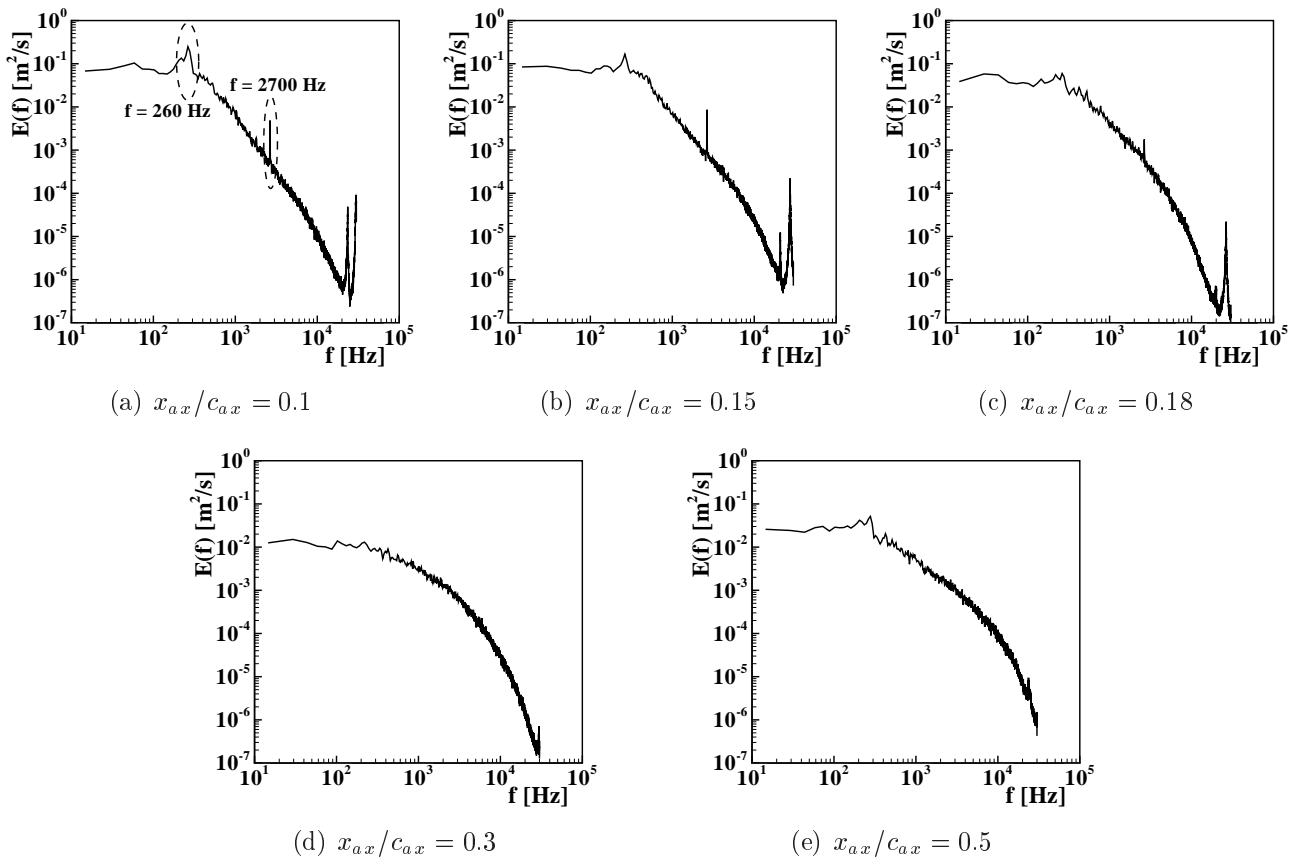
Figure 6.13: Energy spectra for different traverse positions on the *T120C* blade at $Ma_{2,s} = 0.87$, $Re_{2,s} = 390\,k$

(a) $t = 0\,\mathrm{s}$

(b) $t = 0.5 \cdot 10^{-4}\,\mathrm{s}$

(c) $t = 1.0 \cdot 10^{-4}\,\mathrm{s}$

(d) $t = 1.5 \cdot 10^{-4}\,\mathrm{s}$

(e) $t = 2.0 \cdot 10^{-4}\,\mathrm{s}$

(f) $t = 2.5 \cdot 10^{-4}\,\mathrm{s}$

(g) $t = 3.0 \cdot 10^{-4}\,\mathrm{s}$

(h) $t = 3.5 \cdot 10^{-4}\,\mathrm{s}$

(i) $t = 4.0 \cdot 10^{-4}\,\mathrm{s}$

(j) $t = 4.5 \cdot 10^{-4}\,\mathrm{s}$

(k) $t = 5.0 \cdot 10^{-4}\,\mathrm{s}$

(l) $t = 5.5 \cdot 10^{-4}\,\mathrm{s}$
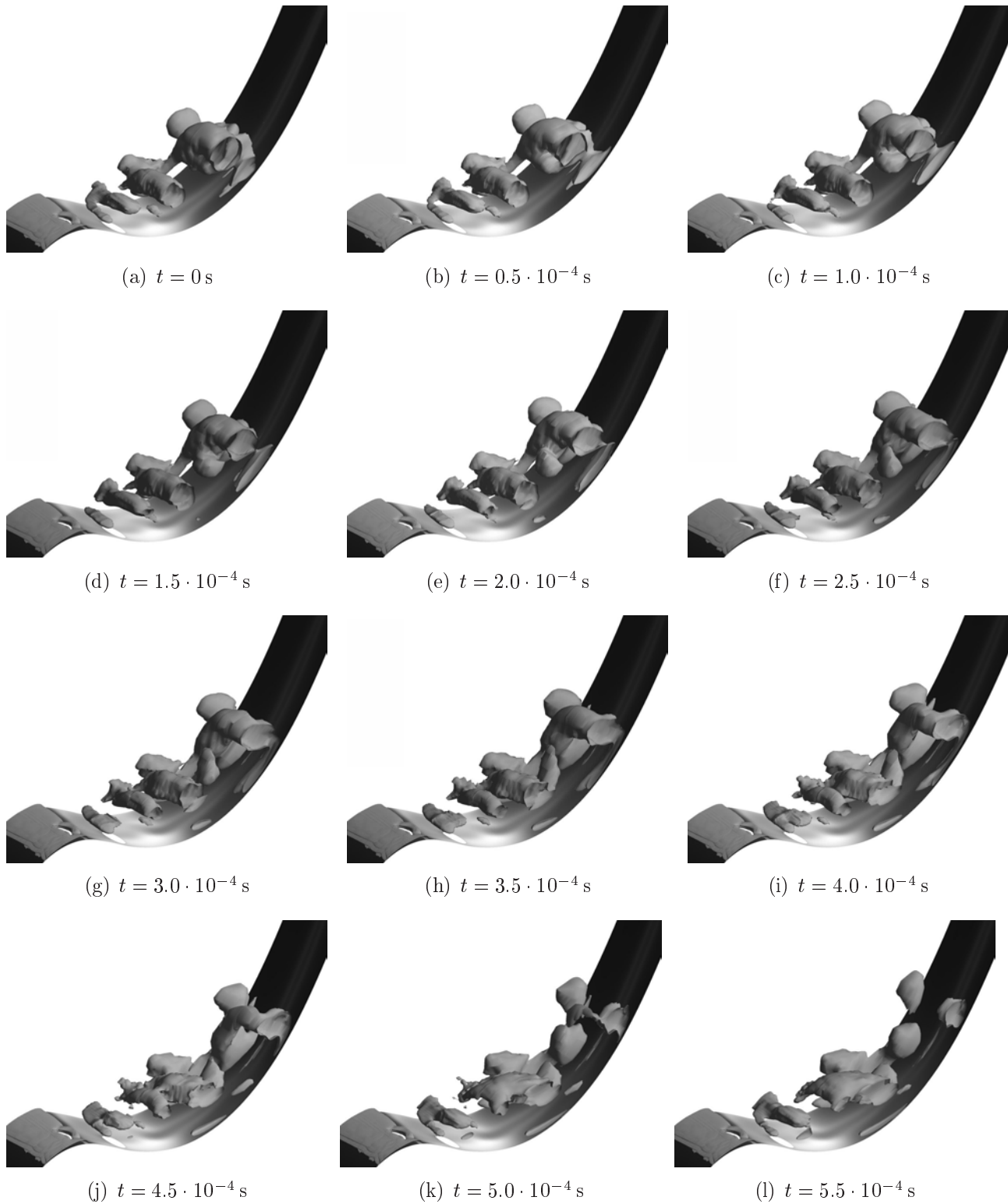
Figure 6.14: Iso-surface of constant swirl normal to blade span on the pressure side for one period — from DES

(a) $x_{ax}/c_{ax} = 0.1$ (b) $x_{ax}/c_{ax} = 0.15$ (c) $x_{ax}/c_{ax} = 0.18$ (d) $x_{ax}/c_{ax} = 0.3$ (e) $x_{ax}/c_{ax} = 0.5$
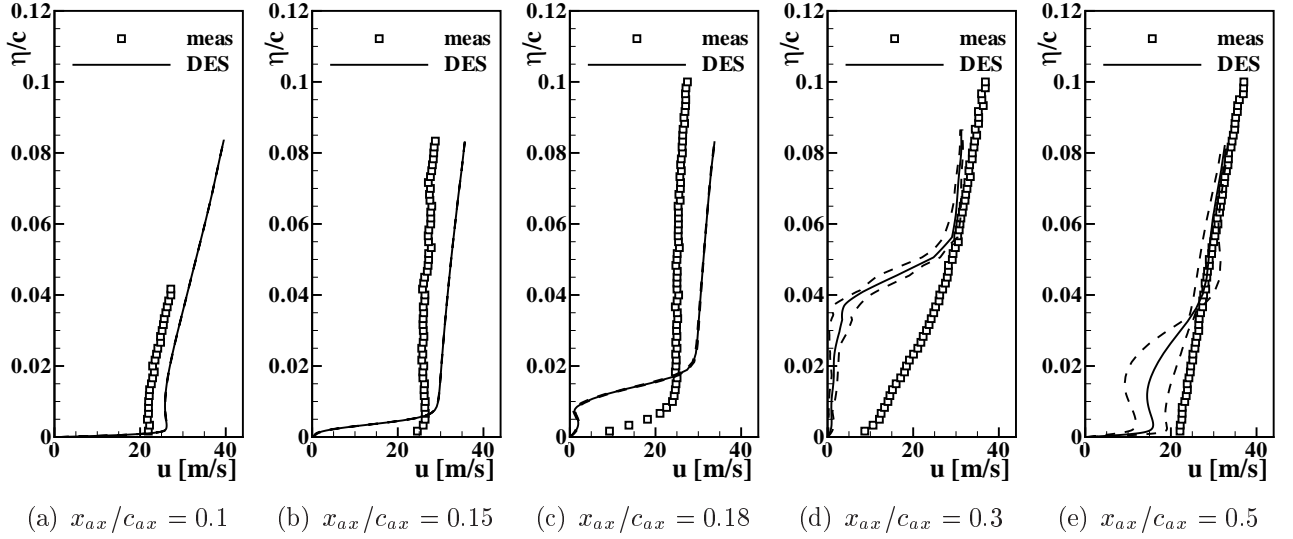
Figure 6.15: Boundary layer velocity profiles on the *T120C* blade from DES at $Ma_{2,s} = 0.87$, $Re_{2,s} = 390\,k$, maximum and minimum values with dashed lines

A detached eddy simulation method is able to reproduce the swirl production and separation process. In fig. 6.14 an iso-surface for constant swirl normal to the blade span is plotted for different time steps of the DE simulation. The view is on the pressure side at the separation zone and the axial flow moves from the bottom left towards the top right. One can see that a small swirl forms close to the separation line and grows until it separates and is convected downstream. A period of the swirl separation process is approximately $5.5 \cdot 10^{-4}\,s$ what gives a frequency of about $1800\,Hz$ which is $1/3$ below the measured value.

The boundary layer values are therefore subjected to a temporal variation which is given in fig. 6.15. There the average velocity profiles from DES are given for the five traverse positions as before and the envelope of the temporary maximum and minimum velocity is plotted with dashed lines. One can see that in the simulation only at the positions $x_{ax}/c_{ax} = 0.3$ and 0.5 large variations are seen, while at the three positions close to the separation line the velocities are nearly constant. In contrast, the measurements show high oscillations at all of the five traverse locations. Obviously, the boundary layer flow is computed with RANS turbulence model at the more upstream located traverse positions and the eddy separation does not have a significant effect on the solution. Only further downstream the solver computes the eddy separation influencing the boundary layer. This is also seen in the Nusselt number distribution shown in fig. 6.16. The flow separation takes place at the same location as with the RANS model leading to a rapid decrease of heat transfer and does not significantly change with time. Though the y^+-values are well below 1 the separation start on the pressure side is predicted too far upstream with RANS as well as with DES. The eddy separation is noticed further downstream, inside the separation bubble, with the small local peak at $x_{ax}/c_{ax} = 0.18$ followed by a further decrease in heat transfer, in contrast to the RANS-model. The reattachment zone is then very unsteady, seen in the large variation of local heat transfer represented by the maximum and minimum envelope. Downstream of the reattachment line the DE simulation does better than the RANS simulation and approximates towards the measured values.
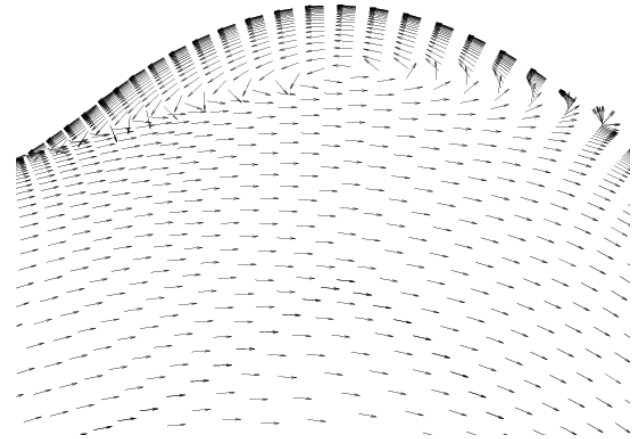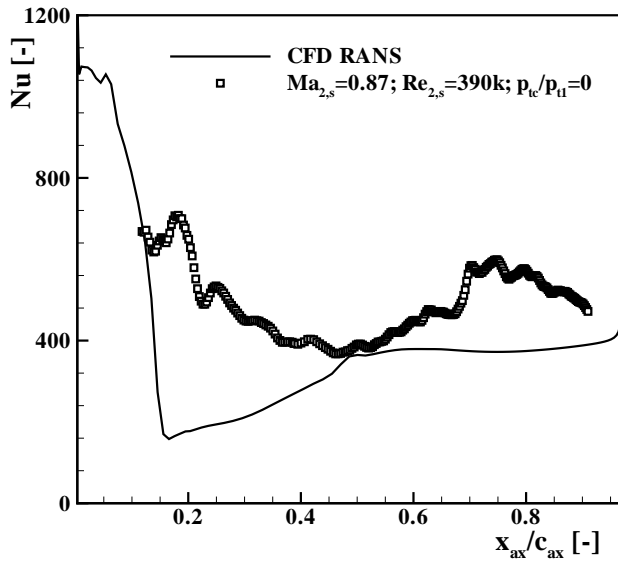
Figure 6.16: Nusselt number on the *T120C* blade at design flow conditions without film cooling, simulation (RANS and DES) and measurement

Since the DES-model shows still some difficulties in predicting correctly the flow in the separation bubble, LES was run on a fully unstructured grid. The simulation with LES is very cost intensive in terms of calculation costs and some compromises had to be made on the grid resolution in order do obtain a solution in a reasonable time. Therefore the resolution in the near wall region is not ideal and upstream of the separation point on the pressure side the y^+-values are of about 5, which limits the accuracy of flow separation prediction. Nevertheless some improvements can be obtained with the LE simulation. As shown in fig. 6.17 the vortex separation frequency is higher with this kind of simulation and a time interval of about $3 \cdot 10^{-4}$ is found for the vortex shedding. This gives a frequency of $3333\,\text{Hz}$ which is 23% higher than the measured.

The high frequency vortex shedding is reflected also in the velocity profiles of fig. 6.18. There the average velocity and the envelope of the extreme values for the LE simulation are compared to the measured velocity at the five traverse positions. At the first two traverse positions, the differences to the other simulations and the variations in time are small. The variations from the simulation are increased at $x_{ax}/c_{ax} = 0.18$, but the grid resolution seems to be too small in order to fetch all the flow structures close to the separation line. Farther downstream and especially at the last traverse position, the previously explained unsteady behaviour is found with a continuous decrease of the average velocity towards the wall and without explicit flow separation.

The reflection of this behaviour on the heat transfer is seen in fig. 6.19(a) where the measured Nusselt number along the blade axial chord is compared to the results from LES with the envelope of the extreme values. The three models are compared in fig. 6.19(b). The LES does better in calculating the heat transfer than do the other models. The flow separation is predicted too far upstream, probably due to limited grid resolution near the wall. The predicted heat transfer inside the separation bubble is higher with LES due to turbulent mixing and the local peak is shifted upstream of the reattachment point. Continuing in flow direction the heat

(a) $t = 0.0 \cdot 10^{-4}$ s

(b) $t = 0.5 \cdot 10^{-4}$ s

(c) $t = 1.0 \cdot 10^{-4}$ s

(d) $t = 1.5 \cdot 10^{-4}$ s

(e) $t = 2.0 \cdot 10^{-4}$ s

(f) $t = 2.5 \cdot 10^{-4}$ s

(g) $t = 3.0 \cdot 10^{-4}$ s
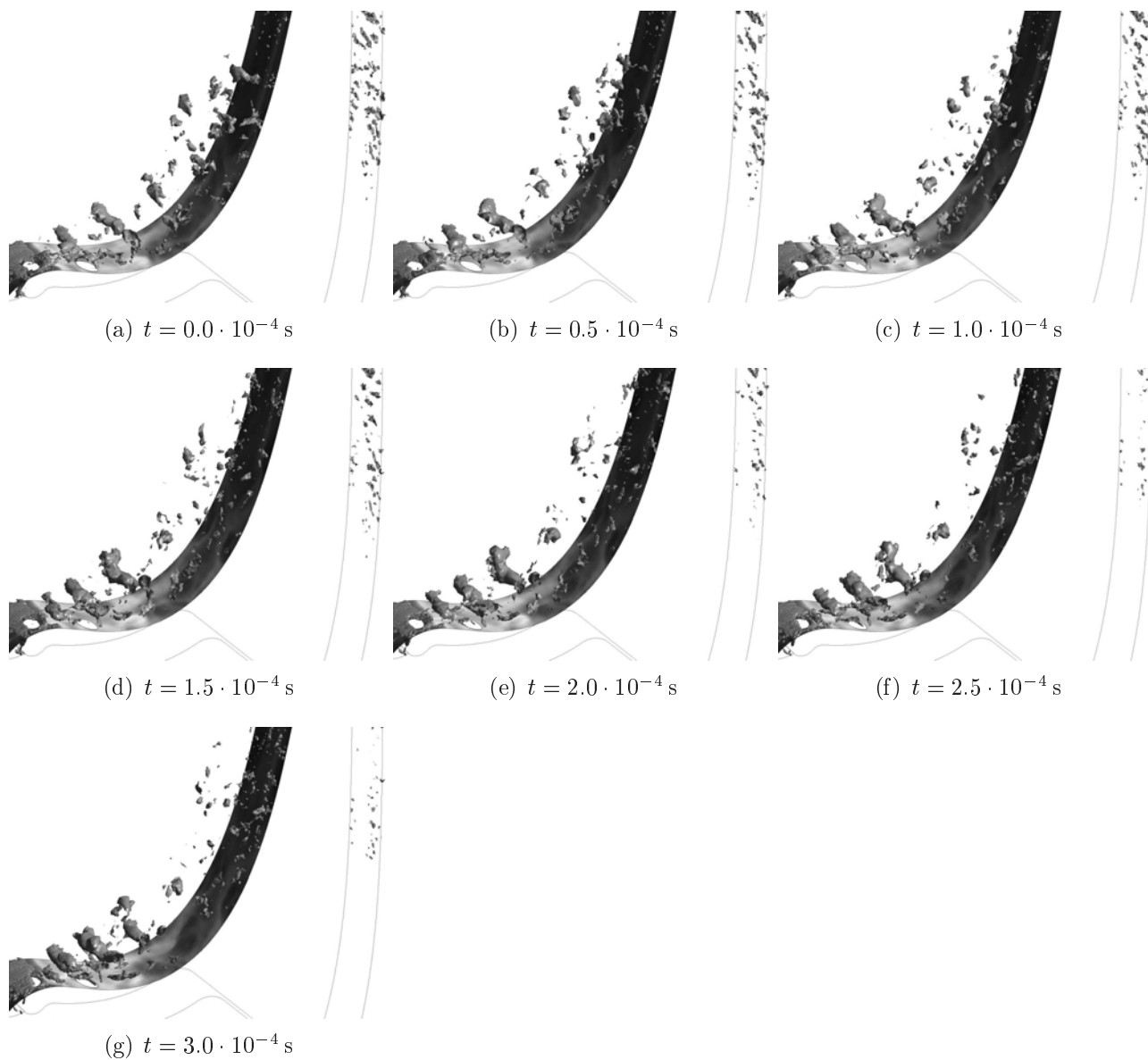
Figure 6.17: Iso-surface for constant swirl normal to blade span on the pressure side for one period — from LES

(a) $x_{ax}/c_{ax} = 0.1$ (b) $x_{ax}/c_{ax} = 0.15$ (c) $x_{ax}/c_{ax} = 0.18$ (d) $x_{ax}/c_{ax} = 0.3$ (e) $x_{ax}/c_{ax} = 0.5$

Figure 6.18: Boundary layer velocity profiles on the *T120C* blade from measurements and LES at $Ma_{2,s} = 0.87$, $Re_{2,s} = 390\,k$, maximum and minimum values of simulation with dashed lines

(a) Large eddy simulation and measurement (b) Different simulation models and measurement
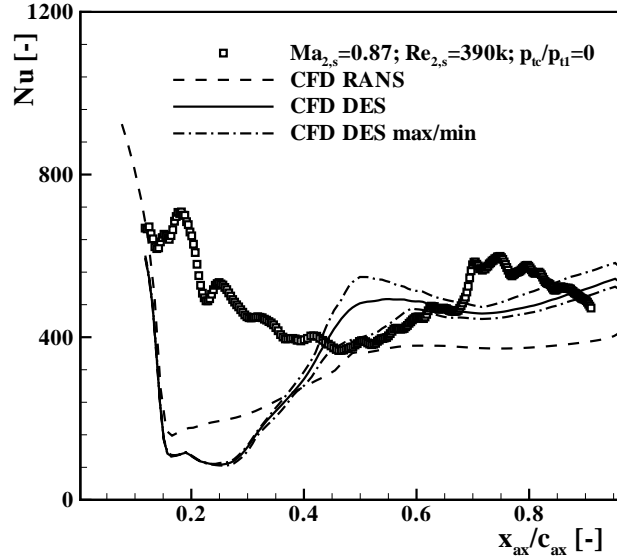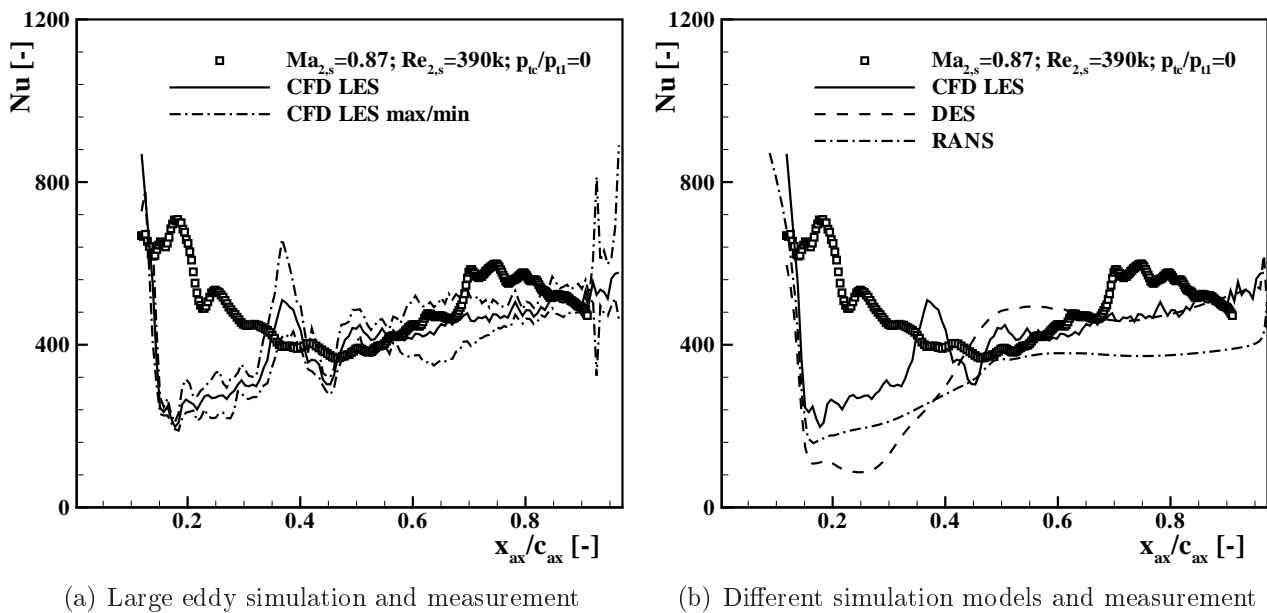
Figure 6.19: Nusselt number on the *T120C* blade at design flow conditions without film cooling, from simulations and measurement

transfer first decreases as in the measurements and increases again after flow reattachment followed by a plateau towards the trailing edge. Though the simulation is not ideal, some basic features are captured. Improvements are expected by increasing the grid resolution towards the wall which would increase the grid elements by some factors. Also the definition of more detailed boundary conditions at the inlet should improve the quality of the simulation. Unfortunately, so far no information is present for the structures of the free stream turbulence at the inlet plane.

6.1.1 Influence of Film Cooling

The influence of film cooling on the local scaled Nusselt number is visible in fig. 6.20(a) for design exit Mach and Reynolds numbers. The heat transfer increases close to the ejection locations due to the disturbances brought in by the cooling jets. An effect widely observed in publications e. g. in Horton et al. [82] or Mick and Mayle [110]. The influence of the film cooling decreases further downstream as reported in Mehendale and Han [103]. At the lowest coolant pressure ratio changes are perceived especially downstream of the second film cooling row indicating preferred ejection of coolant from this row. At the two highest blowing ratios the heat transfer reaches its peak close to both ejection holes and only little differences are seen at this location between both pressure ratios.

At the higher Reynolds number in fig. 6.20(b) the same effects are seen. At low coolant pressure ratio the heat transfer is enhanced downstream of the second row and inside the separation zone. Increasing the pressure ratio to $p_{tc}/p_{t1} = 1.09$ has a strong effect on local heat transfer close to the holes and at the reattachment line. At $x_{ax}/c_{ax} \approx 0.55$ the effect of the jet striking on the opposite wall is seen. A schematic of the streamlines is drawn in fig. 6.21. When the coolant jets have a high momentum ratio they are likely to detach and strike the wall farther downstream due to the concave curvature.

At the higher exit Mach number of 0.95 the impact of film cooling close to the ejection locations is similar to the previous as is shown in fig. 6.20(c). With film cooling the heat transfer remains at a relatively high level up to the kink of the curves at $x_{ax}/c_{ax} \approx 0.7 \ldots 0.8$. Only at this point the three curves have approximately the same values, a sign that at the high Mach number the flow inside the separation bubble is less turbulent. This is also reflected in the lower Nusselt number compared to the design case without film cooling.

The spanwise averaged adiabatic film cooling effectiveness for the three main flow conditions is plotted in fig. 6.22. The effectiveness values are scaled by η_{ref} which is the average effectiveness for the design operation conditions at a pressure ratio of $p_{tc}/p_{t1} = 1.09$. One can see that independently from the operation poin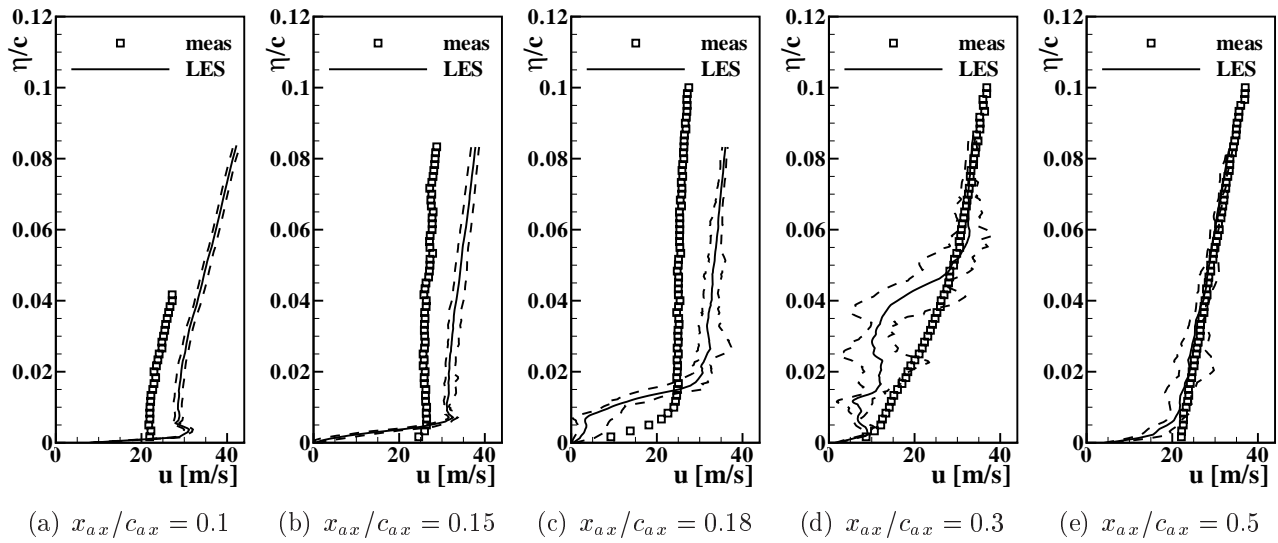t a zone of major film cooling effectiveness is seen at about mid-chord. This effect is stronger at higher pressure ratios. This is due to the jet striking on the concave surface as seen also in the heat transfer measurements and explained with the schematic in fig. 6.21. As shown in Gomes and Niehuis [75] the distribution of the adiabatic film cooling effectiveness agrees well with the measurements of Schwarz and Goldstein [126] on concave surfaces. Downstream of the jet impact region the coolant diffuses into the main flow. Close to the ejection locations the adiabatic film cooling effectiveness is rather low. This is especially true for the first cooling row and is a clear indication of jet detachment. Since the momentum ratio is for all cases larger than unity the jet detachment and reattachment farther downstream is an expectable behaviour according to Ito et al. [85]. Downstream of
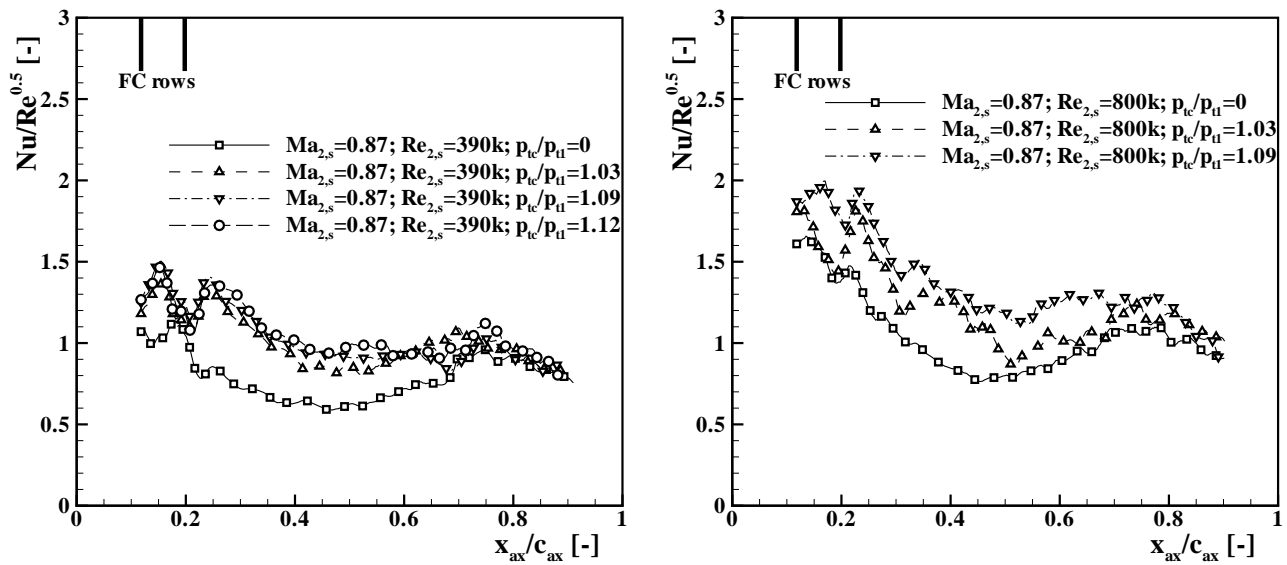
(a) $Ma_{2,s} = 0.87$, $Re_{2,s} = 390\,k$
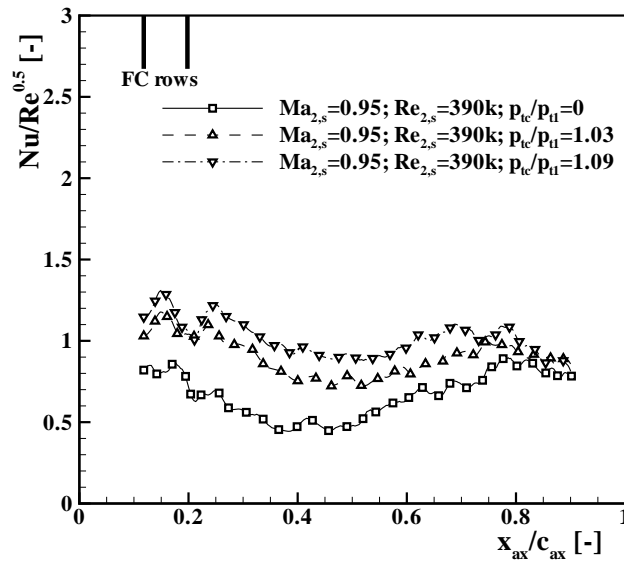
(b) $Ma_{2,s} = 0.87$, $Re_{2,s} = 800\,k$

(c) $Ma_{2,s} = 0.95$, $Re_{2,s} = 390\,k$

Figure 6.20: Nusselt number scaled by Reynolds number on the *T120C* blade with steady inflow
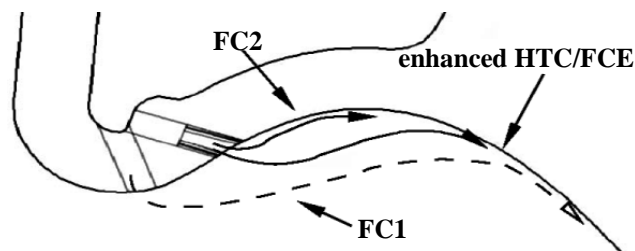
Figure 6.21: Schematic of the streamlines of the film cooling jets
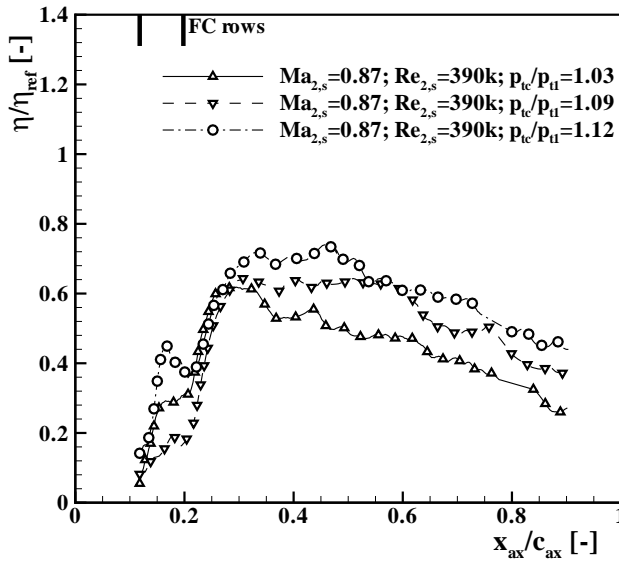
(a) $Ma_{2,s} = 0.87$, $Re_{2,s} = 390\,k$
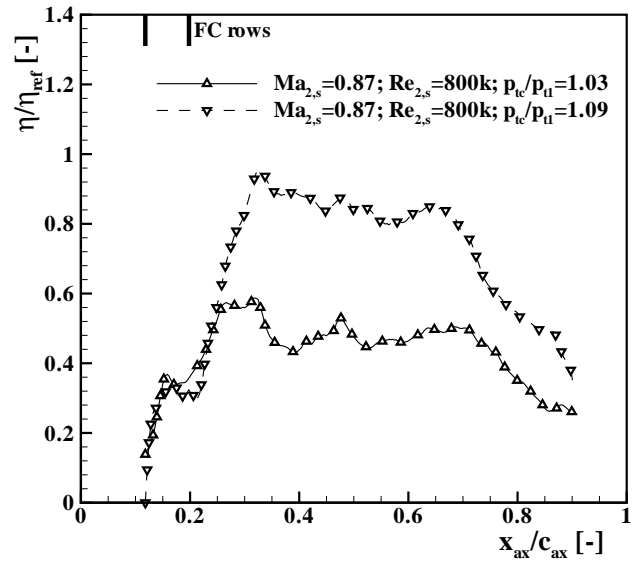
(b) $Ma_{2,s} = 0.87$, $Re_{2,s} = 800\,k$
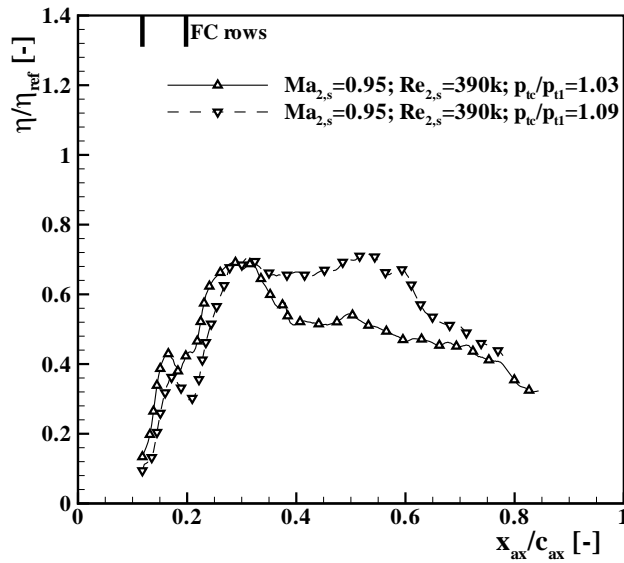
(c) $Ma_{2,s} = 0.95$, $Re_{2,s} = 390\,k$

Figure 6.22: Normalized adiabatic film cooling effectiveness on the *T120C* blade with steady inflow
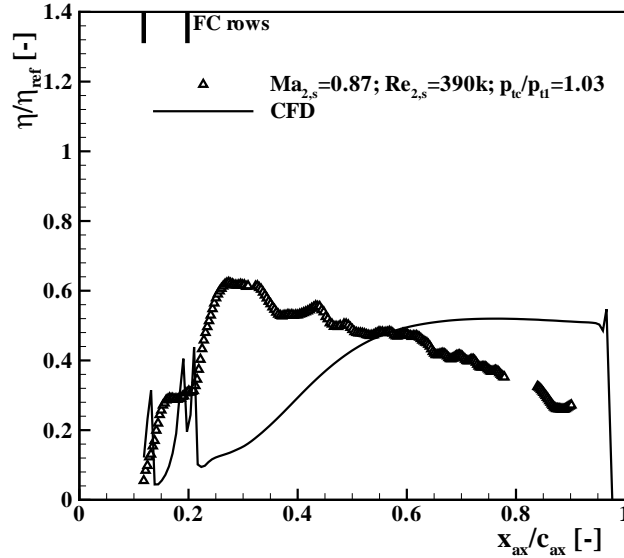
Figure 6.23: Measured and simulated spanwise averaged adiabatic film cooling effectiveness on the $T120C$ blade at $\mathrm{Ma}_{2,s} = 0.87$, $\mathrm{Re}_{2,s} = 390\,\mathrm{k}$, $p_{tc}/p_{t1} = 1.03$

the second film cooling row at $x_{ax}/c_{ax} = 0.2$ the film cooling effectiveness is too high to have normal jet separation, comparing to measurements of Colban et al. [30]. But as the authors also show, film cooling effectiveness is enhanced inside the jet detachment zone with higher flow turbulence. In their case shower head film cooling upstream of the fan-shaped holes trips the boundary layer into turbulent and increases therefore the film cooling effectiveness close to the fan-shaped holes. In the case of the $T120C$ blade the above mentioned vortex shedding at the separation line increases the turbulence of the flow which is seen in the boundary layer traverses and in the heat transfer results.

The RANS simulation with SST turbulence model gives quite different results. In fig. 6.23 the measured and simulated film cooling effectiveness is plotted for the design exit Mach and Reynolds number at a coolant to main flow total pressure ratio of 1.03. The simulation is carried on the 3D mesh with one cooling hole pitch and the results are area averaged in spanwise direction of the blade. The simulation predicts detached jets with the jets striking the surface at about mid chord. This is visible on the low effectiveness shortly downstream of the film cooling holes and the high effectiveness at about mid-chord. Downstream of the flow reattachment the mixing process between coolant and main flow is nearly not existent and the effectiveness stays at the same level. Also inside the separation bubble the predicted turbulent mixing is too low due to the reasons mentioned above. Duchaine et al. [48] show that the LES method is capable of predicting the turbulent mixing inside the separation bubble and the coolant diffusion towards the trailing edge. With their simulations on the $T120D$ blade, which is similar to the $T120C$ but has a different film cooling configuration, they obtain good agreement between simulation and measurement.

The two dimensional distribution of the adiabatic film cooling effectiveness for the same operation point is shown in fig. 6.24. One can see, that the simulation predicts very little cooling downstream of the bores and little mixing of coolant and main flow in spanwise direction. The

(a) Simulation

(b) Measurement
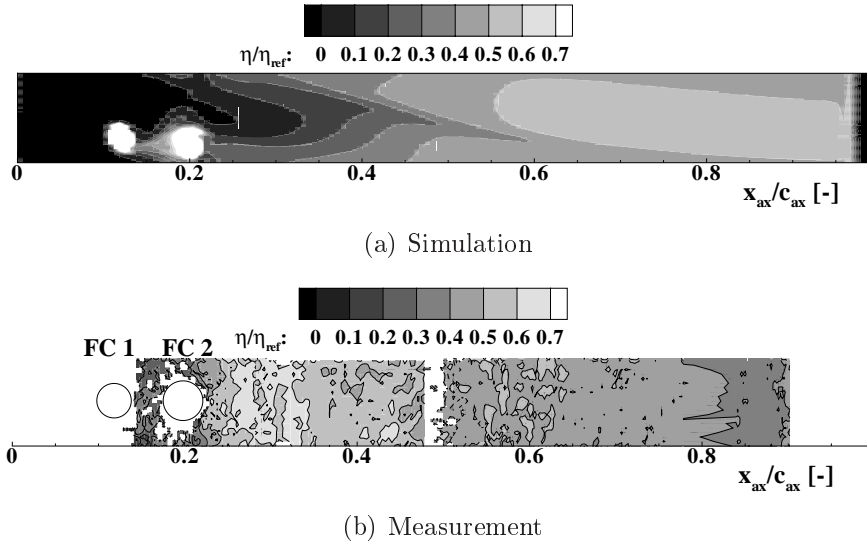
Figure 6.24: Simulated and measured adiabatic film cooling effectiveness on the T120C blade at $\mathrm{Ma}_{2,s} = 0.87$, $\mathrm{Re}_{2,s} = 390\,\mathrm{k}$, $p_{tc}/p_{t1} = 1.03$ as 2D plot

streaks of low cooling besides the cooling holes penetrate very deep in axial direction and even at the jet impact location the mixing of coolant with main flow is too low. From the measurements one can see the spot of highest film cooling effectiveness to be close to the second film cooling row. Also the spanwise distribution is much more homogeneous when the jet hits the surface as also seen in Goldstein and Stone [72] or Schwarz and Goldstein [126].

The overall effect of film cooling on a non adiabatic wall can be seen in fig. 6.25 for all three operation points. Using the temperature difference ratio $\Delta T_0/\Delta T_c$ as defined with eq. (4.57), one can derive different optimal blowing ratios than using the adiabatic film cooling effectiveness. For the design main flow conditions in fig. 6.25(a) one can see that film cooling has a negative effect throughout most of the blade. Especially close to the ejection locations and inside the separation bubble the heat transfer enhancement caused by film cooling is too high to be compensated by the cooling effect of the secondary flow. Only downstream of the reattachment line an overall cooling effect is seen, since the heat transfer values do not diverge too much with film cooling relative to the uncooled case.

At the high exit Reynolds number in fig. 6.25(b) one can see an overall better cooling effect using the temperature difference ratio parameter. Close to the first film cooling hole $\Delta T_0/\Delta T_c$ is smaller unity for the lower pressure ratio while it increases with higher blowing ratio due to increased heat transfer and almost no changes in adiabatic film cooling effectiveness. But downstream of the second film cooling row and due to the strongly increased adiabatic film cooling effectiveness one obtains better cooling performance at a higher coolant pressure. In comparison with the design case, one can state that the overall cooling performance is better at high Reynolds number. This is due to the absolutely and relatively increased heat transfer without film cooling at $\mathrm{Re}_{2,s} = 800\,\mathrm{k}$ due to the higher kinetic energy level inside the boundary layer. An increase in turbulence due to the film cooling will not increase the heat transfer in the same ratio as in the low Reynolds number case, since the increase of heat transfer with turbulence of the flow is not linear, see e. g. Radomsky and Thole [115] or Ekkad et al. [55].
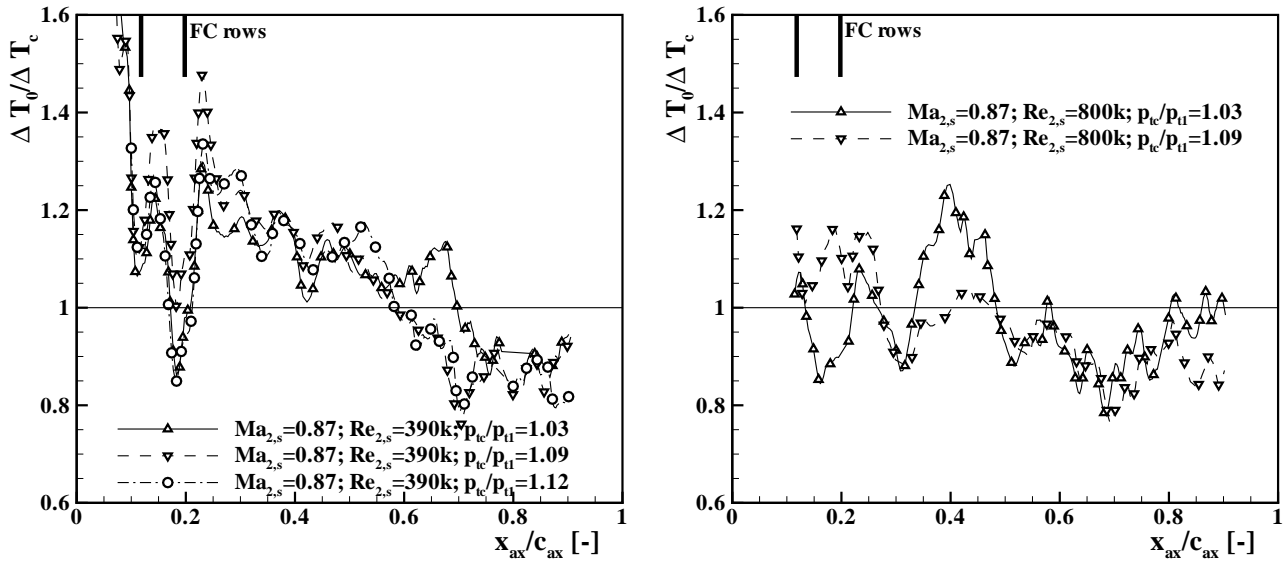
(a) $Ma_{2,s} = 0.87$, $Re_{2,s} = 390\,k$
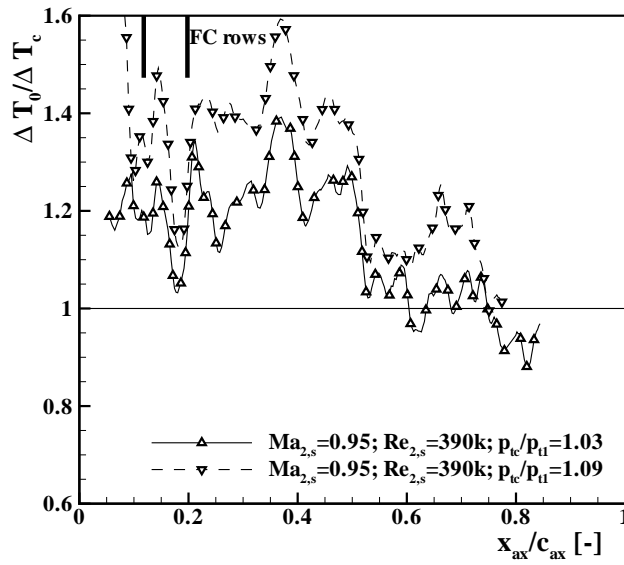
(b) $Ma_{2,s} = 0.87$, $Re_{2,s} = 800\,k$

(c) $Ma_{2,s} = 0.95$, $Re_{2,s} = 390\,k$

Figure 6.25: Temperature difference ratio on the *T120C* blade with steady inflow

(a) constant h_0 (b) variable h_0
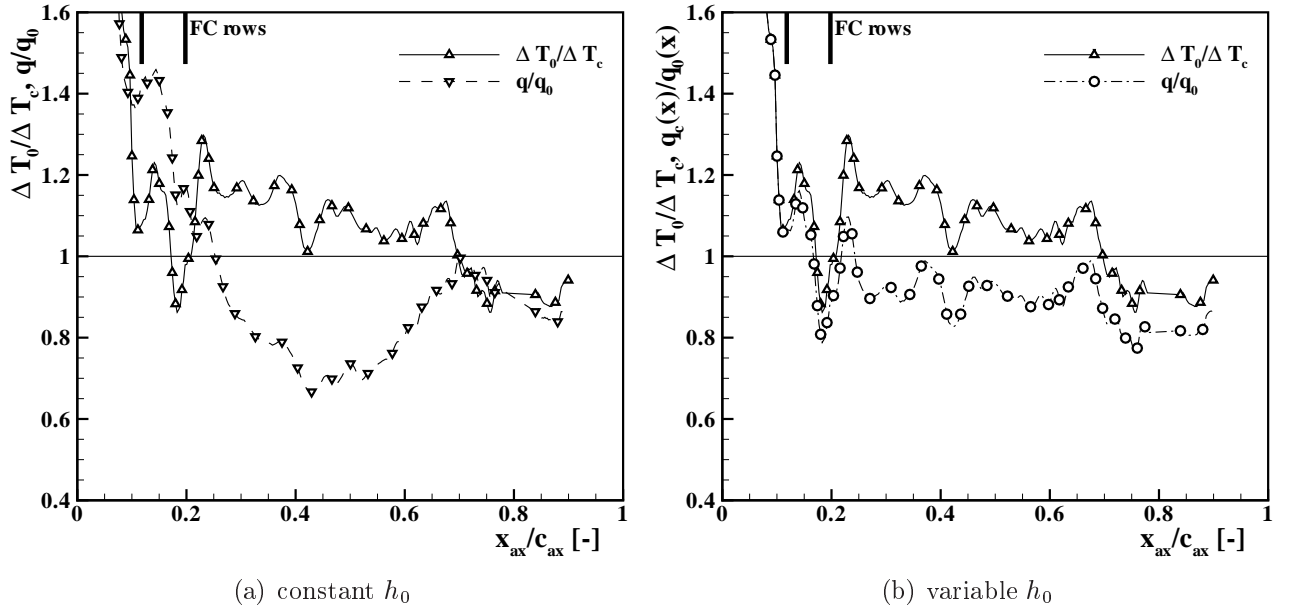
Figure 6.26: Comparison of temperature difference ratio and heat flux ratio on the *T120C* blade at $Ma_{2,s} = 0.87$, $Re_{2,s} = 390$ k, $p_{tc}/p_{t1} = 1.03$

Together with the relatively high adiabatic film cooling effectiveness levels an overall positive cooling effect is then seen throughout most of the blade chord at high Reynolds number.

For the high exit Mach number film cooling leads to worse performance inside the separation bubble. This is due to the relatively low levels of heat transfer verified for the uncooled case in the flow separation area. By using film cooling, the heat transfer can almost double as shown in fig. 6.20(c). The heat transfer increase is seen along almost the entire blade chord and the adiabatic film cooling effectiveness values are too low to compensate this increase. Therefore negative effect of film cooling is perceived for the entire blade chord and this is emphasized with higher coolant pressure.

A comparison between the widely used parameter heat flux ratio q/q_0 and the newly introduced parameter temperature difference ratio $(T_{r,0} - T_w)/(T_{r,c} - T_w)$ is presented in fig. 6.26. In the case of the heat flux ratio the use of constant coefficients leads almost to a shift of the curve of the adiabatic film cooling effectiveness but the shape is not significantly changed. Even by using the local heat transfer values $h_0(x)$ instead of a constant value, shown in fig. 6.26(b), the heat flux ratio would estimate too positively the cooling effect. This is for example true in zones with lower heat transfer coefficient since the convective cooling should be there more efficient than in areas with high heat transfer coefficient. This shows the deficits of using a constant value of the overall effectiveness φ, used in eq. (4.49).

6.1.2 Influence of Periodic Unsteady Inflow

The influence of periodic unsteady inflow on heat transfer is shown in fig. 6.27 as Nusselt number scaled by the Nusselt number for steady inflow. In general the heat transfer increases with periodic inflow at the second film cooling hole and inside the separation bubble. Only
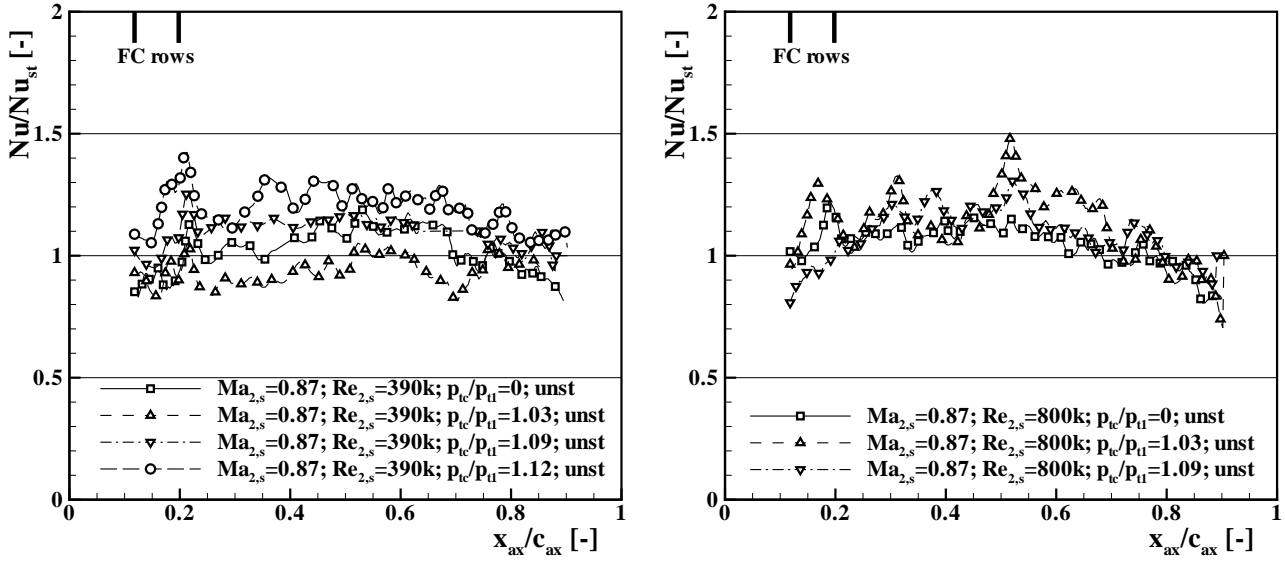
(a) $Ma_{2,s} = 0.87$, $Re_{2,s} = 390\,k$

(b) $Ma_{2,s} = 0.87$, $Re_{2,s} = 800\,k$
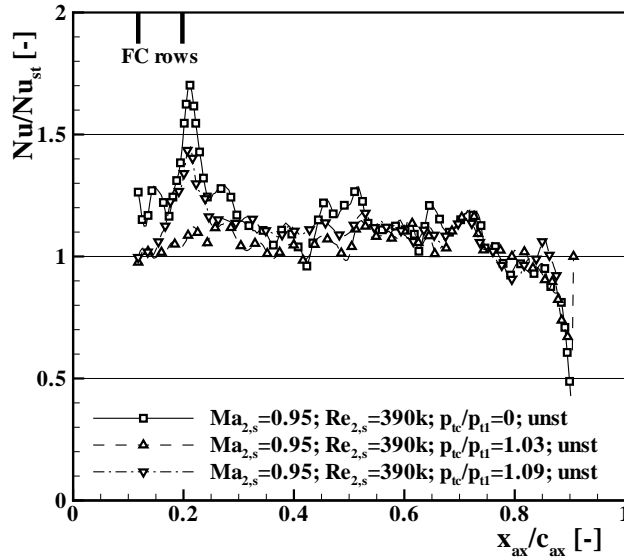
(c) $Ma_{2,s} = 0.95$, $Re_{2,s} = 390\,k$

Figure 6.27: Nusselt number on the *T120C* blade for periodic unsteady inflow scaled by values for steady inflow

towards the trailing edge the Nusselt number decreases with unsteady inflow. This effect is reported in Schobeiri et al. [122] and is explained by the calming process due to the incoming wakes. They measured the boundary layer velocity and RMS at different positions and the flow presents a separation bubble on the pressure side close to the leading edge. With periodic inflow the size of the separation bubble is more stable and the RMS values inside the boundary layer are lower. Therefore the turbulent mixing and heat transport is reduced farther downstream.

The effect of unsteady inflow is stronger for high coolant pressure ratio for all operation points especially inside the separation bubble. This is also a clear indication of separated jets at high blowing ratio. With the high turbulent wakes the mixing process of coolant jet with main stream is enhanced and the turbulent heat transport increased. For the lowest blowing ratio at design exit Mach and Reynolds number in fig. 6.27(a), the Nusselt number decreases with unsteady inflow. For more or less attached jets this is also seen by Womack et al. [160]. At the high exit Mach number the Nusselt number ratio is highest for the uncooled case because the heat transfer without film cooling and with steady inflow is very low inside the separation bubble.

The effect of periodic unsteady inflow on the adiabatic film cooling effectiveness is given in fig. 6.28. The comparison is done by the difference of the values with unsteady inflow and the ones for steady inflow scaled by the reference value η_{ref}. This form of comparison was chosen because the ratio between the film cooling effectiveness values is very sensitive at low values of FCE. This would lead partially to very large numbers which makes it difficult to compare the plots. In some plots at about mid-chord no values of film cooling effectiveness could be measured with unsteady inflow. The illumination with the bars passing in front of the camera was not ideal, so that the signal intensity was too low in order to get a good signal to noise ratio.

When analysing the plots, one should be aware that with unsteady inflow the coolant mass flow increases. The reason therefore is that the total pressure loss downstream of the bars leads to lower static pressure on the blade profile and hence a larger pressure drop between plenum chamber and blade surface. The effects of local static pressure variation on film cooling is extensively discussed in Abhari [1]. So one can expect better cooling with unsteady inflow, especially farther downstream, where the jets strike the surface. This is seen for almost all operation points from $x_{ax}/c_{ax} = 0.4$ on up to the trailing edge. Inside the separation bubble it is more difficult to predict the effects of the turbulent wakes. On the one hand turbulent mixing can deteriorate film cooling effectiveness when without wakes the effectiveness is rather high. On the other hand, in case of detached jet, some coolant can be driven towards the surface by the wakes increasing the adiabatic film cooling effectiveness. For the design exit Mach and Reynolds numbers latter is the case close to the film cooling holes, though the effect is rather weak as is shown in fig. 6.28(a). For the high exit Reynolds number, coolant blowing at lower pressure ratio is strongly enhanced with periodic wakes leading to higher effectiveness at mid-chord. The strong effect of the periodic wakes at this pressure ratio was already seen in the heat transfer results with strongly increased Nusselt numbers at the ejection and surface striking locations. At the higher pressure ratio the adiabatic film cooling effectiveness is increased close to the ejection location where the jet was separated but rapidly decreases shortly downstream. There the effectiveness was relatively high with steady inflow and the turbulent wakes mix the coolant with the hot main flow reducing the film cooling effectiveness.

At the high exit Mach number in fig. 6.28(c), the influence of the unsteady inflow can be
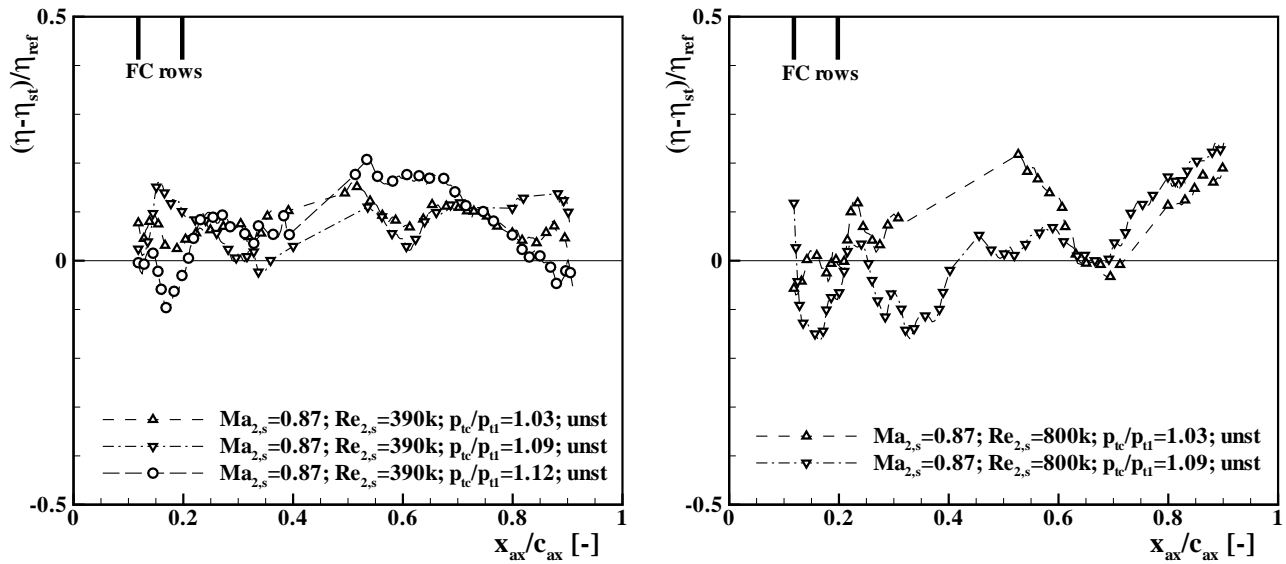
(a) $Ma_{2,s} = 0.87$, $Re_{2,s} = 390\,k$
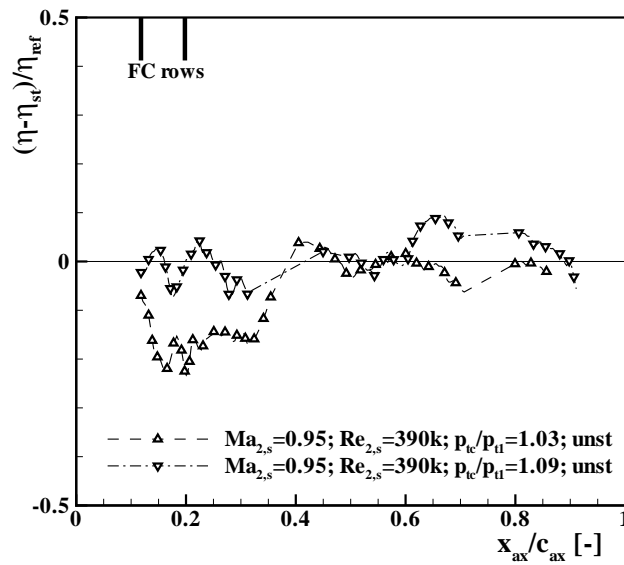
(b) $Ma_{2,s} = 0.87$, $Re_{2,s} = 800\,k$

(c) $Ma_{2,s} = 0.95$, $Re_{2,s} = 390\,k$

Figure 6.28: Difference of the adiabatic film cooling effectiveness on the $T120C$ blade for periodic unsteady inflow and steady inflow
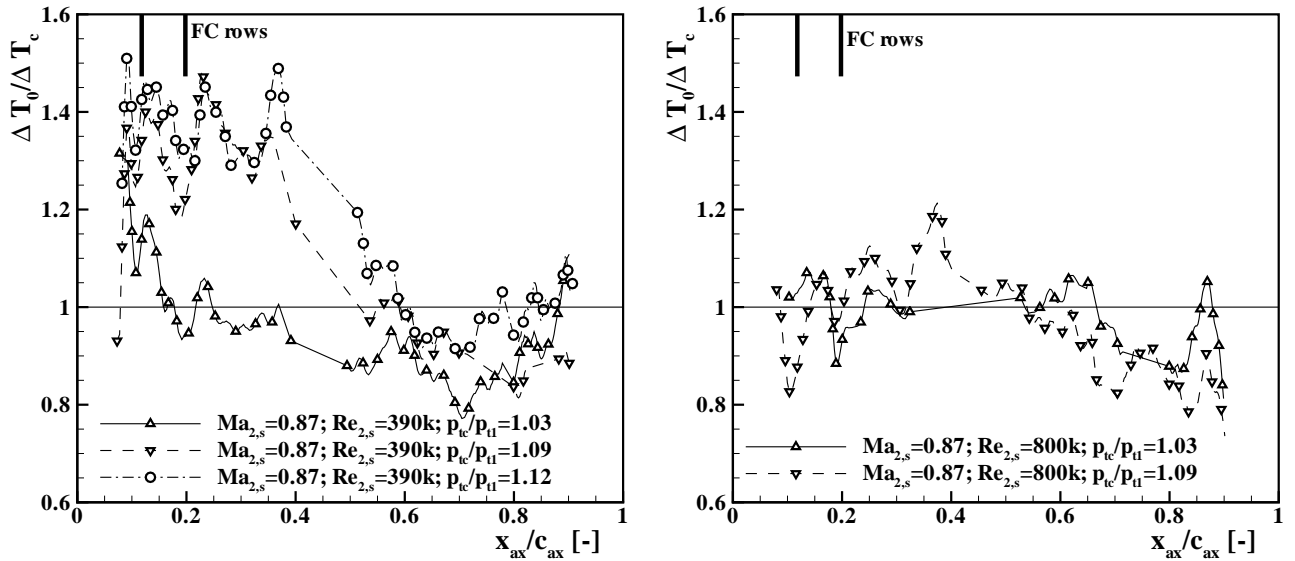
(a) $Ma_{2,s} = 0.87$, $Re_{2,s} = 390\,k$

(b) $Ma_{2,s} = 0.87$, $Re_{2,s} = 800\,k$
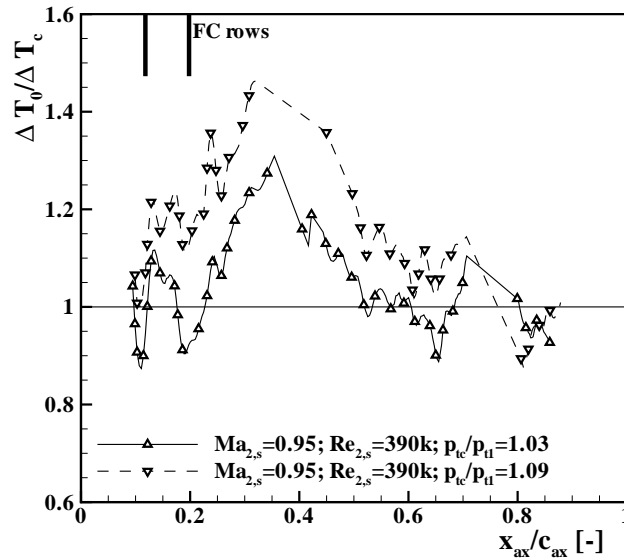
(c) $Ma_{2,s} = 0.95$, $Re_{2,s} = 390\,k$

Figure 6.29: Temperature difference ratio on the *T120C* blade with unsteady inflow

seen at lower pressure ratio inside the flow separation zone. With steady inflow the jets stay attached and relatively high effectiveness was seen close to the ejection location followed by a rapid decrease. With turbulent mixing the cooling is deteriorated close to the holes, but some improvement is seen further downstream where the jets hit the blade due to the greater mass flow. For the higher pressure ratio the effects of the wakes are small .

The effect of film cooling on a non-adiabatic blade with unsteady inflow is analysed with the temperature difference ratio for all operation points in fig. 6.29. Also with unsteady inflow a reduction in temperature difference is observed with film cooling inside the separation bubble since the heat transfer increases with film cooling. At lower pressure ratio and towards the

trailing edge, however, a positive effect of film cooling is observed. Also here at high Reynolds number the temperature difference ratio is less sensitive inside the flow separation zone. At higher exit Mach number and especially inside the flow separation region, film cooling is shown to result in a temperature difference ratio higher than unity over almost the entire blade chord.

6.1.3 Summary of the Analysis on the Pressure Side

The experimental and numerical analysis on the pressure side of the *T120C* blade showed that the flow separation process is highly unsteady and complex. High turbulence is seen inside the separation bubble. Eddies separate from the leading edge and move downstream up to the point where they hit the surface due to the curvature of the same. These eddies enhance greatly the fluid exchange inside the bubble and increase the heat transfer. The periodic separation and convection of the eddies also increase the heat transfer further downstream towards the trailing edge. While the boundary layer is expected to relaminarize with the high flow acceleration after reattachment and to calm, the excitation by the eddies keeps the boundary layer turbulent up to the trailing edge.

The high turbulence levels present inside the separation bubble increase also the adiabatic film cooling effectiveness close to the ejection locations. The momentum ratios are quite large, since the main flow velocity is very low close to the leading edge at the pressure side. Therefore the jets are likely to detach which should lead to low effectiveness values close to the holes. The mixing process increases the FCE, since some coolant is driven towards the surface, and is responsible for a quite uniform spanwise distribution of the coolant.

Periodic unsteady inflow increases in some extend the heat transfer for the uncooled blade. Using film cooling, the heat transfer increase is not as strong as in the uncooled case and the wakes can even lower the heat transfer for some configurations. The influence of unsteady inflow on the adiabatic film cooling effectiveness is twofold. In regions with jet separation the FCE can increase due to better mixing of coolant with the main flow. In other cases, where the FCE is rather high with steady inflow, the turbulent wakes deteriorate the FCE.

Analysing the overall effectiveness on a non-adiabatic wall with the temperature difference ratio showed that film cooling on the pressure side is problematic for such kinds of flows. The overall effectiveness decreased for most of the operation points over most of the area. Only after flow reattachment at mid-chord film cooling had a positive effect on the achievable flow temperatures. Inside the separation bubble, the heat transfer increase was too high and the film cooling effectiveness too low in order to allow an increase of the main flow temperature.

7 Aerodynamic Performance at Higher Loading

The pitch to chord ratio was increased for the *T120S* blade in order to reduce the number of blades per stage in a turbine. The Zweifel number is a blade loading parameter and gives the ratio of the circumferential force divided by the maximum force for constant velocity on the suction side U_2, see Scholz [123]. The Zweifel number is computed here with

$$\text{Zw} = \frac{(U_1 \cdot U_{1,ax} \cdot \rho_1 - U_2 \cdot U_{2,ax} \cdot \rho_2) \cdot t}{U_2^2/2 \cdot \rho_2 \cdot c_{ax}}. \tag{7.1}$$

The Zweifel number is dependent on the pitch to chord ratio and at design point increases from 1.33 for the *T120C* blade to 1.57 for the *T120S* blade. This leads to higher loading of the blade and at those high Mach numbers shock induced separation may occur at the suction side. In this chapter the aerodynamic performance of the blade at varying Mach and Reynolds numbers is analysed as well as the impact of film cooling and vortex generating jets (AJVG) on total pressure loss and flow separation.

7.1 Reference Measurements Without Secondary Flow

Wake traverse and measurements of the profile pressure distribution (PPD) were carried out for the three Mach and Reynolds number combinations without blowing off (FC or AJVG). The inlet conditions were measured with a 3D hot wire probe. For the three operation points the free stream turbulence level varied between 4.3 and 4.9% while the integral length scale was of 3.3 to 3.7 cm.

The Mach number distribution at mid-span for the design point at $\text{Ma}_{2,s} = 0.87$; $\text{Re}_{2,s} = 390\text{k}$ is plotted in fig. 7.1. The strong acceleration on the front part of the suction side is visible as well as the strong shock-wave at $x_{ax}/c_{ax} \approx 0.74$. The peak Mach number is not clearly localized due to the lack of pressure taps at this position, but it should be of about 1.4 at approximately half axial chord. The Mach number distribution shows a large separation on the suction side between $0.62 \leq x_{ax}/c_{ax} \leq 0.78$. The interaction length starts the latest at $x_{ax}/c_{ax} = 0.5$ and extends up to $x_{ax}/c_{ax} = 0.75$. Downstream of the shock location the flow is likely to reattach.

The isentropic Mach number on the blade for the three operation points is plotted in fig. 7.2 on the left. Focusing the interest on the suction side, the main differences are seen around the shock location. A detailed view of the Mach number distribution in this zone is given on the right of fig. 7.2. For $\text{Re}_{2,s} = 800\text{k}$ the separation upstream of the shock is clearly smaller or even almost vanished. Therefore the peak Mach number is shifted downstream, closer to the shock location, when compared to the design operation point. Comparing both curves for $\text{Ma}_{2,s} = 0.87$ after the shock, it seems that for lower Reynolds number the flow reattaches only later than $x_{ax}/c_{ax} = 0.8$. At $x_{ax}/c_{ax} = 0.84$ the pressure is equal for both operation points and the flow seems definitely to reattach before the trailing edge.

For $\text{Ma}_{2,s} = 0.95$ again a strong separation upstream of the shock is visible. It starts around $x_{ax}/c_{ax} = 0.6$ and the reattachment point is at first glance not clearly to recognize. Even a complete separation without reattachment might be possible. Comparing the static pressure measurements on the suction side for the three operation points it seems as if at low Reynolds
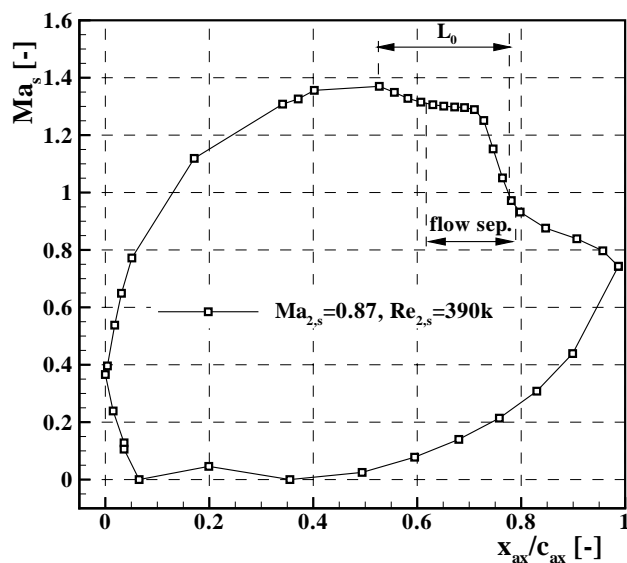
Figure 7.1: Isentropic profile Mach number distribution without FC or AJVG
at $Ma_{2,s} = 0.87$; $Re_{2,s} = 390k$
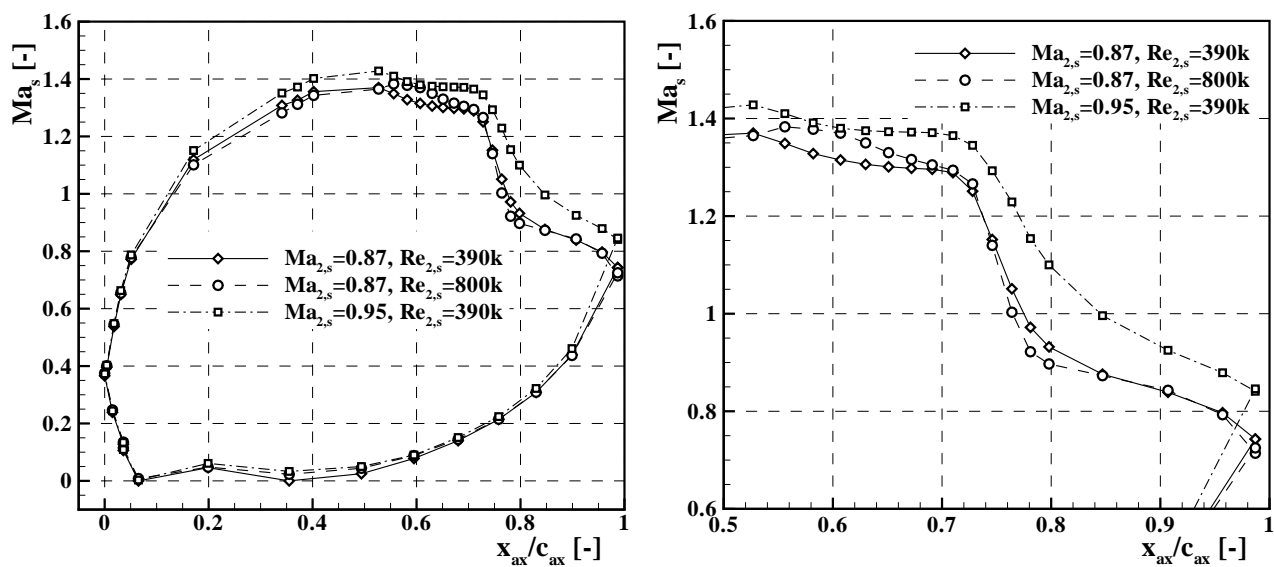
Figure 7.2: Isentropic profile Mach number distribution without FC or AJVG
for different Mach and Reynolds numbers complete (left) and
detail (right)
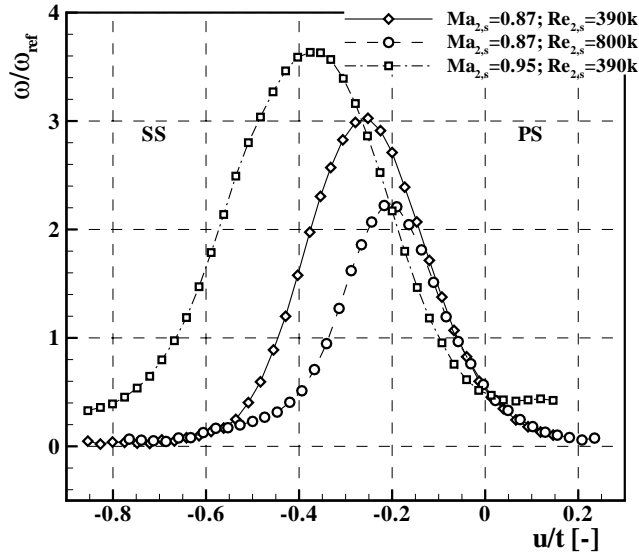
Figure 7.3: Total pressure loss without FC or AJVG at different operation points

number a laminar flow separation is present upstream of the shock. At high Reynolds number the separation is effectively suppressed due to previous boundary layer transition. At design Mach number the shock-wave might be not sufficiently strong to cause shock induced flow separation with higher Reynolds number.

For all operation points the static pressure at the trailing edge is higher than the chamber pressure. The reason therefore is the large supersonic pocket at the suction side extending to the next blade passage. After the trailing edge the flow accelerates to the chamber pressure.

The loss parameter ω/ω_{ref} for one blade pitch for all operation points without FC or AJVG is plotted in fig. 7.3. The reference value ω_{ref} is the average loss value for the design point without film cooling or AJVG. Large differences are seen in the losses for varying main flow exit conditions. For $Re_{2,s} = 800k$ the effect of much smaller or even no separation is reflected in much lower losses than for the design conditions. At the design point the losses increase towards the suction side due to the large separation at the shock location. For $Ma_{2,s} = 0.95$ the total pressure losses increase by a lot and the wake is shifted towards the suction side. Also here the possibility of detached flow at the suction side up to the trailing edge persists. The indications therefore are the shifting of the wake and the large loss increase. In contrast to the other two operation points, there is no undisturbed flow without losses at this distance from the trailing edge. The losses outside the wake could be due to the strong shock, which extends over the whole pitch.

A 2D RANS simulation with SST turbulence model and γ-θ transition model was carried out using CFX 11.0. The computed static pressure at the design operation point is given in fig. 7.4 by means of isentropic Mach number together with the measured values. The curve agrees quite well with the measurement, only the separation zones in the suction and pressure sides are not completely matched. At the outlet average values of $\omega_{sim}/\omega_{meas} = 0.986$ and $\beta_{2,sim} - \beta_{2,meas} = 0.91°$ are obtained. Simulations with the same mesh will later be used to compare predicted to measured heat transfer coefficients on the blade.
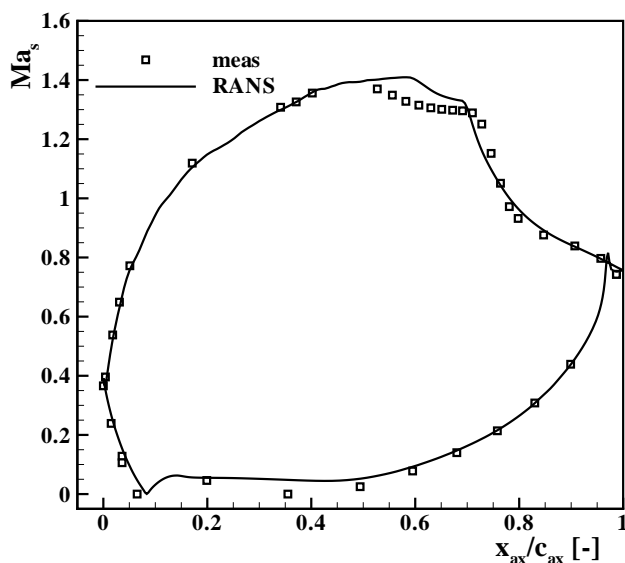
Figure 7.4: Isentropic Mach number on the *T120S* blade from RANS simulation and measurement for $Ma_{2,s} = 0.87$ and $Re_{2,s} = 390\,\mathrm{k}$
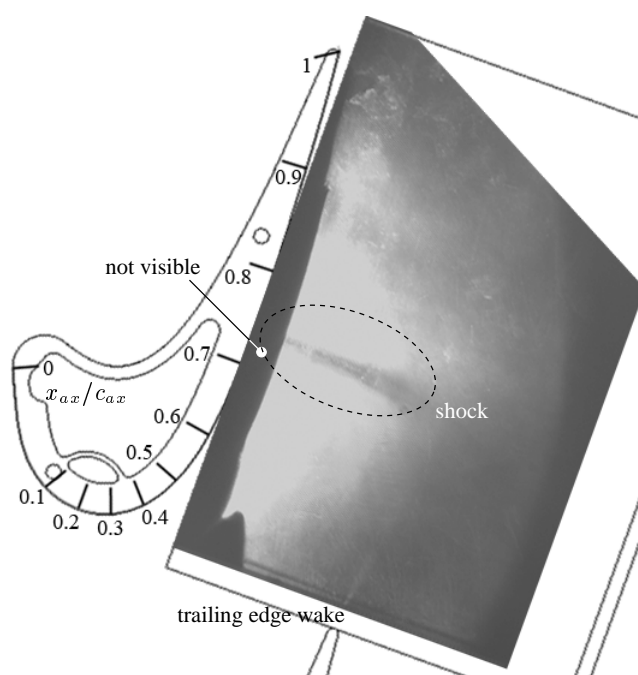
Figure 7.5: Schlieren picture of the suction side passage of the center blade for $Ma_{2,s} = 0.87$; $Re_{2,s} = 390\mathrm{k}$

A Schlieren picture at design conditions is shown in fig. 7.5. The location of the cascade is sketched around the Schlieren photograph and the relative axial coordinates are marked on the center blade. The near wall flow is not visible in this picture. Nevertheless the lambda foot of the shock seems to be not very large since it is completely covered by the tape used to seal the window. The shock is located at about $x_{ax}/c_{ax} \approx 0.74\ldots0.75$ and is almost perpendicular to the surface.
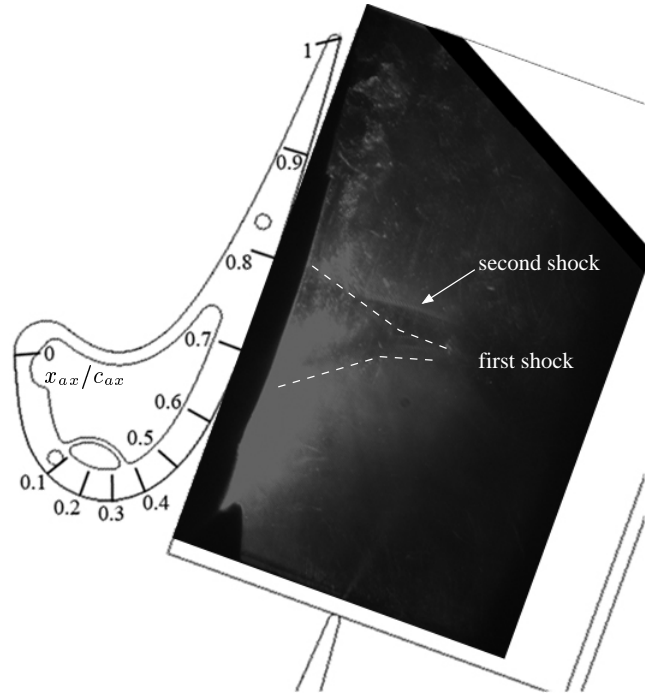
Figure 7.6: Schlieren picture of the suction side passage of the center blade
for $Ma_{2,s} = 0.95$; $Re_{2,s} = 390k$

At $Ma_{2,s} = 0.95$ the shape of the shock presents very different, as shown in fig. 7.6. The lambda foot (marked with dashed lines besides the schlieren) is very large and the influenced area extends from $x_{ax}/c_{ax} \approx 0.65$ to 0.8. This is consistent with the large influence length seen in the Mach number distribution and the smaller pressure gradient at the shock location, which indicates a thick boundary layer. Outside the boundary layer two shocks one at about $x_{ax}/c_{ax} = 0.76$ and a second one after re-expansion at $x_{ax}/c_{ax} = 0.8$ are visible.

7.2 Influence of the AJVG

The use of the AJVG is supposed to reduce the aerodynamic losses due to a reduction of the main flow separation bubble which can be very large as shown before. The design pitch ratio of the AJVG was set in studies from Doerffer et al. [42, 43] to $(t/D)_{AJVG} = 10$. In order to validate this optimized pitch on the *T120S* cascade three different pitches for the AJVG were tested at design main flow conditions. The tested pitches were $(t/D)_{AJVG} = 5$, 10 and 15. After these experiments the pitch for the remaining measurements was set to $(t/D)_{AJVG} = 10$.

The isentropic Mach number distribution on the blade is given in fig. 7.7 for the design main flow conditions and with varying AJVG pitch. For comparison the results from the reference case without AJVG are plotted as rectangular symbols. The differences are essentially in the region around the AJVG holes and the shock location. On the right of the figure a detailed view on the rear suction side is given. The shock moves upstream with the vortex generators in use. This shift of the location is increased with decreasing AJVG pitch and therefore stronger blowing. The interference length is significantly reduced and flow separation seems to be efficiently reduced. With a pitch ratio of 15 a small pressure plateau between $x_{ax}/c_{ax} = 0.64$
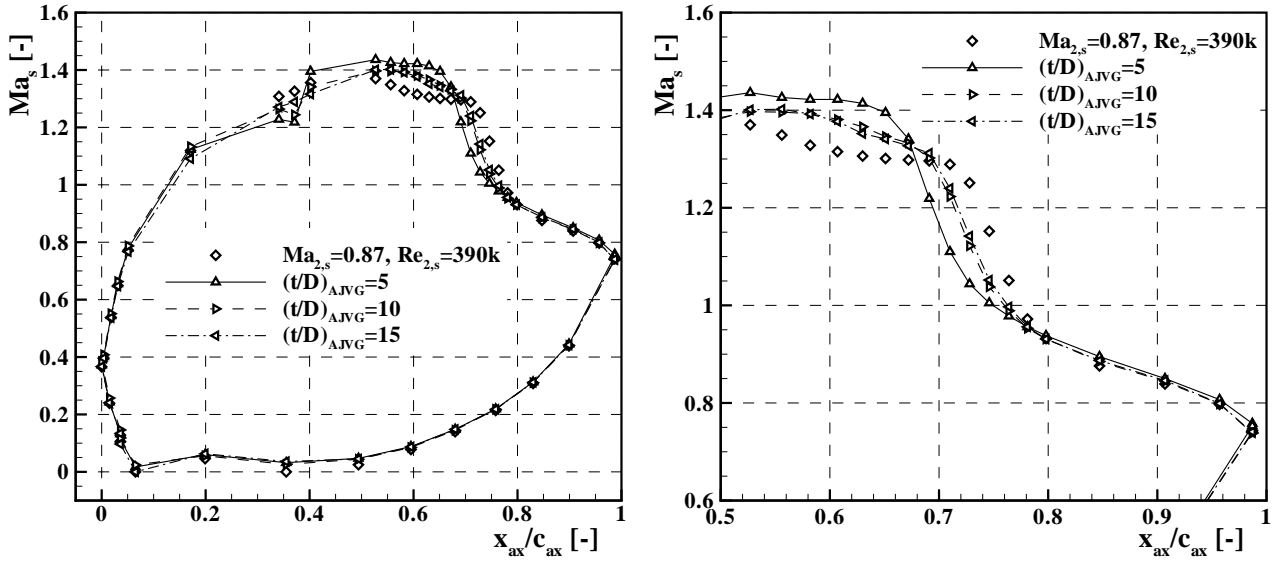
Figure 7.7: Isentropic Mach number distribution for $Ma_{2,s} = 0.87$; $Re_{2,s} = 390k$, with different AJVG pitches and without AJVG; Detail on the right
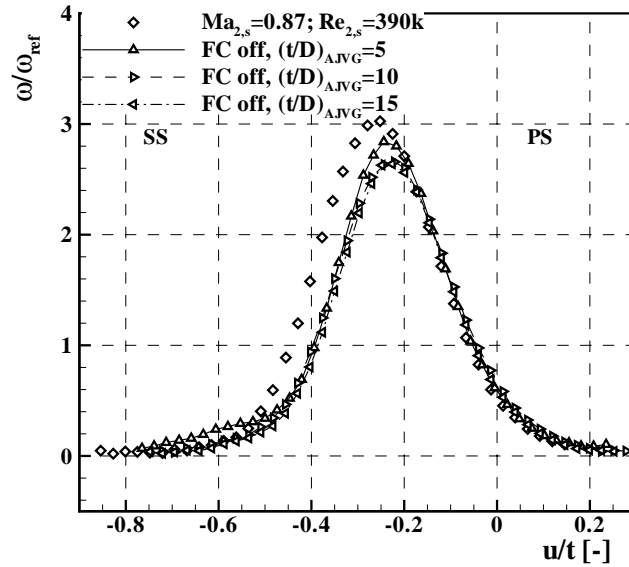
Figure 7.8: Total pressure loss coefficient for wake traverse at $Ma_{2,s} = 0.87$; $Re_{2,s} = 390k$ with AJVG at different pitches and without AJVG

and 0.7 indicates still a small separation. For the normalized pitch $(t/D)_{AJVG} = 10$ almost no indication of separation is seen, while at the smallest pitch the shock location moves significantly upstream. The pressure plateau seen for a $(t/D)_{AJVG} = 5$ at $0.56 \leq x_{ax}/c_{ax} \leq 0.62$ is rather an effect of the recirculating flow due to the vortices created. Blowing off at the smallest pitch also increases the peak Mach number leading to a stronger shock.

The profiles at the outlet of the total pressure loss coefficient ω/ω_{ref} for the design exit Mach
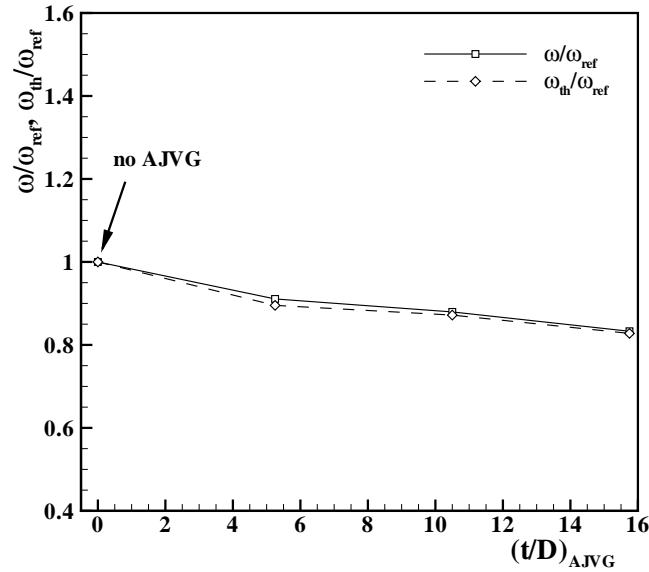
Figure 7.9: Integral total pressure and thermodynamic loss coefficients with AJVG at different pitches and without AJVG for $Ma_{2,s}$ = 0.87; $Re_{2,s} = 390k$

and Reynolds number for different AJVG pitches are plotted in fig. 7.8. The profile for the case without use of AJVG is plotted with rectangular symbols for comparison. A reduction of the losses using AJVG is clearly visible. For the smallest pitch of $(t/D)_{AJVG} = 5$ losses outside the wake for $u/t < -0.5$ are due to a strong shock as is seen on the PPD in fig. 7.7. The reduction of the separation bubble seen in the PPD is reflected in the reduction of the total losses at the suction side branch of the wake. Better performance seems to be given using $(t/D)_{AJVG} = 10$ and 15.

The integral values of the total pressure loss are plotted in fig. 7.9 for the same operation point and for different pitches of AJVG and without AJVG. The thermodynamic losses ω_{th}/ω_{ref} are plotted with dashed lines. The advantages in using AJVG is evident and is present for all pitches. Nevertheless the performance is enhanced with increasing pitch. The reason for a worse performance with the smallest pitch is the strong shock increasing the losses outside the wake and the stronger influence on the main flow applying a strong blockage on the flow. The best relation of reduction of the separation bubble with a minimization of the interference with the main flow seems to be given with a pitch ratio of $(t/D)_{AJVG} = 15$. Nevertheless, this pitch was not chosen for further studies, since the flow seems to be not homogeneous in spanwise direction, as will be discussed in the following.

The Schlieren pictures confirm the shift of the shock location and the increased shift with smaller AJVG pitch as seen in fig. 7.10.

Oil Flow Visualization for Different AJVG Pitches

The visualization of the near wall flow with oil-and-dye technique gives a qualitative impression of the 2D-effects of the vortex generators on the flow field and aid to assess the extension of the main flow separation.

(a) $(t/D)_{AJVG} = 5$

(b) $(t/D)_{AJVG} = 10$

(c) $(t/D)_{AJVG} = 15$
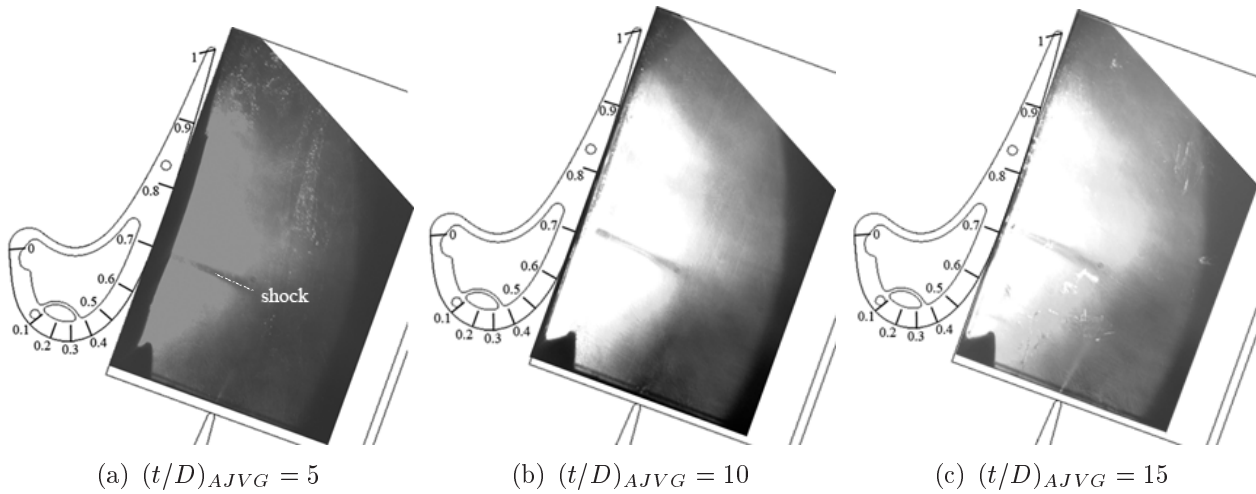
Figure 7.10: Schlieren pictures for $\mathrm{Ma}_{2,s} = 0.87$; $\mathrm{Re}_{2,s} = 390\mathrm{k}$ and AJVG with varying pitches
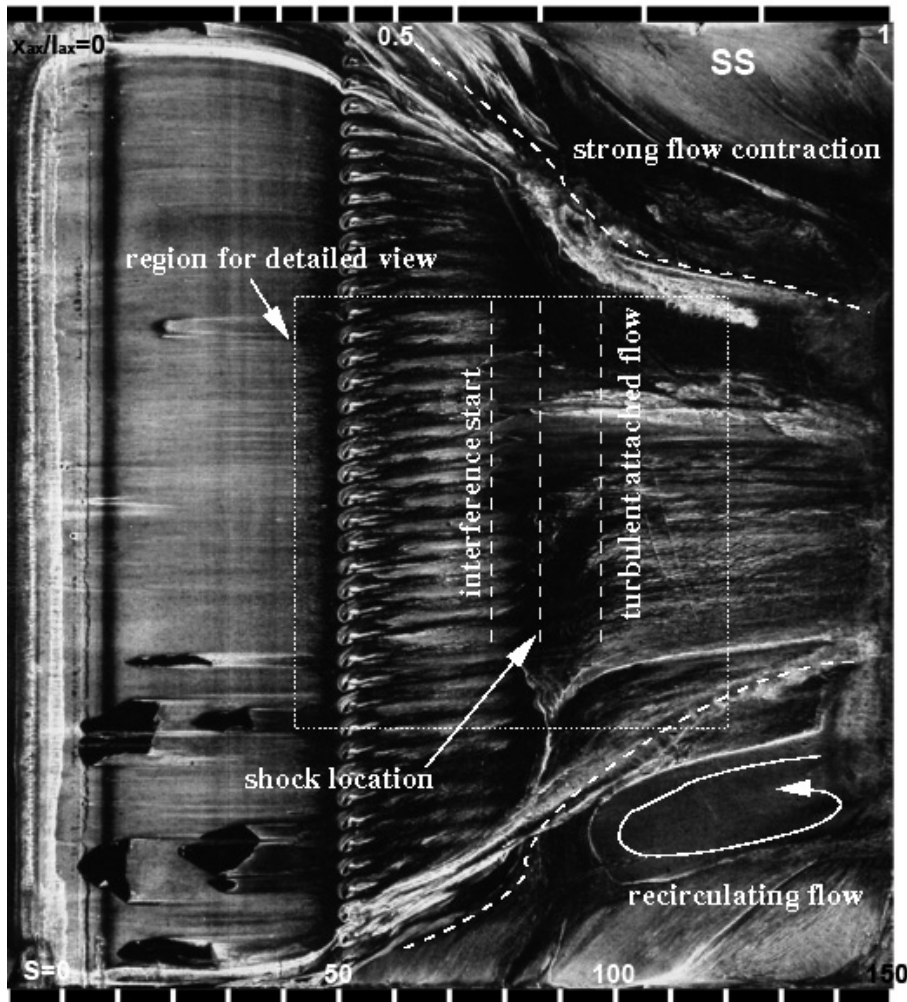
Figure 7.11: Near wall flow visualization of suction side for $\mathrm{Ma}_{2,s} = 0.87$; $\mathrm{Re}_{2,s} = 390\mathrm{k}$ and AJVG pitch ratio of 5
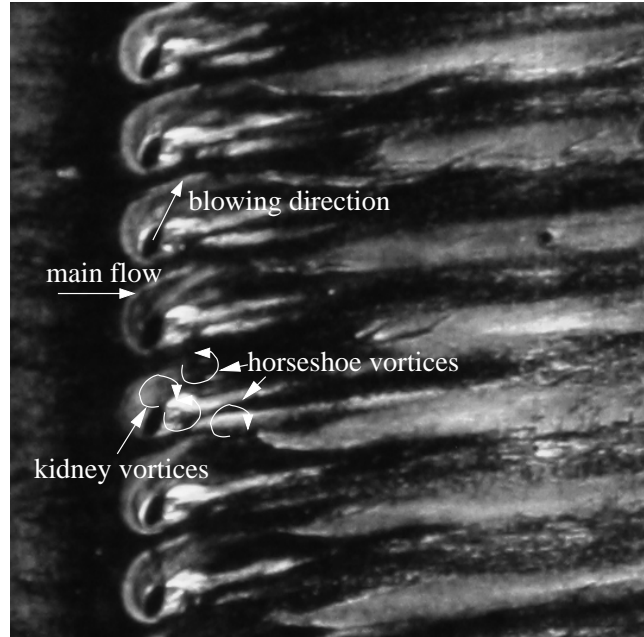
Figure 7.12: Detail from the blow off region of near wall flow visualization for $\mathrm{Ma}_{2,s} = 0.87$; $\mathrm{Re}_{2,s} = 390\mathrm{k}$ and $(t/D)_{AJVG} = 5$

An overview of the flow field on the suction side at $(t/D)_{AJVG} = 5$ is given in fig. 7.11 where the image of the unwrapped surface on the suction side is given. The AJVG have a strong influence on the 3D flow field. The flow contraction is visible in the picture along the dashed lines. The reason for this flow contraction are the secondary flow and the side wall boundary layer. The passage vortex seems to interact with the vortices from the AJVG. At the shock location of $x_{ax}/c_{ax} = 0.7$, the flow suffers a strong contraction which could have a contribution to the higher peak Mach number seen in the static pressure distribution. At the lower side of fig. 7.11 the passage vortex separates from the contracting flow after the shock and a large bubble with circulating flow is formed. At the upper part the passage vortex extends towards the centre of the blade and seems not to separate from the remaining flow as at the bottom. The direction of the swirl seems to play an important role for the strength of the flow contraction. The flow direction of the vortices near the wall point towards the top of the figure. Therefore the vectors near the wall of the passage vortex are accelerated by the swirls from the AJVG (vectors near the wall point into the same direction) while at the top their strength is weakened. The shock interference start is marked at $x_{ax}/c_{ax} \approx 0.65$ and at $x_{ax}/c_{ax} = 0.75$ the turbulent reattached flow is visible.

A closer look on the blow off region is given in fig. 7.12. Downstream of the holes a small dead water region is visible as well as the formation of kidney vortices. Upstream of the holes the supersonic flow suffers a shock due to the obstruction and a small separation forms. A horseshoe vortex forms and rolls up first besides the hole and afterwards under the kidney vortices similar to the observations of Wilfert [158].

At an AJVG pitch ratio of 10 the blockage of the main flow is reduced and leads to a different interaction of the different vortices. In fig. 7.13 the suction side of the near wall flow visualization for the design AJVG pitch is plotted. In contrast to the case with the smallest AJVG pitch

Figure 7.13: Oil flow visualization for $(t/D)_{AJVG} = 10$, SS view
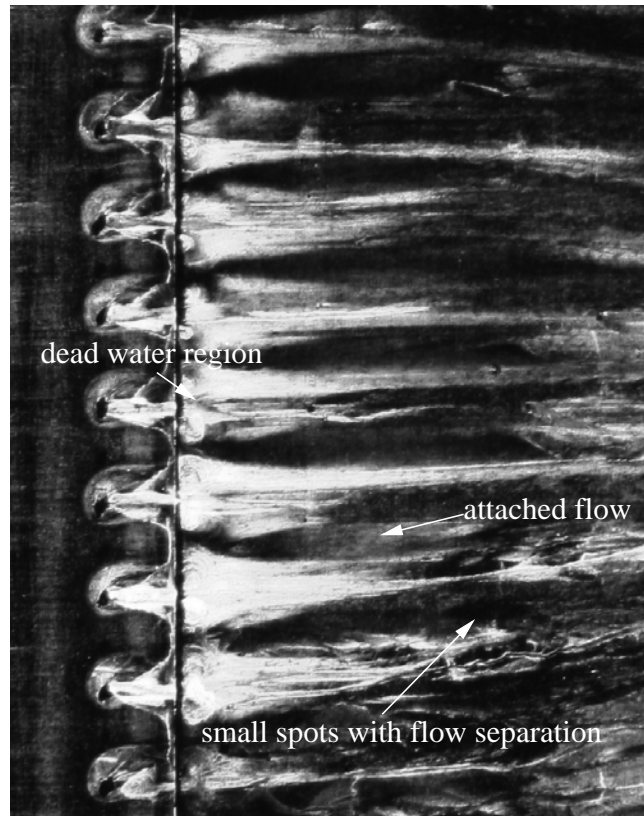
Figure 7.14: Oil flow visualization for $(t/D)_{AJVG} = 10$, detailed view

the 2D contraction of the flow is considered to be normal and the flow is symmetric. The flow is completely reattached at $x_{ax}/c_{ax} \approx 0.7$, where the shock is located, and upstream only some small spots of non-attached flow are visible. A detail of the blow off region and shock location around mid-span is given in fig. 7.14. The straight line seen shortly downstream of the AJVG is a small step in the surface. A tape was glued on the AJVG in order to rapidly change the pitch of the AJVG. Measurements without the tape confirmed that it had no measurable influence on the flow when the AJVG are used. Behind the holes a large dead water region with recirculating flow is visible. The main flow stays attached in-between the AJVG jets and the small spots with separated flow are located between the jets. In spanwise direction the flow seems to be uniform. This is confirmed by wake traverses at different blade heights. In fig. 7.15 the integral aerodynamic losses are plotted for the middle AJVG pitch for traverses at different blade heights. One traverse at mid span $z/t_{AJVG} = 0$ and a second one at half pitch between two AJVG holes. The plot confirms that the differences are marginal and within the uncertainty of the measurement.

Finally for the large pitch ratio of 15 a look on the near wall flow of the SS with oil-and-dye technique is given in fig. 7.16 and a detailed view on the blow off region is plotted in fig. 7.17. It becomes visible why the pitch of the AJVG is too large to reduce the separation efficiently over the whole span. In between the jets large zones with flow separation are seen. After the shock at $x_{ax}/c_{ax} \approx 0.72$ the flow starts to reattach, whereas it seems as if flow from downstream of the jets is deviated to the sides to the regions downstream of the separation bubbles. Reattachment lines are visible downstream of the jets which seem to be due to vortices created by pressure
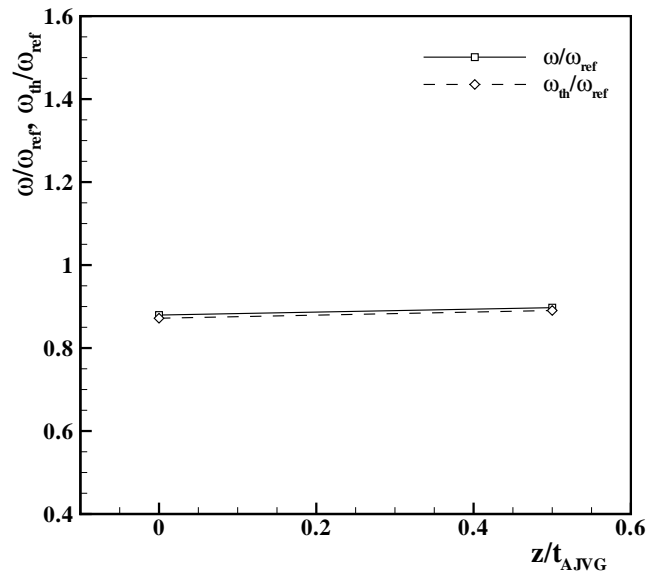
Figure 7.15: Integral total pressure and thermodynamic loss coefficients for design exit Mach and Reynolds numbers with $(t/D)_{AJVG} = 10$ at different blade heights

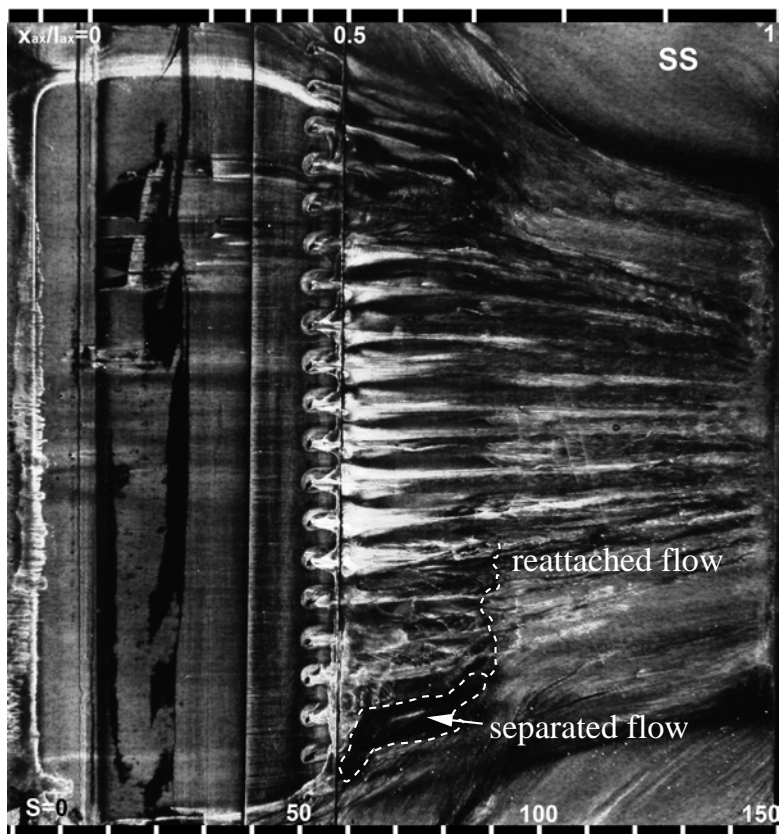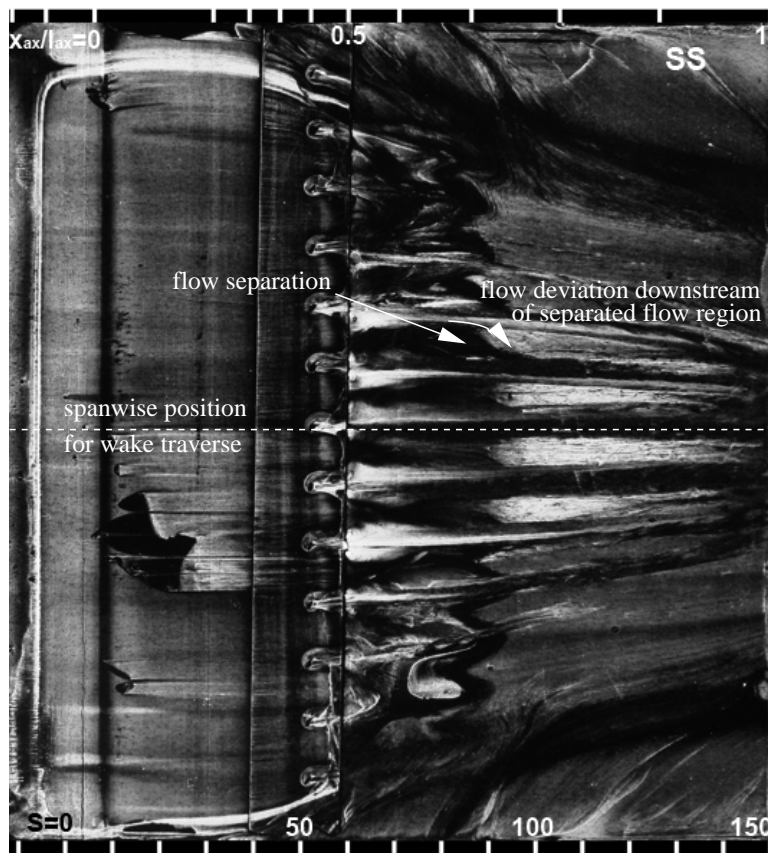Figure 7.16: Oil flow visualization for $(t/D)_{AJVG} = 15$, SS view
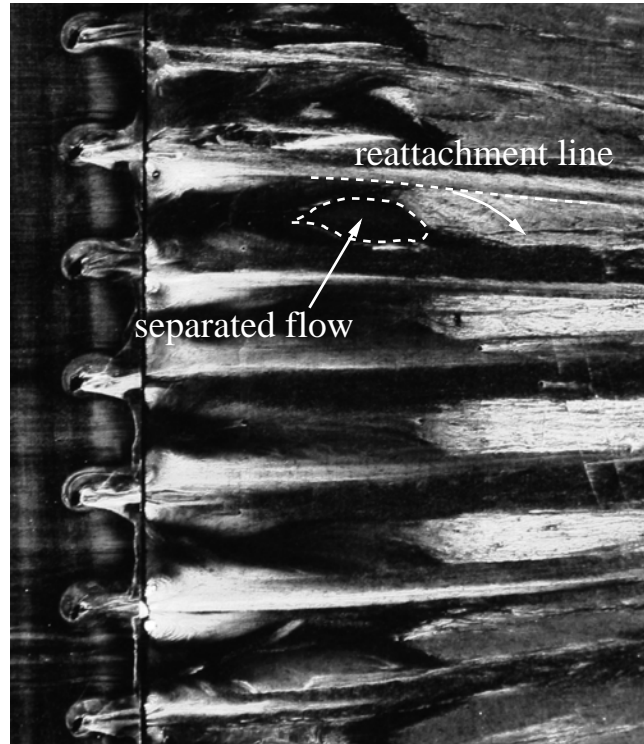
Figure 7.17: Oil flow visualization for $(t/D)_{AJVG} = 15$, detailed view

differences in span height. The non-uniformity of the flow along the blade span is visible up to the trailing edge and it is to presume that it will not be homogenized up to the traverse plane for the determination of the total pressure losses. The wake traverse is done at mid span (marked in fig. 7.16) and therefore downstream of a jet without main flow separation at the shock location. The measured losses for this pitch in fig 7.8 and 7.9 are therefore very likely to be too optimistic and not valid over one complete AJVG pitch along the blade span direction, reason why the middle normalized pitch of 10 was used for the further experiments.

Influence of AJVG at Different Operating Points

For the higher Reynolds number, it was previously seen that the separation bubble is reduced and so are the total pressure losses. The comparison between the PPD for the case without any secondary mass flow and the one with the use of AJVG alone at $(t/D)_{AJVG} = 10$ is given in fig. 7.18. In the plot it is again visible how the AJVG obstruct the flow on the blade leading to a compression upstream of the holes and how the shock is shifted upstream. The apparent (small) separation bubble without AJVG is now not visible anymore and the shock strength increases.

The effect on the losses is visible in fig. 7.19 where the total pressure loss coefficient with and without the use of AJVG is plotted over one blade pitch. Since the separation on the suction side is already very small without blowing off, the AJVG can not contribute much to a reduction of the aerodynamic losses. They rather increase slightly the total pressure loss in the wake due to the obstruction created to the main flow. Due to the stronger shock the losses increase slightly in the suction side branch of the undisturbed flow. The relative integral losses increase
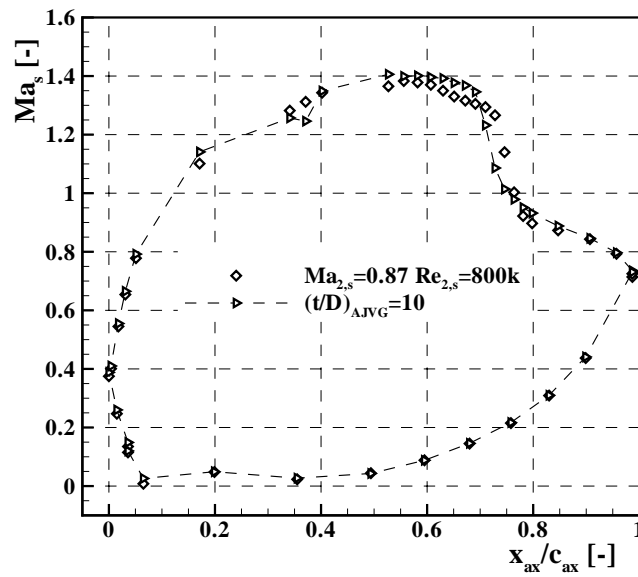
Figure 7.18: Isentropic Mach number distribution on the blade at $Ma_{2,s} = 0.87$; $Re_{2,s} = 800k$ with and without AJVG

Figure 7.19: Total pressure loss at the outlet plane for $Ma_{2th} = 0.87$; $Re_{2th} = 800k$ with and without AJVG
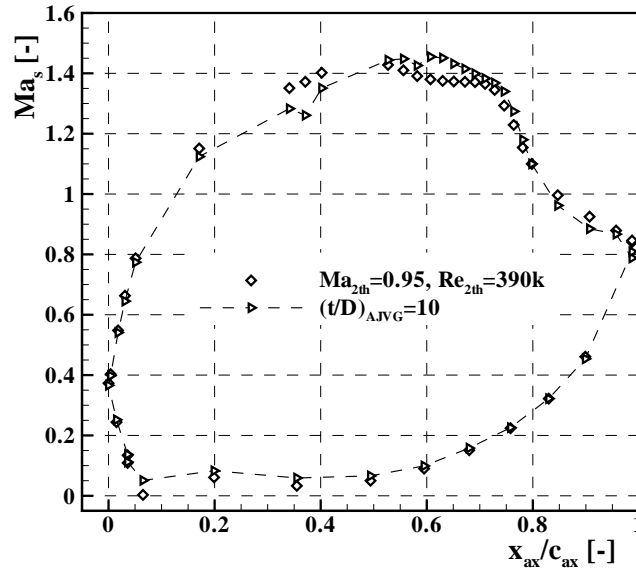
Figure 7.20: Isentropic Mach number distribution on the blade at $Ma_{2,s} = 0.95$; $Re_{2,s} = 390k$ with and without AJVG

from 0.68 without secondary flow to 0.77 as primary losses with AJVG and 0.75 as normalized thermodynamic losses ω_{th}/ω_{ref}.

At the higher Mach number a large separation bubble with the possibility of non-reattachment up to the trailing edge was previously seen. In fig. 7.20 the isentropic Mach number distributions on the blade without and with AJVG at $(t/D)_{AJVG} = 10$ is plotted. The efficient reduction of the size of the separation bubble upstream of the shock is clearly visible. Also downstream of the shock the pressure is quite different enforcing the assumption of completely separated flow without AJVG. In contrast to the design point the shock location is not significantly shifted.

The effectiveness of the AJVG in reducing the size of the separation bubble is reflected in the total pressure loss at the outlet plane plotted in fig. 7.21. The size of the wake is reduced by large using the AJVG and the influence is so strong that the wake is displaced towards the pressure side. The slightly higher losses in the undisturbed flow due to a stronger shock have only little influence in the integral values. While without AJVG the normalized integral losses add up to 1.67, they can be reduced to 1.34 with AJVG or 1.33 as relative thermodynamic losses.

Comparing the total pressure losses with the ones for the original cascade at lower pitch (*T120C*) gives the values of fig. 7.22. The values for the *T120C* cascade were taken from Homeier [81] and all results were scaled with the value for the original cascade at design main flow conditions. One can see clearly that the losses increase to the double or more at lower Reynolds number by increasing the pitch. The use of AJVG reduces the aerodynamic losses at lower Reynolds number, but the values of the *T120C* cascade are not reached. This is mainly due to the high shock intensity and additionally either flow disturbances by the AJVG or flow separation. Latter plays a dominant role for the low Reynolds number flows.
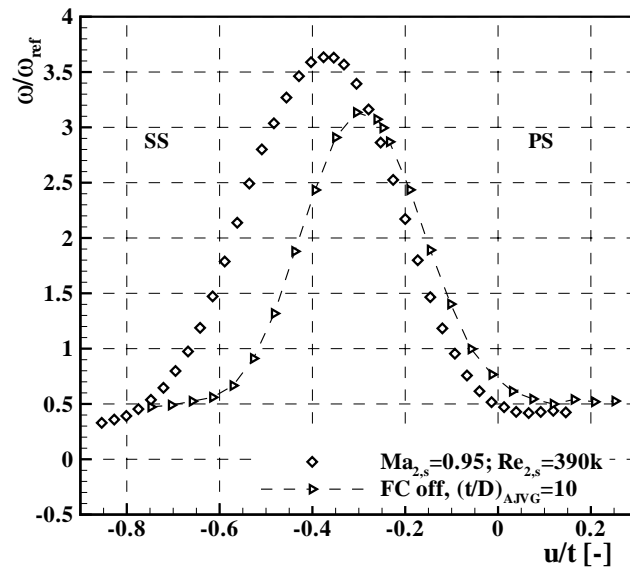
Figure 7.21: Total pressure loss at the outlet plane for $Ma_{2,s} = 0.95$; $Re_{2,s} = 390k$ with and without AJVG
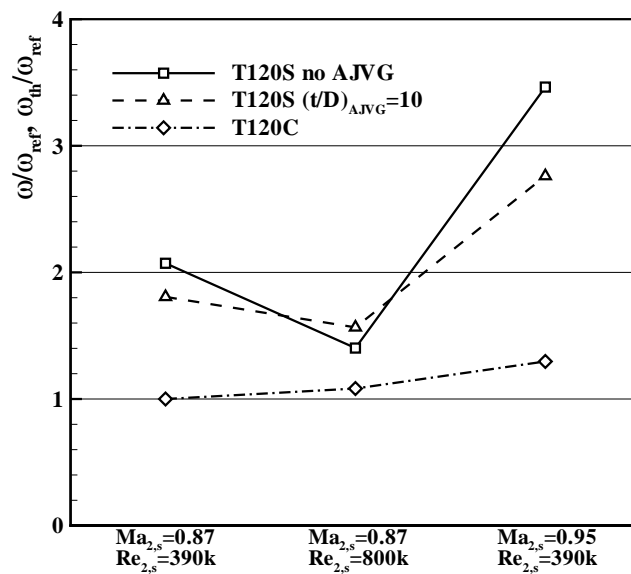
Figure 7.22: Scaled total pressure losses without film cooling for *T120C* and *T120S* cascades

Figure 7.23: Isentropic Mach number distribution for $Ma_{2,s} = 0.87$ and $Re_{2,s} = 390k$ with film cooling and without AJVG; detail on the right

7.3   Influence of Film Cooling

First an analysis on the influence of film cooling on the aerodynamic behaviour of the cascade without the use of AJVG is done. Afterwards the combination of both film cooling and AJVG is analysed.

7.3.1   Film Cooling Without AJVG

Analysing film cooling at different blowing ratios without AJVG for the design operation point, the isentropic Mach number distributions on the blade of fig. 7.23 are obtained. With film cooling the shock location is shifted upstream and the interference length is significantly reduced. Also the separation bubble seems to be reduced but not completely suppressed. The detail view on the right of fig. 7.23 shows more clearly how the FC pressure ratio has only little influence on the shock location and extension of a possible small separation.

Film cooling alone at the design operating point reduces slightly the total pressure loss at the outlet compared to the case without any cooling or AJVG, as can be seen in fig. 7.24. This is due to efficient reduction of the flow separation at the suction side, as seen before in the Mach number distribution on the blade, and the higher momentum of the coolant flow. The benefits from that are high enough to overcome the expected loss increase due to interaction of the cooling jets with the main flow. With increasing blowing ratio this interaction increases the losses but shows still better performance than without any blowing off.

At high exit Reynolds number the separation at the suction side is weak. Therefore in fig. 7.25, where the isentropic Mach number on the blade is plotted as function of the relative axial chord, no large differences are seen between the case with the solid blade and using film cooling at a pressure ratio of 1.03 and 1.06. With film cooling there seems to be either a complete

117

Figure 7.24: Total pressure loss coefficient for $Ma_{2,s} = 0.87$ and $Re_{2,s} = 390k$ with film cooling and without AJVG

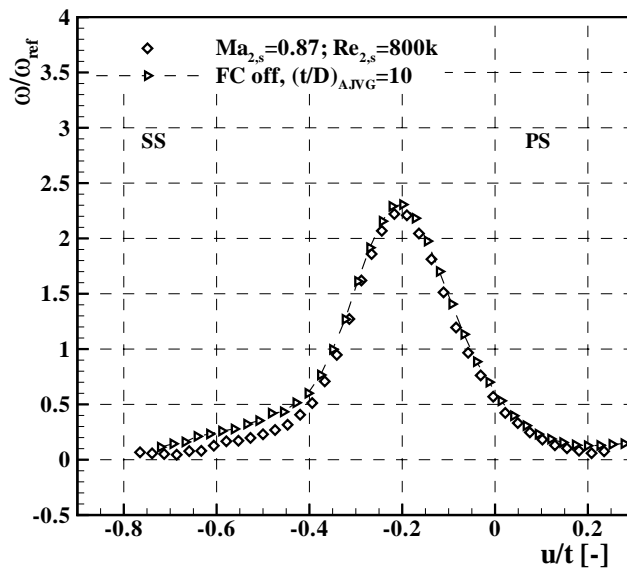
Figure 7.25: Isentropic Mach number distribution for $Ma_{2,s} = 0.87$ and $Re_{2,s} = 800k$ with film cooling and without AJVG; detail on the right

suppression of the flow separation or a longer flow acceleration due to an increased boundary layer size. The shock location is slightly shifted upstream.

The wake of the total pressure losses at the outlet for the high Reynolds number case with film cooling and without AJVG is plotted in fig. 7.26. Since almost no separation is present on the suction side without blowing off, the film cooling can not contribute much to total pressure reduction by diminishing the size of the separation bubble. In fact the losses increase with ever-growing coolant pressure ratio due to the interaction with the main flow and stronger
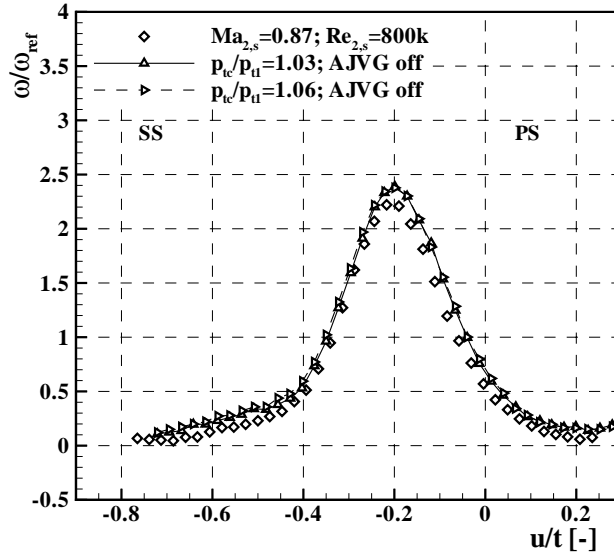
Figure 7.26: Total pressure loss coefficient for $Ma_{2,s} = 0.87$ and $Re_{2,s} = 800k$ with film cooling and without AJVG

shock.

In contrast to the previous operation point, at high Mach and design Reynolds number the extension of the separation bubble is significantly reduced with film cooling, as can be seen in fig. 7.27 where the case with the solid blade is compared to the case with film cooling at $p_{tc}/p_{t1} = 1.06$ and 1.09. The flow on the suction side suffers a stronger acceleration in the upstream half of the axial chord due to the blowing off. At the rear part, which is plotted in detail at the right of fig. 7.27, the pressure plateau due to flow separation is visibly reduced. The shock location is again almost not affected by the blowing off, as was seen with the use of AJVG alone.

The significant reduction of the flow separation is reflected in the total pressure loss coefficient profile of fig. 7.28. With film cooling the total pressure loss is again significantly reduced and the wake peak is shifted towards the pressure side. It seems that the interaction of the film cooling jets with the main flow is strong enough to transport the boundary layer disturbances up to the shock location in such manner that the flow is less likely to separate, i. e. the turbulent boundary layer after jet blowing off does not fully relaminarize up to the expected separation point with laminar boundary layer. The positive effects due to the reduction of the size of the separation bubble exceed well the losses due to the interaction of the jets with the main flow and upstream start of the turbulent boundary layer.

7.3.2   Combined Use of Film Cooling and AJVG

Experiments using both film cooling and AJVG together at the three operation points with three coolant to total inlet pressure ratios show the influence of the AJVG when using film cooling.

The isentropic Mach number on the blade is plotted on the left of fig. 7.29 for the design outlet Mach and Reynolds number with use of AJVG and at the three different coolant to total inlet
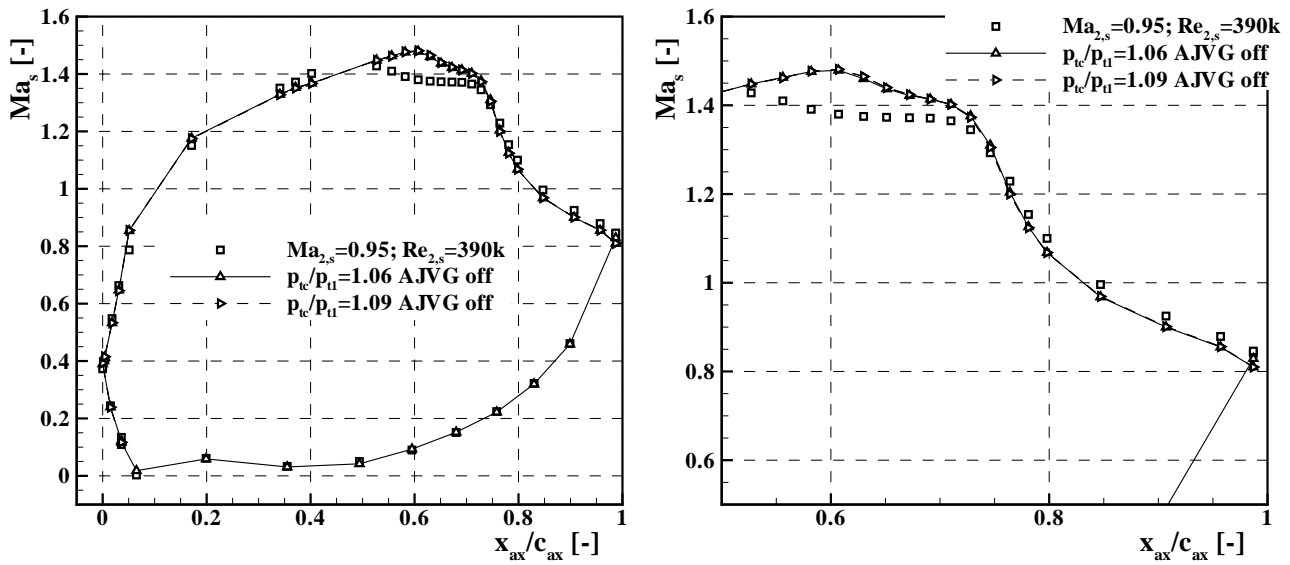
Figure 7.27: Isentropic Mach number distribution for $Ma_{2,s} = 0.95$ and $Re_{2,s} = 390k$ with film cooling and without AJVG; detail on the right
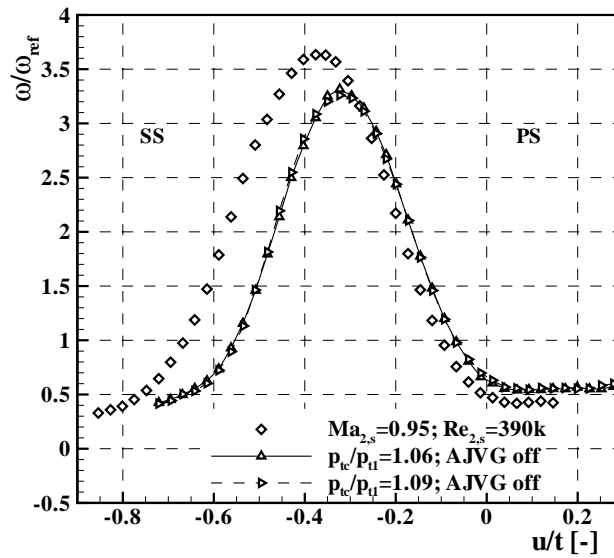
Figure 7.28: Total pressure loss coefficient for $Ma_{2,s} = 0.95$ and $Re_{2,s} = 390k$ with film cooling and without AJVG
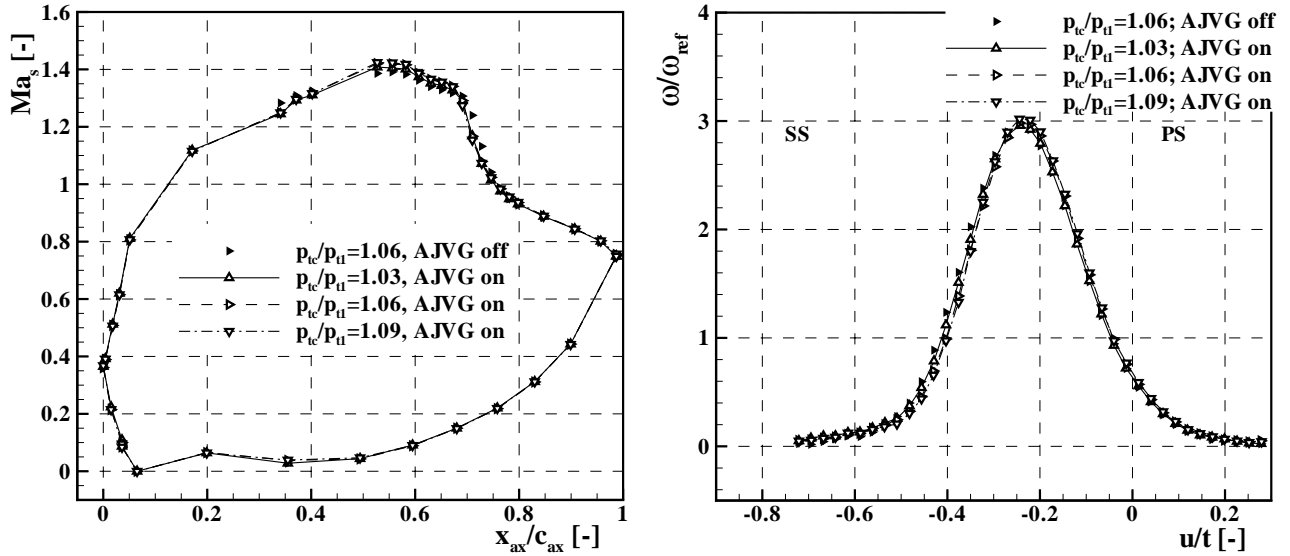
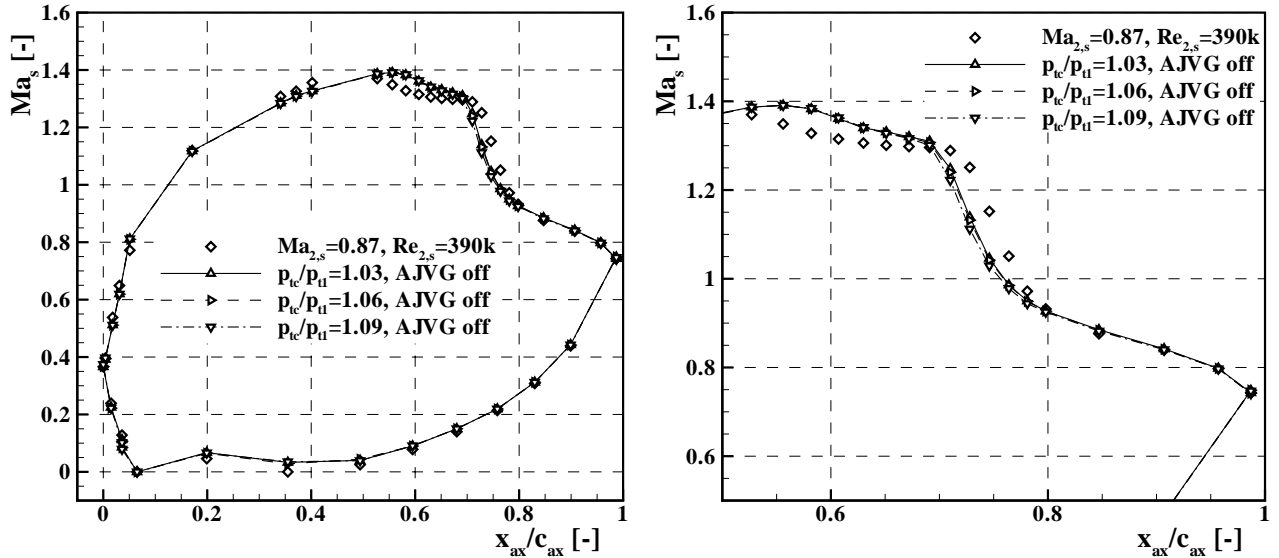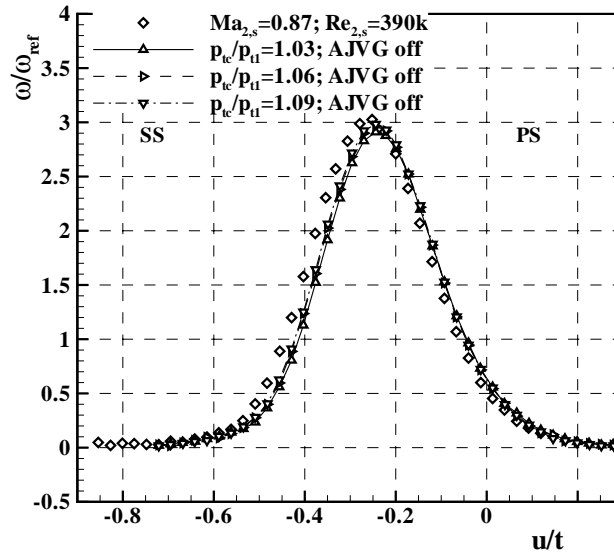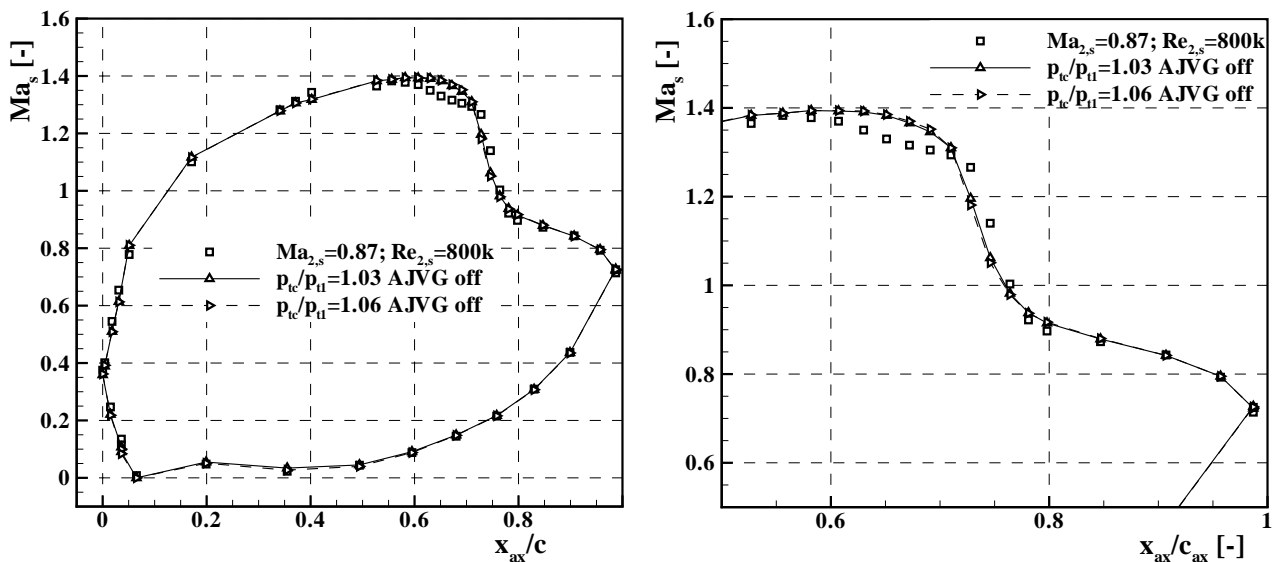Figure 7.29: Isentropic Mach number distribution (left) and total pressure loss (right) for $Ma_{2,s} = 0.87$ and $Re_{2,s} = 390k$ with film cooling and AJVG

pressure ratios. The distribution for the middle pressure ratio $p_{tc}/p_{t1} = 1.06$ without AJVG is given in the same plot with filled symbols and without connecting line for a better comparison. Differences are only seen on the suction side upstream of the AJVG jet location, where with use of AJVG the blockage of the main stream is perceived and in the upstream shift of the shock location due to the use of the AJVG. Latter is accompanied by a previous acceleration of the flow towards higher Mach numbers. Also for the total pressure losses the experienced differences between the use or not of the AJVG is very weak as can be seen on the right of fig. 7.29. There the total loss parameter is plotted as function of the dimensionless pitch for the three coolant pressure ratios with use of the AJVG. Again for comparison purposes the wake without use of AJVG at $p_{tc}/p_{t1} = 1.06$ is plotted with filled symbols. With AJVG the lines show a slightly narrower wake and also a small increase of the peak loss. This might be an indication of smaller oscillations with the use of AJVG as reported in Doerffer et al. [44] or Szwaba [142]. Since the five hole probe only captures time averaged pressure values, with an oscillating wake the measured wake becomes broader and the peak less accentuated.

For the case with high outlet Reynolds number, the same effect as at the design operation point is seen in the isentropic Mach number distribution on the left of fig. 7.30. With film cooling and AJVG the blockage just upstream of the AJVG location is seen as well as a higher peak Mach number and an upstream shift of the shock location compared to film cooling without the use of AJVG. The total pressure loss traversing across one blade pitch at mid span at the outlet of the cascade for the three coolant pressure ratios with AJVG is plotted on the right of fig. 7.30. The losses increase substantially by using AJVG compared to the case without AJVG at the middle coolant pressure ratio. The same was already seen comparing the usage of AJVG without film cooling in chapter 7.2. Since the boundary layer might have tripped upstream of the shock into turbulent, which reduces the size of the separation bubble substantially, the interaction of the AJVG with the main flow is only increasing the losses.

For the high outlet Mach number, the isentropic Mach number on the blade is plotted on the
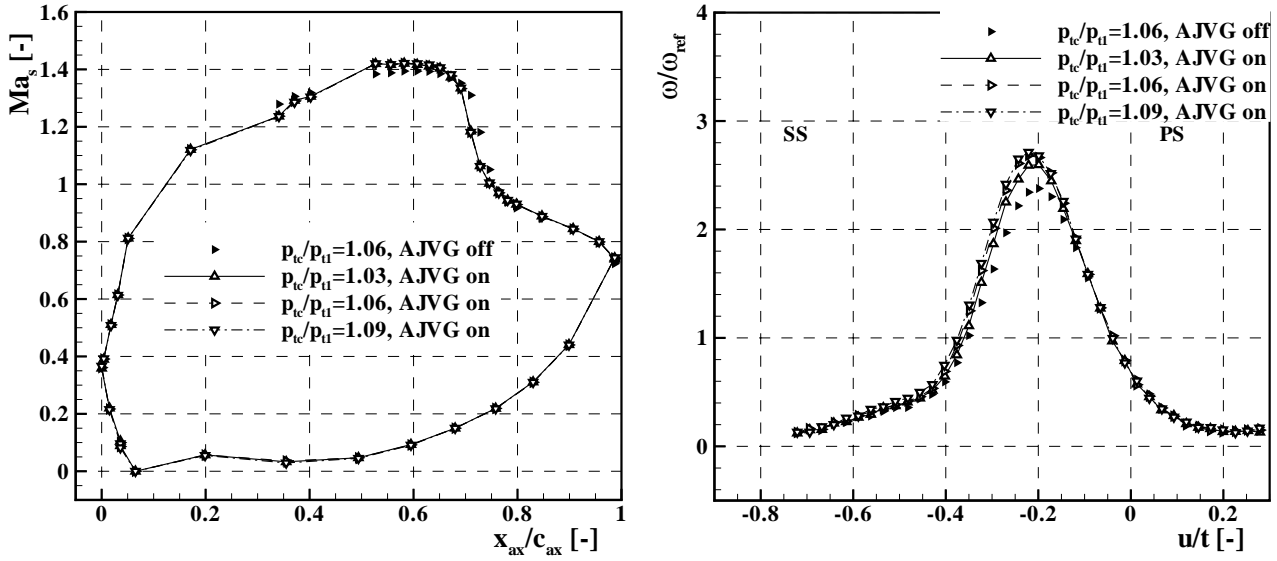
Figure 7.30: Isentropic Mach number distribution (left) and total pressure loss (right) for $\mathrm{Ma}_{2,s} = 0.87$ and $\mathrm{Re}_{2,s} = 800\mathrm{k}$ with film cooling and AJVG

left of fig. 7.31 for film cooling and AJVG combined. The same as for the previous points is true for this operation point. Only at the lowest coolant pressure ratio the shock location is almost equal as for film cooling without AJVG. At $p_{tc}/p_{t1} = 1.03$ also the increase of the maximum Mach number upstream of the shock is very low. For the other two pressure ratios a upstream shift of the shock and an increase of the peak Mach number is seen. The total pressure loss is plotted on the right of fig. 7.31. The trend of the primary losses is not very clear since after a clear increase in losses changing the coolant pressure ratio from 1.03 to 1.06 they decrease again by a further increase in coolant pressure. Comparing to the case with film cooling at $p_{tc}/p_{t1} = 1.06$ and without AJVG the wake is again narrowed and the maximum loss value is higher.

7.3.3 Integral Values

In this sub-chapter the area averaged values of the total pressure loss $\overline{\omega}/\omega_{ref}$ and the thermodynamic loss ω_{th}/ω_{ref} as well as the average outlet angle deviation over one blade pitch are presented. The outlet angle deviation is defined as difference from the outlet angle at design operation point without film cooling nor AJVG. Since for an HPT blade film cooling is in general necessary, the main comparison parameter is the use or not of the AJVG with film cooling and the results are plotted as function of the coolant pressure ratio p_{tc}/p_{t1}. In the plots displaying the total pressure losses, the reference values for the cases without film cooling and without as well as with AJVG at a pitch ratio of 10 are indicated as horizontal dashed-dotted lines.

In fig. 7.32(a) the integral values for the design operation point are shown. The total pressure loss parameter decreases by over 10 % using the AJVG alone compared to the case on the solid blade. By adding film cooling, the total pressure losses increase again, but remain at a constant level below the solid blade case. The thermodynamic losses instead increase continuously with
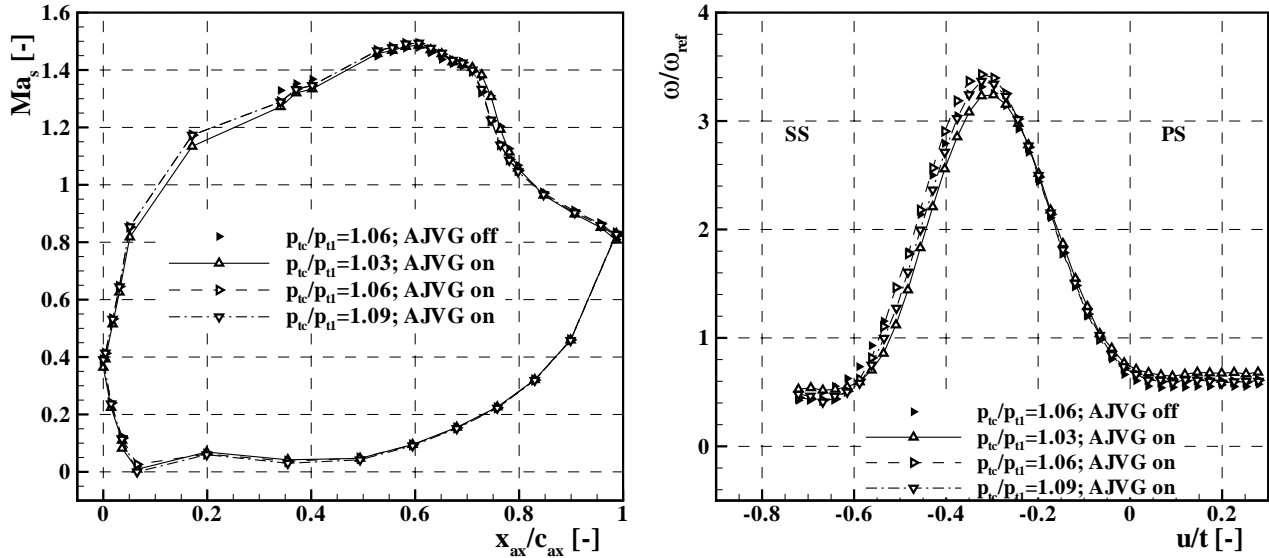
Figure 7.31: Isentropic Mach number distribution (left) and total pressure
loss (right) for $\mathrm{Ma}_{2,s} = 0.95$ and $\mathrm{Re}_{2,s} = 390\mathrm{k}$ with film cooling
and AJVG

growing coolant pressure ratio. The differences between the film cooled cases with and without
AJVG are very small and within the absolute accuracy of the experiments. Nevertheless there
seems to be a trend to lower losses using AJVG at higher coolant pressure ratios. The outlet
angle deviation, shown in fig. 7.32(b), does not change much by the use of film cooling, but as
a constant throughout all operation points the outlet angle increases slightly with the use of
the AJVG.

For the high Reynolds number case the losses increase whenever air is blown off either from the
AJVG or the film cooling holes or both together, as can be seen on fig. 7.33(a). The AJVG alone
are responsible in the cases with and without film cooling in an increase of the total pressure
loss of about $0.08 \cdot \omega_{ref}$. Since there is no significant separation bubble to be suppressed, the
losses due to the interference of the jets with the main flow are nearly constant. The film
cooling adds at least about $0.12 \cdot \omega_{ref}$ to the total pressure loss and increases with growing
coolant pressure ratio. On fig. 7.33(b) the outlet angle deviation shows again no significant
difference between all the cases. Film cooling without AJVG creates a small overturning of
about 0.2° while using the AJVG brings it back to the outlet angle at the solid blade.

The benefits of film cooling or the use of AJVG for the average total pressure losses is clearly
visible for the high Mach number case in fig. 7.34(a). The use of the AJVG alone reduces
the aerodynamic losses by about 1/5 compared to the case on the solid blade, where a very
large separation zone is present. By using film cooling, the losses increase again due to the
interference of the coolant jets with the main flow. Whenever film cooling is used, the use of
the AJVG has small effects on the total pressure loss. But the trend is here as for the design
case such that it is beneficial to use AJVG at high coolant blowing ratio while the opposite is
true for low blowing ratios. The outlet angle (fig. 7.34(b)) is again not very much affected by
blowing off, but the angle is about 1° larger than for the other two operating points.

In fig. 7.35 the thermodynamic losses are compared to the external losses ω_{ex}/ω_{ref}. While in the

(a) Total pressure losses

(b) Outlet angle deviation
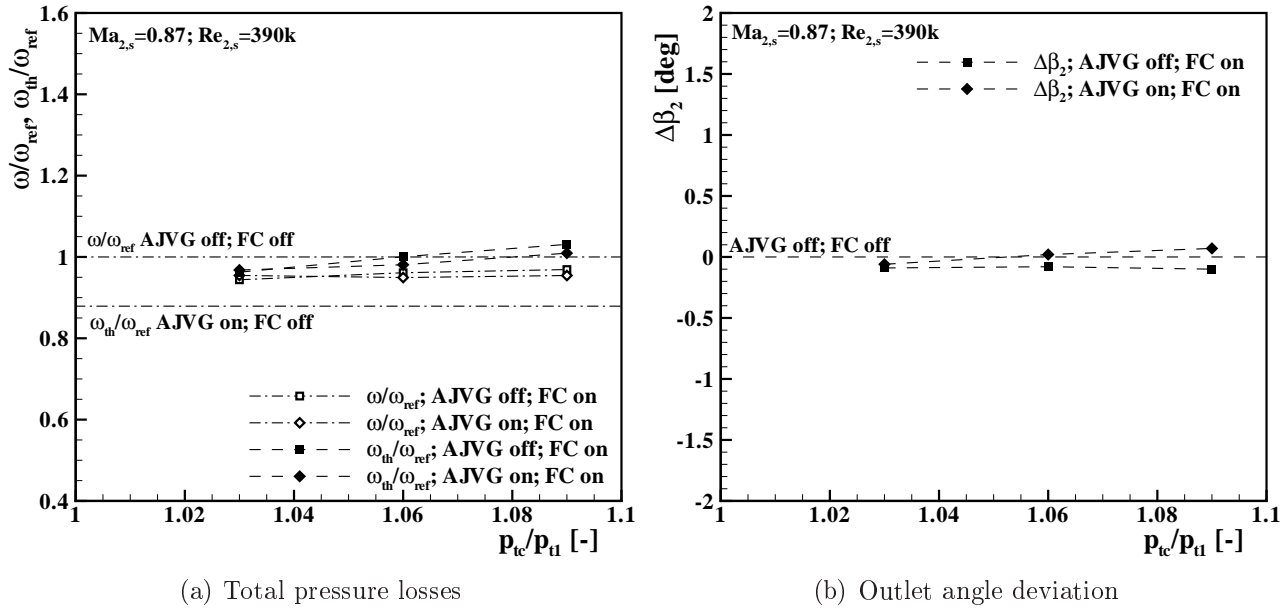
Figure 7.32: Average total pressure loss and outlet angle deviation $\Delta\beta_2$ over one blade pitch for $Ma_{2,s} = 0.87$ and $Re_{2,s} = 390k$ with film cooling and AJVG

(a) Total pressure losses

(b) Outlet angle deviation
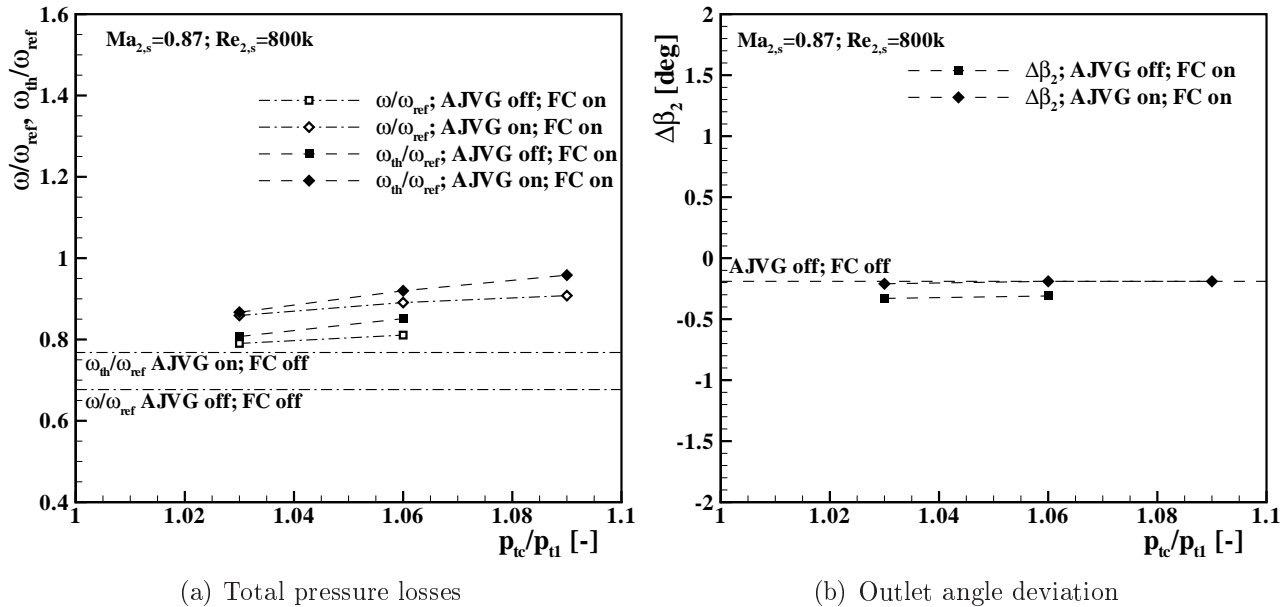
Figure 7.33: Average total pressure loss and outlet angle deviation $\Delta\beta_2$ over one blade pitch for $Ma_{2,s} = 0.87$ and $Re_{2,s} = 800k$ with film cooling and AJVG

(a) Total pressure losses

(b) Outlet angle deviation
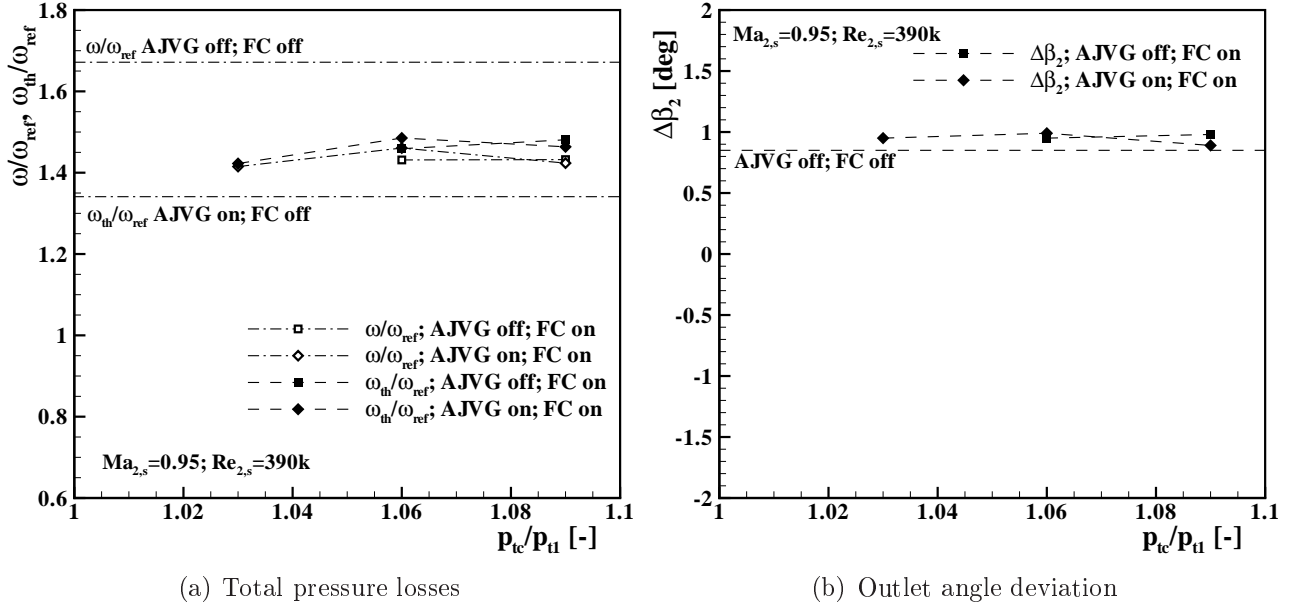
Figure 7.34: Average total pressure loss and outlet angle deviation $\Delta\beta_2$ over one blade pitch for $\mathrm{Ma}_{2,s} = 0.95$ and $\mathrm{Re}_{2,s} = 390\mathrm{k}$ with film cooling and AJVG

thermodynamic loss coefficient the losses inside the coolant holes are taken into consideration, the external loss parameter accounts only for the losses in the main stream with the coolant total pressure taken at the outlet of the hole. One can see for the design operation point with AJVG that with increasing coolant mass flow almost only the losses inside the film cooling holes increase while the external losses remain at a constant level. Though the differences are very small, it seems as if without AJVG the external losses also increase with increasing coolant pressure. At the high Reynolds number the external losses increase slightly with higher coolant blowing ratio, since no benefits due to suppression of flow separation can be gained by stronger blowing. The losses inside the holes increase also with higher blowing ratio similar to the cases at lower Reynolds number. At high Mach number the increase of the external losses with higher coolant mass flow is again marginal while the losses inside the cooling holes increase constantly with higher coolant pressure ratio. Summarizing the coolant effect on the total pressure losses, the measured increase in the thermodynamic losses parallel to the increase of the blowing ratio is essentially due to losses inside the cooling holes.

7.4 Influence of Periodic Unsteady Inflow

A wake generator is installed in the test section for creation of periodic unsteady inflow. The wake generator moves cylindrical bars in a plane between nozzle exit and cascade inlet, as is explained in chapter 4.2. Therefore gaps are left at the bottom and top of the nozzle exit in order to allow the bars to pass through and make a full turn around the cascade. In that way it keeps on running continuously. In order to check for influences of the installation of the wake generator on the cascade flow, measurements were carried out for the three operation points with the wake generator installed but not running and without any bars mounted. In such
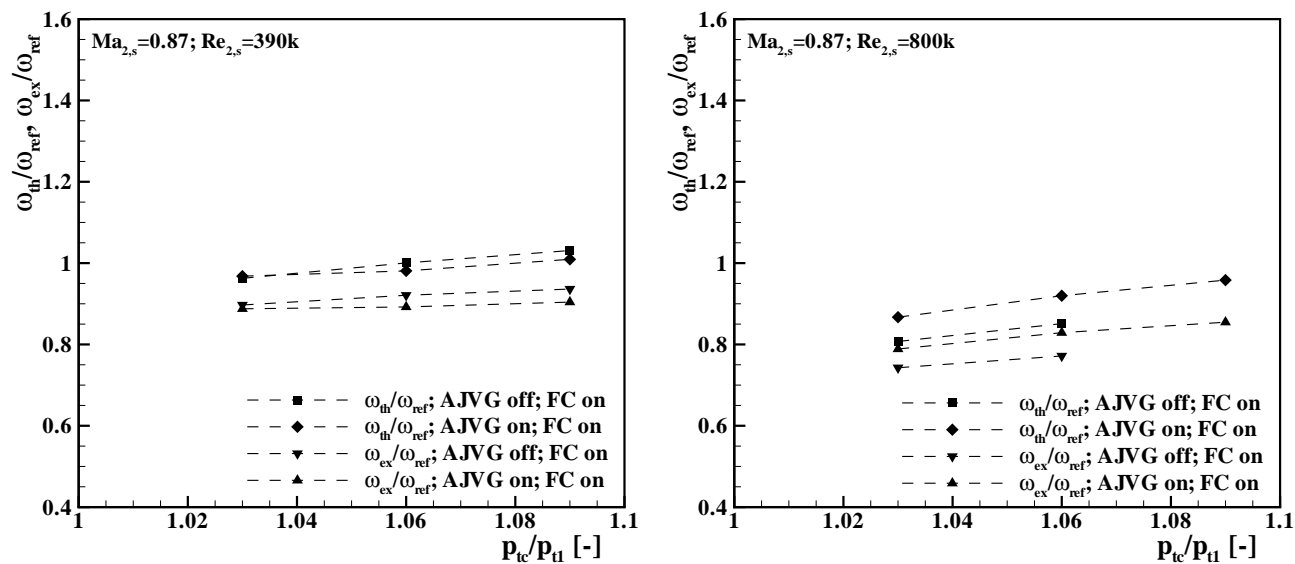
(a) $Ma_{2,s} = 0.87$; $Re_{2,s} = 390k$

(b) $Ma_{2,s} = 0.87$; $Re_{2,s} = 800k$
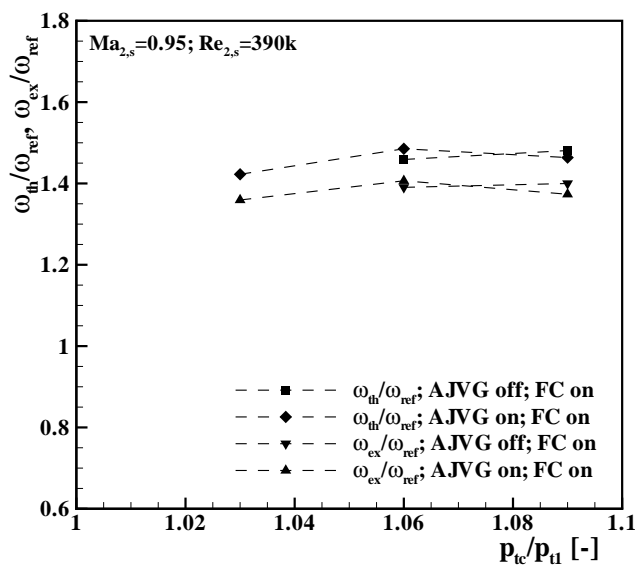
(c) $Ma_{2,s} = 0.95$ $Re_{2,s} = 390k$

Figure 7.35: Average external and thermodynamic total pressure loss parameter with film cooling
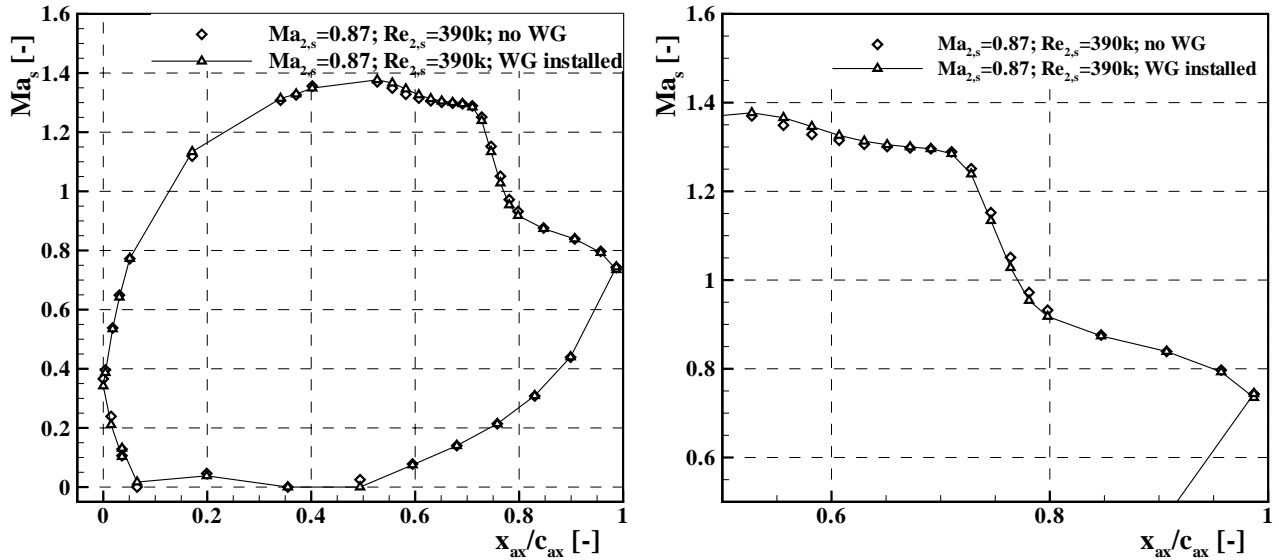
Figure 7.36: Isentropic Mach number on the blade for steady inflow with and without installed wake generator at $\mathrm{Ma}_{2,s} = 0.87$ and $\mathrm{Re}_{2,s} = 390k$

manner the flow should experience approximately the same conditions as without the wake generator installed.

The profile isentropic Mach number for the design outlet Mach and Reynolds number with steady inflow and no film cooling or AJVG but with the wake generator mounted is plotted in fig. 7.36. The results are compared to the case without wake generator and therefore completely closed nozzle which results are plotted with rectangular symbols. It can clearly be seen that both experiments show the same stagnation location and similar acceleration on both suction and pressure side. At the separation location (shown in detail on the right of fig. 7.36) the installation of the wake generator leads to a small reduction of the size of the separation bubble. The effect of the reduction of the total size of the separation bubble on the total pressure losses parameter ω is shown in fig. 7.37 for the design operation point. By installing the wake generator the wake gets visibly smaller and the losses are reduced with the smaller flow separation. The reason found for this influence of the wake generator is the three dimensional flow contraction, as is explained in Gomes and Niehuis [74]. There it is shown that due to the large boundary layer at the limits of the blade in spanwise direction, the flow contraction is relatively large which increases the extension of the separation bubble at mid span.

In the extensive studies of Gomes and Niehuis [74] it is shown for the *T120S* cascade that the influence of the wake generator is limited to cases with very large separation bubble, i. e. at lower Reynolds number without film cooling nor AJVG. An overview given as relative difference of the total pressure loss parameter due to the installation of the wake generator into the test section is plotted in fig. 7.38. The parameter is calculated with

$$\frac{\Delta\overline{\omega}}{\overline{\omega}} = \frac{\overline{\omega}_{noWG} - \overline{\omega}_{WG}}{\overline{\omega}_{noWG}} \cdot 100\% \tag{7.2}$$

with the subscript "*noWG*" for the case without wake generator. When film cooling and AJVG are used together at the low Reynolds number cases, the differences get ever smaller with

Figure 7.37: Total pressure loss coefficient for $Ma_{2,s} = 0.87$ and $Re_{2,s} = 390k$ without film cooling nor AJVG; steady inflow with and without installed wake generator
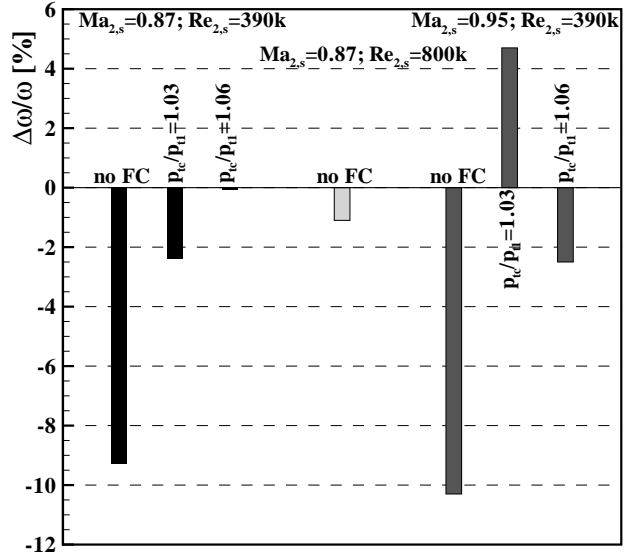
Figure 7.38: Relative difference of total pressure loss coefficient with and without installed wake generator for all operation points on solid blade and with film cooling and AJVG

increasing coolant to main stream total pressure ratio. In this cases the differences amount to in general around 4% or less. Therefore the results for steady and unsteady inflow are comparable for the cases with film cooling which are analysed here. Nevertheless, for reasons of consistency, all the results for unsteady inflow are directly compared to the ones with steady inflow but installed wake generator.

The influence of periodic wakes was analysed for the operation points at a Reynolds number of 390,000 since these are, due to the presence of a large separation bubble on the suction side, the most interesting cases for this investigation. The results presented here were obtained with a bar pitch of $t_{bar} = 80\,\text{mm}$ and a bar velocity of $u_{bar} = 20\,\text{m/s}$ resulting in a Strouhal number of 0.21. With different outlet Mach numbers the Strouhal number changes just marginally.

The measured time dependent inlet velocity and turbulence level as well as the inlet angle are plotted in fig. 7.39 and 7.40 for the design point and for the high exit Mach number case respectively. The inlet flow was measured in flow direction directly upstream of the leading edge at an axial distance of $1.02 \cdot c_{ax}$ from the cascade inlet. One can see that, at a distance from the bars of $0.21 \cdot c_{ax}$, the turbulence level reaches values of about 14% behind the wake and the velocity deficit in its core is of about 15%. Between the wakes a turbulence level of about 5% was measured, which is similar to the one measured with closed nozzle and steady inflow.

The isentropic Mach number distribution on the blade at the design operation point is plotted on the left of fig. 7.41 with steady inflow and with periodic wakes. The pressure side shows a strong sensitivity due to the unsteady inlet flow angle variation. The flow suffers a deviation
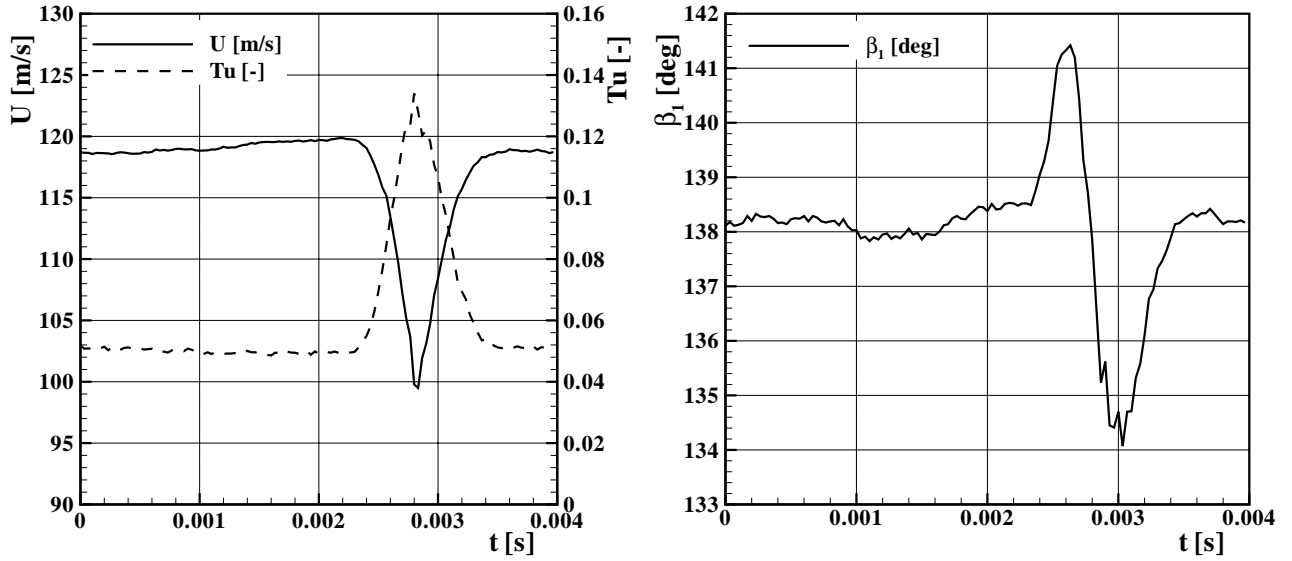
Figure 7.39: Inlet profile of the inlet velocity and turbulence level (left) and of the inlet angle (right) over one bar period of 4 ms with periodic unsteady inflow at $Ma_{2,s} = 0.87$ and $Re_{2,s} = 390k$
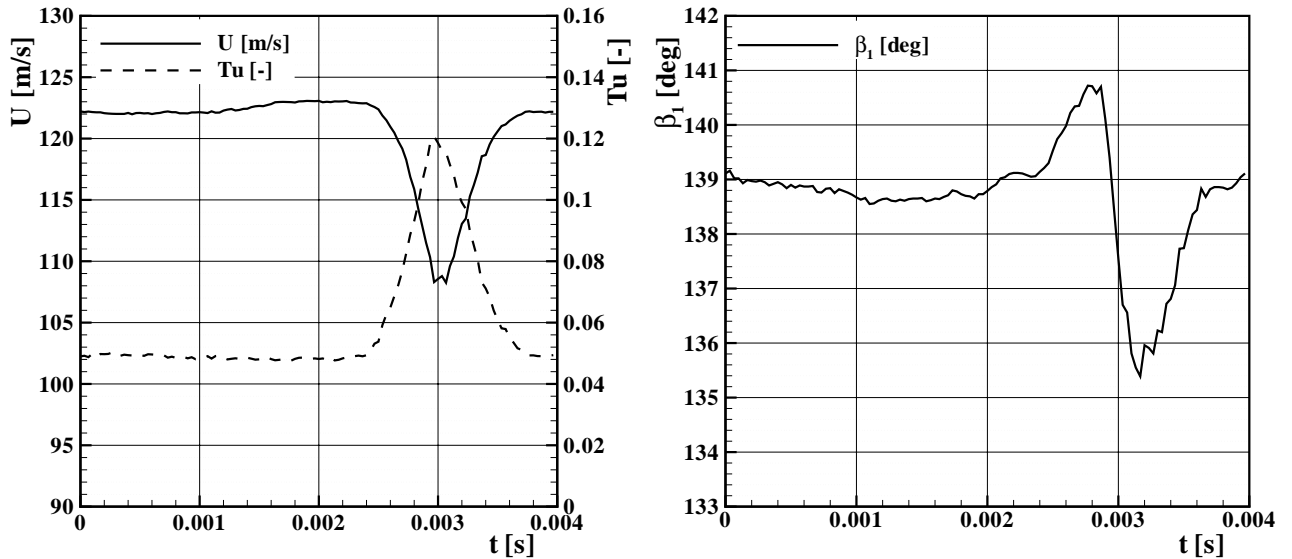
Figure 7.40: Inlet profile of the inlet velocity and turbulence level (left) and of the inlet angle (right) over one bar period of 4 ms with periodic unsteady inflow at $Ma_{2,s} = 0.95$ and $Re_{2,s} = 390k$

Figure 7.41: Isentropic Mach number on the blade for steady and periodic unsteady inflow at $Ma_{2,s} = 0.87$ and $Re_{2,s} = 390k$

towards smaller inlet flow angle downstream of the wakes. This will increase temporarily the size of the separation bubble on the pressure side, see Homeier [81]. On the suction side only small differences are seen at the location with flow separation, as can be seen on the detailed view on the right of fig. 7.41. The shock location moves forward with periodic wakes and the pressure plateau changes slightly to a curve with continuous static pressure increase. The high turbulent wakes seem to diminish the laminar flow separation on the suction side, an effect well known in literature (see e. g. Mayle [101]). The effect of the periodic wakes on the total pressure losses is shown in fig. 7.42 for $Ma_{2,s} = 0.87$ and $Re_{2,s} = 390k$ by comparing the total pressure loss parameter for steady and unsteady inflow. The wakes lead to an increase of the losses in the undisturbed region between the wakes due to the total pressure loss behind the bars. Inside the wake the losses are reduced due to the reduction of the flow separation on the suction side.

At the high exit Mach number the influence of the periodic wake is stronger, due to the increased size of the separation bubble on the suction side. As seen in the isentropic Mach number distribution in fig 7.43, the separation start is moved downstream with unsteady inflow and the pressure gradient at the shock location is higher. Both indicate on an average basis a smaller extension of the separation bubble and a smaller boundary layer thickness at the shock location. This means for the total pressure losses that they are well reduced, at least inside the wake as is shown in fig. 7.44. Between the wakes the losses increase somewhat due to the bar induced total pressure drop.

With film cooling and AJVG the separation bubble on the suction side is much reduced due to the disturbances to the flow and the unsteady wakes are not expected to contribute much to the reduction of flow separation. In fact, as can be seen in fig. 7.45 for the design exit Mach and Reynolds number with AJVG and film cooling at $p_{tc}/p_{t1} = 1.03$, the isentropic Mach number on the blade is almost not affected by the unsteady inflow. A very small upstream shift of the shock location seems to be present, but the variation is minimal. The total losses as function of
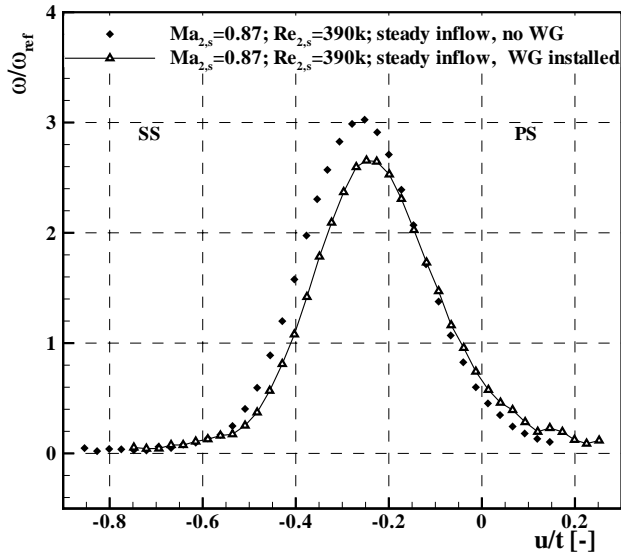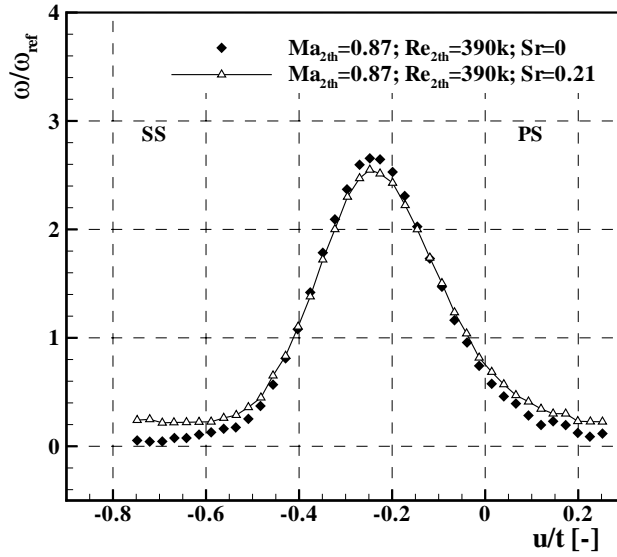
Figure 7.42: Total pressure loss coefficient for $Ma_{2,s} = 0.87$ and $Re_{2,s} = 390k$ without film cooling nor AJVG; steady and periodic unsteady inflow
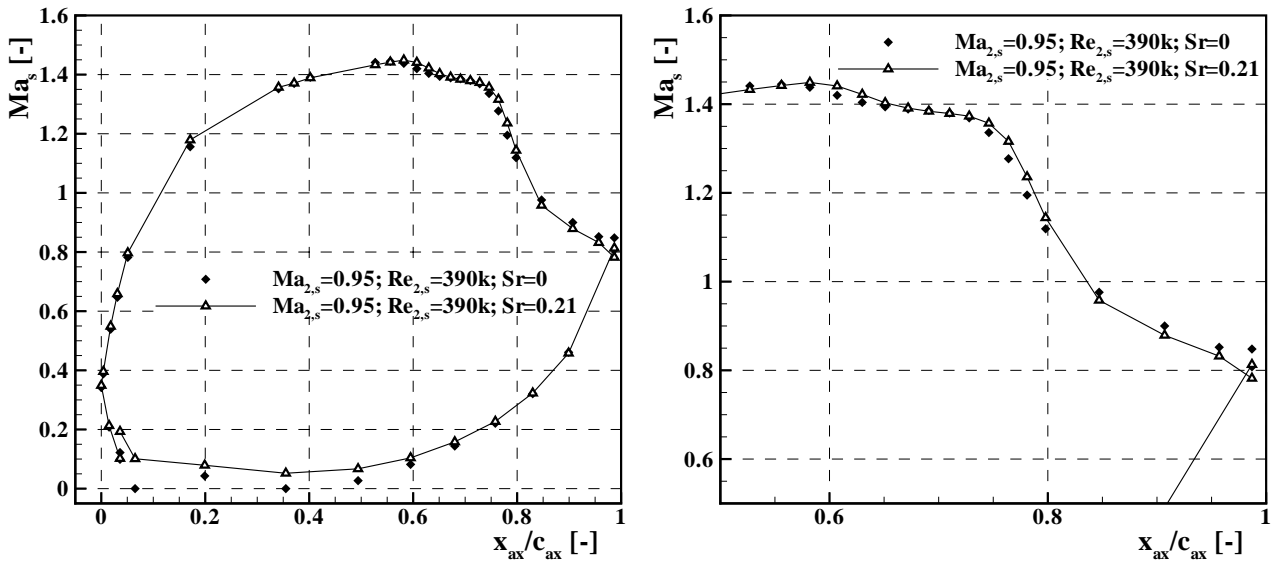
Figure 7.43: Isentropic Mach number on the blade for steady and periodic unsteady inflow at $Ma_{2,s} = 0.95$ and $Re_{2,s} = 390k$
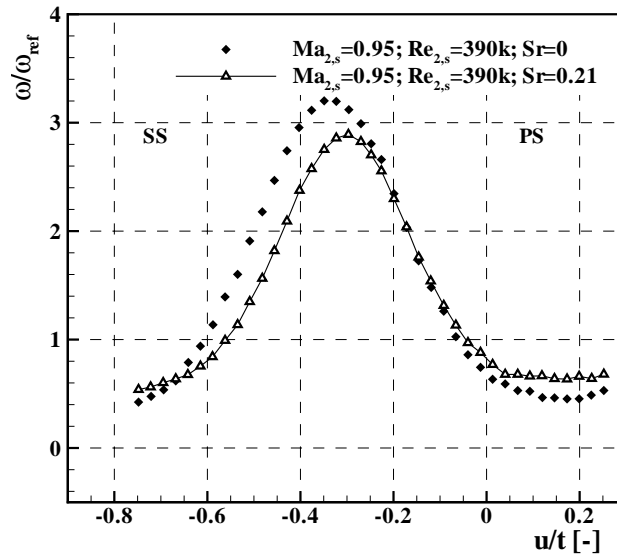
Figure 7.44: Total pressure loss coefficient for $Ma_{2,s} = 0.95$ and $Re_{2,s} = 390k$ without film cooling nor AJVG; steady and periodic unsteady inflow
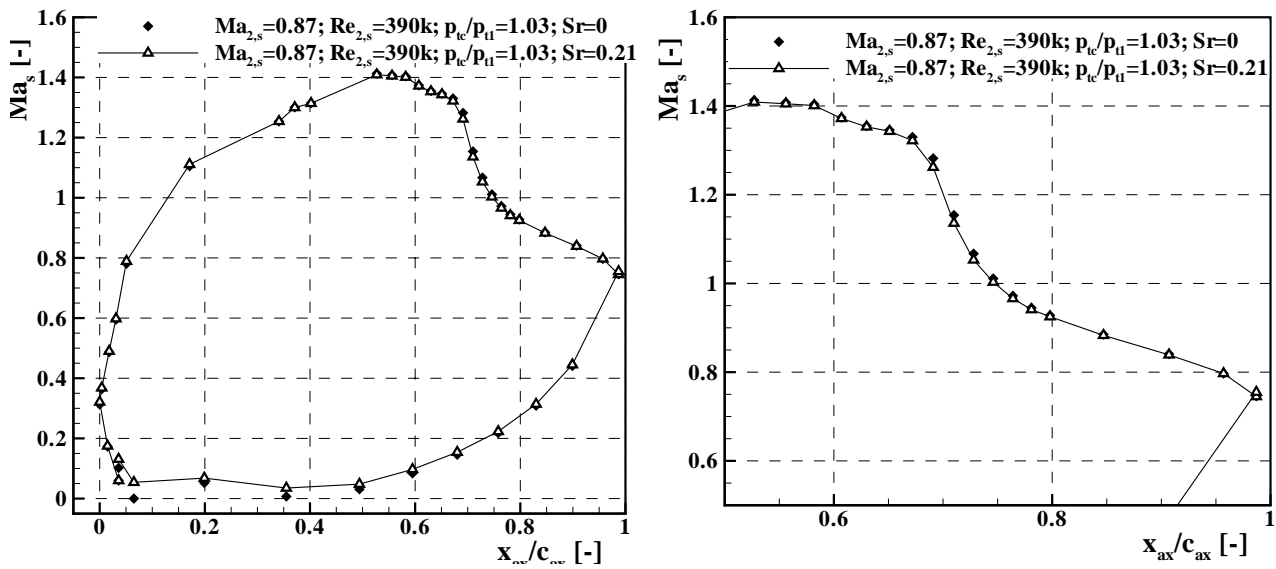
Figure 7.45: Isentropic Mach number on the blade for steady and periodic unsteady inflow at $Ma_{2,s} = 0.87$ and $Re_{2,s} = 390k$ with film cooling at $p_{tc}/p_{t1} = 1.03$ and AJVG
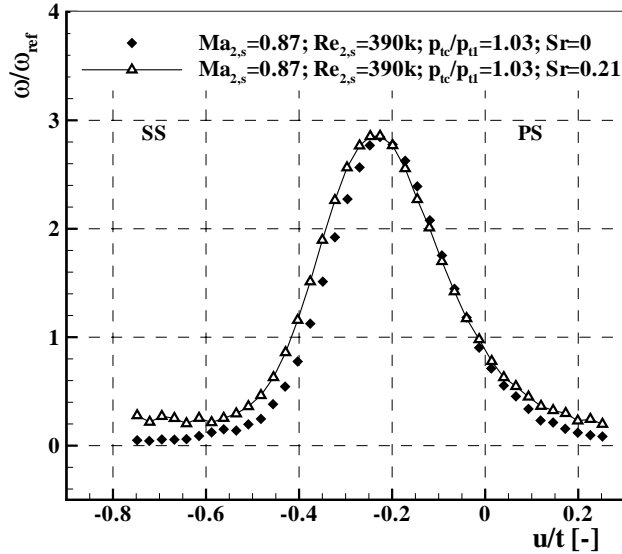
Figure 7.46: Total pressure loss coefficient for $Ma_{2,s} = 0.87$ and $Re_{2,s} = 390k$ with film cooling at $p_{tc}/p_{t1} = 1.03$ and AJVG; steady and periodic unsteady inflow

the blade pitch location with periodic unsteady and with steady inflow are plotted in fig. 7.46. It is visible, that the periodic wakes do not reduce the peak values. In fact the unsteady inflow leads to a loss increase between the wakes and broadens the wake itself. It seems as if with periodic unsteady inflow, the trailing edge wake is fluctuating stronger.

In contrast, at high exit Mach number with a coolant to total inlet pressure ratio of 1.03 and AJVG, some small differences are seen between steady and unsteady inflow. The isentropic Mach number distribution of fig. 7.47 shows a stronger pressure gradient at the shock location with periodic high turbulent wakes which is interpreted as a reduction of the flow separation and boundary layer thickness at the shock location. This reduction in the extension of the shock influence is reflected in the total pressure loss parameter curve of fig. 7.48. One can see in this picture how the periodic wakes lead to a reduction of the losses inside the wake but again to an increase between the wake.

The integral values of the total pressure loss parameter $\overline{\omega}/\omega_{ref}$ and $\overline{\omega}_{th}/\omega_{ref}$ for both Mach numbers are plotted in fig. 7.49. At the design operation point (fig. 7.49(a)) periodic wakes lead always to a loss increase of either $0.05 \cdot \omega_{ref}$ without film cooling or AJVG or $0.26 \cdot \omega_{ref}$ percentage values with film cooling and AJVG. At the high exit Mach number (fig. 7.49(b)) without blowing off from the holes, the losses are well reduced with periodic unsteady inflow to a value close to the one with steady inflow and use of AJVG without film cooling. With film cooling and AJVG the values tend to increase but the periodic high turbulent wakes influence only slightly the total pressure losses with film cooling.

7.5 Summary of the Aerodynamic Analysis on the Suction Side at Higher Loading

A series of measurements were carried out in order to check the influence of film cooling, unsteady inflow and vortex generating devices on the aerodynamics of a HPT blade cascade
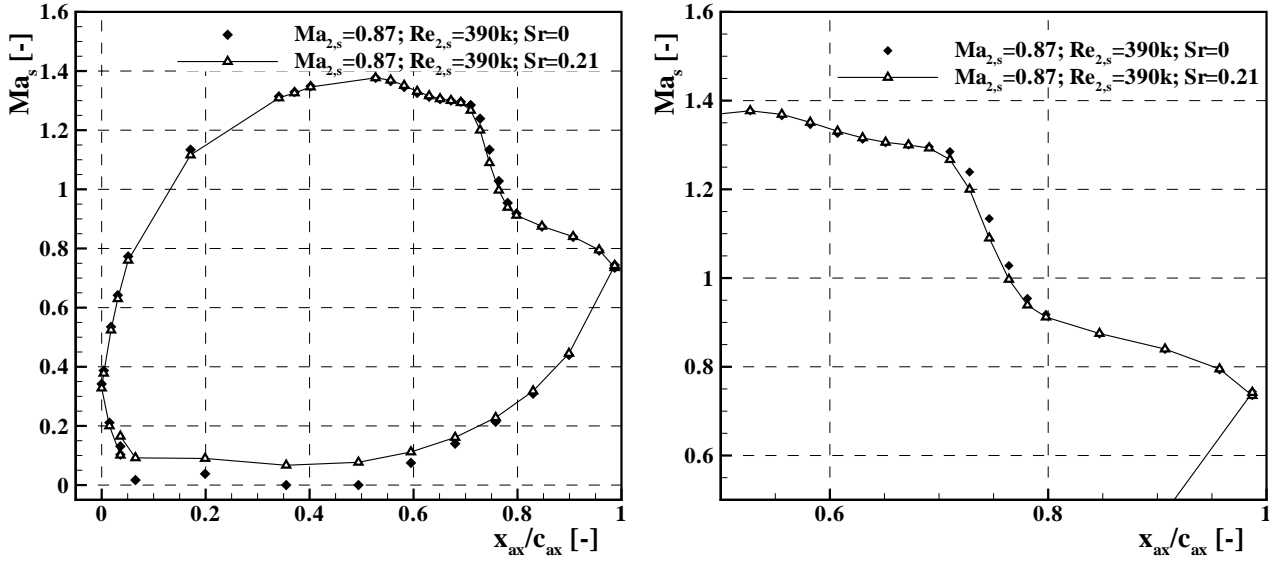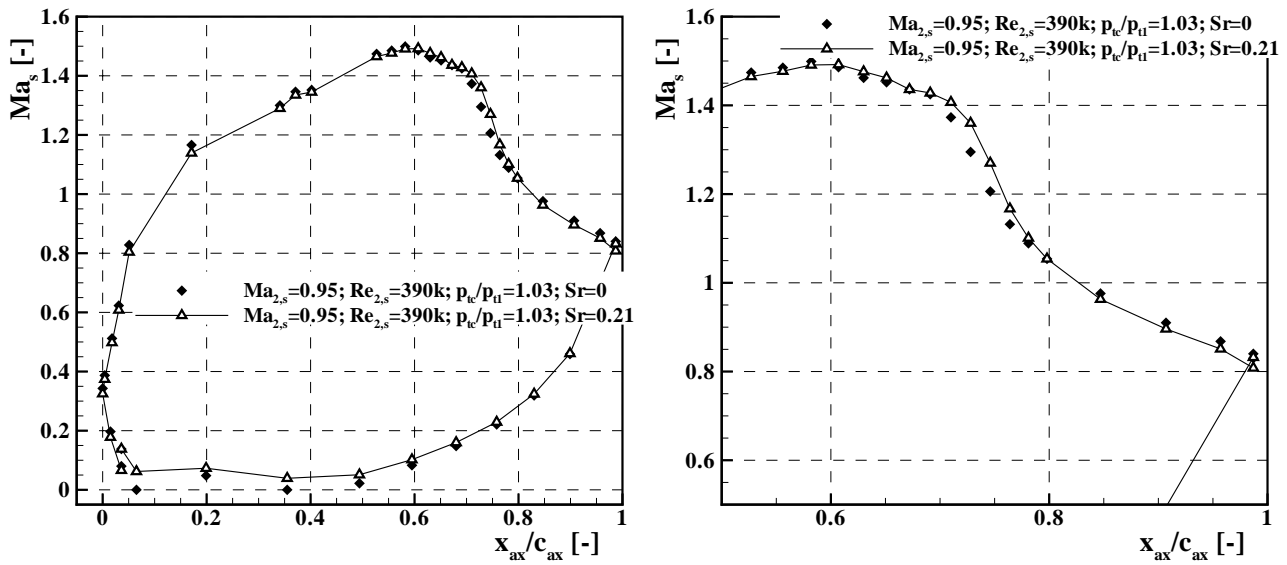
Figure 7.47: Isentropic Mach number on the blade for steady and periodic unsteady inflow at $Ma_{2,s} = 0.95$ and $Re_{2,s} = 390k$ with film cooling at $p_{tc}/p_{t1} = 1.03$ and AJVG
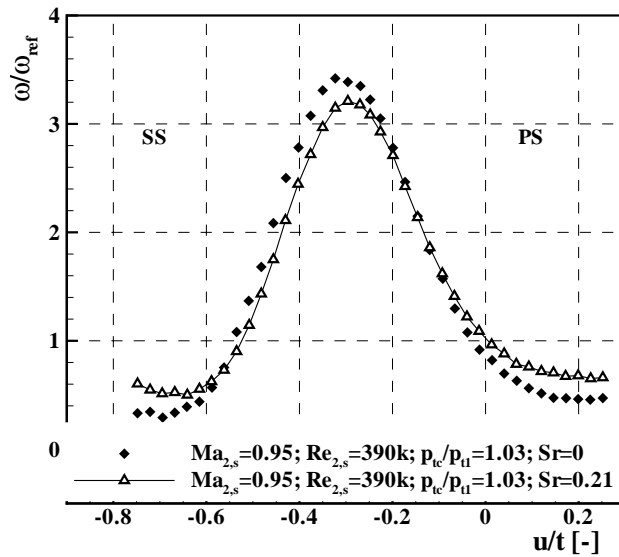
Figure 7.48: Total pressure loss coefficient for $Ma_{2,s} = 0.95$ and $Re_{2,s} = 390k$ with film cooling at $p_{tc}/p_{t1} = 1.03$ and AJVG; steady and periodic unsteady inflow

(a) $\mathrm{Ma}_{2,s} = 0.87$; $\mathrm{Re}_{2,s} = 390\,\mathrm{k}$
(b) $\mathrm{Ma}_{2,s} = 0.95$; $\mathrm{Re}_{2,s} = 390\,\mathrm{k}$
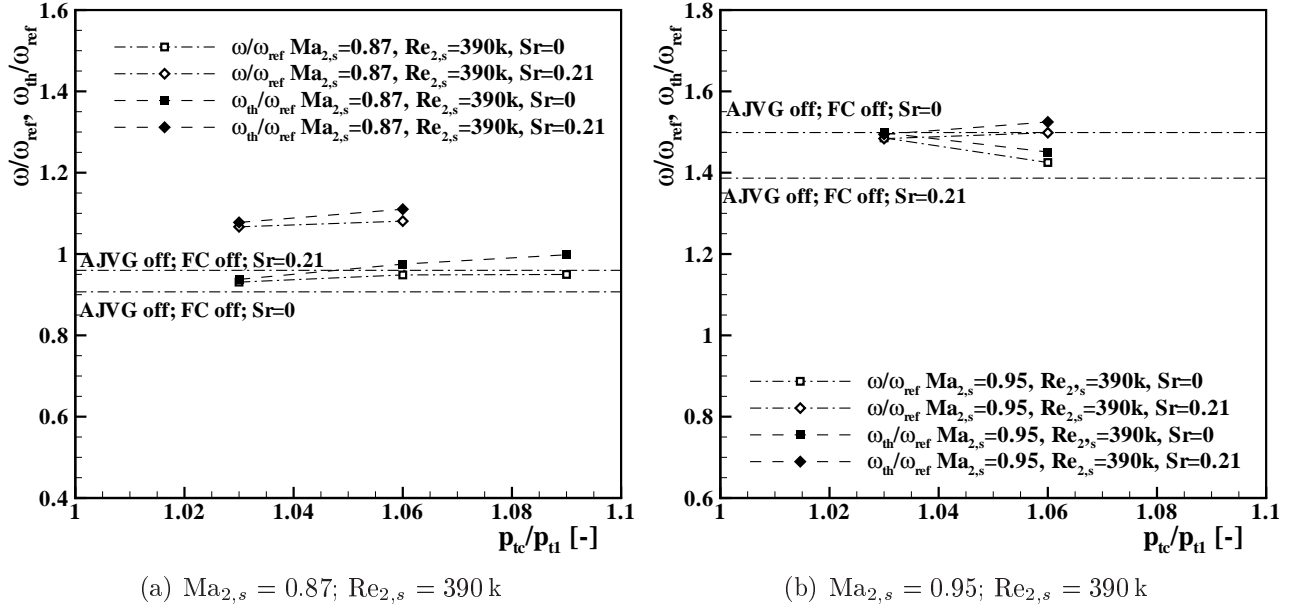
Figure 7.49: Average total pressure loss over one blade pitch for steady and periodic unsteady inflow with film cooling and AJVG

with very high loading at different Mach and Reynolds numbers. The flow on the suction side is accelerated to Mach numbers of about 1.4 and the strong shockwave at the deceleration of the flow leads to a strong flow separation at lower Reynolds number. At the high Reynolds number the flow separation is relatively small.

The AJVG have shown to efficiently suppress flow separation and to reduce total pressure losses at the low Reynolds number. It is also shown that film cooling alone as well as periodic high turbulent wakes reduce the size of the separation bubble. It turned out quite clear that, for the cases analysed here, the AJVG are not needed for reduction of the total pressure losses. On the other hand, they do not increase the losses at low outlet Reynolds number. At high Reynolds number film cooling and AJVG contribute both on their own to an increase of the total pressure losses.

8 Thermal Results on Suction Side Film Cooling at Higher Loading

For the thermal experiments a slice at mid span with a width of three film cooling hole pitches was evaluated. The presented results are besides the 2D-plots area averaged values in spanwise direction for the mentioned width.

8.1 Datum Heat Transfer on Solid Blade

At design outlet flow also numerical simulations with "ANSYS CFX 11.0" were run for the solid blade. In fig. 8.1 the measured and computed heat transfer coefficient distribution along the pressure and suction side are presented. For most of the blade chord the results agree very well, especially on the suction side. On the pressure side the heat transfer after flow separation falls very steep in the simulation and it is well under-predicted along the whole extension of the separation bubble. The simulation and measurement results are almost equal to the ones on the pressure side of the $T120C$ blade and the same process with vortex shedding and highly turbulent flow inside the separation bubble can be identified for the discrepancies between simulation and measurement. On the suction side the agreement is very good up to the start of separation. As seen in the aerodynamic measurements in chapter 7, CFD predicts the separation bubble to be smaller than measured. The measured HTC drops by 50% at $x_{ax}/c_{ax} = 0.62$, the location were separation start is seen in the static pressure distribution. The boundary layer increase at the shock location contributes to a reduction of the heat transfer but the dramatic drop seen here is most probably also due to flow separation. The heat transfer increases again from $x_{ax}/c_{ax} = 0.7$ on and the flow reattaches at $x_{ax}/c_{ax} = 0.8$, visible by the large increase of the HTC. This peak is well above the increase expected by transition to turbulent and is in the author's opinion only explainable by flow reattachment with the creation of a new thermal boundary layer. In this region CFD fails again to predict heat transfer accurately.

The measured heat transfer coefficient on the suction side for the three outlet Mach and Reynolds number combinations is given on the left of fig. 8.2. When comparing the heat transfer on the suction side, one can see that the curves for the low Reynolds number cases are similar up to the separation start. Flow separation at $\mathrm{Ma}_{2,s} = 0.95$ starts earlier and the continuous decrease at $x_{ax}/c_{ax} = 0.5$ to 0.6 could be an indication of unsteady behaviour of the separation bubble with oscillations of the separation start between these points. Downstream of the shock no explicit peak as at the design operation point is seen. This could also be due to strong oscillations. At higher Reynolds number the absolute values are as expected higher but the trend of the curve is not much different as for the design case. The heat transfer coefficient decreases around the shock location, but not as steep as for the design case and the region with very low heat transport is much more reduced. The gentle decrease is probably due to the boundary layer thickness increase prior to the shock but the results indicate still a possible small separation bubble. Reasons for this assumption are the small region with very low heat transfer and the strong increase downstream of the shock which lies well above the values for flat plate correlation with turbulent boundary layer.

Similar to the approach taken in the pressure side studies on heat transfer at different Reynolds numbers the relations

$$h \propto \mathrm{Re}^{0.5}, \quad \text{for laminar boundary layer}$$
$$h \propto \mathrm{Re}^{0.8}, \quad \text{for turbulent boundary layer,} \tag{8.1}$$
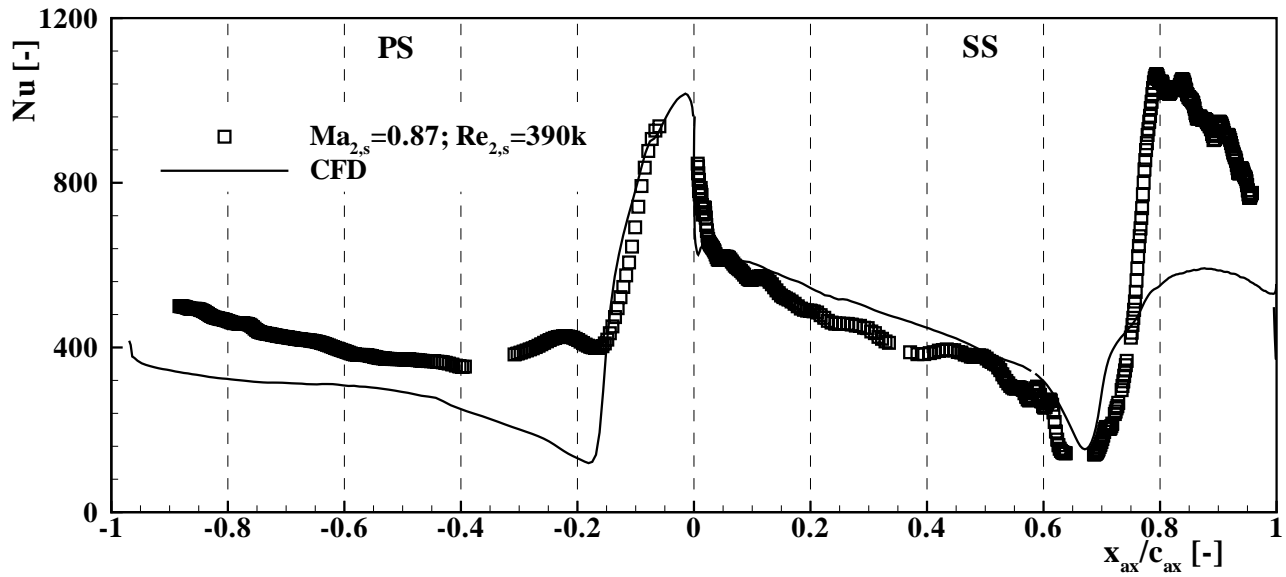
Figure 8.1: Heat transfer coefficient on pressure and suction side of the solid
blade at $Ma_{2,s} = 0.87$ and $Re_{2,s} = 390k$; comparison measure-
ments with CFD
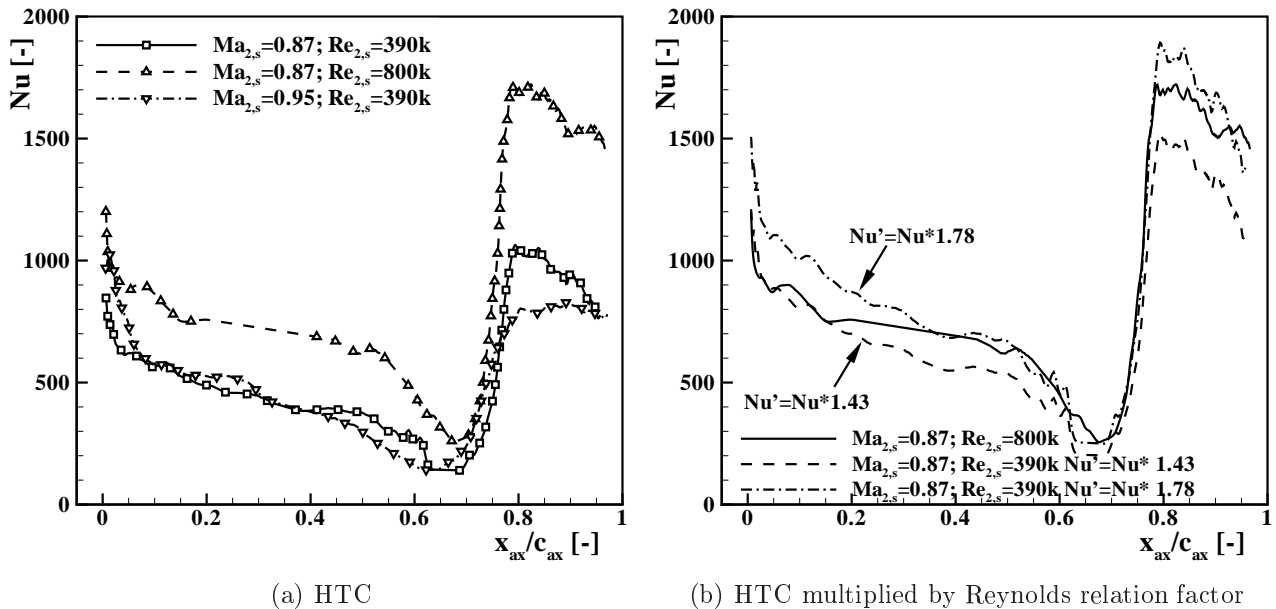
(a) HTC

(b) HTC multiplied by Reynolds relation factor

Figure 8.2: Heat transfer coefficient on suction side of the solid blade at
different main flow conditions
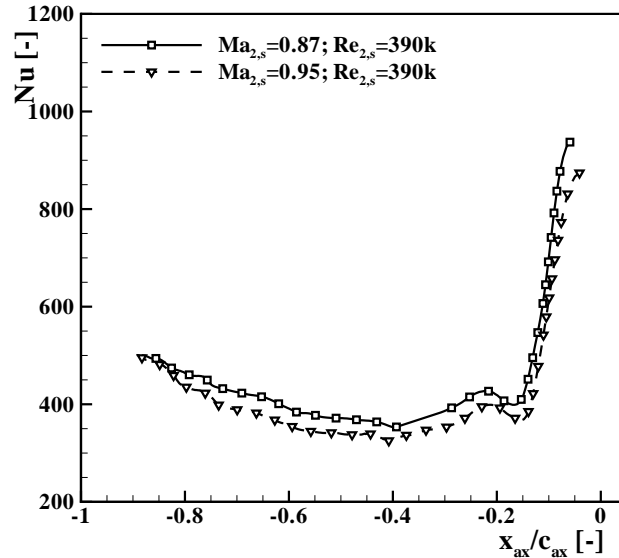
Figure 8.3: Heat transfer coefficient on pressure side of the solid blade at different main flow conditions

are used to compare the heat transfer at different Reynolds numbers and then to deduce the state of the boundary layer. For a Reynolds number ratio of $800,000/390,000=2.05$ and similar boundary layer for both flows, the heat transfer coefficients for the operation point $Ma_{2,s} = 0.87$, $Re_{2,s} = 800k$ should be either $2.05^{0.5} = 1.43$ or $2.05^{0.8} = 1.78$ times higher than the ones for the design point ($Re_{2,s} = 390k$) for laminar or turbulent boundary layers respectively. On the right of fig. 8.2 the heat transfer coefficient for the high Reynolds number case is plotted with a solid line and the values for the design point multiplied by the factors 1.43 and 1.78 are displayed with dashed lines. Up to $x_{ax}/c_{ax} = 0.15$ the curves correlate with the relation for laminar boundary layer, which indicates that for both operation points laminar flow is present. From $x_{ax}/c_{ax} = 0.4$ on the similarity is shifted towards the relation for turbulent boundary layer which is another indicator that at the high Reynolds number the flow starts transition into a turbulent state upstream of the shock. Downstream of the shock the heat transfer coefficient for the high Reynolds number case is between the lines for laminar and turbulent ratio. This is possible for turbulent boundary layer in both cases where the reattachment after flow separation is not as strong as for the design point.

The heat transfer on the pressure side was measured for both low Reynolds number cases. As seen in fig. 8.3 the differences for both Mach numbers are very small, which is in conformity with the results from Arts and Lambert de Rouvroit [9]. But still for the high Mach number case the flow separation seems to start a little earlier and the heat transfer inside the separation region is slightly lower, which were also the conclusions for the *T120C* blade.

8.2 Influence of Film Cooling With and Without AJVG

When film cooling is applied, the heat transfer usually increases in vicinity of the coolant holes. Additionally, in the aerodynamic tests it was found that film cooling with and without the use of AJVG suppresses the separation on the suction side and it is therefore expected to increase the heat transfer close to the shock location. The influence of film cooling was not measured for

(a) $Ma_{2,s} = 0.87$; $Re_{2,s} = 390k$ (b) $Ma_{2,s} = 0.95$; $Re_{2,s} = 390k$
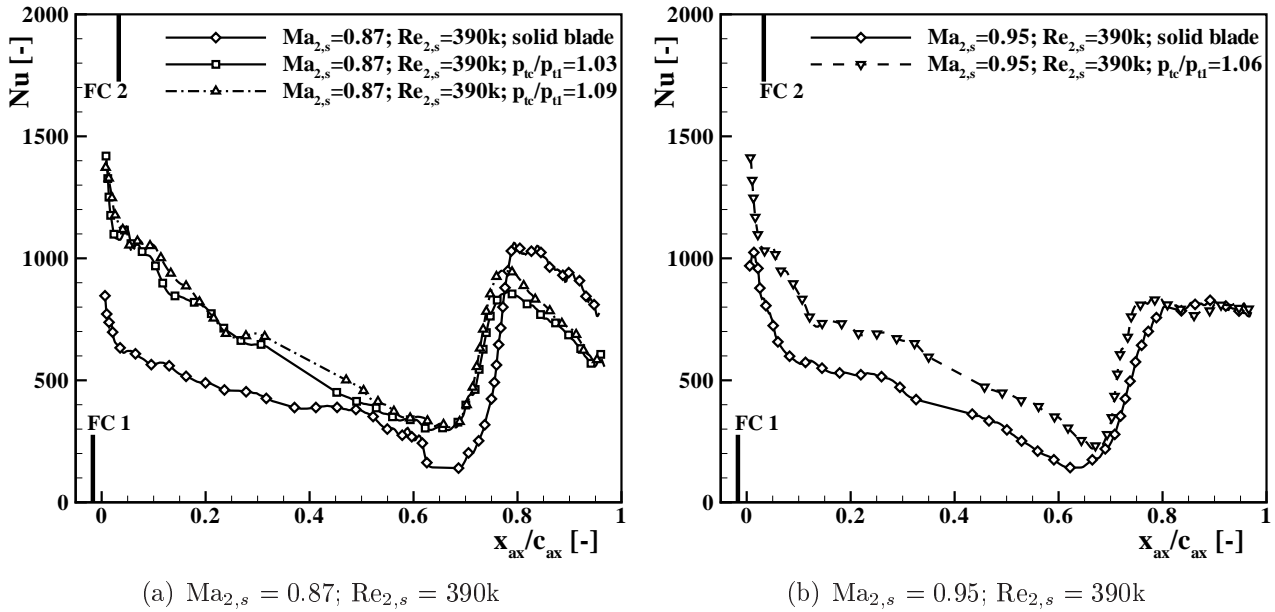
Figure 8.4: Heat transfer coefficient on suction side with film cooling and
without AJVG

the high Reynolds number case since no indications of severe flow separation are seen without film cooling.

The heat transfer coefficient for cases with film cooling but without AJVG is plotted in 8.4(a) for the design main flow conditions. The influence of the film cooling is visible in the region starting at the ejection locations (marked with bars) up to the region upstream of the shock location at $x_{ax}/c_{ax} \approx 0.6$. The film cooling increases the heat transfer due to the high turbulent mixing. Getting nearer to the shock location, the flow tends to pass a calming process due to the acceleration and the heat transfer gets more similar for cases with and without film cooling. With film cooling no evident indications of flow separation are seen and the heat transfer increase downstream of the shock is much less. This also indicates a smaller separation of the main flow with film cooling since the reattachment of the flow is less pronounced. No major differences are seen between both film cooling pressure ratios. Only after the shock the increase of heat transfer is slightly higher with high FC pressure ratio.

At the higher exit Mach number and without AJVG only a film cooling pressure ratio of 1.06 was run. The comparison of the heat transfer coefficient on the suction side between this case and at the same main flow conditions but without any cooling or AJVG is shown in fig. 8.4(b). Here again the heat transfer is increased downstream of the film cooling locations up to the shock location. The flow separation is strongly diminished but might still be present at $0.6 < x_{ax}/c_{ax} < 0.7$. Another possibility for the decrease in heat transfer coefficient could be the strongly increased boundary layer thickness at the shock. Downstream of the shock the flow is reattached and a local maximum of HTC is seen.

When applying AJVG with film cooling, the heat transfer coefficient distributions of fig. 8.5(a) and 8.5(b) are obtained for the design operation point and for $Ma_{2,s} = 0.95$ respectively. At $Ma_{2,s} = 0.87$ and $Re_{2,s} = 390k$ the sensitivity to the film cooling pressure ratio is reduced and limited to the region between the second film cooling row and the AJVG location. At the lowest

(a) $Ma_{2,s} = 0.87$; $Re_{2,s} = 390k$

(b) $Ma_{2,s} = 0.95$; $Re_{2,s} = 390k$
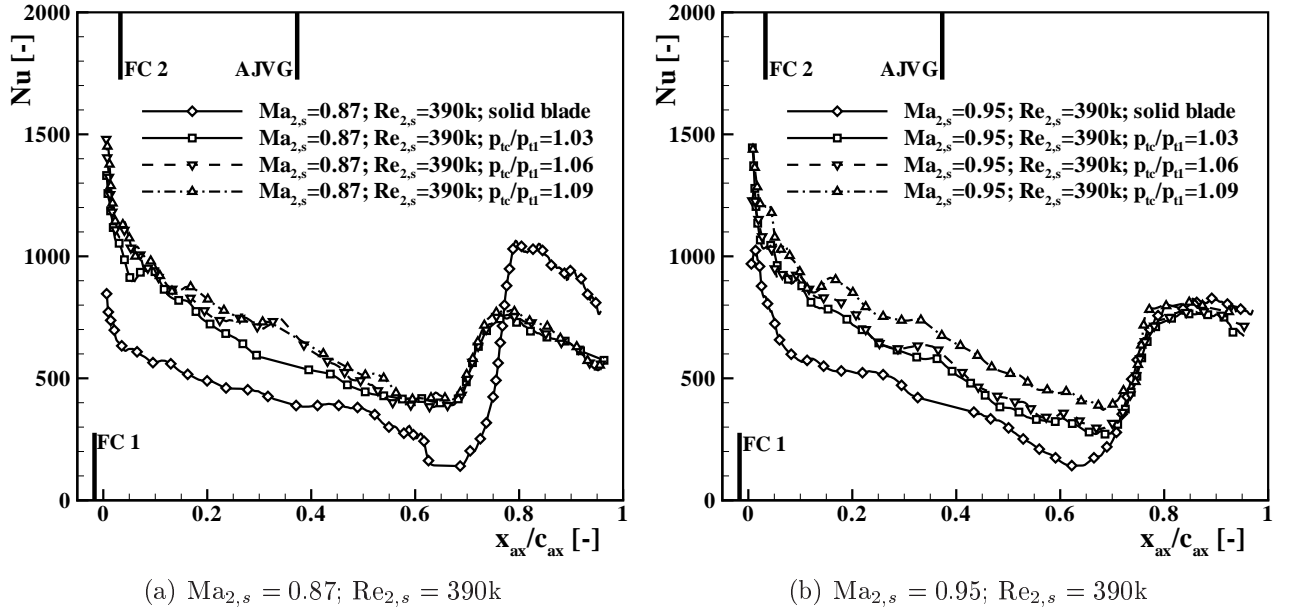
Figure 8.5: Heat transfer coefficient on suction side with film cooling and AJVG

pressure ratio of $p_{tc}/p_{t1} = 1.03$ the boundary layer seems to start relaminarization earlier, while for the other two coolant pressure ratios same levels of HTC are obtained indicating for both a smaller tendency to relaminarization and smaller sensitivity to the AJVG. Downstream of the AJVG and especially shortly upstream of the shock the values of HTC are very similar. As was shown already in the aerodynamic measurements, the shock location does not change with varying coolant pressure. The increase of HTC downstream of the shock is due to transition of the boundary layer into turbulent.

At $Ma_{2,s} = 0.95$ the heat transfer is increased with film cooling from the film cooling rows up to the shock, compared to the solid blade case. While between $p_{tc}/p_{t1} = 1.03$ and $p_{tc}/p_{t1} = 1.06$ almost no differences are seen in this region the heat transfer increases with a higher blowing ratio at $p_{tc}/p_{t1} = 1.09$. In coherence to the static pressure distribution the shock location does not move with film cooling and AJVG but the flow separation is significantly reduced. From the heat transfer distribution downstream of the shock one can see that the heat transfer is somewhat reduced with coolant and AJVG.

In fig. 8.6(a) the heat transfer coefficients for the solid blade and using film cooling at a pressure ratio of $p_{tc}/p_{t1} = 1.09$ with and without film cooling are plotted for $Ma_{2,s} = 0.87$ and $Re_{2,s} = 390,000$. The heat transfer obtained from flat plate correlations calculated with the local Reynolds number Re_x are displayed as reference lines. One can see that without film cooling the heat transfer follows approximately the line for the laminar boundary layer correlation up to the separation point. The shift of the measured line towards higher values is due to the accelerating flow and therefore smaller boundary layer thickness. Using film cooling the measured values are well above the lines for the correlations due to the strong mixing of coolant jets with main flow but drops to values between laminar and turbulent boundary layer flow. The effect of using AJVG is essentially seen around the shock location. The use of the vortex generators leads to higher heat transfer upstream of the shock compared to film cooling without

141

(a) $Ma_{2,s} = 0.87$; $Re_{2,s} = 390k$ (b) $Ma_{2,s} = 0.95$; $Re_{2,s} = 390k$
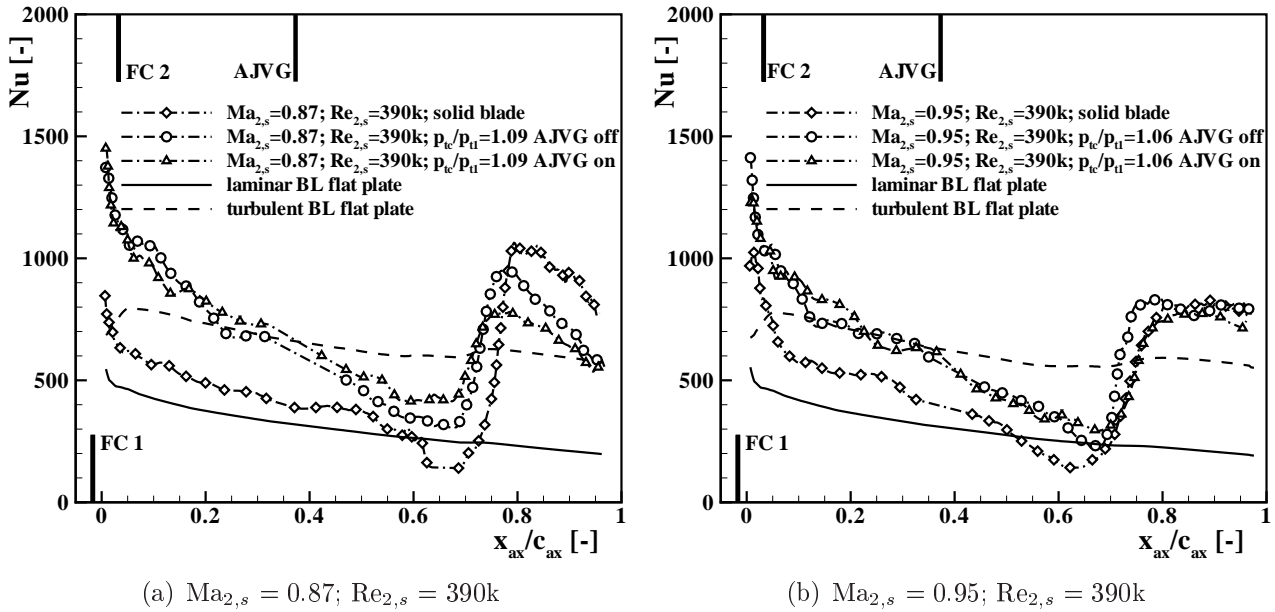
Figure 8.6: Heat transfer coefficient on suction side; comparison with correlations for flow over flat plate with constant heat flux
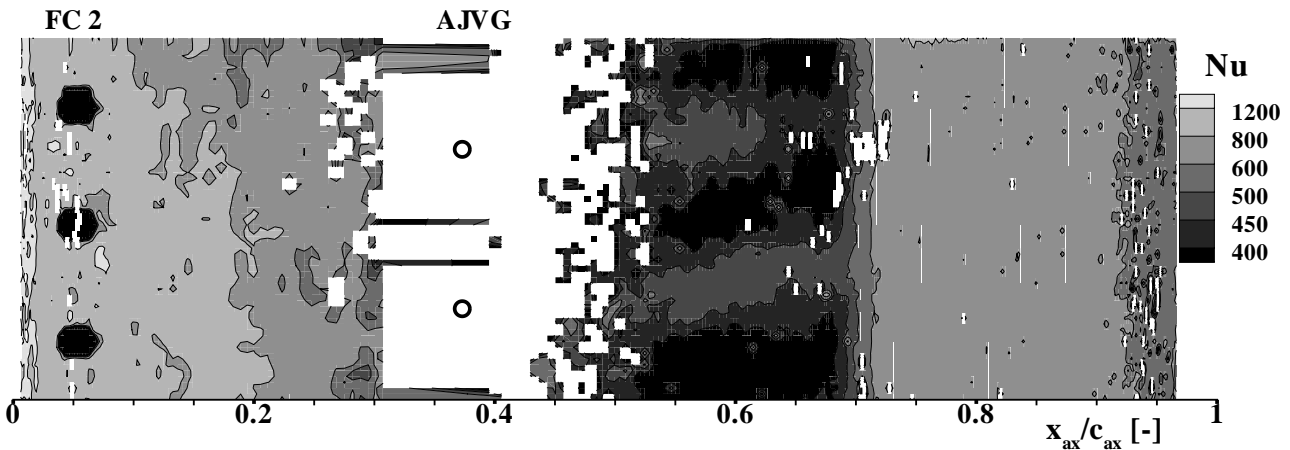
Figure 8.7: Two-dimensional heat transfer coefficient distribution on the suction side at $Ma_{2,s} = 0.87$, $Re_{2,s} = 390k$, $p_{tc}/p_{t1} = 1.03$ with AJVG

.

AJVG due to stronger turbulent mixing in the vortices created by the AJVG. Downstream of the shock the peak in heat transfer coefficient is significantly reduced using AJVG and the heat transfer curve follows almost the path of normal transition to a turbulent boundary layer.

The influence of the AJVG on heat transfer can also be seen as 2D-plots in fig. 8.7 and 8.8 for the film cooled blade with and without AJVG respectively. While without AJVG the heat transfer is uniform in span direction at $0.5 < x_{ax}/c_{ax} < 0.7$, structures are found with AJVG at this location which have the same pitch as the AJVG and can only derive from the flow structures
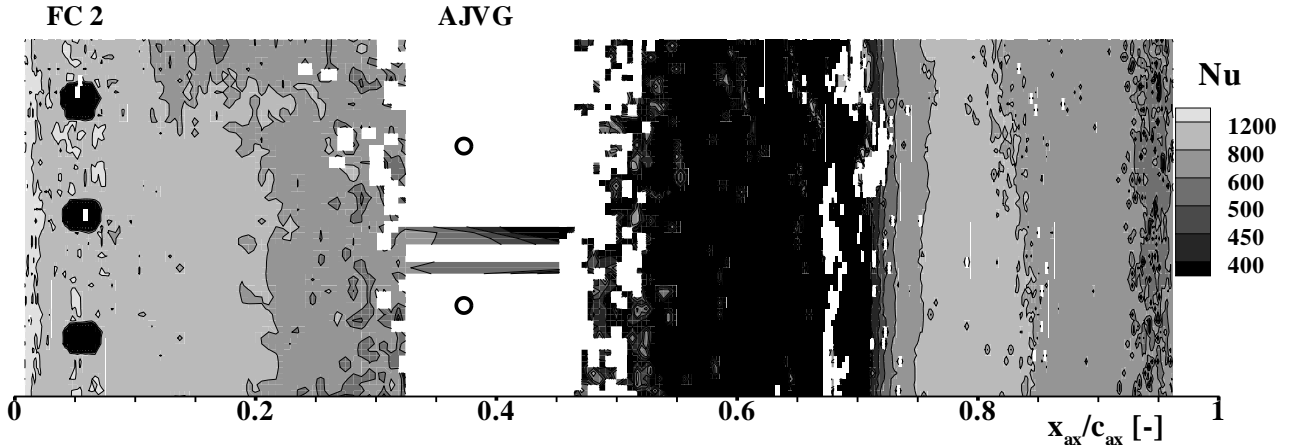
Figure 8.8: Two-dimensional heat transfer coefficient distribution on the suction side at $Ma_{2,s} = 0.87$, $Re_{2,s} = 390k$, $p_{tc}/p_{t1} = 1.03$ without AJVG

introduced by them. A closeup view on this region is given in fig. 8.9(a) and the explanation found for these structures is the creation of vortices with the downwash in the regions of high heat transfer and upwash in the regions of low heat transfer. The same structures are found in the near wall flow visualisations carried out with oil-and-dye technique in the aerodynamic measurements. In fig. 8.9(b) a closeup view on the same region is given and the reattachment line and upwash region are well visible. Comparing both figures 8.9(a) and fig. 8.9(b), the regions with few oil deposition in the near wall flow visualisation correspond to regions with low heat transfer while the reattachment lines are located in the regions with locally highest heat transfer.

Almost the same observations can be made for the high Mach number case at $p_{tc}/p_{t1} = 1.06$ in fig.8.6(b). Without AJVG lower heat transfer is present upstream to the shock, i. e. at $0.6 < x_{ax}/c_{ax} < 0.7$. Shortly downstream of the shock the use of AJVG leads again to a more gentle increase in HTC. For the solid blade this increase is also relatively moderate but the reason therefore is most likely a non permanently reattached flow.

The spanwise averaged film cooling effectiveness results as function of the axial chord are plotted in fig. 8.10 for the two operation points with use of the AJVG. Looking on the left plot for the design main flow exit conditions, one can see how the film cooling effectiveness close to the first row increases by increasing the coolant pressure ratio p_{tc}/p_{t1} from 1.03 to 1.06. The values for the highest pressure ratio are in between the other two. At the lowest pressure ratio a rapid increase in film cooling effectiveness is seen downstream of the second row while at the other two pressure ratios signs of coolant jet separation are present. Further downstream, the film cooling effectiveness increases considerably before the shock. Downstream of the shock the film cooling effectiveness decreases strongly.

For the high exit Mach number the film cooling effectiveness downstream of the first row is rather low for the lowest coolant to main flow total pressure ratio compared to the cases at $p_{tc}/p_{t1} = 1.06$ and 1.09. Downstream of the second row the film cooling jet seems to be
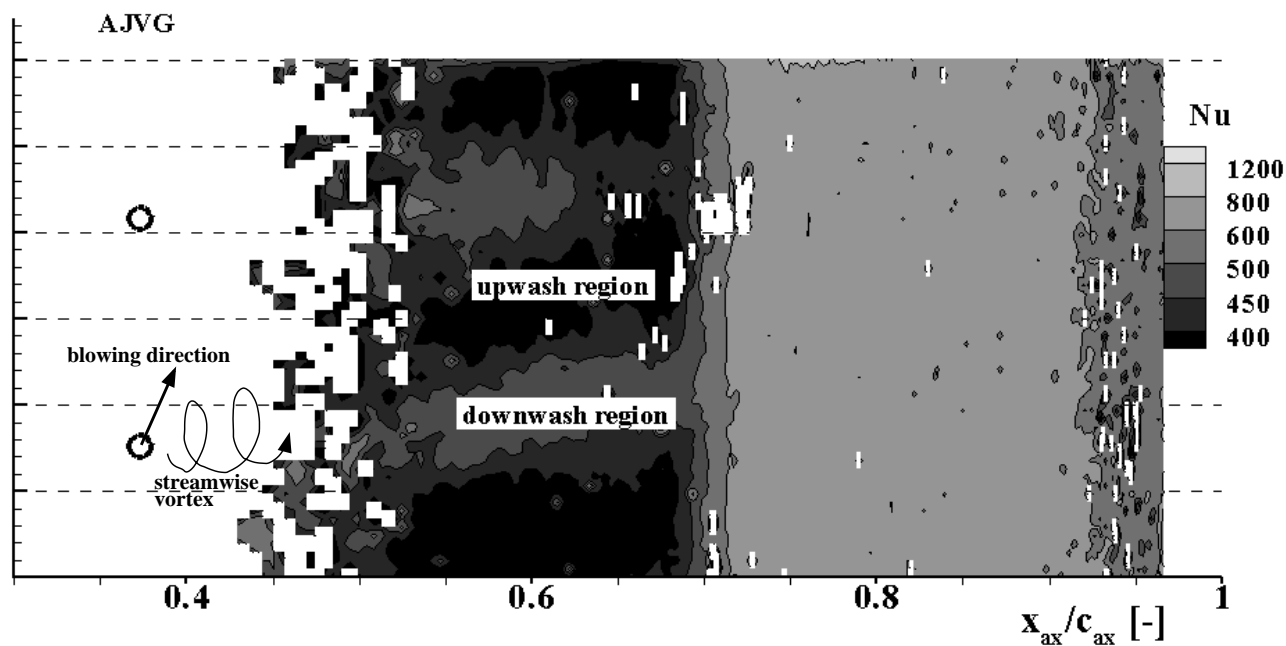
(a) Heat transfer coefficient
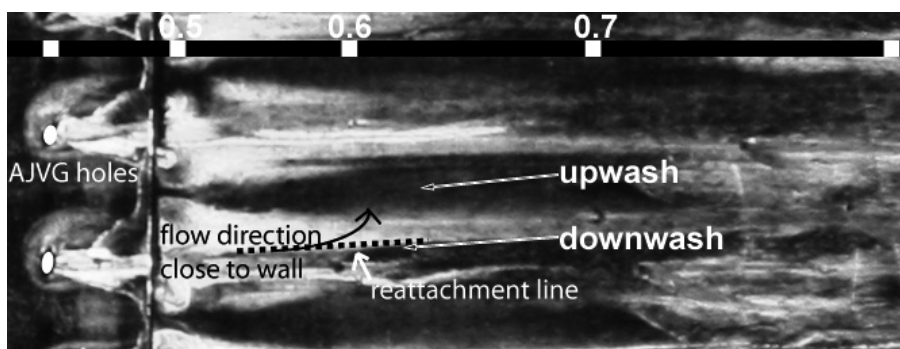
(b) Near wall flow visualization

Figure 8.9: Two-dimensional heat transfer coefficient distribution on the suction side at $Ma_{2,s} = 0.87$, $Re_{2,s} = 390k$, $p_{tc}/p_{t1} = 1.03$ with AJVG (closeup view) and near wall flow visualization
.

(a) $Ma_{2,s} = 0.87$, $Re_{2,s} = 390\,k$ (b) $Ma_{2,s} = 0.95$, $Re_{2,s} = 390\,k$
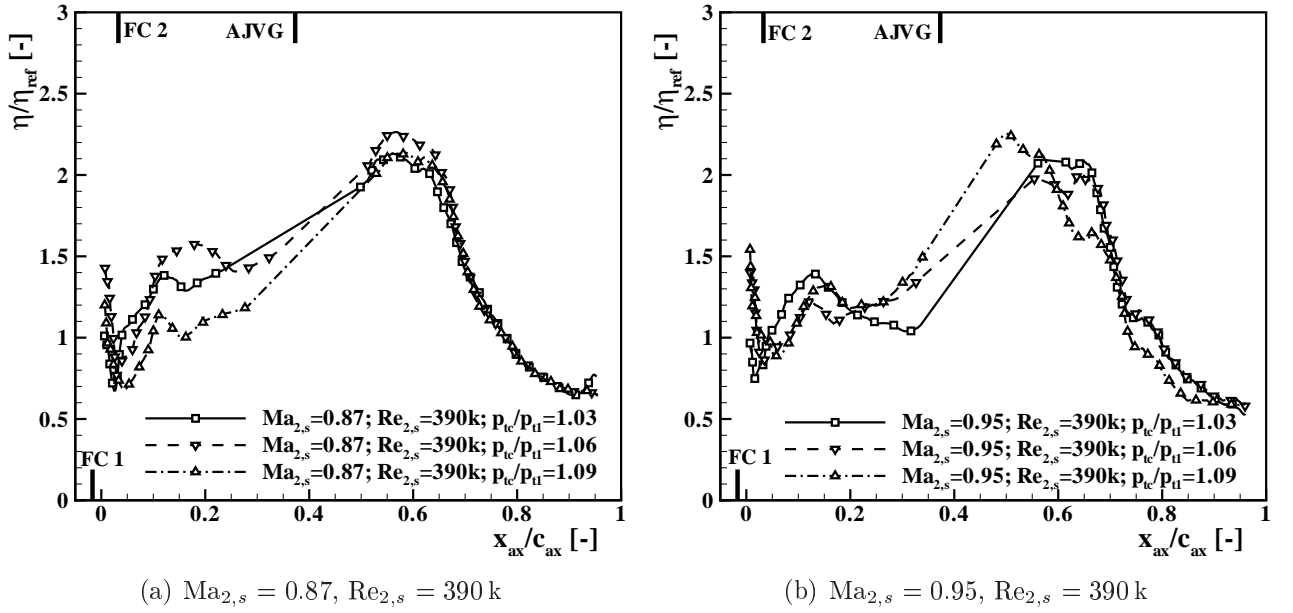
Figure 8.10: Adiabatic film cooling effectiveness with use of AJVG for $Ma_{2,s} = 0.87$, $Re_{2,s} = 390\,k$ and $Ma_{2,s} = 0.95$, $Re_{2,s} = 390\,k$

attached at a pressure ratio of 1.03 while at higher pressure ratios the jets seem to lift off from the surface. Also here an increase in film cooling effectiveness is observed upstream of the shock, but the curves depend largely on the coolant pressure ratio. As seen in the aerodynamic and heat transfer results at $Ma_{2,s} = 0.95$ the size of the separation bubble is sensitive to the coolant pressure ratio, while at $Ma_{2,s} = 0.87$ the pressure ratio does not influence much the separation zone.

The increase of film cooling effectiveness towards the shock location might at first glance be unusual but an explanation for this behaviour might be given by some thoughts on film cooling on convex surfaces by Ito et al. [85]. There the area forces are applied on a finite volume of coolant and it is shown that on convex surfaces the coolant tends to bend towards the surface if the jet is slower than the main flow. That means the film cooling effectiveness on a convex surface is going to be higher than on a flat plate if the momentum ratio in tangential direction is smaller than unity — $I \cdot \cos^2(\alpha) < 1$ — which is the case for these investigations.

In the appendices in fig. A.4 a snapshot is shown where coolant flow visualization was carried out with smoke blown off from the film cooling holes. On the right the contrast of the same image was increased in order to enhance the visibility of the coolant film. The image shows a film of coolant — seen in the images as light blue — with small height up to $x_{ax}/c_{ax} \approx 0.6$ which indicates a strong concentration of coolant close to the surface. Close to the shock location the boundary layer increases strongly and the pressure gradient acts like a ramp for the coolant. The thickness of the smoke tracer increases and is dispersed very quickly. So, two reasons may be identified for the shape of the film cooling effectiveness curves of fig. 8.10: The jets detach from the surface close to the holes and, due to the low momentum of the coolant flow and the convex curvature of the surface, are bent towards the surface. The flow acceleration calms the boundary layer state reducing turbulent mixture of coolant with main flow. A strong concentration of coolant close to the surface is then present upstream of the shock location. At
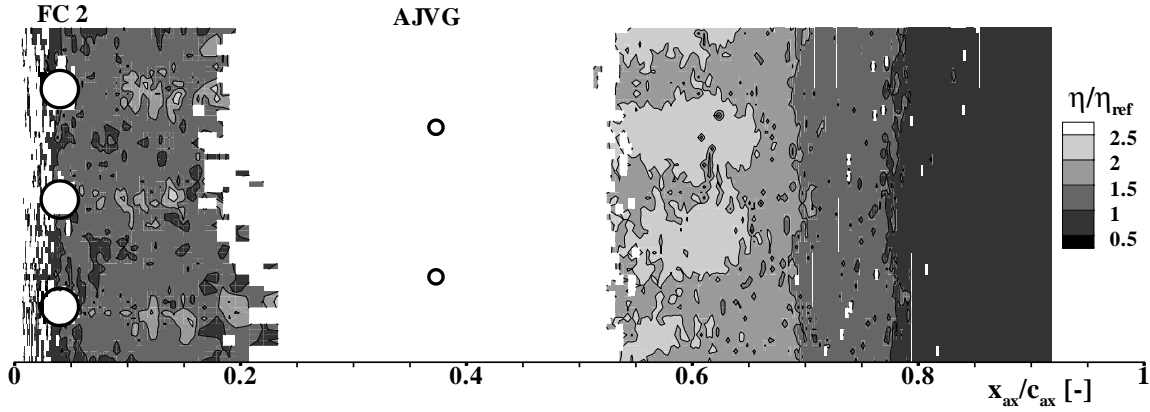
Figure 8.11: Film cooling effectiveness at $Ma_{2,s} = 0.87$, $Re_{2,s} = 390k$ with AJVG and at $p_{tc}/p_{t1} = 1.03$ (contour plot)

(a) $p_{tc}/p_{t1} = 1.03$

(b) $p_{tc}/p_{t1} = 1.09$
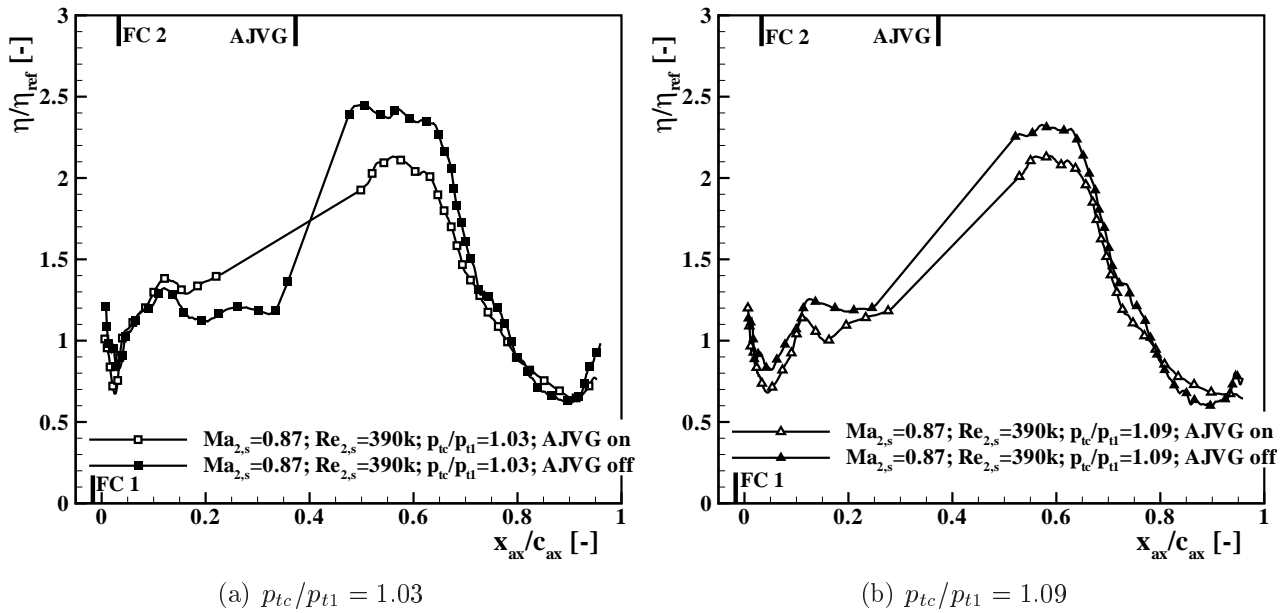
Figure 8.12: Film cooling effectiveness at $Ma_{2,s} = 0.87$, $Re_{2,s} = 390k$ with and without AJVG

about the shock location the coolant is deviated from the surface and dispersed quickly into the main flow.

This effect is also visible in fig. 8.11 where the film cooling effectiveness is plotted in 2D for the design exit Mach and Reynolds numbers at coolant pressure ratio of $p_{tc}/p_{t1} = 1.03$. Spots of very high η are seen upstream of the shock at $x_{ax}/c_{ax} \approx 0.6$. Downstream of the shock the cooling is homogeneous along the blade span due to the coolant convection. Traces of moderate film cooling effectiveness are seen downstream of the second film cooling holes indicating jet detachment close to the holes and low mixing of the coolant with the main flow in spanwise direction.

The influence of the AJVG on film cooling effectiveness at $Ma_{2,s} = 0.87$ and $Re_{2,s} = 390k$ for
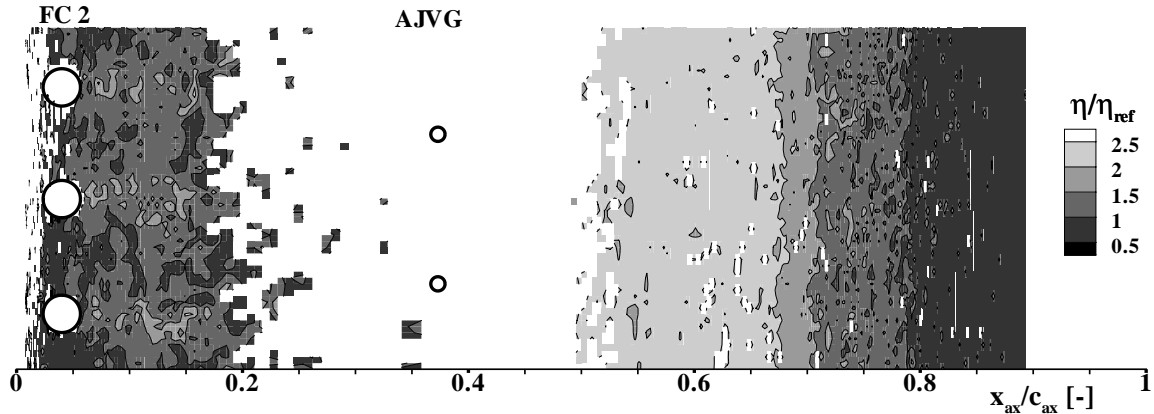
Figure 8.13: Film cooling effectiveness at $Ma_{2,s} = 0.87$, $Re_{2,s} = 390$k without AJVG and at $p_{tc}/p_{t1} = 1.03$ (contour plot)

the coolant pressure ratios of 1.03 and 1.09 is shown in fig. 8.12. For both pressure ratios the AJVG reduce film cooling effectiveness upstream of the shock due to stronger interaction of the boundary layer flow with the main flow as seen in the heat transfer measurements in chapter 8.2. Downstream of the second film cooling row and upstream of the AJVG the blockage of the main flow and deceleration leads to a small enhancement of the film cooling with AJVG at the lowest coolant pressure ratio.

The influence of the AJVG on the film cooling is especially visible on the 2D plot of fig. 8.13 without AJVG compared to the one of fig. 8.11. Both plots are for $Ma_{2,s} = 0.87$, $Re_{2,s} = 390$k and $p_{tc}/p_{t1} = 1.03$. Without AJVG the distribution of the film cooling effectiveness upstream of the shock is homogeneous in spanwise direction. By contrast, the shape of the vortices created by the AJVG is visible in fig. 8.11. As can be seen on the closeup view of the film cooling effectiveness with AJVG in fig. 8.14, the regions with lower heat transfer using the AJVG correspond to the locations of the upwash flow which drives the coolant away from the surface. The locations of the downwash and upwash regions are the same as for the HTC plot in fig. 8.9(a).

At high exit Mach number the effect of the AJVG is essentially the same as at design main flow conditions, as can be seen in fig. 8.15. Without AJVG the film cooling effectiveness is enhanced upstream of the shock and the use of AJVG increases slightly the effectiveness upstream of the AJVG ejection location.

The overall cooling effectiveness on a non-adiabatic blade is shown as temperature difference ratio in fig. 8.16 for all coolant pressure ratios with AJVG. For both measured operation points the benefits of film cooling are seen along almost the entire blade. The heat transfer increase close to the second film cooling row can lead to lower temperature difference with film cooling as well as at the separation bubble for the design point in fig. 8.16(a). Due to the upstream shift of the shock location, the local strong increase of heat transfer and the rapid decrease of the adiabatic film cooling effectiveness downstream of the shock, the overall cooling effectiveness is lower with film cooling at $x_{ax}/c_{ax} \approx 0.7$. The same is true for the high exit Mach number at highest coolant pressure since the heat transfer is well increased and the shock is shifted upstream at this pressure ratio.
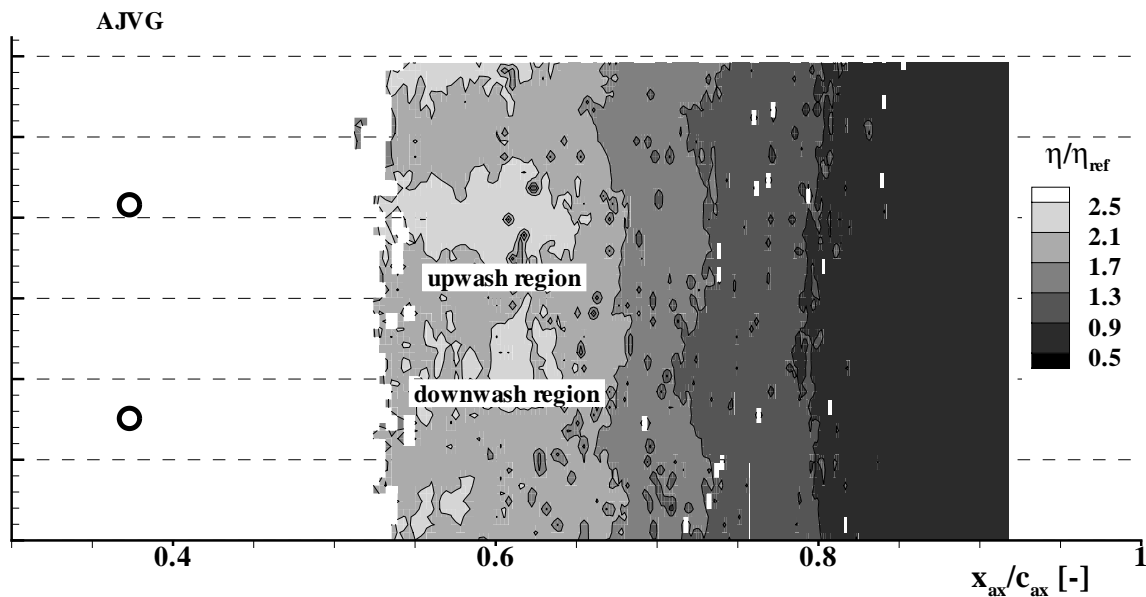
Figure 8.14: Film cooling effectiveness at $Ma_{2,s} = 0.87$, $Re_{2,s} = 390k$ with AJVG and at $p_{tc}/p_{t1} = 1.03$, closeup view
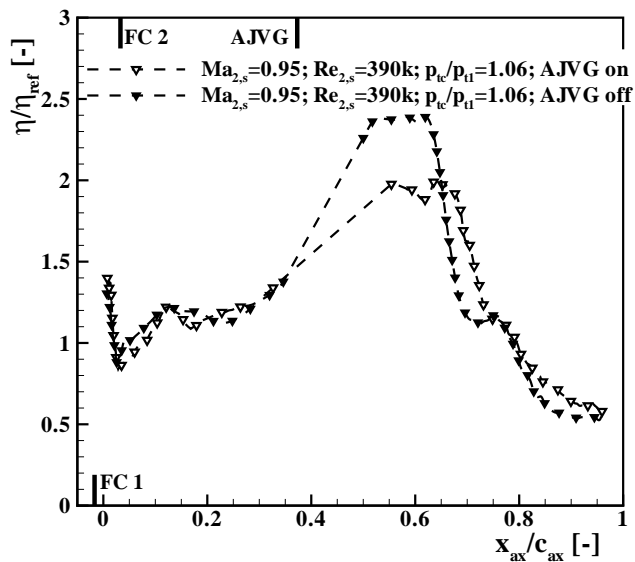
Figure 8.15: Film cooling effectiveness at $Ma_{2,s} = 0.95$, $Re_{2,s} = 390k$ and $p_{tc}/p_{t1} = 1.06$ with and without AJVG
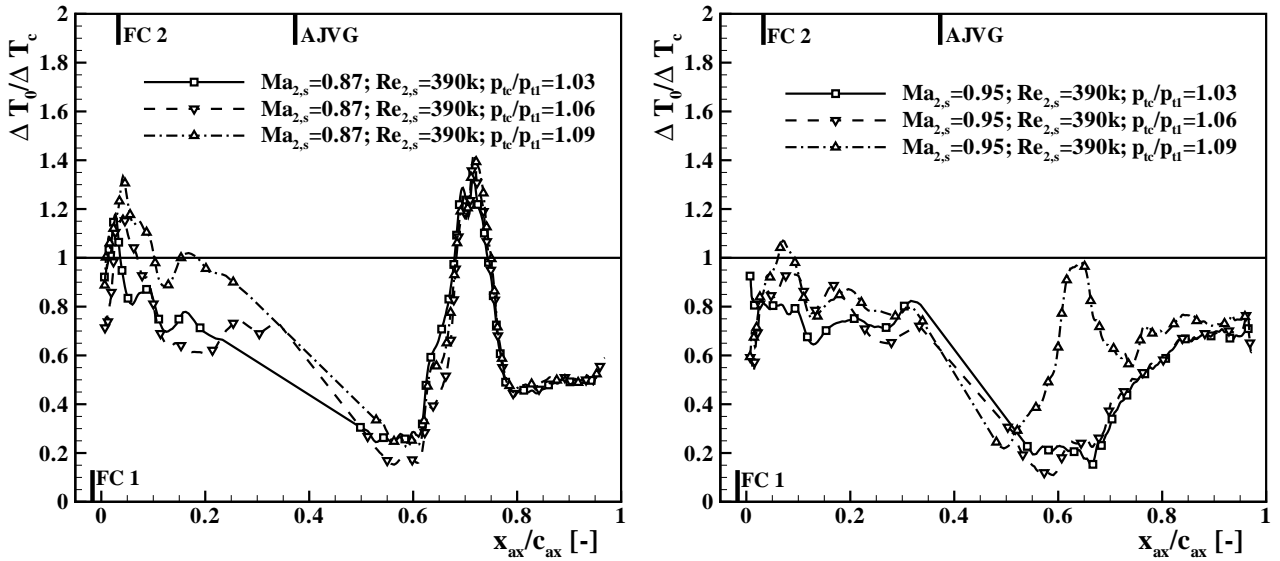
(a) $Ma_{2,s} = 0.87$; $Re_{2,s} = 390\,k$

(b) $Ma_{2,s} = 0.95$; $Re_{2,s} = 390\,k$

Figure 8.16: Temperature difference ratio on the *T120S* blade with AJVG
and steady inflow
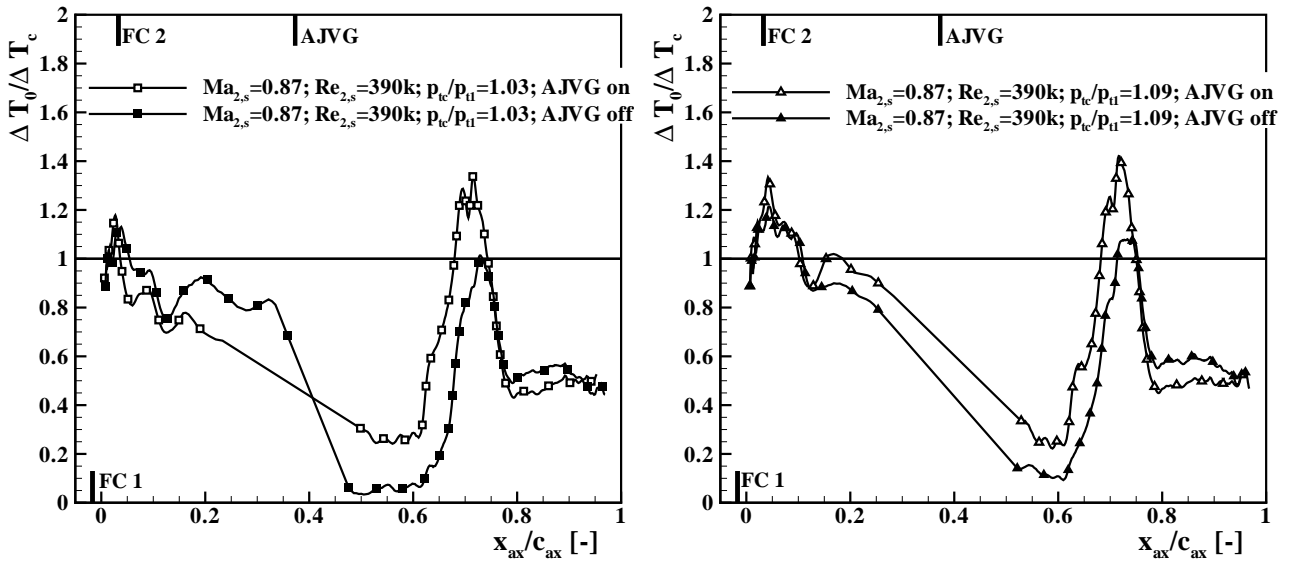
(a) $p_{tc}/p_{t1} = 1.03$

(b) $p_{tc}/p_{t1} = 1.09$

Figure 8.17: Temperature difference ratio on the *T120S* blade at $Ma_{2,s} =$
0.87, $Re_{2,s} = 390\,k$ and steady inflow (with and without AJVG)
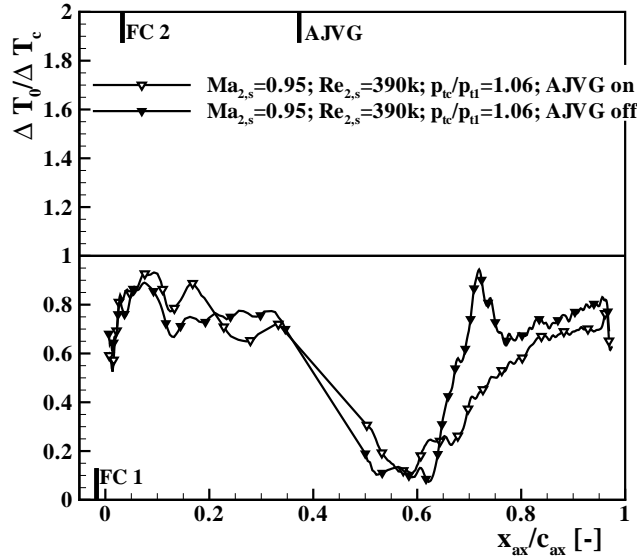
Figure 8.18: Temperature difference ratio on the *T120S* blade at $Ma_{2,s} = 0.95$, $Re_{2,s} = 390\,k$, $p_{tc}/p_{t1} = 1.06$ and steady inflow (with and without AJVG)

A comparison of the overall cooling effectiveness with and without the use of the AJVG is given in fig. 8.17 for the design operation point and in fig. 8.18 for the high exit Mach number. For the design point the overall effectiveness with AJVG is reduced at the separation bubble due to the increased heat transfer while downstream of the shock the opposite is true due to the same reasons but in opposite direction. For the high exit Mach number the effectiveness is increased with AJVG at the shock location, see fig. 8.18. As was also seen in the results of the adiabatic film cooling effectiveness, the AJVG seem to be able to transport some coolant through the lambda foot at the shock, but not to deep into it since the coolant is then also convected very quickly.

8.3 Influence of Periodic Unsteady Inflow

Using periodic wakes at the inlet for simulation of the interaction of stator and rotor, the influence of highly turbulent periodic wakes on the heat transfer was analysed. The heat transfer with periodic unsteady inflow was measured at both operation points at Re = 390k with film cooling at coolant pressure ratios of 1.03 and 1.06 and using the AJVG.

At $Ma_{2,s} = 0.87$, $Re_{2,s} = 390k$ the periodic wakes influence essentially the regions further downstream of the film cooling holes as can be seen in fig. 8.19(a). The interaction of the coolant jets with the main flow is the predominant factor close to the holes. Further downstream, with steady inflow, the flow tends to calm and shows signs of relaminarization. With periodic wakes the heat transfer keeps at high values and follows essentially the line from flat plate correlations with turbulent boundary layer up to the shock. Downstream of the shock the heat transfer coefficient increases to higher values than with steady inflow.

At the high exit Mach number the heat transfer coefficient values with unsteady inflow are slightly lower than at the design main flow conditions, as can be seen in fig. 8.19(b). The heat

(a) $Ma_{2,s} = 0.87$; $Re_{2,s} = 390k$ (b) $Ma_{2,s} = 0.95$; $Re_{2,s} = 390k$
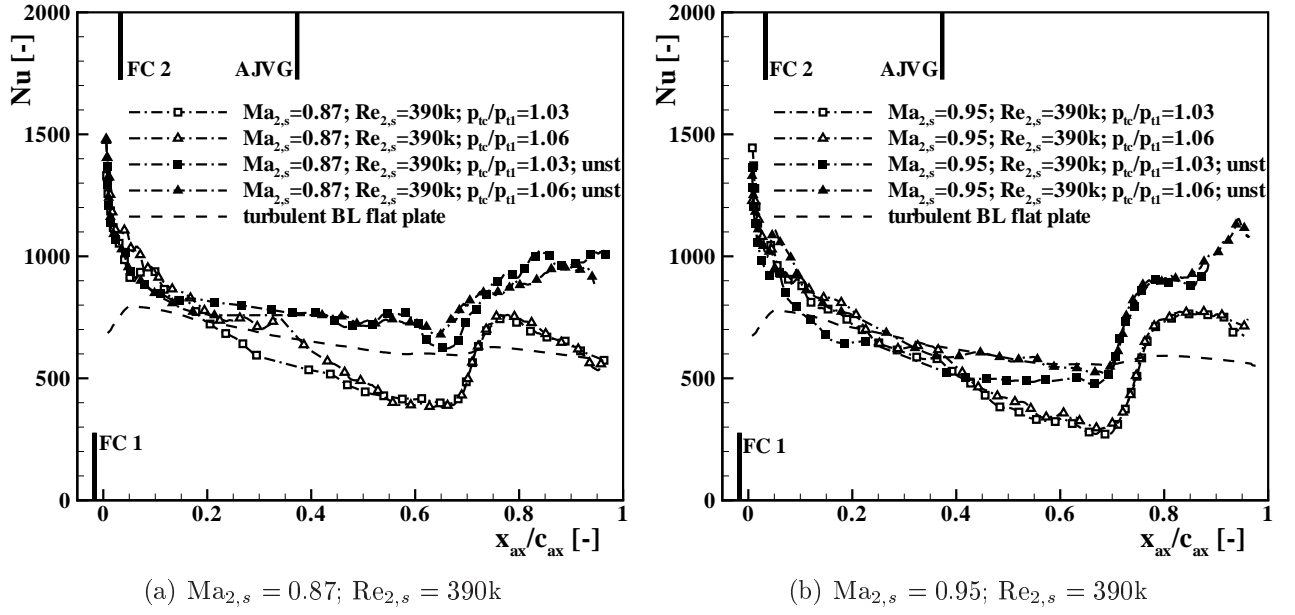
Figure 8.19: Heat transfer coefficient on suction side with steady and periodic unsteady inflow

(a) $p_{tc}/p_{t1} = 1.03$ (b) $p_{tc}/p_{t1} = 1.06$
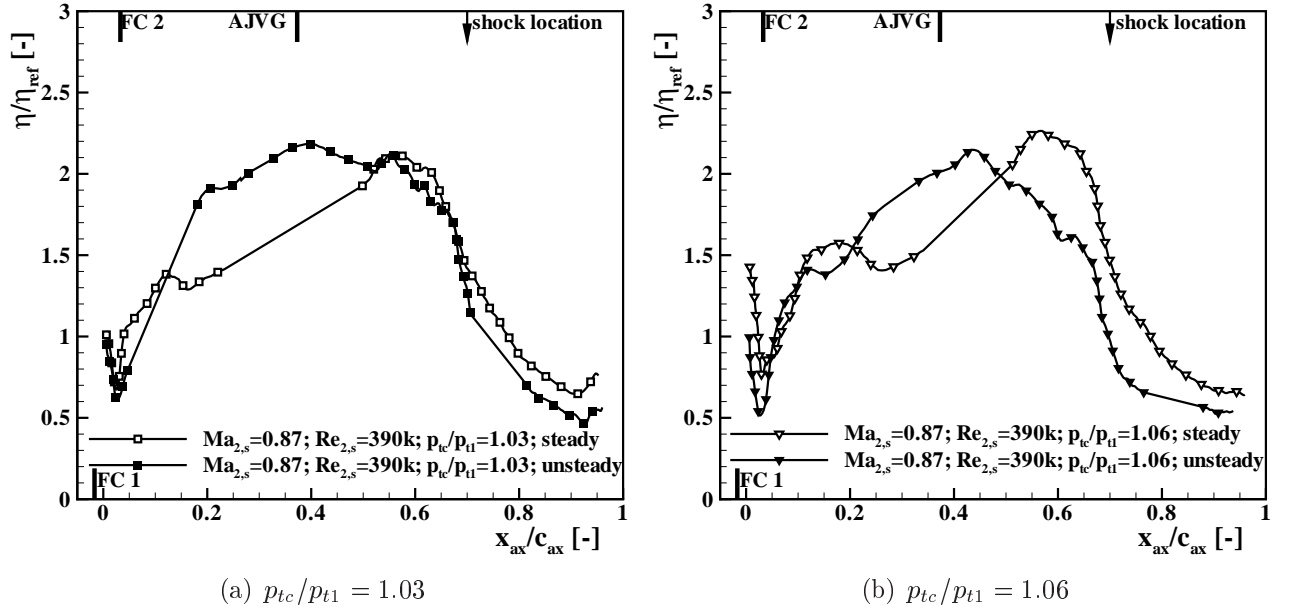
Figure 8.20: Film cooling effectiveness at $Ma_{2,s} = 0.87$, $Re_{2,s} = 390k$ and AJVG with steady and periodic unsteady inflow

transfer coefficient close to the leading edge is slightly reduced with unsteady wakes and lowest pressure ratio. From $x_{ax}/c_{ax} = 0.4$ on, the heat transfer with unsteady wakes follows the trend of the curve for turbulent boundary layer and increases by the same amount as with steady inflow at the shock location.

The effect of periodic unsteady inflow on the spanwise averaged adiabatic film cooling effec-

(a) $p_{tc}/p_{t1} = 1.03$ (b) $p_{tc}/p_{t1} = 1.06$
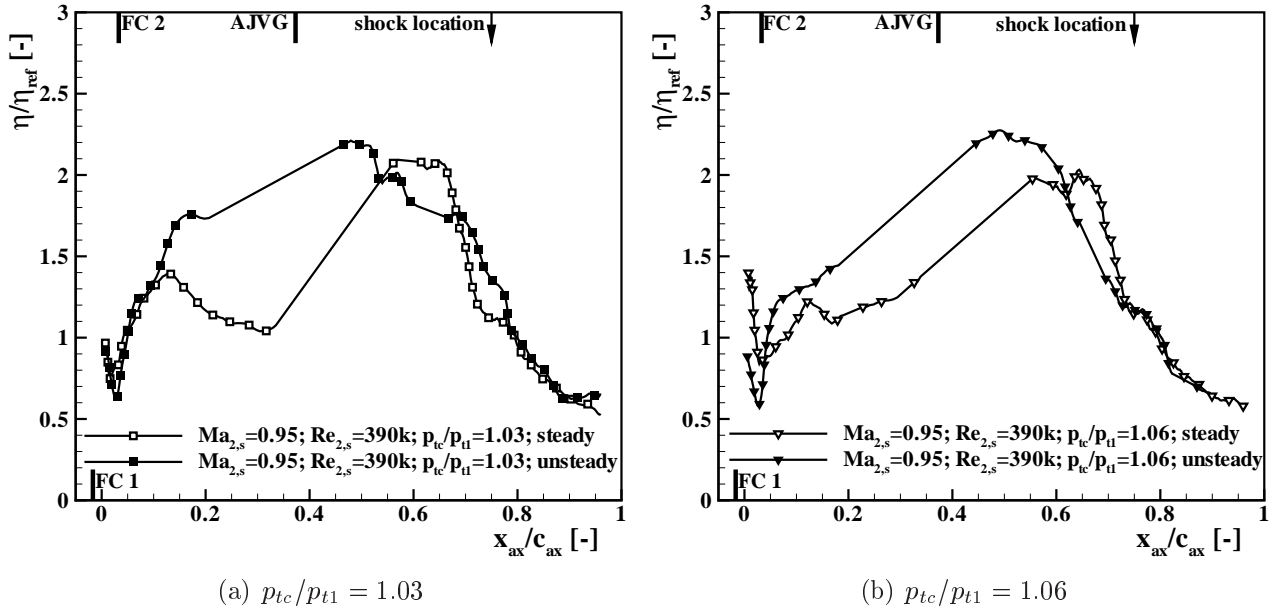
Figure 8.21: Film cooling effectiveness at $Ma_{2,s} = 0.95$, $Re_{2,s} = 390k$ and AJVG with steady and periodic unsteady inflow

tiveness is shown in fig. 8.20 for the design exit Mach and Reynolds number. At low coolant pressure ratio in fig. 8.20(a) the peak values of FCE upstream of the shock are not affected by the high turbulent wakes. It seems as if the AJVG have the largest effect on film cooling effectiveness in this region. The region at $0.3 < x_{ax}/c_{ax} < 0.5$ could not be monitored with steady inflow but with periodic unsteady inflow the coolant seems to bend stronger towards the surface and the cooling effectiveness is enhanced around $x_{ax}/c_{ax} = 0.2$. For both pressure ratios the coolant dissipation downstream of the shock is stronger with periodic unsteady inflow resulting in lower effectiveness values, which is consistent with the high heat transfer values measured with unsteady inflow in this region.

At medium pressure ratio of $p_{tc}/p_{t1} = 1.06$ cooling deteriorates close to the second film cooling hole but also here it is enhanced from $x_{ax}/c_{ax} = 0.2$ on up to $x_{ax}/c_{ax} \approx 0.5$ with unsteady inflow. The peak in film cooling effectiveness is reached much earlier with unsteady inflow and the coolant is then already dissipated prior to the shock.

Almost similar effects are seen for the high exit Mach number in fig. 8.21 where the spanwise averaged film cooling effectiveness with steady and periodic unsteady inflow is compared for $p_{tc}/p_{t1} = 1.03$ and 1.06. It can be seen that the wakes prevent jet lift off downstream of the second row of film cooling holes — especially at higher pressure ratio in fig. 8.21(b) — and the jets are stronger bent towards the surface shifting the effectiveness peak further upstream. The effectiveness downstream of the shock is not very much affected by the turbulent wakes. At the lowest coolant pressure ratio the shift of the shock downstream is also perceived in the distribution of the adiabatic film cooling effectiveness.

For an evaluation of the overall cooling effectiveness on a non-adiabatic blade the heat transfer values without film cooling and with periodic unsteady inflow are needed. This was not possible to measure due to lack of time during the measurement campaign. Nevertheless, when computing the temperature difference ratio with the heat transfer on the solid blade with steady

(a) $Ma_{2,s} = 0.87$ (b) $Ma_{2,s} = 0.95$
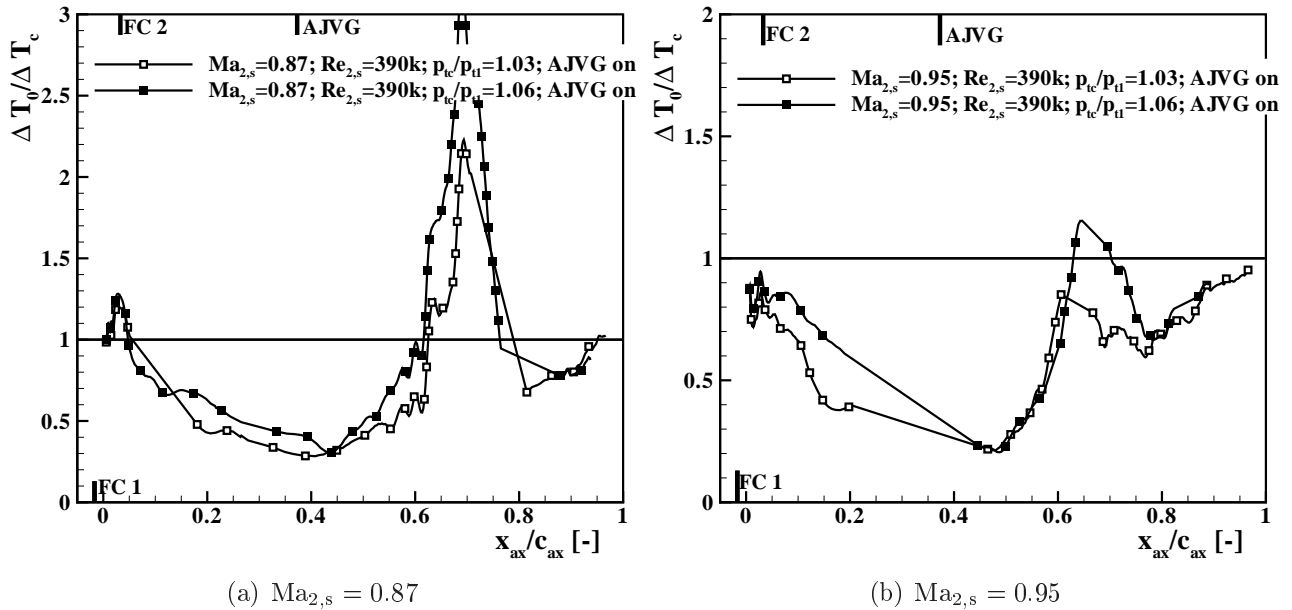
Figure 8.22: Temperature difference ratio on the suction side of the *T120S* blade for both Mach numbers at low Reynolds number and with periodic unsteady inflow

inflow still a good cooling performance is obtained as shown in fig. 8.22 (please note the scale change in fig. 8.22(a)). Using the heat transfer values for periodic unsteady inflow one could expect even better performance, especially at the separation location, since the unsteady inflow alone reduces the separation bubble size and increases therefore local heat transfer.

8.4 Summary of the Thermal Analysis on the Suction Side at Higher Loading

Measurements of the heat transfer coefficient and of the adiabatic film cooling effectiveness on the suction side were carried out for a HPT blade cascade at very high loading. The heat transfer measurements confirm the presence of a large separation bubble at low Reynolds number of the main flow. The use of film cooling increases strongly the heat transfer close to the holes but the flow is calmed due to the strong acceleration and the heat transfer values fall to numbers close to the ones in the uncooled case. It is shown that film cooling reduces the flow separation and the shape of the vortex structures created by the AJVG is seen in 2D plots of the heat transfer coefficient. The shock-wave destroys these structures and very high values of heat transfer were measured downstream of the shock. The heat transport downstream of the shock can be reduced by film cooling and vortex generation.

The adiabatic film cooling effectiveness is very high some hole lengths downstream of the ejection location due to the strong curvature of the surface. The relaminarization of the flow enhances also the film cooling effectiveness. The AJVG reduce the film cooling effectiveness upstream of the shock due to the vortices transporting coolant away from the wall in the upwash region. The high turbulent mixing downstream of the shock decreases strongly the adiabatic film cooling effectiveness towards the trailing edge. The overall effect of film cooling on a non-adiabatic blade is over most of the surface length positive and AJVG can increase the positive

153

effect downstream of the shock.

Periodic unsteady inflow increases the heat transfer and prevents the flow from relaminarization upstream of the shock location. The film cooling effectiveness is also reduced by the turbulent wakes but an overall positive effect of film cooling can still be seen.

9 Conclusions and Outlook

Turbomachines are perhaps one of the most sophisticated machines available today and the most advanced technologies are used in order to improve the efficiency and durability as well as to reduce manufacturing and maintenance costs. Though the basic work principle of a jet engine or gas turbine has not significantly changed in the past seven decades, the machines have suffered considerable modifications in detail and the design principles are now very different than they were for the first machines. A very critical part of the turbomachine is the high pressure turbine due to the high temperatures of the fluid in this region. The turbine inlet temperature has been increased in order to enhance the cycle efficiency of the machine and is now well beyond the melting temperature of the materials used in the engine. Combinations of different cooling techniques are therefore used in order to keep the material temperature below a critical value. One of these techniques is film cooling, where cooler fluid is blown out from the airfoils and end-walls of the turbine and protects the metallic surfaces of the machine against the hotter fluid. These cooling techniques are well established and further improvements are difficult to realize.

Modern turbine design tries also to reduce the size and weight of the engine in order to reduce manufacturing and maintenance costs as well as fuel consumption. A way to achieve this goal is to reduce the number of blades per stage by increasing the spacing between each blade. A drawback of this increase in blade pitch is the higher aerodynamic loading which leads to high supersonic velocities on the suction side. The deceleration between peak velocity and trailing edge is then accompanied by shock waves and in many cases also by strong flow separation. Both increase the total pressure losses considerably and limit the increase of the blade pitch.

Future turbine designs at higher pitch need therefore to control the flow separation in order to keep the degradation of the efficiency at acceptable levels. Though the aerodynamic efficiency of a turbine with conventional pitch might never be reached at very high loading, a higher efficiency could be achieved in overall due to less weight, less coolant consumption and less wall friction.

This thesis shows thorough investigations on film cooled blades with large zones of main flow separation. The investigations are in great part done experimentally and selected numerical analysis are carried out in order to test the predictability of such complex flows with modern numerical tools. The experiments were carried out with linear turbine blade cascades in the high-speed cascade wind tunnel of the Institute of Jet Propulsion of the University of the Federal Armed Forces Munich. The investigations were run at engine relevant Mach and Reynolds numbers and aerodynamic as well as thermal parameters were measured. The first of the two cascades investigated here has a conventional blade pitch, but has a strong concave curvature on the pressure side in order to force a large flow separation. Film cooling is used in order to reduce the flow separation and to cool the region with separated flow and at the reattachment line. A large database of the cascade aerodynamics was previously acquired. Homeier [81] shows in his thesis experimental results of the Mach number distributions on the blade, total pressure loss traverses at the outlet, near wall flow visualizations and measurements with hot film. Here, this database and flow analysis is enhanced by measurements of the local heat transfer coefficient and adiabatic film cooling effectiveness. As said before, temperature is a critical issue in the high pressure turbine and turbine designers have not only to optimize

the aerodynamics but have also to consider the temperature distribution on the blade. The knowledge of the heat transfer and film cooling effectiveness is mandatory to estimate the metal temperature at different operating points.

The pressure side investigations show a highly complex and unsteady flow separation process and a high turbulence intensity inside the separation bubble. With the use of hot wire anemometry, also the presence of a characteristic vortex shedding frequency could be demonstrated. The intense velocity fluctuations have a strong impact on the local heat transfer coefficient and film cooling effectiveness. Standard RANS solvers are by far not able to predict the thermal aspects of this flow as is also shown in this work. More advanced techniques, such as DES and LES, are able to improve the predictability but the available computer resources limit strongly the applicability of these more advanced techniques.

The application of the high lift technology was then tested on a cascade with the same blade geometry but largely increased pitch. The pitch increase by 13% leads to high supersonic Mach numbers on the suction side with the supersonic pocket extending along the complete blade pitch. Measurements of the aerodynamic properties, such as the static pressure on the blade and the total pressure losses were carried out as well as of the heat transfer and adiabatic film cooling effectiveness. The strong separation on the suction side is controlled by means of air jet vortex generators. The vortex generators suppress efficiently the flow separation and reduce the total pressure loss, though the values as on the cascade with moderate pitch are not achieved. Reasons therefore are the losses behind the strong shock and some turbulent mixing. Film cooling showed also to be able to suppress flow separation on the suction side and the use of the vortex generators might be of use in order to increase the cooling effectiveness downstream of the shock wave. The heat transfer measurements confirmed the flow separation without film cooling and streamwise vortices and its effective suppression whenever film cooling or vortex generating devices are used. Steady RANS simulations showed also to be able to predict quite reasonably the heat transfer without film cooling on the suction side, but the flow separation is not completely matched.

The blade surface temperature was measured with thermochromic liquid crystals (TLC). The measurement technique was introduced and a new method was developed in order to account for heat conduction inside the test blade. This technique makes use of finite element analysis with a commercial solver. The process established at the institute runs fully automatized and transfers the data to and from the FEM solver autonomously in order to estimate the heat transfer coefficient and the adiabatic film cooling effectiveness. It is shown that the account for thermal conduction can change considerably the measured values of these parameters and that measurements on walls with small thickness need urgently to account for this influence.

A viewing angle correction method for measurements with TLC is presented which corrects the colour perception at different illumination and observation angles. It is demonstrated that an on-axis arrangement with light source and camera on the same axis is the most effective way of measuring the temperature with TLC. The uncertainty due to different viewing and illumination angle is, with this disposition of the devices, less than 0.02° C. In cases with a high oblique observation angle a different position of the light source can enhance the intensity of the acquired signal. In this case, it is shown that the correction method implemented here is needed in order to transform the perceived wavelength to the pitch of the crystals.

The adiabatic film cooling effectiveness is measured on a quasi adiabatic blade and the definition of this parameter is equivalent to the concentration of coolant close to the blade surface. In a

real engine the blade is non-adiabatic and a transformation of the measured values has to be done in order to estimate the cooling performance and the wall temperature on the metal blade. A method widely found in open literature is the heat flux ratio. This can be evaluated directly by measuring the heat transfer into a non-adiabatic blade with and without film cooling. In this case the temperature ratio between coolant and main flow in the experiments has to be equal as in the machine. A change in the interior of the blade, changing the heat conduction, may also influence the heat flux ratio. Whenever the adiabatic film cooling effectiveness is measured, the heat flux ratio is computed with a constant overall film cooling effectiveness typical for modern turbines, but which is not really known. As can be easily understood, this transformation from measured heat transfer coefficient and adiabatic film cooling effectiveness to heat flux parameter is not completely satisfactory. In order to estimate the overall cooling performance only with known values, a parameter called temperature difference ratio was derived which uses the measured heat transfer coefficient and adiabatic film cooling effectiveness. This method allows to use iterative computational methods in order to correctly estimate the cooling performance, even with different internal geometries of the blade and different internal cooling configurations.

The computation of the temperature difference ratio for a random configuration of the interior of the blade showed that it is difficult to cool the flow separation zone on the pressure side with film cooling. The coolant flow enhances the heat transfer inside the separation bubble largely and little coolant is convected towards the surface. In general it turns out easier to cool the surface from the reattachment line up to the trailing edge. Film cooling on the suction side was effective even on a non-adiabatic blade and the vortex generators enhanced slightly the cooling performance downstream of the shock.

Future studies on the pressure side could focus firstly on the simulation of the heat transfer and film cooling effectiveness. Deeper studies with LES models could improve the predictability of the flow and give hints for efficient turbulence modelling. Also the flow after flow reattachment up to the trailing edge needs improvements to the available turbulence models.

On the suction side, some further experimental studies on the air jet vortex generators could be made in order to drive more coolant through the shock allowing improved cooling further downstream. With the configurations tested here the coolant is convected very quickly at the shock. Numerical studies with film cooling should be continued in order evaluate the predictability of the conventional flow solvers.

Bibliography

[1] R. Abhari. Impact of Rotor-Stator Interaction on Turbine Blade Film Cooling. *J. Tur-bomachinery*, 118:123–133, 1996.

[2] J. Ackeret, F. Feldmann, and N. Rott. Untersuchungen an Verdichtungsstößen und Grenz-schichten in schnell bewegten Gasen. Technical Report Mitteilung Nr. 10, Eidgenössische Hochschule Zürich, Institut für Aerodynamik, 1946.

[3] P. Acton and L. Fottner. The Generation of Instationary Flow Conditions in the High-Speed Cascade Wind Tunnel of the German Armed Forces University Munich. In *13th Symposium on Measuring Techniques*, Zurich, Switzerland, 1996.

[4] W. Allan, R. Ainsworth, and S. Thorpe. Unsteady Heat Transfer Measurements from Transonic Turbine Blades at Engine Representative Conditions in a Transient Facility. *Journal of Engineering for Gas Turbines and Power*, 130:041901–1–041901–12, July 2008.

[5] A. Alonso and P. de la Calzada. Steady/Unsteady Numerical Simulation of Heat Transfer in Turbine Cascades With Separated Flows. In *5th European Conference on Turboma-chinery, Fluid Dynamics and Thermodynamics*, Praha, Czech Republic, March 2003.

[6] J. Amecke. Auswertung von Nachlaufmessungen an ebenen Schaufelgittern. Technical Report 67 A 49, AVA Göttingen, 1967.

[7] H. Ammari, N. Hay, and D. Lampard. Effect of Acceleration on the Heat Transfer Co-efficient on a Film Cooled Surface. In *Proceedings of the Gas Turbine and Aeroengine Congress and Exposition*, number 90-GT-8, Brussels, Belgium, June 1990. ASME.

[8] S. Ardey. *Untersuchung der aerodynamischen Effekte von Vorderkanten-Kühlluftausblasung an einem hochbelasteten Turbinengitter*. PhD thesis, Universität der Bundeswehr München, 1998. Fakultät für Luft- und Raumfahrttechnik.

[9] T. Arts and M. L. de Rouvroit. Aero-Thermal Performance of a Two-Dimensional Highly Loaded Transonic Turbine Nozzle Guide Vane: A Test Case for Inviscid and Viscous Flow Computations. *Journal of Turbomachinery*, 114:147–154, January 1992.

[10] T. Arts and I. Lapidus. Thermal Effects of a Coolant Film Along the Suction Side of a High Pressure Turbine Nozzle Guide Vane. In *Heat Transfer and Cooling in Gas Turbines AGARD CP527*, Antalya, Turkey, 1992.

[11] G. Barigozzi and G. Benzoni. Film Cooling Effectiveness and Heat Transfer Coefficient Distributions on a Gas Turbine Nozzle Vane. In *The 9th International Symposium on Transport Phenomena and Dynamics of Rotating Machinery*, 2002.

[12] T. Barth and D. Jesperson. The Design and Application of Upwind Schemes on Unstruc-tured Meshes. In *AIAA 27th Aerospace Sciences Meeting*, number 89-0366, 1989.

[13] M. Behle, K. Schulz, W. Leiner, and M. Fiebig. Color-Based Image Processing to Measure Local Temperature Distributions by Wide-Band Liquid Crystal Thermography. *Applied Scientific Research*, 56:113–143, 1996.

[14] R. M. Bell. *Untersuchungen zur Stoß-Grenzschicht-Interferenz an aerodynamisch hochbe-lasteten Transsonik-Verdichtergittern*. PhD thesis, Universität der Bundeswehr München, 1995. Fakultät für Luft- und Raumfahrttechnik.

[15] W. Bellows and R. Mayle. Heat Transfer Downstream of a Leading Edge Separation Bubble. In *International Gas Turbine Conference and Exhibit*, number 86-GT-59, Düsseldorf, West Germany, June, 8-12 1986. ASME.

[16] H. Blasius. Grenzschichten in Flüssigkeiten mit kleiner Reibung. *Z. Math. und Phys.*, 56:1–37, 1908.

[17] D. Bohn and H. Simon. Mehrparametrige Approximation der Eichräume und Eichflächen von Unterschall- bzw. Überschall-5-Loch-Sonden. *ATM Messtechnische Praxis*, 1975.

[18] M. P. Boyce. *Gas Turbine Engineering Handbook*. Gulf Professional Publishing, third edition, 2006.

[19] W. Boyle and G. Smith. Charge coupled semiconductor devices. *Bell Syst. Tech. J.*, 46:587–593, 1970.

[20] W. Bräunling, A. Quast, and H.-J. Dietrichs. Detection of Separation Bubbles by Infrared Images in Transonic Turbine Cascades. *Journal of Turbomachinery*, 110:504–511, October 1988.

[21] M. Breuer. Sensitivitätsanalyse der TLC Messtechnik in Wärmeübergangsuntersuchungen, 2008. DA 2007/4.19.

[22] T. Brückner. Programmierung eines Auswerteprogramms zur Kalibrierung von Fünflochsonden am Hochgeschwindigkeits-Gitterwindkanal und Vergleich der Kalibrierungen, 2003. SA 2003/3.19.

[23] R. Bunker. Gas Turbine Heat Transfer: Ten Remaining Hot Gas Path Challenges. *Journal of Turbomachinery*, 129:193–201, April 2007.

[24] L. Burmeister. *Convective Heat Transfer*. John Wiley & Sons, New York, 1983.

[25] C. Camci and T. Arts. An Experimental Convective Heat Transfer Investigation Around a Film-Cooled Gas Turbine Blade. *Journal of Turbomachinery*, 112:497–503, 1990.

[26] T. Chan, S. Ashforth-Frost, and K. Jambunathan. Calibrating for viewing angle effect during heat transfer measurements on a curved surface. *International Journal of Heat and Mass Transfer*, 44:2209–2223, 2001.

[27] S. Chandrasekhar. *Liquid Crystals*. Cambridge University Press, first edition, 1977. ISBN: 0-521-21149-2.

[28] S. Churchill. A comprehensive correlating equation for laminar, assisting, forced and free convection. *AIChE Journal*, 23(10):10–16, 1977.

[29] S. Churchill. *A Correlating Equation for Almost Everything*. Etaner Press, Thornton, 1982.

[30] W. Colban, A. Gratton, K. Thole, and M. Haendler. Heat Transfer and Film-Cooling Measurements on a Stator Vane With Fan-Shaped Cooling Holes. *Journal of Turbomachinery*, 128:53–61, 2006.

[31] S. Coulthard, R. Volino, and K. Flack. Effect of Jet Pulsing on Film Cooling — Part I: Effectiveness and Flow-Field Temperature Results. *J. Turbomachinery*, 129(2):232–246, 2007.

[32] N. A. Cumpsty. Preparing for the Future: Reducing Gas Turbine Environmental Impact. In *Proceedings of the ASME Turbo Expo 2009*, number GT2009-60367, Orlando, FL, June 2009.

[33] T. Daris and H. Bézard. Analysis of adverse pressure gradient thermal turbulent boundary layers and consequence on turbulence modelling. In *8th International Conference on Boundary and Interior Layers (BAIL 2004)*, July 2004.

[34] P. G. de Gennes. *The Physics of Liquid Crystals*. Oxford University Press, London, first edition, 1974.

[35] P. de la Calzada and A. Alonso. Numerical Investigation of Heat Transfer in Turbine Cascades With Separated Flows. *Journal of Turbomachinery*, 125:260–266, 2003.

[36] H. de Vries. Rotatory Power and Other Optical Properties of Certain Liquid Crystals. *Acta Crystallographica*, 4:219–226, 1951.

[37] J. M. Delery. Shock Wave/Turbulent Boundary Layer Interaction and Its Control. *Progress in Aerospace Sciences*, 22:209–280, 1985.

[38] R. Dénos, T. Arts, G. Paniagua, V. Michelassi, and F. Martelli. Investigation of the Unsteady Rotor Aerodynamics in a Transonic Turbine Stage. *Journal of Turbomachinery*, 123:81–89, 2001.

[39] P. Doerffer and P. Flaszynski. Flow field structure for reference case (cascade T120 with flow separation). Technical Report AITEB-2-D1.2.2-P12-06, AITEB-2, 2006.

[40] P. Doerffer and P. Flaszynski. Optimisation of the air jet hole geometry for vortex generation in the considered flow field. Technical Report AITEB-2-D1.2.3-P12-07, AITEB-2, 2007.

[41] P. Doerffer, P. Flaszynski, and K. Namiesnik. New test section 2006. Technical Report AITEB-2-D1.2.4-P12-01/06-IMP-2, AITEB-2, 2006.

[42] P. Doerffer, P. Flaszynski, and R. Szwaba. AJVG effect on the separation flow control, effect of the holes diameter and spacing. Technical Report AITEB-2-D1.2.5-P12-08, AITEB-2, 2008.

[43] P. Doerffer, P. Flaszynski, and R. Szwaba. Comparison between air cooling holes and air jet holes application. Technical Report AITEB-2-D1.2.6-P12-08, AITEB-2, 2008.

[44] P. Doerffer, P. Flaszynski, and R. Szwaba. Effect of AJVG on separation unsteadiness. Technical Report AITEB-2-D1.2.7-P12-09, AITEB-2, 2009.

[45] P. Doerffer, P. Flaszyński, and R. Szwaba. New Concept of Test Section for Flow Modeling on Suction Side of Gas Turbine Blade. In *Proceedings of the XIX. International Symposium on Air Breathing Engines (ISABE)*, number ISABE-2009-1324, September 2009. Montreal, Canada.

[46] R. Dreher and G. Meier. Optical Properties of Cholesteric Liquid Crystals. *Physical Review A*, 8:1616–1623, 1973.

[47] U. Drost and A. Bölcs. Ivestigation of Detailed Film Cooling Effectiveness and Heat Transfer Distributions on a Gas Turbine Airfoil. In *International Gas Turbine & Aeroengine Congress & Exhibition*, number 98-GT-20, Stockholm, Sweden, June 1998. ASME.

[48] F. Duchaine, A. Corpron, L. Pons, V. Moreau, F. Nicoud, and T. Poinsot. Development and assessment of a coupled strategy for conjugate heat transfer with Large Eddy Simulation. Application to a cooled turbine blade. *International Journal of Heat and Fluid Flow*, 30:1129–1141, 2009.

[49] K. Dullenkopf and R. Mayle. The Effects of Incident Turbulence and Moving Wakes on Laminar Heat Transfer in Gas Turbines. *Journal of Turbomachinery*, 116:23–28, January 1994.

[50] K. Dullenkopf and R. Mayle. An Account of Free-Stream-Turbulence Length Scale on Laminar Heat Transfer. *Journal of Turbomachinery*, 117:401–406, July 1995.

[51] M. G. Dunn. Convective Heat Transfer and Aerodynamics in Axial Flow Turbines. *Journal of Turbomachinery*, 123:637–686, October 2001. International Gas Turbine Institute Gas Turbine Scholar Lecture.

[52] E. Eckert. Cross transport of energy in fluid streams. *Wärme- und Stoffübertragung*, 21:73–81, 1987.

[53] E. Eckert and R. Drake. *Analysis of Heat and Mass Transfer*. McGraw-Hill, New York, 1972.

[54] E. Eckert and W. Weise. Messungen der Temperaturverteilung auf der Oberfläche schnell angeströmter unbeheizter Körper. *Forschung im Ingenieurwesen*, 13(6):246–254, November 1942.

[55] S. V. Ekkad, J.-C. Han, and H. Du. Detailed Film Cooling Measurements on a Cylindrical Leading Edge Model: Effect of Free-Stream Turbulence and Coolant Density. In *International Gas Turbine & Aeroengine Congress & Exhibition, Orlando, Florida, June 2–5*, number 97-GT-181, 1997.

[56] M. G. el Hak. *Flow Control — Passive, Active and Reactive Flow Management*. Cambridge University Press, first edition, 2000.

[57] T. Esch, F. Menter, and W. Vieser. Heat Transfer Predictions Based on Two-Equation Turbulence Models. In *Proceedings of the 6th ASME-JSME Thermal Engineering Joint Conference*, number TED-AJ03-542, March 2003.

[58] M. I. Ethridge, J. M. Cutbirth, and D. G. Bogard. Scaling of Performance for Varying Density Ratio Coolants on an Airfoil With Strong Curvature and Pressure Gradient Effects. *Journal of Turbomachinery*, 123:231–237, April 2001.

[59] D. J. Farina, J. M. Hacker, R. J. Moffat, and J. K. Eaton. Illuminant Invariant Calibration of Thermochromic Liquid Crystals. In *Visulization of Heat Transfer Processes-HTD*, volume 252, 1993.

[60] J. Fergason. Cholesteric Structure — 1 Optical Properties. *Molecular Crystals and Liquid Crystals*, 1:293–307, 1966.

[61] A. C. for Aeronautics Research in Europe. strategic Research Agenda 1 — Volume 2. Technical report, 2002.

[62] A. C. for Aeronautics Research in Europe. 2008 Addendum to the Strategic Research Agenda. Technical report, 2008.

[63] H. Frey. *Digitale Bildverarbeitung in Farbräumen.* PhD thesis, Technische Universität München, 1988.

[64] L. Fulachier, E. Verollet, and I. Dekeyser. Resultats experimentaux concernant une couche limite turbulente avec aspriation et chauffage a la paroi. *International Journal of Heat and Mass Transfer*, 20:731–739, 1977.

[65] K. Funazaki, M. Yokota, and S. Yamawaki. The Effect of Periodic Wake Passing on Film Effectiveness of Discrete Cooling Holes Around the Leading Edge of a Blunt Body. In *International Gas Turbine and Aeroengine Congress & Exhibition*, number 95-GT-183, Houston, Texas, June 1995. ASME.

[66] W. Ganzert. *Untersuchung zur Optimierung der Kühlluft-Ausblasekonfigurationen fortschrittlicher Turbinenbeschaufelungen.* PhD thesis, Universität der Bundeswehr München, 2000. Fakultät für Luft- und Raumfahrttechnik.

[67] P. W. Giel, R. J. Boyle, and R. S. Bunker. Measurements and Predictions of Heat Transfer on Rotor Blades in a Transonic Turbine Cascade. In *Proceedings of Turbo Expo 2003*, number 2003-GT-38839, Atlanta, Georgia, USA, June 2003. ASME.

[68] P. W. Giel, R. S. Bunker, G. J. V. Fossen, and R. J. Boyle. Heat Transfer Measurements and Predictions on a Power Generation Gas Turbine Blade. In *Proceedings of Turbo Expo 2000*, number 2000-GT-0209, Munich, Germany, May 2000. ASME.

[69] V. Gnielinski. *Chem.-Ing.-Techn.*, 61:160/161, 1989.

[70] V. Gnielinski. *Forsch. im Ing.-Wes.*, 61(9):240–248, 1995.

[71] R. Goldstein and K. Kulkarni. Energy Separation in the Wake of a Cylinder. *Journal of Heat Transfer*, 130:061703–1–061703–9, June 2008.

[72] R. Goldstein and L. Stone. Row-of-Holes Film Cooling of Curved Walls at Low Injection Angles. *Journal of Turbomachinery*, 119:574–579, 1997.

[73] R. Gomes. Validation of Measurement Technique. Technical Report R-D1.1.2-P17-2008, AITEB, 2008.

[74] R. Gomes and R. Niehuis. Aerodynamic Testing of the T120S Cascade. Technical Report AITEB-2-D1.3.3-P17-2009, AITEB-2, 2009.

[75] R. Gomes and R. Niehuis. Film Cooling Effectiveness Measurements on Highly Loaded Blades With Flow Separation. In *8th European Conference on Turbomachinery (ETC)*, number 237, Graz, Austria, March 2009.

[76] Hallcrest. *Handbook of Thermochromic Liquid Crystal Technology.* http://www.hallcrest.com/downloads/RT006 20randtk_TLC_Handbook.pdf.

[77] F. Haselbach and H. Schiffer. Aerothermal Investigations on Turbine Endwalls and Blades (AITEB). In *Proceedings of the ASME Turbo Expo 2004*, number GT2004-53078, Vienna, Austria, June 2004.

[78] J. D. Heidmann, B. L. Lucci, and E. Reshotko. An Experimental Study of the Effect of Wake Passing on Turbine Blade Film Cooling. In *Proceedings of GT1997*, number 97-GT-255, Orlando, FL, June 1997.

[79] L. Hilgenfeld. *Turbulenzstrukturen in hochbelasteten Transsonik-Verdichtergittern unter besonderer Berücksichtigung der Verdichtungsstoß-Grenzschicht-Interferenz.* PhD thesis, Universität der Bundeswehr München, 2006. Fortschritt-Berichte VDI, Reihe 7 Nr. 487.

[80] L. Homeier. The aerodynamic effects of film cooling with steady and periodic unsteady inflow conditions on HPT T120 with 2 different cooling configurations. Technical Report R-D1.5-P14/04, AITEB, 2004.

[81] L. Homeier. *Experimentelle Untersuchungen an hochbelsteten Hochdruckturbinengittern mit Filmkühlung in Gebieten mit positiven Druckgradienten.* PhD thesis, Universität der Bundeswehr München, 2006. Fakultät für Luft- und Raumfahrttechnik.

[82] F. Horton, D. Schultz, and A. Forest. Heat Transfer Measurements With Film Cooling on a Turbine Blade Profile in Cascade. In *Gas Turbine Conference and Exhibit*, number 85-GT-117, Houston, Texas, March 1985.

[83] M. Howes and D. Morgan. *Charge-coupled Devices and Systems.* John Wiley & Sons, first edition, 1979.

[84] P. Ireland and T. Jones. Liquid crystals measurements of heat transfer and surface shear stress. *Measurement Science and Technology*, 11:969–986, 2000.

[85] S. Ito, R. Goldstein, and E. Eckert. Film Cooling of a Gas Turbine Blade. *Journal of Engineering for Power*, 100:476–481, July 1978.

[86] E. Janke. CFD Investigation of T120 Airfoil with and without film cooling using FLU-ENT. Technical Report R-D1.6-P01/04, AITEB, 2004.

[87] J. P. Johnston and M. Nishi. Vortex Generator Jets — Means for Flow Separation Control. *AIAA Journal*, 28:989–994, June 1990.

[88] R. Johnston and S. Fleeter. Compressible flow hot-wire calibration. *Experiments in Fluids*, 22:444–446, 1997.

[89] N. Kasagi, R. Moffat, and M. Hirata. *Handbook of Flow Visualization*, chapter 8. Hemisphere Publishing Corp., New York, 1989.

[90] W. Kays, M. Crawford, and B. Weigand. *Convective Heat and Mass Transfer*. McGraw-Hill, New York, fourth edition edition, 2005. ISBN: 0-07-246876-9.

[91] H. Kelker and R. Hatz. *Handbook of Liquid Crystals*. Verlag Chemie, Weinheim, 1980. ISBN: 3-527-25481-1.

[92] L. V. King. On the Convection of Heat from Small Cylinders in a Stream of Fluid: Determination of the Convection Constants of Small Platinum Wires with Applications to Hot-Wire Anemometry. *Philosophical Transactions of the Royal Society of London*, 214(Series A):373–432, 1914.

[93] K. Küblbeck. *Laminare und turbulente Ausbreitungsvorgänge infolge freier und erzwungener Konvektion*. PhD thesis, TU München, 1981.

[94] B. Lackshminarayana. *Fluid Dynamics and Heat Transfer of Turbomachinery*. John Wiley & Sons, Inc., New York, 1996.

[95] G. Lowery and R. Vachon. Effect of Turbulence on Heat Transfer From Heated Cylinders. *International Journal of Heat and Mass Transfer*, 18(1):1229–1242, 1975.

[96] E. Lutum and B. Johnson. Influence of the Hole Length-to-Diameter Ratio on Film Cooling With Cylindrical Holes. *Journal of Turbomachinery*, 121:209–216, April 1999.

[97] E. Lutum, J. von Wolfersdorf, K. Semmler, S. Naik, and B. Weigand. Film Cooling on a Concave Surface: Influence of External Pressure Gradient on Film Cooling Performance. In *Symposium on Advanced Flow Management*, Norway, May 2001. RTO Applied Vehicle Technology Panel (AVT) Meeting Week.

[98] H. Martin. *Vorlesung Wärmeübertragung II*. Univ. Karlsruhe (TH), 1990.

[99] M. Marziale and R. Mayle. Effect of an Oscillating Flow Direction on Leading Edge Heat Transfer. *Journal of Engineering for Gas Turbines and Power*, 106:222–228, January 1984.

[100] R. Mayle, F. Kopper, M. Blair, and D. Bailey. Effect of Streamline Curvature on Film Cooling. *Journal of Engineering for Power*, 99:77–82, January 1977.

[101] R. E. Mayle. The Role of Laminar-Turbulent Transition in Gas Turbine Engines. *J. Turbomachinery*, 113:509–537, 1991.

[102] J. D. McGervey. *Quantum Mechanics — Concepts and Applications*. Academic Press, San Diego, CA, first edition, 1995.

[103] A. Mehendale and J. Han. Influence of High Mainstream Turbulence on Leading Edge Film Cooling Heat Transfer. *Journal of Turbomachinery*, 114:707–714, October 1992.

[104] A. Mehendale, J. Han, and S. Ou. Influence of High Mainstream Turbulence on Leading Edge Heat Transfer. *Journal of Heat Transfer*, 113:843–850, 1991.

[105] A. Mehendale, J.-C. Han, S. Ou, and C. Lee. Unsteady Wake Over a Linear Turbine Blade Cascade With Air and CO2 Film Injection: Part II — Effect on Film Effectiveness and Heat Transfer Distributions. *Journal of Turbomachinery*, 116:730–737, October 1994.

[106] F. Menter. Two-Equation Eddy-Viscosity Turbulence Models for Engineering Applications. *AIAA-Journal*, 32(8):1598–1605, 1994.

[107] F. Menter, J. C. Ferreira, T. Esch, and B. Konno. The SST Turbulence Model with Improved Wall Treatment for Heat Transfer Predictions in Gas Turbines. In *Proceedings of the International Gas Turbine Congress*, number IGTC2003-TS-059, November 2003.

[108] F. Menter, R. Langtry, S. Likki, Y. Suzen, P. Huang, and S. Völker. A Correlation-Based Transition Model Using Local Variables: Part I — Model Formulation. In *ASME TURBO EXPO 2004*, number GT2004-53452, 2004.

[109] G. Merker. *Konvektive Wärmeübertragung*. Springer-Verlag, Berlin, 1987. ISBN: 3-540-16995-4.

[110] W. Mick and R. Mayle. Stagnation Film Cooling and Heat Transfer, Including Its Effect Within the Hole Pattern. *Journal of Turbomachinery*, 110:66–72, January 1988.

[111] H. Pfeil and J. Eifler. Messungen im turbulenten Nachlauf des Einzelzylinders. *Forschung im Ingenieurwesen*, 5:137–168, 1975.

[112] J. Pluim, C. Memory, J. Bons, and J.-P. Chen. Designing a High Fidelity Wake Simulator for Research Using Linear Cascades. In *Proceedings of ASME Turbo Expo 2009, Orlando, Florida, June 8–12*, number GT2009-59276, 2009.

[113] E. Pohlhausen. Der Wärmeaustausch zwischen festen Körpern und Flüssigkeiten mit kleiner Reibung und kleiner Wärmeleitung. *Z. Angew. Math. Mech.*, 1:115–121, 1921.

[114] L. Pons and R. Gomes. Definition of CFD pre- and post-processing guidelines for blade T120 C-D. Technical Report AITEB-2-D1.1.7-P07&P17-2009_add, AITEB-2, 2009.

[115] R. Radomsky and K. Thole. Effects of High Freestream Turbulence Levels and Length Scales on Stator Vane Heat Transfer. In *International Gas Turbine & Aeroengine Congress & Exhibition, Stockholm, Sweden, June 2–5*, number 98-GT-236, 1998.

[116] G. S. Rixon and H. Johari. Development of a Steady Vortex Generator Jet in a Turbulent Boundary Layer. *Journal of Fluids Engineering*, 125:1006–1015, November 2003.

[117] Rolls-Royce, editor. *The Jet Engine*. Renault Printing Co Ltd, fifth edition, 1996.

[118] H. Schlichting and K. Gersten. *Grenzschicht-Theorie*. Springer-Verlag, tenth edition, 2006.

[119] D. L. Schmidt and D. G. Bogard. Effects of Free-Stream Turbulence and Surface Roughness on Film Cooling. In *International Gas Turbine and Aeroengine Congress & Exhibition*, number 96-GT-462, Birmingham, UK, June 1996. ASME.

[120] U. Schmidt. *Ein Beitrag zur systemtheoretischen Bewertung von CCD-Bildaufnahmesystemen*. PhD thesis, Technische Universität Ilmenau, 1993.

[121] M. Schobeiri, P. Chakka, and K. Pappu. Unsteady Wake Effects on Boundary Layer Transition and Heat Transfer Characteristics of a Turbine Blade. In *Proceedings of the International Gas Turbine & Aeroengine Congress & Exhibition*, number 98-GT-291, Stockholm, Sweden, June 1998. ASME.

[122] M. Schobeiri, B. Ötztürk, M. Kegalj, and D. Bensing. On the Physics of Heat Transfer and Aerodynamic Behavior of Separated Flow Along a Highly Loaded Low Pressure Turbine Blade Under Periodic Unsteady Wake Flow and Varying of Turbulence Intensity. *International Journal of Heat Transfer*, 130:051703–1–051703–20, 2008.

[123] N. Scholz. *Aerodynamik der Schaufelgitter*, volume 1. Verlag G. Braun, 1965.

[124] H. Schreiber and H. Starken. An Investigation of a Strong Shock-Wave Turbulent Boundary Layer Interaction in a Supersonic Compressor Cascade. *Journal of Turbomachinery*, 114:494–503, 1992.

[125] H.-A. Schreiber. Shock-Wave Turbulent Boundary Layer Interaction in a Highly Loaded Transonic Fan Blade Cascade. In *85th AGARD PEP Symposium*, number 17, UK, May 1995.

[126] S. Schwarz and R. Goldstein. The Two-Dimensional Behavior of Film Cooling Jets on Concave Surfaces. *Journal of Turbomachinery*, 111:124–130, April 1989.

[127] S. Schwarz, R. Goldstein, and E. Eckert. The Influence of Curvature on Film Cooling Performance. *Journal of Turbomachinery*, 113:472–478, July 1991.

[128] F. W. Sears. *Optics*. Addison-Wesley Publishing Company, Inc., third edition, 1975. p. 241.

[129] R. Shah and A. London. *Laminar Flow Forced Convection in Ducts*. Academic Press, New York, San Francisco, London, 1978.

[130] A. Z. Shahneh and F. Motallebi. An Experimental Study on the Influence of Vortex Generators on the Shock-Induced Boundary Layer Separation at M=1.4. *Journal of Applied Mechanics*, 76:041009–1–041009–8, July 2009.

[131] J. Smagorinsky. General Circulation Experiments With the Primitive Equations. *Monthly Weather Review*, 91(3):99–164, March 1963.

[132] S. Solomon, D. Qin, M. Manning, Z. Chen, M. Marquis, K. Averyt, M. Tignor, and H. M. (eds.). IPCC Fourth Assessment Report — Climate Change 2007: The Physical Scinece Basis. Technical report, Intergovernmental Panel on Climate Change, 2007.

[133] Sony Business Europe. *Datenblatt Sony Network Camera SNC–CS3P*.

[134] P. R. Spalart. Young Person's Guide to Detached-Eddy Simulation Grids. Technical Report CR 2001-211032, NASA, 2001.

[135] P. Stainback and K. Nagabushana. Review of Hot-Wire Anemometry Techniques and the Range of their Applicability for Various Flows. *Electronic Journal of Fluids Engineering*, 1996.

[136] C. Starke and E. Janke. Prediction of T120 at higher pitch-to-chord with Mises and Numeca. Technical Report AITEB-2-D1.2.1-P01-07, AITEB-2, 2007.

[137] J. Stasiek. Thermochromic liquid crystals and true colour image processing in heat transfer and fluid-flow research. *Heat and Mass Transfer*, 33:27–39, 1997.

[138] J. Stasiek and T. Kowalewski. Thermochromic liquid crystals applied for heat transfer research. *Opto-Electronics Review*, 10(1):1–10, 2002.

[139] K. Stephan. *Chem.-Ing.-Techn.*, 31:773–778, 1959.

[140] M. Strelets. Detached Eddy Simulation of Massively Separated Flows. In *39th Aerospace Science Meeting and Exhibit*, number AIAA paper 2001-0879, Reno, NV, 2001.

[141] W. Sturm and L. Fottner. The High-Speed Cascade Wind-Tunnel of the German Armed Forces University Munich. In *8th Sympsium on Measuring Techniques for Transonic and Supersonic Flows in Cascades and Turbomachines*, Genova, Italy, October 1985.

[142] R. Szwaba. Shock Wave Induced Separation Control by Air-Jet Vortex Generators in the Curved Nozzle. In *Proceedings of the XIX. International Symposium on Air Breathing Engines (ISABE)*, number ISABE-2009-1292, Montreal, Canada, September 2009.

[143] R. Szwaba, P. Flaszynski, J. Szumski, and J. Telega. Shock Wave — Boundary Layer Interaction Control by Air-Jet Streamwise Vortices. In *Proceedings of 8th International Symposium on Experimental and Computational Aerothermodynamics of Internal Flows*, number ISAIF8-0035, Lyon, France, July 2007.

[144] J. Täge. Design of Suction Side Film-Cooling Hole. Technical Report AITEB-2-D1.3.1-P01-07, AITEB-2, 2007.

[145] G. Taylor. The Spectrum of Turbulence. *Proceedings of the Royal Society of London. Series A, Mathematical and Physical Sciences*, 164(919), 1938.

[146] S. Teng, D. K. Sohn, and J.-C. Han. Unsteady Wake Effect on Film Temperature and Effectiveness Distributions for a Gas Turbine Blade. *Journal of Turbomachinery*, 122:340–347, April 2000.

[147] V. Terekhov, N. Yarygina, and R. Zhdanov. Heat transfer in turbulent separated flows in the presence of high free-stream turbulence. *International Journal of Heat and Mass Transfer*, 46:4535–4551, 2003.

[148] A. J. Toepler. *Beobachtung nach einer neuen optischen Methode*. Number 157 in Ostwald's Klassiker der exakten Wissenschaften. Engelmann Verlag, Leipzig, 1906.

[149] B. van Oudheusden. Energy Separation in Steady Separated Wake Flow. *Journal of Fluids Engineering*, 127:611–614, May 2005.

[150] Verein Deutscher Ingenieure, editor. *VDI-Wärmeatlas.* Springer Verlag, Berlin, ninth edition, 2002.

[151] W. Vieser, T. Esch, and F. Menter. Heat Transfer Predictions using Advanced Two-Equation Turbulence Models. Technical Report CFX-VAL10/0602, CFX, 2002.

[152] R. Volino and T. Simon. Boundary Layer Transition Under High Free-Stream Turbulence and Strong Acceleration Conditions: Part 1 — Mean Flow Results. *Journal of Heat Transfer*, 119:420–426, August 1997.

[153] R. Volino and T. Simon. Velocity and Temperature Profiles in Turbulent Boundary Layer Flows Experiencing Streamwise Pressure Gradients. *Journal of Heat Transfer*, 119:433–439, August 1997.

[154] R. Wallis. A Preliminary Note on a Modified Type of Air Jet for Boundary Layer Control. Technical Report C.P. No. 513, Aeronautical Research Council, Australia, 1960.

[155] S. K. Waye and D. G. Bogard. High-Resolution Film Cooling Effectiveness Measurements of Axial Holes Embedded in a Transverse Trench With Various Trench Configurations. *Journal of Turbomachinery*, 129:294–302, April 2007.

[156] R. Wilcock, J. Young, and J. Horlock. The Effect of Turbine Blade Cooling on the Cycle Efficiency of Gas Turbine Power Cycles. *Journal of Engineering for Gas Turbines and Power*, 127:109–120, January 2005.

[157] D. Wilcox. Multiscale model for turbulent flows. In A. I. of Aeronautics and Astronautics, editors, *AIAA 24th Aerospace Sciences Meeting*, 1986.

[158] G. Wilfert. *Experimentelle und numerische Untersuchungen der Mischungsvorgänge zwischen Kühlfilmen und Gitterströmung an einem hochbelasteten Turbinengitter.* PhD thesis, Universität der Bundeswehr München, 1994. Fakultät für Luft- und Raumfahrttechnik.

[159] S. Wolff, L. Homeier, and L. Fottner. Experimental Investigation of Heat Transfer in Separated Flow on a Highly Loaded LP Turbine Cascade. In *Proceeding of the RTO/AVT Symposium and Specialists Meeting*, Loen, Norway, May 2001.

[160] K. Womack, R. Volino, and M. Schultz. Measurements in Film Cooling Flows With Periodic Wakes. In *Proceedings of GT2007*, number GT2007-27917, Montreal, Canada, May 2007.

[161] D. Wunderwald. *Untersuchung der Turbulenzstrukturen in hochbelasteten Verdichter- und Turbinengitter.* PhD thesis, Universität der Bundeswehr München, 1995. Fakultät für Luft- und Raumfahrttechnik.
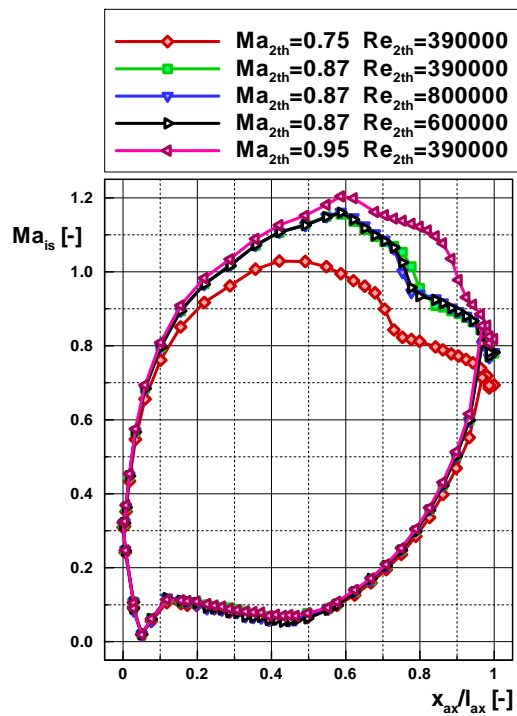
A Figures

Figure A.1: Profile isentropic Mach number distribution on the *T120C* blade for $\beta_1 = 138.6°$, from [80]

Figure A.2: Colour transition of the reflected light as function of the temperature

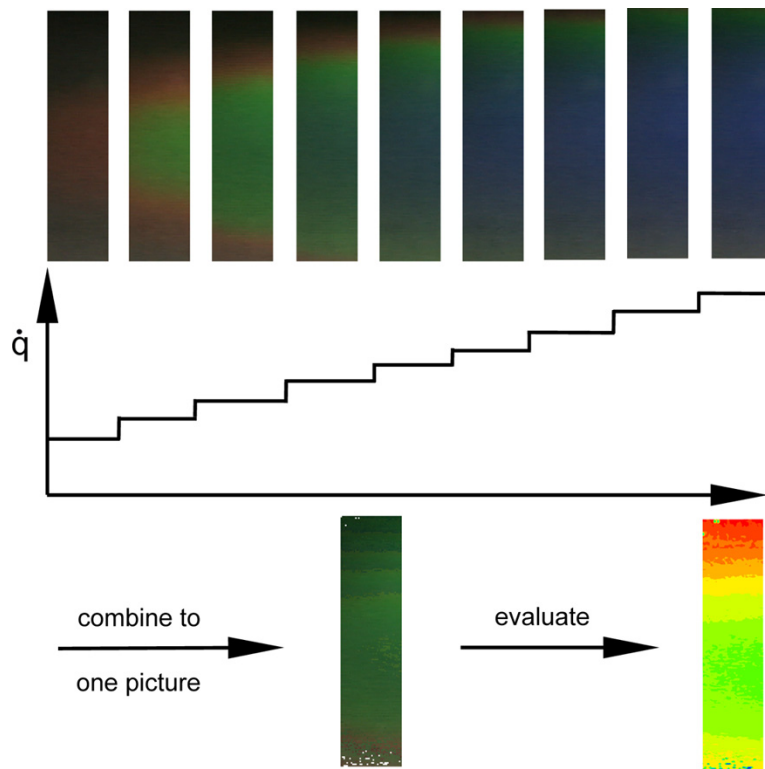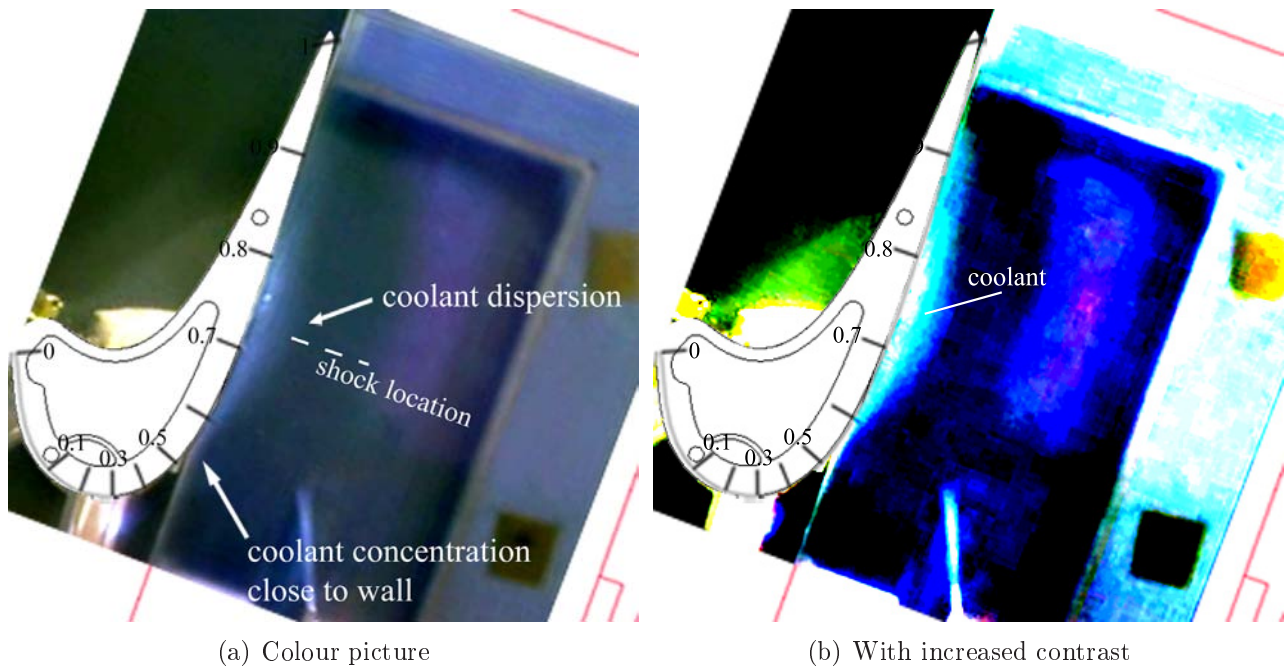Figure A.3: Schematic of the measuring technique

(a) Colour picture

(b) With increased contrast

Figure A.4: Visualization of coolant flow with smoke tracer

wind-tunnel data :

- a.c. electric motor	$P = 1300$ kW
- axial compressor	6 stages
- air flow rate	$\dot{V} = 30 \, \text{m}^3/\text{s}$
- rotational speed	$n_{max} = 6300 \, \text{min}^{-1}$
- total pressure ratio	$P_{t1}/p_K = 2.14$
- tank pressure	$p_k = 0.04 - 1.2$ bar

test section data:

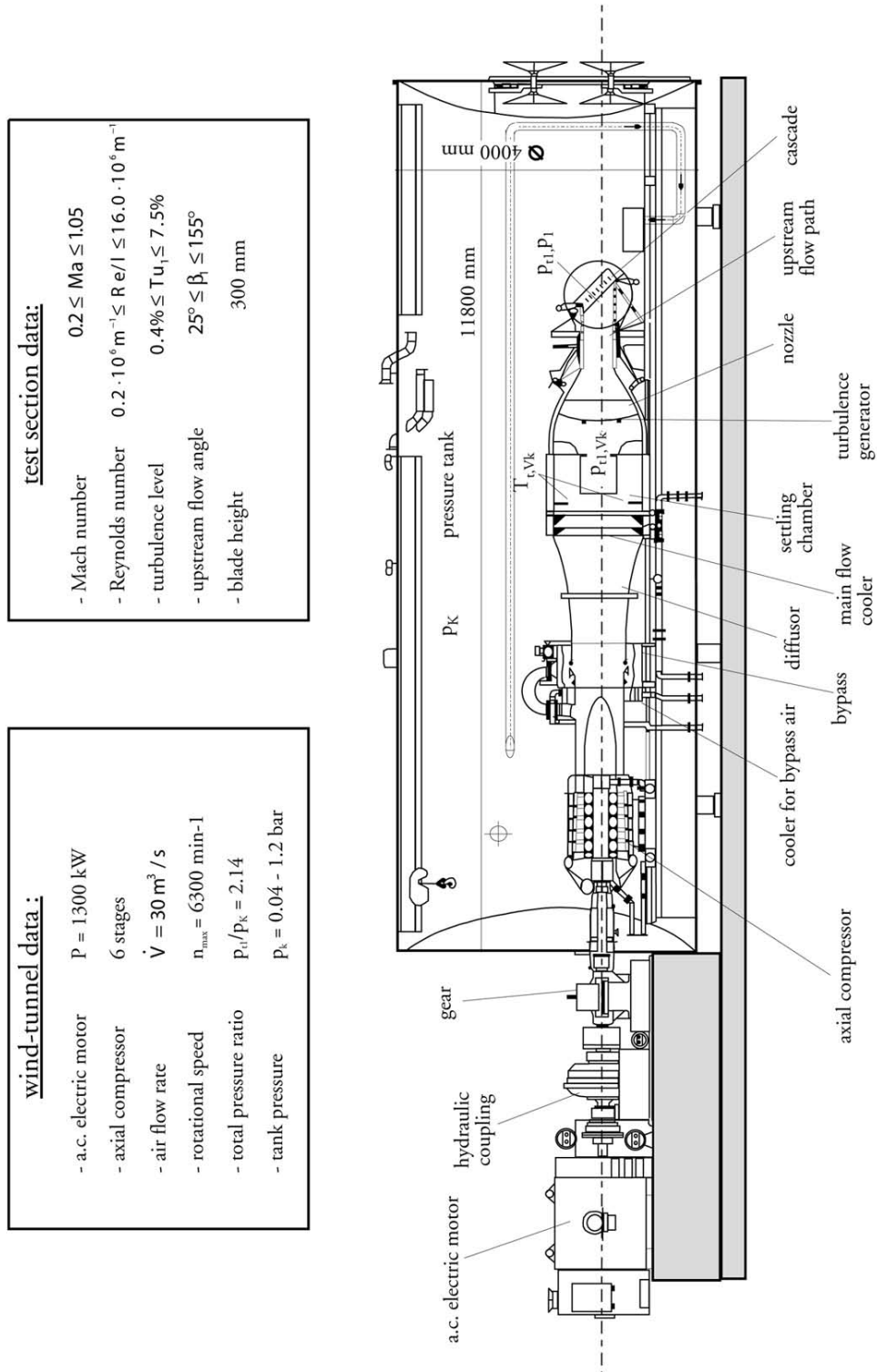|	
- Mach number	$0.2 \leq Ma \leq 1.05$
- Reynolds number	$0.2 \cdot 10^6 \, \text{m}^{-1} \leq Re/l \leq 16.0 \cdot 10^6 \, \text{m}^{-1}$
- turbulence level	$0.4\% \leq Tu_1 \leq 7.5\%$
- upstream flow angle	$25° \leq \beta_1 \leq 155°$
- blade height	300 mm

Figure A.5: The High-Speed Cascade Wind-Tunnel with technical description
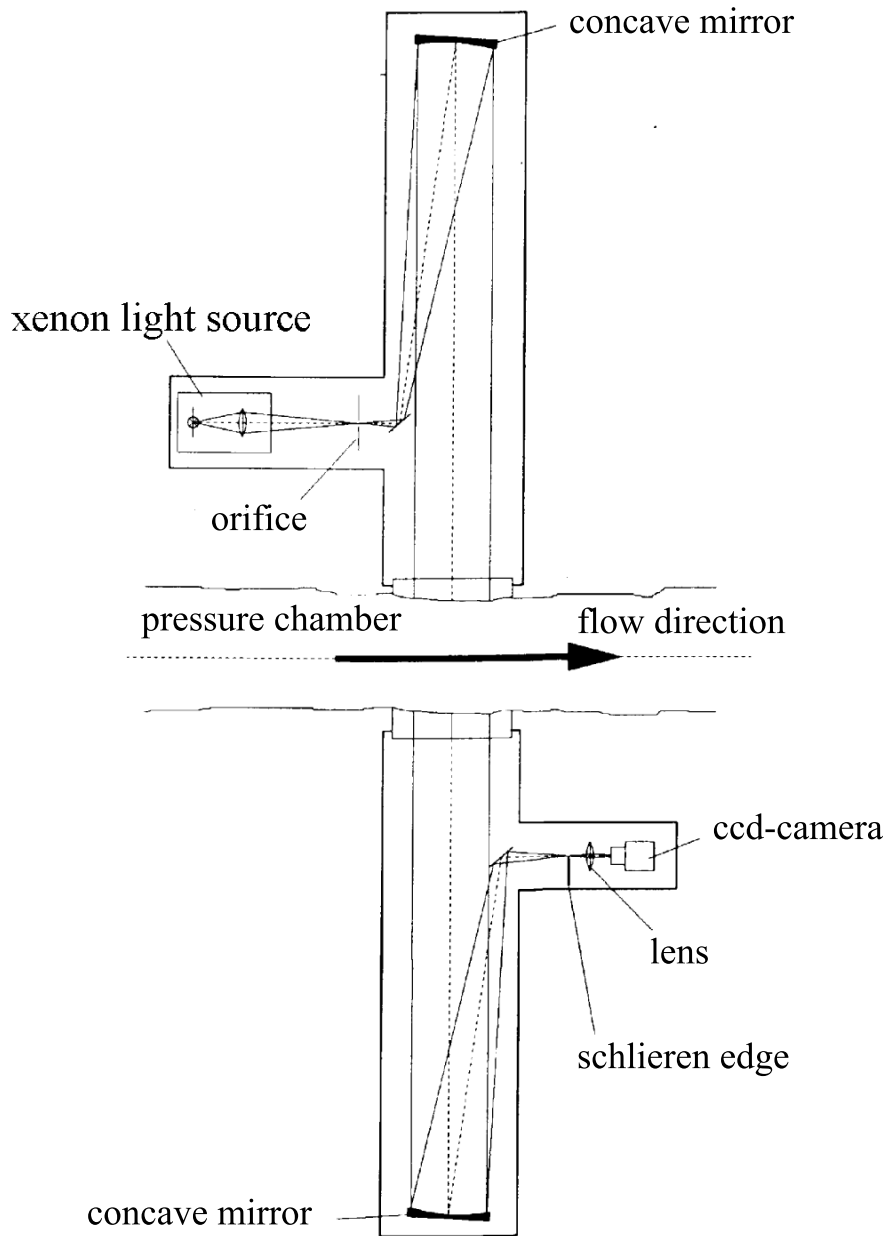
173

Figure A.6: Sketch of the test arrangement for Schlieren pictures

B On the Energy Separation Effect

The phenomenon of energy separation is reported the latest since the 40's of the twentieth century. A typical configuration for those analysis is a cylinder in cross-flow at Reynolds numbers where flow separation occurs. In Eckert [52] an overview on this topic is given and experiments, numerical and theoretical studies are reported e. g. in Eckert and Weise [54], van Oudheusden [149] and Goldstein and Kulkarni [71]. The flow downstream of the cylinder shows diminishing recovery or total temperatures in the wake regions, which can lead to the recovery temperature at the cylinder to be lower than the static temperature of the stream outside the boundary layer. An explanation for this effect taken from Goldstein and Kulkarni [71] is presented in fig. B.1. The relative velocity of the vortex moving with the free stream is located close to the border between the viscous and inviscid part of the vortex. Due to viscous effect the relative velocity tends to zero at the center of the vortex. In the absolute frame both velocity components have to be superimposed leading to the velocity distribution on the right of fig. B.1.

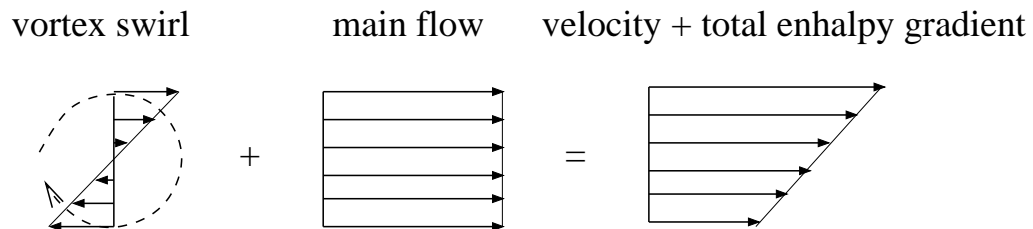vortex swirl   main flow   velocity + total enhalpy gradient

Figure B.1: Velocity superposition of vortex with free stream

For the flow on the suction side of the *T120S* blade it is shown that the boundary layer at the shock location increases dramatically due to the pressure gradient[1]. In this cascade the increase of the boundary layer can get larger than usual, because there is no solid wall on the opposite side limiting the flow channel and the boundary layer increase leads even to a deviation of the trailing edge of the neighboring blade. When the boundary layer decreases downstream of the shock the flow rolls up and creates vortices as shown in fig. B.2. These vortices lead to lower absolute velocities close to the wall and therefore lower recovery temperature.

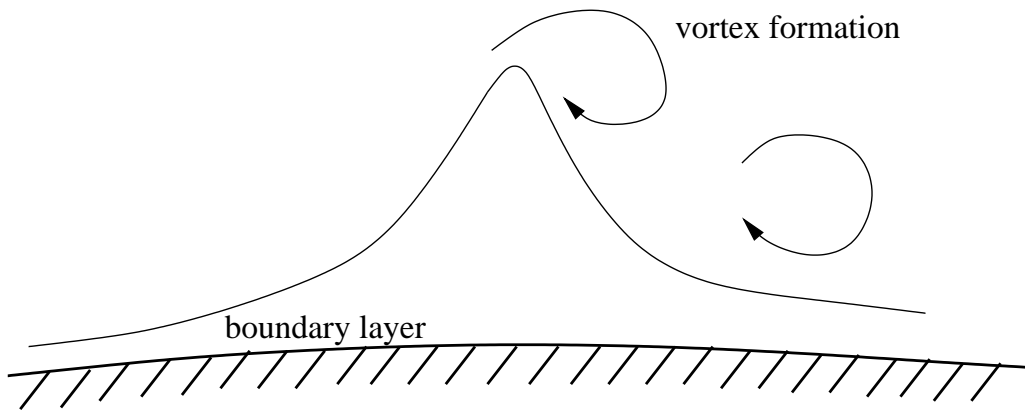[1]In fact this is reported in many publications about transonic flow

vortex formation

boundary layer

Figure B.2: Schematic of the boundary layer at the shock location and vortex
          shedding at the shock location

Curriculum Vitae

Name	Reinaldo Araújo Gomes
Date of Birth	26 March 2010
Place of Birth	Schopfheim, Germany
Nationalities	German / Portuguese

Education

1985-1989	Grundschule Hausen
1989-1990	Montfort-Realschule-Zell
1990-1995	Theodor-Heuss Gymnasium Schopfheim
1995-1998	Technisches Gymnasium Lörrach

University

1998-2004	University Stuttgart
	Diploma Degree in Mechanical Engineering

Work Experience

since 2004	Universität der Bundeswehr München
	Research Assistant at the Institute of Jet Propulsion